Numerical methods for frustrated magnetism:

From quantum to classical spin systems

zur Erlangung des Grades einer Doktorin
der Naturwissenschaften (Dr. rer. nat.)

am Fachbereich Physik
der Freien Universität Berlin

vorgelegt von MARIA LAURA BAEZ

Berlin, 2018

Erstgutachter: Prof. Dr. Johannes Reuther (Freie Universität Berlin und Helmholtz-Zentrum Berlin)

Zweitgutachter: Prof. Dr. Jens Eisert (Freie Universität Berlin)

Tag der Disputation: 27.07.2018

To my dad.
For the telescopes at night,
the experiments he let me do in his labs,
and all the Asimov books he taught me to read.
For the love of science he passed onto me.

Abstract

In this thesis, we will concentrate on the numerical study of classical and quantum frustrated magnets. If we focus on the full set of problems which are contained in the class of quantum spin systems, we see that the techniques which can deal with them are plenty, but that the presence of frustration introduces several methodological hindrances. Whether it is the presence of a sign problem, or the extensive resources needed to perform the computation, many of these methods are efficient only on a reduced subset of frustrated systems. We will employ the pseudofermion-Functional Renormalization Group (pfFRG) method as our method of choice to tackle two dimensional frustrated quantum magnets, all of them modeled via a Heisenberg Hamiltonian. We will extend the pfFRG formalism to include spin systems where the spin length is unrestricted, $S \geq 1/2$. With this extension we are able to study in detail what the effect of quantum fluctuations are on the system. From the extreme quantum limit ($S = 1/2$) to the classical limit ($S \to \infty$), the large-S extension of pfFRG allows us to manipulate the strength of the quantum fluctuations and study in detail how the quantum to classical transition happens. We apply this method to the study of incommensurate phases in the Heisenberg honeycomb model. We map the phase diagram for different values of the spin length and analyze how this length, and subsequently quantum fluctuations, affect the phases found in the classical limit. Furthermore, we prove that in the classical limit, pfFRG reduces to the Luttinger-Tisza formalism.

When quantum fluctuations can be neglected, we model our frustrated magnet as a classical spin system. While this limit can easily be obtained from the large-S extension of pfFRG, this methodology is constrained to the study of two point correlators at zero temperature. To collect information regarding the behavior of our classical magnet beyond the two point correlators we study classical spin systems via Monte Carlo simulations. In this case we show how the method can be applied to continuous spin systems with strong anisotropic interaction. Furthermore, we employ this technique to numerically study α-Li_2IrO_3, a material which exhibits an incommensurate ground state but for which a minimal model has not been determined. We study and compare the possible minimal models that have been proposed. We reduce the number of minimal models by showing that many of those that have been proposed do not reproduce the full set of experimental results. Furthermore, we predict the magnetic behavior (for those models which reproduce the experimental results) in the presence of an external magnetic field. With this study we obtain magnetization processes and propose experiments which can confirm if one of the studied models is the correct minimal model for α-Li_2IrO_3.

ZUSAMMENFASSUNG

In dieser Dissertation werden wir uns mit der numerischen Erforschung frustrierter klassischer und Quantenmagneten befassen. Wenn wir die vollstände Menge an Problemen in der Klasse der Quanten-Spin-Systeme betrachten, dann sehen wir, dass diese durch eine breite Anzahl von Methoden bearbeitet werden kann, Frustration jedoch einige methodische Hindernisse mit sich bringt. Sei es das Vorhandensein eines Vorzeichenproblems oder die erheblichen für die Rechnung benötigten Ressourcen, viele dieser Methoden sind nur bei einer kleinen Menge frustrierter System effizient. Die pseudofermionische funktionale Renormalisierungsgruppe (pfFRG) wird die Methode unserer Wahl sein um zweidimensionale frustrierte Quantenmagneten, modelliert mittels eines Heisenberg Hamiltonians, anzugehen. Wir werden den pfFRG Formalismus so erweitern, dass er Spinsysteme unbeschränkter Spinlänge, $S \geqslant 1/2$, umfasst. Durch diese Erweiterung sind wir in der Lage den Effekt von Quantenfluktuationen auf das System zu untersuchen. Die Erweiterung der pfFRG für große S erlaubt uns die Stärke der Quantenfluktuationen vom extremen Quantenlimit ($S = 1/2$) bis zum klassischen Limit ($S \to \infty$) zu manipulieren und genau zu untersuchen wie der Quanten-klassische Übergang stattfindet. Wir wenden diese Methode auf die inkommensurablen Phasen des Heisenberg-Honeycomb-Modells an. Wir erkunden das Phasendiagramm für verschiedene Werte der Spinlänge und analysieren wie sie und später Quantenfluktuation die die Phase im klassischen Limes beeinflussen. Des Weiteren beweisen wir, dass pfFRG im klassischen Limes den Luttinger-Tisza-Formalismus ergibt.

Wenn Quantenfluktuationen vernachlässigt werden können modellieren wir unseren frustrierten Magneten als ein klassisches Spinsystem. Zwar kann dieser Limes leicht aus der Erweiterung der pfFRG für große S gewonnen werden, ist jedoch auf Zweipunkt-Korrelatoren bei $T = 0$ beschränkt. Um Informationen über das Verhalten unseren klassischen Magneten über Zweipunkt-Korrelatoren hinaus zu gewinnen, untersuchen wir klassische Spinsysteme mit Hilfe von Monte Carlo-Simulationen. In diesem Fall zeigen wir wie diese Methode auf System mit kontinuierlichem Spin mit stark anisotropen Wechselwirkungen angewendet werden kann. Weiterhin benutzen wir diese Methode um α-Li_2IrO_3, ein Material, das einen inkommensurablen Grundzustand aufweist und für das noch noch kein minimales Modell gefunden wurde, numerisch zu untersuchen. Wir untersuchen und vergleichen die möglichen, vorgeschlagenen minimalen Modelle. Wir reduzieren die Anzahl minimaler Modelle indem wir zeigen, dass viele der vorgeschlagenen Modelle nicht den vollen Umfang experimenteller Ergebnisse reproduziert. Weiterhin sagen wir das magnetische Verhalten in einem externen Magnetfeld der Modelle, die die

experimentellen Resultate reproduzieren, voraus. Mit Hilfe dieser Voraussage erhalten wir Magnetisierungsprozesse und schlagen Experimente vor, die bestätigen können ob eines der minimalen Modelle das Modell für α-Li_2IrO_3 ist.

TABLE OF CONTENTS

LIST OF TABLES

TABLE **Page**

List of Figures

CHAPTER 1

INTRODUCTION

I'm smart enough to be confused,
but not smart enough to resolve
the confusion.

Christian Fräßdorf, 2018

The central topic of this thesis will consist on the numerical study of frustrated magnetic insulators. There are different ways in which magnetism can arise in materials. From itinerant magnets modeled via RKKY interactions [2], to impurity models exhibiting Kondo effects [3], the models which represent magnetic behavior are plenty. In our case we will be interested in magnetic materials which can be described by the Heisenberg Hamiltonian [4] and associated models. In its more general formulation, the Heisenberg model takes the form

$$\mathscr{H} = \sum_{ij} J_{ij} \mathbf{S}_i \mathbf{S}_j \,, \tag{1.1}$$

where the spins $\mathbf{S}_i$ are located at sites i of a given lattice, and they interact via an *exchange* coupling J_{ij}. We want to study the particular case when this model is frustrated. A system is called frustrated when not all terms of the representative Hamiltonian can be minimized simultaneously. More specifically, in the systems we are interested in, many interacting degrees of freedom are present, and frustration can be understood as these interactions competing with each other, each one favoring one particular type

of correlation, which cannot all be realized at the same time. Frustration in magnetic systems started to be intensively studied after the initial proposals by Anderson [5, 6]. He suggested that competing interactions can make it impossible for certain magnetic systems to order, leading to a disordered ground state, the so called *spin liquid* state.

We can distinguish different classes of frustration in magnetic materials. One one hand we have *geometric frustration*, where the lattice structure imposes several constraints on the system inhibiting the minimization of every term of the Hamiltonian simultaneously. An example of this is that of an antiferromagnetic Ising model on the triangular lattice [7]. In this case, not all spins can fulfill the antiferromagnetic condition at the same time. This leads to an extensive configurational disorder in the spin orientation and a remnant zero point entropy. On the other hand, we can have *non-geometric frustration* where the interactions themselves affect the behaviour of the system. An example on non-geometric frustration emerges from different competing interactions in the Hamiltonian. This competition leads to non-trivial spatial correlations, as e.g on the honeycomb lattice with nearest and second neighbour antiferromagnetic Heisenberg interactions [8]. Another form of non-geometric frustration arises from systems with strong anisotropies. For example, Kitaev models [9], where the bond anisotropy induces different interactions on different lattice bonds, and this leads to non-trivial phases, which cannot always be observed in geometrically frustrated systems.

The Heisenberg model (Eq. 1.1) shines in its simplicity, it states that our insulating magnet can be simply considered as spins localized on lattice sites, and completely omits the existence of electrons and nuclei. However, even though the model is very simple, a large number of materials can be modeled with it. With the Heisenberg model as a starting point, many different associated models can be created. The Heisenberg model is not constrained to act only on nearest neighbors, and not all spin components need to be coupled via the same exchange coupling, an example of this last point is the famous XXZ model, where two spin components are coupled via the same exchange, while the third can be very different, changing not only in value, but sign. What is even more important, the Heisenberg model can be studied both in their classical and quantum version giving rise to some of the canonical examples not only for magnetic materials, but also for the study of both quantum and thermal phase transitions. Some canonical examples in the classical realm of associated Heisenberg models are those of the Ising and XY models. The Ising model is a playground in which to study and learn spontaneous symmetry breaking and thermal phase transitions, while the XY model was one of the first examples of topological phase transitions exhibiting a Kosterlitz-Thouless transitions [10]. On the

quantum limit, the transverse field Ising model is the canonical example for quantum phase transitions, and the much more recent Kitaev model [9] is extremely studied for it's disordered ground states and exotic excitations.

With all of this in mind, we have to restrict our study to some part of the field, now quite large, of frustrated magnetic insulators. In this thesis, we will study both sides of the spectrum, those of classical and quantum magnetism, and we will analyze how this limit comes about, and what the effects of quantum fluctuations are on the physics of our model. Furthermore, we will study a particular set of ground states (helimagnetic states) which arise in many different forms, either from a pure Heisenberg model, or from extended models arising from the Heisenberg Hamiltonian.

Of course, a study like this, while interesting from a purely theoretical point of view, is also motivated by experiments. Many materials exhibit Heisenberg like physics, both in the quantum and classical limit. For example, $LiHo_xY_{1-x}F_4$ [11] is a material that exhibits physics like the one found in the transverse field Ising model, and $ZnCu_3(OH)_6Cl_2$ [12] seems to realize a disordered ground state, a spin liquid, and can be modeled as a quantum Heisenberg model. Another example of interesting quantum frustrated magnets are those in which Kitaev interactions arise, as for example in α-$RuCl_3$ [13] and a big family of Iridate materials (IrO_6) [14], which both are cases of Heisenberg-Kitaev models. On the other hand, classical Heisenberg models also touch on reality. While it is not expected that a purely quantum model (as a model fundamentally composed of quantum objects as spins is) can be fully treated as a classical one, the study of the classical version of Heisenberg models has been extremely fruitful. Many materials posses very small quantum fluctuations which, when disregarded, can be seen as examples of classical spin systems. The spin ices, $Dy_2Ti_2O_7$ and $Ho_2Ti_2O_7$ [15] are important examples of Ising models where the fundamental excitations can be considered magnetic monopoles, and $YbMgGaO_4$ [16] seems to mimic a spin liquid state, in which the strong interactions, and possibly a small amount of impurities, mimic the behavior of a spin liquid, and can too be modeled as a classical magnetic system. This is by far not a comprehensive list of all the materials which realize Heisenberg interactions, the list is extensive and here we just wanted to point out many examples which indicate that the study of Heisenberg models is not only interesting as a theoretical exercise, but fruitful from the experimental point of view.

The question that arises is how one would model all of these materials, until one finds that a Heisenberg model or associates are a good choice. Modeling any of these materials is a joint effort, from the point of view of experimentalists and theorists alike.

Whether theorists propose a model in which interesting physics arise, and this model is later realized experimentally (as was the case of Kitaev interactions in the Iridates family), or a material shows strange properties which pick the interest of theorists (as the residual zero point entropy in $Dy_2Ti_2O_7$), the modeling is usually non trivial.

As theorists interested in magnetic systems and magnetic order, the holy grail of experimental techniques resides with the different neutron scattering and diffraction techniques. Via neutron scattering and diffraction experiments, both in single crystal or powder samples, we can study if our system orders magnetically, and if it does, what the nature of this ordering is. This points in a theoretical direction, as not all models will present the same types of order, and the minimal model of our system will rely on the type of order it presents. If the material orders magnetically at low temperature, we can consider as a first order approximation the neglect of quantum fluctuations, this is, we treat our system as a classical spin system. This neglect readily present us with many different tools to study the effective Hamiltonian, as analytical and numerical techniques which can deal with classical magnetism are well known. If, on the other hand, the system is not ordered at low temperature, we cannot neglect quantum fluctuations, and the approaches treating the resulting Hamiltonian will be vastly different than in the classical case.

But this is not the end of the story. To even start modeling a material we believe realizes Heisenberg-like interactions, we need to know what the atoms in the material are, which is the crystalline structure, and where each atom is in this structure. The effort of experimentalists appears here through different experimental techniques, as i.e. X-ray diffraction experiments, which can give us answers to questions related to the crystal structure. Furthermore, the purity of the samples is a topic which cannot be left aside, as the behavior of magnetic systems can drastically change (as is the case of spin glass systems) in the presence of impurities. As such, the growth of pure samples, and the theoretical understanding of the effect of impurities in the system is crucial.

Once the crystal lattice is clear, we need to know what the hybridization and possible gap between atomic orbitals is, and what effects are at play, whether it is spin orbit coupling or hyperfine interactions. Again, an effort from the theory part resides in employing analytical and numerical techniques as DFT, likewise these efforts are supported by experiments such as μSR and NMR, which can give us information regarding the microscopics of the material, for example, regarding line shifts and widths of the atomic orbitals produces by crystal field effects (where the electronic levels of the magnetic ions in our compound feel an electromagnetic field produced by the environment of the other

atoms present in the material) and nuclear interactions, as well as providing information regarding the magnetic order of our sample. At the same time, experiments as μSR and NMR can give us information of whether the crystal field induces an easy axis or easy plane anisotropy, which will point us, theorist, in the direction of Ising or XY models respectively. Furthermore, these techniques allow us to probe the relaxation time of the sample, which tells us something regarding the possible quantum fluctuations, as well as possible freezing, of the magnetic degrees of freedom. This information determines whether we are in the presence of spin glass-like states or spin liquids. It is also used to study fundamentally different phenomena, as critical slowing down [17] and persistent dynamics [18], which both are realized in pyrochlore materials. This is by no means an exhaustive list of experimental techniques, extremely useful experiments (as for example those regarding the thermodynamics of the materials) have not been mentioned here. The aim of this section was to exemplify the effort, from experimentalist and theorist alike, that are required to model these materials.

From a theoretical point of view, even though frustrated magnetic materials can be described by well defined microscopic Hamiltonians, they cannot always be efficiently solved. The field of frustrated quantum magnetic materials has seen a recent surge in the production of numerical and analytical techniques aimed at tackling these problems, but still a general and efficient methodology to solve these types of Hamiltonians is lacking. Many methods work well in a reduced part of the field, as exact diagonalization and tensor networks algorithms which are ideal to study systems with a small number of lattice sites, as 1D and quasi-1D spin chains. However, many of these types of methods are inefficient at studying 2 and 3D systems. On the other hand we could use Monte Carlo method to deal with quantum systems. But the existence of a sign problem also constrains the lattice sizes that can be studied considerably. Still, quantum magnetic systems in 2 and 3D can be tackled theoretically employing novel numerical and theoretical techniques. Employing quantum field theoretical methods [19, 20] or mapping the interesting Hamiltonian to another basis in which the problem becomes tractable via existent numerical methods [21] allows us to gain a valuable insight into the physics of these systems. The situations becomes less complex in the realm of frustrated classical magnetic materials, where quantum fluctuations can be neglected. In this case many different techniques exist which can be employed to attack these problems. While the methodology for these systems has been developed and used for much longer than for their quantum counterparts, solving the classical analogous is still non-trivial, and amounts to intense numerical and analytical efforts. Developing novel techniques to

tackle the quantum and classical problems is still an active field of research, which has seen a good number of successes in the past years. In particular we mention the pseudofermion-functional renormalization group method, which will be treated in detail in this thesis. Nonetheless, with the currently know techniques, the theoretical studies for both quantum and classical frustrated magnetic systems provide a framework, which not only can be used to interpret the available experimental results, but which allows us to employ magnetic materials as a playground in which to study several different phenomena.

In this thesis, we will not model materials from first principles, but we will instead concentrate on the study of either models which show interesting physics and could or have already been realized in experiments (as in Chapter 4 [8, 22–25]), or in materials for which different models have been proposed but a careful comparative study employing the same theoretical techniques has not been performed in full (we will study one of these materials in Chapter 6 [14]). In Chapter 3 we will put a technique forward, pseudofermion-functional renormalization group, which allows us to study and resolve the ground state properties of quantum Heisenberg models in arbitrary lattices for 2 and 3D systems. Furthermore, we will apply this technique to study what happens when quantum fluctuations are slowly suppressed, arriving at the classical limit in the end. In Chapter 4 we will show how this method can be applied to study spin spiral states in Heisenberg honeycomb models, both in spin 1/2 as well as higher spin systems, which have already been realized experimentally. In Chapter 5 we will switch gears and move to the purely classical realm of spin systems, also with the hopes of studying spin spiral states. We will show how Monte Carlo simulations can be simply modified to study classical Heisenberg magnets, what are the advantages and disadvantages of the method, and how it can be modified to surpass some of the disadvantages. In Chapter 6 we will apply it to study α-Li_2IrO_3, a material which seems to realize Heisenberg and Kitaev interactions and which possesses a spin spiral ground state. For this particular material the question of which minimal model corresponds to it is still open, and it will be our effort to reduce the number of possible models, as well as predicting the magnetic behavior in a way which is experimentally realizable.

CHAPTER 2

THE HUBBARD AND HEISENBERG MODELS

Frustration is the name of the game.

Linus Pauling.

The first question that arises when one looks at the Heisenberg model is: where exactly does it come from? How can it be that the magnetic interactions in a crystal, arising from atomic magnetic moments which are connected in an arbitrary lattice structure, can be explained by such a simple Hamiltonian?

The derivation of the Heisenberg Hamiltonian from a full electronic model is well known, and the aim of this introduction is to derive it again in a way that will make clear not only it's properties, but also how and why we will use it in this thesis. We will also employ different extensions of the Heisenberg model, but the derivation of each one of these can be traced back to a similar procedure as the one we will show next.

2.1 Electronic Hamiltonian and Hubbard model

Our derivation starts with a solid state system, a crystal composed of atoms localized on lattice sites. Furthermore, and for the sake of simplicity, we will assume that we have already performed the Born-Oppenheimer approximation and that the nuclei are fixed on the lattice sites, such that we can concentrate on electronic Hamiltonians. The

effects of lattice distortions as phonons or Jahn-Teller effects will not be considered in the following.

With these considerations in mind we can assume that our Hamiltonian consists of two parts, a term describing electron dynamics

$$\mathscr{H}_0 = \int d\mathbf{r} a_\sigma^\dagger(\mathbf{r}) \left[\frac{\mathbf{p}^2}{2m} + V(\mathbf{r}) \right] a_\sigma(\mathbf{r}), \tag{2.1}$$

and another term describing electron-electron interactions

$$\mathscr{H}_{ee} = \frac{1}{2} \int d\mathbf{r} \int d\mathbf{r}' V_{ee}(\mathbf{r}-\mathbf{r}') a_\sigma^\dagger(\mathbf{r}) a_\sigma^\dagger(\mathbf{r}') a_{\sigma'}(\mathbf{r}') a_{\sigma'}(\mathbf{r}), \tag{2.2}$$

where $a_\sigma^\dagger(\mathbf{r})$ creates an electron with spin σ at position $\mathbf{r}$, $V(\mathbf{r})$ is the periodic lattice potential, and $V_{ee}(\mathbf{r}-\mathbf{r}')$ is the electron-electron interaction potential. We have also ignored relativistic terms as spin-orbit coupling. As this thesis progresses we will see that these terms have to be taken into account in certain cases, specially when dealing with heavy ions. We will omit these terms and concentrate on the *atomic limit* of this Hamiltonian, where the nuclei are separated by a distance greater that the Bohr radius of the valence electrons, in other words, the overlap of the electron wave function is small.

If our interaction Hamiltonian were zero, we would be able to solve $\mathscr{H}_0$ employing Bloch's theorem, and we would obtain energy levels $\epsilon_{n\mathbf{k}}$ and wave functions $|\psi_{n\mathbf{k}}\rangle = e^{i\mathbf{kr}}|u_{n\mathbf{k}}\rangle$. Since we don't want to study free electrons in a periodic potential, but instead want to study the effect of interactions on electrons localized at the atomic positions, it is worth to write our Hamiltonian in a basis of single particle states, which labels the states according to their positions on the lattice sites, $\mathbf{R}$. For this purpose we will use Wannier states

$$|\psi_{\mathbf{R}n}\rangle = \frac{1}{\sqrt{N}} \sum_{\mathbf{k}}^{\text{B. Z.}} e^{-i\mathbf{kR}} |\psi_{n\mathbf{k}}\rangle, \tag{2.3}$$

where $\mathbf{R}$ labels the lattice sites, and the sum is over wavevectors inside the first Brillouin zone. If the atomic overlap is zero, the Wannier states are simply atomic orbitals, but usually a finite overlap exists. As such, the different energy levels become energy bands. We will consider the simplest possible case, where the bands do not overlap and the Fermi energy is contained fully within one band. With this we can drop the band

index, n, and define the creation operator of Wannier states in terms of the creation operators of Bloch states

$$a^\dagger_\sigma(\mathbf{r}) = \sum_{\mathbf{R}} \psi^*_{\mathbf{R}}(\mathbf{r}) a^\dagger_{\mathbf{R}\sigma} = \sum_i \psi^*_{\mathbf{R}_i}(\mathbf{r}) a^\dagger_{i\sigma}\,, \tag{2.4}$$

where $a^\dagger_\sigma(\mathbf{r})$ is a creation operator in real space, $a^\dagger_{i\sigma}$ is a Wannier creation operator, and we have indexed the lattice sites by i. The connection with Bloch wavefunctions comes from the Fourier transform of these operators

$$a^\dagger_{\mathbf{k}\sigma} = \frac{1}{\sqrt{N}} \sum_i e^{i\mathbf{k}\mathbf{R}_i} a^\dagger_{i\sigma}\,. \tag{2.5}$$

Expressing the non interacting Hamiltonian in terms of Bloch wavefunctions, and then using Eq.(2.5) we obtain

$$\mathscr{H}_0 = \sum_{\mathbf{k}} \epsilon_{\mathbf{k}} a^\dagger_{\mathbf{k}\sigma} a_{\mathbf{k}\sigma} = \frac{1}{N} \sum_{ii'} \sum_{\mathbf{k}} e^{i\mathbf{k}(\mathbf{R}_i - \mathbf{R}_{i'})} \epsilon_{\mathbf{k}} a^\dagger_{i\sigma} a_{i'\sigma} = \sum_{ii'} a^\dagger_{i\sigma} t_{ii'} a_{i'\sigma}\,, \tag{2.6}$$

where $t_{ii'} = N^{-1} \sum_{\mathbf{k}} e^{i\mathbf{k}(\mathbf{R}_i - \mathbf{R}_{i'})} \epsilon_{\mathbf{k}}$ are the hopping matrix elements. By the same procedure the interaction term takes the form

$$\mathscr{H}_{ee} = \sum_{ii'jj'} \sum_{\sigma\sigma'} U_{ii'jj'} a^\dagger_{i\sigma} a^\dagger_{i'\sigma'} a_{j'\sigma'} a_{j\sigma}\,, \tag{2.7}$$

where the matrix elements of the interaction are

$$U_{ii'jj'} = \frac{1}{2} \int d\mathbf{r} \int d\mathbf{r}' \psi^*_{\mathbf{R}_i}(\mathbf{r}) \psi_{\mathbf{R}_j}(\mathbf{r}') V(\mathbf{r} - \mathbf{r}') \psi^*_{\mathbf{R}_{i'}}(\mathbf{r}') \psi_{\mathbf{R}_{j'}}(\mathbf{r}')\,. \tag{2.8}$$

Adding both terms we obtain the *tight binding model*

$$\mathscr{H} = \sum_{ii'} a^\dagger_{i\sigma} t_{ii'} a_{i'\sigma} + \sum_{ii'jj'} U_{ii'jj'} a^\dagger_{i\sigma} a^\dagger_{i'\sigma'} a_{j'\sigma'} a_{j\sigma}\,. \tag{2.9}$$

Please note that here we are not considering matrix elements that couple different bands, so we are effectively working in a single band model. While models where more than one band are relevant exist, we will not consider them here.

Certain terms in Eq.(2.9) deserve a special mention. The direct terms, containing the elements U_{ijji} couple density fluctuations at different sites, which lead to the description of charged density waves. Here we are interested in the study of spin fluctuations that lead to magnetic phases, so we will not consider the direct terms in the following. Terms that couple spin fluctuations are the exchange terms, where $ii' = jj' = ij$. These terms can be written in a more amenable way noting that $\frac{1}{2}a^\dagger_{i\alpha}\sigma^\mu_{\alpha\beta}a_{i\beta} = S^\mu_i$, obtaining

$$\sum_{i\neq j} U_{ijij} a^\dagger_{i\sigma} a^\dagger_{j\sigma'} a_{i\sigma'} a_{j\sigma} = -2\sum_{i\neq j} J_{ij}(\mathbf{S}_i\mathbf{S}_j + \frac{1}{4}\hat{n}_i\hat{n}_j),. \tag{2.10}$$

where $\hat{n}_i$ is the number operator on site i and $J_{ij} = U_{ijij}$. This is a kinetic ferromagnetic exchange term, and can contribute to ordering tendencies in metals. There can be another way of obtaining this type of exchange following Hund's rules: if we assume the wave functions of the electrons can be factorized into the orbital part times the spin part. Thinking of only two neighboring electrons, the Coulomb repulsion between them will be minimized when the orbital wave function has the minimal possible overlap, which means this wave function will be antisymmetric. Since the total wave function needs to be antisymmetric, then the spin part will have to be symmetric, with both spins pointing in the same direction. While this is a mechanism which can lead to magnetic interactions, it is usually small in the atomic limit, since in this case the overlap between wave functions decay exponentially with the atomic distance. In this limit, where the direct ferromagnetic exchange is small, the dominant interaction arises from the matrix elements which describe an on-site Coulomb interaction, U_{iiii}, which generates terms of the form

$$\sum_{\sigma\sigma'} U_{iiii} a^\dagger_{i\sigma} a^\dagger_{i\sigma'} a_{i\sigma'} a_{i\sigma} = \sum_i U_i \hat{n}_{i\uparrow}\hat{n}_{i\downarrow}\,. \tag{2.11}$$

One more consideration needs to be taken into account, in the atomic limit, the hopping amplitude t_{ij} also decays fast with distance, which effectively means that we will at most have hopping up to first neighbors. With these considerations in mind, and further assuming the system is translational invariant so the couplings are the same for every bond in the lattice, the resulting Hamiltonian takes the form

$$\mathscr{H} = -t\sum_{\langle ij\rangle} a^\dagger_{i\sigma} a_{j\sigma} + U\sum_i \hat{n}_{i\uparrow}\hat{n}_{i\downarrow} = \mathscr{H}_t + \mathscr{H}_u\,. \tag{2.12}$$

This is the famous *Hubbard model*, which while simple looking is non trivial to solve, and which describes a lot of highly correlated electron systems in solid state physics. The Heisenberg model we are interested in, arises as a natural, low energy effective model, of the large U limit of the Hubbard model.

2.2 Large U limit and Heisenberg model

The behavior of the Hubbard model is determined by three parameters: the filling fraction n, the interaction ratio U/t, and the adimensional temperature T/t. We will study the large U limit, $U/t \gg 1$, as the principal mechanism for magnetic order in insulators.

At half filling, and in the limit $U/t \gg 1$, double occupancy is inhibited, since the Hubbard interaction U is large, and as such the energy cost of double occupancy is large. In these cases, the lowest energy configurations will be given by singly occupied states. On the other hand, states with double occupancy are higher in energy. In the limit of large U we can consider that our Hubbard term, $\mathscr{H}_U$, will be perturbed by the hopping term, H_t, and as such attempt to project out the higher energy states to obtain an effective low energy theory of the Hubbard model [26, 27]. We will perform this projection following the downfolding technique, which aims at integrating out the high-energy degrees of freedom. In this technique, we start by partitioning the Hilbert space in two sets, one containing the low energy states without double occupancy

$$S = \left\{ |n_{1\uparrow}, n_{1\downarrow}, n_{2\uparrow}, n_{2\downarrow}, ...\rangle | \forall i : n_{i\uparrow} + n_{i\downarrow} \leq 1 \right\} \tag{2.13}$$

and another containing the high energy states with one or more doubly occupied states

$$D = \left\{ |n_{1\uparrow}, n_{1\downarrow}, n_{2\uparrow}, n_{2\downarrow}, ...\rangle | \exists i : n_{i\uparrow} + n_{i\downarrow} = 2 \right\} \tag{2.14}$$

The hopping term will couple the S and D subspaces, given that this term produces the hopping of one electron in or out of an occupied site. Furthermore, it will partially lift the degeneracy of the subspaces. Even though the dimension of these subspaces is infinite, we can attempt to write the Hamiltonian in a matrix-like form

$$\mathscr{H} = \begin{bmatrix} P_S(\mathscr{H}_t + \mathscr{H}_U)P_S & P_S\mathscr{H}_t P_D \\ P_D\mathscr{H}_t P_S & P_D(\mathscr{H}_t + \mathscr{H}_U)P_D \end{bmatrix}, \tag{2.15}$$

where P_S is an operators which projects on the low energy configurations S, and P_D projects on subspace D. Here, the upper left term is the Hamiltonian restricted to the lowest energy states, S, while the lower right is restricted to the states in D. The off diagonal elements describe transitions between states in S and D. We can obtain an effective Hamiltonian which acts on the low energy subspace by studying the Green's function of the problem

$$G(E) = (E - \mathscr{H})^{-1}, \tag{2.16}$$

which can also be partitioned by introducing Eq. 2.15 into the expression for $G(E)$. By calculating the inverse of this "matrix" (please note that the elements are matrix themselves so they won't commute) and projecting over S we obtain

$$P_S G(E) P_S = \left(E - \left[P_S(\mathscr{H}_t + \mathscr{H}_U)P_S + P_S\mathscr{H}_t P_D\left(E - P_D(\mathscr{H}_t + \mathscr{H}_U)P_D\right)^{-1} P_D\mathscr{H}_t P_S\right]\right)^{-1}, \tag{2.17}$$

which looks as the Green's function for an effective Hamiltonian

$$\mathscr{H}^{\text{eff}} = P_S(\mathscr{H}_t + \mathscr{H}_U)P_S + P_S\mathscr{H}_t P_D\left[E - P_D(\mathscr{H}_t + \mathscr{H}_U)P_D\right]^{-1} P_D\mathscr{H}_t P_S\,. \tag{2.18}$$

Furthermore, noting that $P_S\mathscr{H}_U = \mathscr{H}_U P_S = 0$ we obtain

$$\mathscr{H}^{\text{eff}} = P_S\mathscr{H}_t P_S + P_S\mathscr{H}_t P_D\left[P_D\left(E - (\mathscr{H}_t + \mathscr{H}_U)\right)P_D\right]^{-1} P_D\mathscr{H}_t P_S\,. \tag{2.19}$$

There is no way to evaluate the inverse in the second term explicitly, so we will perform perturbation theory in powers of t/U. In this expansion the first order in t vanishes, and we obtain a Hamiltonian which is second order in t, which we call the $t-J$ *model*

$$\mathscr{H}^{t-J} = P_S\left[\mathscr{H}_t - \frac{t^2}{U}\sum_{\langle ij\rangle\langle jk\rangle\sigma\sigma'} a^\dagger_{k\sigma'}a_{j\sigma'}\hat{n}_{j\uparrow}\hat{n}_{j\downarrow}a^\dagger_{j\sigma}a_{i\sigma}\right]P_S\,. \tag{2.20}$$

We can further write the $t-J$ Hamiltonian as

$$\mathscr{H}^{t-J} = P_S\left[\mathscr{H}_t + \mathscr{H}_H + \mathscr{J}'\right], \tag{2.21}$$

where, if we write $\frac{1}{2}a^{\dagger}_{i\alpha}\sigma^{\mu}_{\alpha\beta}a_{i\beta} = S^{\mu}_{i}$ we obtain

$$\mathscr{H}_H = \frac{4t^2}{U}\sum_{\langle ij\rangle}\left(\mathbf{S}_i\mathbf{S}_j - \frac{\hat{n}_i\hat{n}_j}{4}\right), \tag{2.22}$$

and

$$J' = \frac{t^2}{U}\sum_{\langle ij\rangle}\sum_{\langle jk\rangle i\neq j}\sum_{\sigma}(a^{\dagger}_{k\sigma}(1-\hat{n}_{j\sigma})a_{i\sigma} - a^{\dagger}_{k-\sigma}a^{\dagger}_{j\sigma}a_{j-\sigma}a_{i\sigma})\hat{n}_{j-\sigma} \tag{2.23}$$

In the case of half filling, both terms $\mathscr{H}_t$ and J' are annihilated by the projector P_S, and the only term that remains, minus a constant is the **Heisenberg model**

$$\mathscr{H}_H = J\sum_{\langle ij\rangle}\left(\mathbf{S}_i\mathbf{S}_j\right) + \text{const}, \tag{2.24}$$

with $J = \frac{4t^2}{U}$.

Even though the hopping is restricted to nearest neighbour, we can consider spin exchange terms which extend beyond nearest neighbours. This is the superexchange mechanism proposed by Anderson [26, 27], where the magnetic ions "communicate" with each other through an intermediary ion, not necessarily magnetic, usually Oxygen or Fluorine.. In these cases we would obtain again a Heisenberg Hamiltonian, but the exchange coupling J would be modified. This exchange coupling would not only depend on the orbitals through which the hopping is taking place, but also in the angle of the atomic bond between orbitals. This hopping via an intermediary ion will be the basis of the study of magnetism in insulators, given that this implies that even in the case of insulating materials where the magnetic ions are not nearest neighbors, and as such we do not expect direct hopping between them, the spins will be able to talk to each other.

For example, the simplest case we can think of is that of CuO_2, where the hopping occurs between the $d-$orbitals of Cu and the p_x-orbitals of Oxygen. Furthermore these bonds form an 180^o angle. When this is taken into account we obtain an exchange integral J of the form

$$J = \frac{t_{pd}^4}{U_d + \Delta_{pd}}\left(\frac{1}{U_d} + \frac{1}{U_d + \Delta_{pd}}\right) > 0, \tag{2.25}$$

where t_{pd} and Δ_{pd} are the strength of the hopping and the level splitting, between p- and d-orbitals respectively, and U_d is the Coulomb interactions on the Cu ions. In this

case we see that the exchange is antiferromagnetic in nature. On the other hand, if we would consider a 90^o angle, the hopping would occur between the d-orbitals of Cu and the p_x and p_y- orbitals of the Oxygen, obtaining

$$J = -\frac{8t_{pd}^4 J_{xy}}{(U_d + \Delta_{pd})^2} \frac{1}{4(U_d + \Delta_{pd})^2 - J_{xy}^2} < 0\,, \tag{2.26}$$

In this case the exchange is ferromagnetic.

We see then, that the angle between the atoms can drastically change the behavior of the system. Furthermore, there can be other types of interactions, for example spin-orbit coupling, which would also drastically change not only the strength of the coupling but the form of the interaction. For example, as we will see in Chapter 6, in systems where the magnetic ion is surrounded by oxygens in an octahedral fashion, the exchange paths change, and together with the spin-orbit coupling we obtain strongly anisotropic bond dependent interaction. The study of magnetic insulators where the relevant mechanism for the spin interaction is superexchange will be the central point of this thesis. We will study in detail how the resulting Hamiltonians can be solved, both in the classical and quantum limits, how different materials can be modeled by these Hamiltonians, and what the effect of quantum fluctuations are on these systems.

CHAPTER 3

FUNCTIONAL RENORMALIZATION GROUP METHOD

We appear to live in the best of all possible worlds, where the computable functions make life predictable enough to be survivable, while the noncomputable functions make life (and mathematical truth) unpredictable enough to remain interesting, no matter how far computers continue to advance.

Gottfried Wilhelm von Leibniz

Functional renormalization group (FRG) methods have been around for a considerable amount of time. Initially developed in the context of high energy physics, they have been employed to tackle problems in various subfields (QCD[28],QED[29–31], quantum gravity[32–34], etc). It has since then been adopted by the condensed matter community, to study Hubbard-like systems, non-equilibrium phenomena, the Kondo effect, and many other subjects. In this thesis, we will employ a pseudofermionic version of FRG to treat 2 and 3D frustrated spin systems, study the effects that quantum fluctuations produce in these systems, and search for one of their most sought after phases, the spin liquid phase.

The pseudofermionic FRG approach (PFFRG) to treat frustrated quantum magnetism is a relatively new concept (the first paper dating back to 2010 [35]) and it was put forward motivated by the lack of methodology currently existent to treat these type of systems. While different analytical theories are developed to study some properties of frustrated magnets, a general numerical treatment able to study different lattices and Hamiltonians, detect their ground state properties, and give results that can be compared with experiments was lacking. From the numerical point of view, most existent methods fail at these type of studies, exact and powerful methods as exact diagonalization and DRMG are extremely powerful to calculate energy spectrum and entanglement entropies of 1D systems, but become extremely inefficient at higher dimensionality than 1. Other more sophisticated tensor networks based algorithms, as PEPS, MERA, etc. are currently in development, but whether they'll be efficient in 2 and 3D highly entangled quantum frustrated spin systems is an open question. As such, PFFRG was developed to explore the ground state phase diagram of systems that cannot currently be efficiently studied with other methods.

We will start this chapter by introducing the general FRG framework and later on we will derive the precise flow equations for Heisenberg like Hamiltonians.

3.1 General FRG framework

Following the comment by Kopietz, Bartosch, and Schütz [36], renormalization group theories are proud owners of the status of meta-theories, that is, theories about theories. FRG shares this status, as an approach that analyzes in detail the underlying structure of the quantum field theory of our choosing, and tries to solve it by studying one energy scale at a time (from this the renormalization part in the FRG name). Since we want to study a many body strongly interacting fermion system, the natural starting point is the partition function. In essence, if we manage to calculate the partition function, then we can get all the statistical/thermodynamical information we desire, the correlation functions being of particular interest in this thesis. So we concentrate in the partition function, the path integral form in particular, it's underlying structure, and on the basic building blocks, the bare Green's function and the bare interactions. From here on, is just a question of understanding how all this elements together can be manipulated into giving us a structured way of studying the fundamental Hamiltonian.

We will sketch the derivation of the FRG framework (for more details please look at Ref. ([36]), starting with a primer on functional methods. The starting point is repre-

senting the correlation functions of the fermionic system by a functional integral of the exponent of a general action $S[\psi]$, and a properly normalized integration measure, such that the partition function can be written as

$$\mathcal{Z} = \int \mathcal{D}[\bar{\psi},\psi] e^{-S[\bar{\psi},\psi]}, \tag{3.1}$$

where $\bar{\psi}$ and ψ represent Grassmann fields (we will concentrate on a fermionic description, but a bosonic one is also possible). If we collect all the indices for Matsubara frequencies and quantum numbers in a variable we denote k, and assume we are interested in treating Hamiltonians consisting of a kinetic part

$$H_0(\bar{\psi},\psi) = \sum_{k',k} \xi_{k',k} \bar{\psi}_{k'} \psi_k \,, \tag{3.2}$$

which defines the free propagator G_0 (note that energy conservation means that G_0 is diagonal in the Matsubara frequencies), and a two body interaction part

$$H_{int}(\bar{\psi},\psi) = \sum_{k'_1,k'_2,k_1,k_2} V_{k'_1,k'_2,k_1,k_2} \bar{\psi}_{k'_1} \bar{\psi}_{k'_2} \psi_{k_2} \psi_{k_1} \,, \tag{3.3}$$

then we can assume that the action can also be decomposed as $S[\bar{\psi},\psi] = S_0[\bar{\psi},\psi] + S_{int}[\bar{\psi},\psi]$, where $S_0[\bar{\psi},\psi]$ is of a Gaussian form

$$S_0[\bar{\psi},\psi] = -\sum_{k',k} \bar{\psi}_{k'} [G_0]^{-1}_{k',k} \psi_k \equiv -(\bar{\psi}, [G_0]^{-1}\psi). \tag{3.4}$$

As such, the non interacting partition function takes the form

$$\mathcal{Z}_0 = \int \mathcal{D}[\bar{\psi},\psi] e^{(\bar{\psi},[G_0]^{-1}\psi)}, \tag{3.5}$$

Adding source fields η that are of the same nature as the field components, i.e, Grassmann variables, we obtain the generalized partition function $Z(\bar{\eta},\eta)$

$$Z[\bar{\eta},\eta] = \int D[\bar{\psi},\psi] e^{-S[\bar{\psi},\psi]+(\bar{\psi},\eta)+(\psi,\bar{\eta})}. \tag{3.6}$$

And we can define the generating functional $W(\bar{\eta},\eta) = Z(\bar{\eta},\eta)/Z$

$$W[\bar{\eta},\eta] = \frac{\int D[\bar{\psi},\psi] e^{-S[\bar{\psi},\psi]+(\bar{\psi},\eta)+(\psi,\bar{\eta})}}{\int D[\psi] e^{-S[\psi]}}. \tag{3.7}$$

The n-particle Green's function is no other than the coefficient of a functional Taylor expansion of the generating functional, with respect to the fields

$$G(k_1,....k_n : k'_1,....k'_n) = \frac{\delta^n}{\delta\bar{\eta}_{k'_1}...\delta\bar{\eta}_{k'_n}} \frac{\delta^n}{\delta\eta_{k_1}...\delta\eta_{k_n}} W(\bar{\eta},\eta)|_{\bar{\eta}=\eta=0} \tag{3.8}$$

We can perform a perturbative expansion of this Green's function in terms of the interaction, $S_{int}[\bar{\psi},\psi]$. The two basic building blocks of this expansion are the bare Green's functions and the irreducible functions, and we can represent them in diagrammatic form in terms of directed lines representing the bare propagators, G_0, and vertices with n-points corresponding to an interaction between n/2 particles.

$G_0 =$ 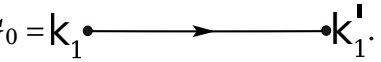 (3.9)

Eq. (3.9) shows the diagrammatic representation of the bare propagator, G_0.

One subsequent point needs to be made, if we write the full diagrammatic expansion we would notice that it contains subdiagrams that do not connect all the external points. This means that the expansion of the n-particle Green's functions contains diagrams belonging also to Green's functions of lower order. This in turn means that a n-th particle Green's function would not exclusively contain information about correlations involving n-th fields. We can obtain a diagrammatic expansion only containing connected diagrams. Literally, a diagram contributing to the n-particle Green's function is called *connected* if all vertices are connected by a sequence of lines and other vertices. The generators of these objects can be obtained by the logarithm of W,

$$W_c(\bar{\eta},\eta) = \ln[W(\bar{\eta},\eta)]. \tag{3.10}$$

The connected n-particle Green's functions can then be obtained by the functional derivative of W_c[36]:

$$G_c(k_1,....k_n : k'_1,....k'_n) = \frac{\delta^n}{\delta\bar{\eta}_{k'_1}...\delta\bar{\eta}_{k'_n}} \frac{\delta^n}{\delta\eta_{k_1}...\delta\eta_{k_n}} W_c(\bar{\eta},\eta)|_{\bar{\eta}=\eta=0} \tag{3.11}$$

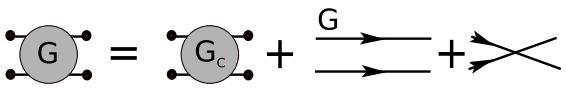

Figure 31: Relationship between the two particle connected and usual Green's function. We represent the two particle Green's functions by a gray circle. The single lines indicate single particle Green's functions.

The connection between the usual Green's functions and the connected Green's functions can be obtained simply by the above expression. The single particle connected Green's function equals the usual Green's function, as any single particle vertex contains only one propagation line and as such is always a connected diagram. For the two particle Green's function, evaluating the derivative and expressing it in diagrammatic language, we find the expression shown in Fig. 31. In general the nth-particle Green's function will be given in terms of al the ith-particle Green's functions, with $i \leq n$.

The connected Green's functions can also be decomposed in more fundamental pieces, the one-particle irreducible n-particle vertex function. A one particle irreducible diagram is such that cannot be disconnected by removing a single propagator line. An example of this is given in Fig. 32.

The generating functionals for the these objects can be found renaming the derivatives of W_c as new Grassmann fields, $\phi = -\frac{\delta W_c(\bar{\eta},\eta)}{\delta \bar{\eta}}$ and $\bar{\phi} = \frac{\delta W_c(\bar{\eta},\eta)}{\delta \eta}$, and performing a Legendre transform. As a consequence we obtain the generating functional

$$\Gamma(\bar{\phi},\phi) = -W_c(\bar{\eta},\eta) - (\bar{\phi},\eta) - (\bar{\eta},\phi) + (\bar{\phi},[G_0]^{-1}\phi). \tag{3.12}$$

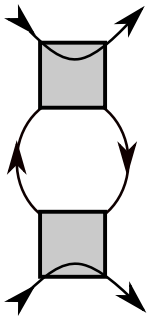

Figure 32: Example of a one particle irreducible diagram that contributes to the one particle irreducible two particle vertex function.

Finally, via a functional derivative we can find the one-particle irreducible vertex functions with n-legs

$$\gamma_n(k_1,....k_n : k'_1,....k'_n) = \frac{\delta^n}{\delta\bar{\phi}_{k'_1}...\delta\bar{\phi}_{k'_n}} \frac{\delta^n}{\delta\phi_{k_1}...\delta\phi_{k_n}} \Gamma(\bar{\phi},\phi)|_{\bar{\phi}=\phi=0}. \tag{3.13}$$

The relation between one-particle irreducible vertex functions, γ_n, and the connected Green's functions can be extracted as well from the diagrammatic expansion. There are diagrams which can be decomposed into two pieces when cutting one fermion line. An example of this is the three particle vertex shown in Fig. 33.

These diagrams are called one-particle reducible and are also contained in the connected Green's functions. However, for the FRG formulation we will use the so called one-particle irreducible vertices, which are characterized by the fact that they cannot

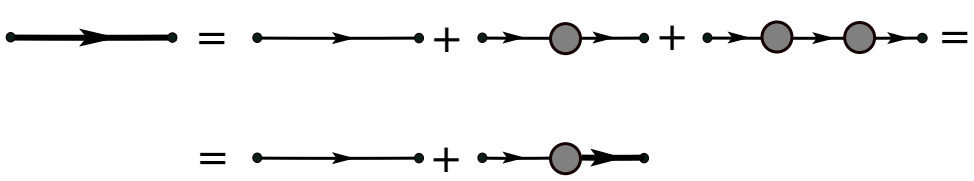

Figure 34: Diagrammatic expansion for the one particle vertex. The thick line represents the one particle Green's function. The thin lines are bare propagators G_0, and the circles represent one particle vertices.

be decomposed into two pieces when cutting one fermion line. The n-particle Green's function will be the sum of all one particle irreducible vertices.

For example, the explicit expansion for the one particle Green's function $G(k:k')$ is of the form

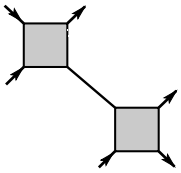

Figure 33: One-particle reducible diagram contributing to the three particle vertex.

$$G_c(k:k') = G_0(k:k') + G_0(k:l')\gamma_1(l':l)G_0(l:k') + G_0(k:l)\gamma_1(l:l')G_0(l':m)\gamma_1(m:m')G_0(m:k') + \ldots \tag{3.14}$$

where a sum over internal indices is implicit. This series expansion can be re-written as

$$G_c(k:k') = G_0(k:k') + G_0(k:l')\gamma_1(l':l)G_c(l:k'), \tag{3.15}$$

which can be compared to Dyson's equation

$$G_c(k:k') = G_0(k:k') + G_0(k:l')\Sigma(l':l)G_c(l:k'), \tag{3.16}$$

where Σ is the self energy. This way we can identify the one particle vertex with the self energy, $\gamma_1 = \Sigma$. Diagrammatically this means that the particle vertex functions γ_1 will be connected by propagators to a chain that starts in k and ends in k'. Summing over all possible chain lengths we obtain the expansion of the one particle connected Green function, which is Dyson's equation, which is shown in diagrammatic form in Fig. 34.

Please note that this means that the exact propagator is the one which is fully dressed with the exact self-energy, which correspond to a sum of all terms in Fig. 34, an example of this procedure is shown in Fig. 35.

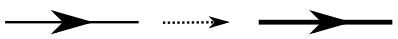

Figure 35: Two particle vertex after the self energy resumations (*right*) have been performed. Thick lines correspond to full propagators, while thin ones are the bare propagators

Now we are ready to derive our FRG equations. We will work with the one-particle irreducible vertices that we have shown can be traced back all the way to the Green's functions. The heart of FRG resides in the regularization of the bare Green's function by applying an infrared cutoff to the Matsubara frequencies,

$$G_0^\Lambda = \Theta(|\omega| - \Lambda) G_0(\omega). \tag{3.17}$$

Physically, this means that we are suppressing all the fermionic frequency components below Λ, and as such we will obtain physical information about the original Hamiltonian when all the propagators are considered, i.e. when $\Lambda = 0$. If we approach the limit $\Lambda \to 0$ from the right we are successively adding the fermionic frequencies to our system until we reach the original Hamiltonian (at $\Lambda = 0$).

There is a certain freedom regarding the choice of cutoff. We could implement it in momentum space, or not necessarily with a Heaviside theta function, all these choices depend on the system we want to study. What cannot be changed though is that two limits need to be respected: $G_0^\Lambda = 0$ when $\Lambda \to \infty$, and $G_0^\Lambda = G_0$ when $\Lambda = 0$. In our case, we will choose a sharp cutoff function in frequency space, since this will lead to the cancellation of internal frequency integrations in the FRG equations.

The FRG procedure studies how the changes in Λ affect the vertex functions by retrieving differential equations for this elements. When we replace G_0 by G_0^Λ every one particle irreducible diagram contributing to the one particle irreducible vertex becomes also Λ dependent. Given that the bare propagator enters multiplicatively in the diagrams, via the product rule, these one particle irreducible diagrams will transform into a sum over different subdiagrams, all of them differing only by one propagator line that is differentiated with respect to Λ. We obtain γ_n^Λ summing up all possible Λ dependent one particle irreducible n-particle diagrams terms.

In functional language: when we replace G_0 by G_0^Λ the action and the different generating functionals become Λ dependent. From the action

$$\frac{dS^\Lambda[\bar\psi,\psi]}{d\Lambda} = \frac{d}{d\Lambda}\left(-(\bar\psi,[G_0^\Lambda]^{-1}\psi) + S_{int}[\bar\psi,\psi]\right) = \bar\psi Q^\Lambda \psi \tag{3.18}$$

where $Q^\Lambda = \frac{d}{d\Lambda}[G_0^\Lambda]^{-1}$. And

$$\frac{dZ^\Lambda[\bar\eta,\eta]}{d\Lambda} = \int D[\bar\psi,\psi] i\bar\psi Q^\Lambda \psi e^{-S[\bar\psi,\psi]+(\bar\psi,\eta)+(\psi,\bar\eta)}. \tag{3.19}$$

then, the generating functional for the connected Green's functions becomes Λ dependent $W_c \to W_c^\Lambda$, and from Eqs. (3.7) and (3.10) we obtain

$$\frac{d}{d\Lambda}W_c^\Lambda = -\mathrm{Tr}[Q^\Lambda G_0^\Lambda] + \mathrm{Tr}\left[Q^\Lambda \frac{\delta^2 W_c^\Lambda}{\delta\bar{\eta}\delta\eta}\right] - \left(\frac{\delta W_c^\Lambda}{\delta\eta}, Q^\Lambda \frac{\delta W_c^\Lambda}{\delta\bar{\eta}}\right), \tag{3.20}$$

We remind the reader that we are not interested in the connected Green's functions but in the one-particle irreducible vertex functions. Using equations (3.12) and (3.20) we can find the differential equation for the generators of the vertex functions, Γ^Λ

$$\frac{d}{d\Lambda}\Gamma^\Lambda(\bar{\phi},\phi) = \mathrm{Tr}[Q^\Lambda G_0^\Lambda] - \mathrm{Tr}\left[Q^\Lambda \frac{\delta^2 W_c}{\delta\bar{\eta}\delta\eta}\right]. \tag{3.21}$$

Please note that since we performed a Legendre transform to go from one generating functional to the other, the variables $\bar{\eta}$ and η now are Λ dependent. We can eliminate W_c from the above expression using the relation between the derivatives of W_c and the generators Γ, which is

$$\begin{bmatrix} \frac{\delta^2 W_c}{\delta\bar{\eta}\delta\eta} & -\frac{\delta^2 W_c}{\delta\bar{\eta}\delta\bar{\eta}} \\ -\frac{\delta^2 W_c}{\delta\eta\delta\eta} & \frac{\delta^2 W_c}{\delta\eta\delta\bar{\eta}} \end{bmatrix} = \begin{bmatrix} \frac{\delta^2\Gamma}{\delta\bar{\phi}\delta\phi} + [G_0]^{-1} & \frac{\delta^2\Gamma}{\delta\bar{\phi}\delta\bar{\phi}} \\ \frac{\delta^2\Gamma}{\delta\phi\delta\phi} & \frac{\delta^2\Gamma}{\delta\phi\delta\bar{\phi}} - [[G_0]^{-1}]^T \end{bmatrix} \tag{3.22}$$

with this we obtain

$$\frac{d}{d\Lambda}\Gamma^\Lambda(\bar{\phi},\phi) = \mathrm{Tr}[Q^\Lambda G_0^\Lambda] - \mathrm{Tr}[G^\Lambda Q^\Lambda R_{11}], \tag{3.23}$$

with R_{11} a matrix element of the R matrix

$$R = \left[\mathbb{1} - \begin{bmatrix} -G^\Lambda & 0 \\ 0 & [G^\Lambda]^T \end{bmatrix}\begin{bmatrix} U & \frac{\delta^2\Gamma^\Lambda}{\delta\bar{\phi}\delta\bar{\phi}} \\ \frac{\delta^2\Gamma^\Lambda}{\delta\phi\delta\phi} & -U^T \end{bmatrix}\right]^{-1} \tag{3.24}$$

with

$$U = \frac{\delta^2\Gamma^\Lambda}{\delta\bar{\phi}\delta\phi} - \gamma_1^\Lambda. \tag{3.25}$$

Now, to find the differential equations for the vertex functions we can expand Γ^Λ in powers of $\bar{\phi}$ and ϕ using Eq. (3.13)

$$\Gamma^\Lambda(\bar{\phi},\phi) = \sum_{n=0}^{\infty}\frac{(-1)^n}{(n!)^2}\sum_{k'_1,\ldots,k'_n}\sum_{k_1,\ldots,k_n}\gamma_n^\Lambda(k'_1\ldots k'_n : k_1\ldots k_n)\bar{\phi}_{k'_1}\ldots\bar{\phi}_{k'_n}\phi_{k_1}\ldots\phi_{k_n}, \tag{3.26}$$

and expand the matrix R in a geometric series. Finding the flow equations is then just a matter of comparing coefficients of the fields $\bar{\phi}$ and ϕ on both sides of Eq. (3.23). The differential equations we obtain for γ_1^Λ and γ_2^Λ are:

$$\frac{d}{d\Lambda}\gamma_1^\Lambda(k_1',k_1) = \frac{1}{\beta}\sum_{k_2',k_2}\gamma_2^\Lambda(k_1',k_2':k_1,k_2)S^\Lambda(k_2,k_2') \tag{3.27}$$

$$\begin{aligned}\frac{d}{d\Lambda}\gamma_2^\Lambda(k_1',k_2':k_1,k_2) = &\frac{1}{\beta}\sum_{k_3',k_3}\gamma_3^\Lambda(k_1',k_2',k_3':k_1,k_2,k_3)S^\Lambda(k_3,k_3') \\ &+\frac{1}{\beta}\sum_{k_3',k_3}\sum_{k_4',k_4}[\gamma_2^\Lambda(k_1',k_2':k_3,k_4)\gamma_2^\Lambda(k_3',k_4':k_1,k_2) \\ &-\gamma_2^\Lambda(k_1',k_4':k_1,k_3)\gamma_2^\Lambda(k_3',k_2':k_4,k_2)-(k_3'\leftrightarrow k_4',k_3\leftrightarrow k_4) \\ &+\gamma_2^\Lambda(k_2',k_4':k_1,k_3)\gamma_2^\Lambda(k_3',k_1':k_4,k_2)+(k_3'\leftrightarrow k_4',k_3\leftrightarrow k_4)] \\ &\times G^\Lambda(k_3,k_3')S^\Lambda(k_4,k_4'),\end{aligned} \tag{3.28}$$

where S^Λ is the so called single scale propagator given by $S^\Lambda = G^\Lambda Q^\Lambda G^\Lambda$.

Eq. (3.27) and (3.28) are the so called flow equations for the self energy and two particle vertex respectively. We notice that these equations are coupled to each other. Since the Green's function contains γ_1^Λ, the flow of this vertex will depend on γ_1^Λ itself and on γ_2^Λ. For γ_2^Λ the story is similar, with the flow depending on γ_1^Λ, γ_2^Λ, and γ_3^Λ. In general the flow of the nth-particle vertex will depend on the ith-particle vertices where $i \leq n$. The first term of the flow equation for the two particle vertex corresponds to the three particle vertex. The next two are direct particle-hole terms, while the remaining two are crossed particle-hole terms. We will describe each term in more detail in the next section.

All that remains is identifying the initial conditions for these equations, which can be derived remembering that the initial point of the calculation is $\Lambda \to \infty$ and $G_0^\Lambda = 0$ in this limit. Since the bare Green's function vanishes, the particle propagation disappears and only the bare vertices remain. Extracting the bare vertices from the Hamiltonian in Eq. (3.2) and (3.3) we obtain the following initial conditions

$$\begin{aligned}\gamma_1^{\Lambda\to\infty}(k',k) &= -\Sigma(k',k) = -\xi_{k',k}\,, \\ \gamma_2^{\Lambda\to\infty}(k_1',k_2':k_1,k_2) &= V_{k_1',k_2',k_1,k_2}\,, \\ \gamma_n^{\Lambda\to\infty}(k_1',\ldots,k_n':k_1,\ldots,k_n) &= 0 \quad \text{for} \quad n\geq 3\,,\end{aligned} \tag{3.29}$$

the third condition is special, in the sense that if the Hamiltonian would contain interactions involving more than two particles some of these terms would be nonzero.

3.2 Slave fermionic approach for spin operators

Our implementation of the PFFRG method to spin systems is based on the Heisenberg Hamiltonian, here we will study the case of 1/2-spins, to later concentrate on arbitrary length spins. The Hamiltonian thus has the form

$$\mathscr{H} = \sum_{(ij)} J_{ij} \mathbf{S}_i \cdot \mathbf{S}_j \,. \tag{3.30}$$

The basis of the implementation starts by expressing the elements of the spin operators in terms of two fermionic operators, $f_\downarrow$ and $f_\uparrow$ [37] such that

$$S^z = f_\uparrow^\dagger f_\uparrow - f_\downarrow^\dagger f_\downarrow \,, \quad S^+ = f_\uparrow^\dagger f_\downarrow \,, \quad S^- = f_\downarrow^\dagger f_\uparrow \,. \tag{3.31}$$

equivalently,

$$S_i^\mu = \frac{1}{2} \sum_{\alpha\beta} f_{i\alpha}^\dagger \sigma_{\alpha\beta}^\mu f_{i\beta} \,, \tag{3.32}$$

where $\alpha, \beta = \uparrow, \downarrow$ denote spin indices, $f_{i\alpha}^{(\dagger)}$ are fermionic annihilation (creation) operators on site i, and σ^μ ($\mu = x, y, z$) represent the Pauli matrices. This representation fulfills the correct angular momentum algebra of spin operators

$$[S^\mu, S^\nu] = i \epsilon_{\mu\nu\eta} S^\eta \tag{3.33}$$

If we consider the pseudofermionic operators as our field operators then the resulting Hamiltonian has the form (3.3). This quadratic form is precisely what we need to use diagrammatic Feymann techniques. An important point needs to be dealt with now: denoting the vector space of an arbitrary angular momentum operator $\mathbf{L}$ by $\mathbb{V}^L$, the pseudo fermionic representation extends the spin-1/2 vector space $\mathbb{V}^{1/2}$ according to

$$\mathbb{V}^{1/2} \to \mathbb{V}^0 \oplus \mathbb{V}^0 \oplus \mathbb{V}^{1/2} \,, \tag{3.34}$$

where the symbol $\oplus$ denotes a direct sum. One finds that the physical spin-1/2 subspace $\mathbb{V}^{1/2}$ is represented by the two basis states $|f^\dagger_{i\uparrow}f_{i\uparrow}, f^\dagger_{i\downarrow}f_{i\downarrow}\rangle = |1,0\rangle$ and $|0,1\rangle$ while the two spin-0 subspaces $\mathbb{V}^0$ are given by the states $|0,0\rangle$ and $|1,1\rangle$. In order to treat the original spin-1/2 model one needs to project out possible spurious admixtures from the unphysical spin-0 states. This could be achieved by imposing a constraint on the pseudofermion number,

$$Q_i = \sum_\alpha f^\dagger_{i\alpha} f_{i\alpha} = 1\,. \tag{3.35}$$

This is an extremely non trivial constraint to treat, given that the fermion number has to be constrained at each point of the lattice (in cases where only one interacting particle carry a spin, like a Kondo model where one magnetic impurity interacts with a sea of non interacting electrons, the constraint can be dealt with exactly). We could always treat the system approximately and replace the constraint (3.35) by the average $\langle Q_i\rangle = 1$. In cases where the system is translational invariant the constraint is identical in each lattice point, so only one such condition remains. Furthermore, in our case case the Hamiltonian presents particle-hole antisymmetry, which means that the Hamiltonian changes sign under the exchange of creation and annihilation operators (this can be proven simply by interchanging the creation and annihilation operators in Eqs. 3.31 and using the anticommutation relations for the pseudofermions). As such this constraint is equivalent to enforcing a $\mu = 0$ chemical potential since the constraint aims to remove two of the four states per site.

Another method to handle this constraint exactly has been proposed by Popov and Fedotov [38]. We will briefly present this method for the sake of completeness, but please note that in the next chapter we will show that this method is not necessary in our zero temperature case.

Popov and Fedotov propose the introduction of an imaginary chemical potential of the form $\mu^{PF} = -\frac{i\pi}{2\beta}$. This amounts to replacing the original Hamiltonian H by

$$H^{PF} = H - \mu^{PF} N\,, \tag{3.36}$$

where $N = \sum_i Q_i$, and H is written in terms of the fermionic operators. In their work, Popov and Fedotov show that there is a mutual cancellation of unphysical contributions arising from the sectors with $Q_i = 0$ and $Q_i = 2$ such that the expectation value of a physical operator $\mathcal{O}$, calculated with H^{PF} within the entire Hilbert space, $\langle\mathcal{O}\rangle^{PF}$,

is identical to the expectation value calculated with the original Hamiltonian in the constrained Hilbert space. While this approach has been applied to spin models at half filling, it cannot be extended away from this limit. Furthermore, at $T = 0$, the schemes with $\mu = 0$ and $\mu = \mu^{PF}$ are in principle not equivalent, given that the limit $T \to 0$ and the calculation of $\langle \mathcal{O} \rangle^{PF}$ do not necessarily commute. In our formulation of PFFRG we will consider a zero chemical potential as our Hamiltonian is particle hole symmetric and it is easier to treat numerically. We can interpret this choice from a phenomenological point of view: if we note that non or doubly occupied spin-0 sites are equivalent to vacancies in the spin lattice, then creating such vacancy (via a fermion number fluctuation on a particular site) means that the binding energy of a spin to its environment needs to be overcome. It therefore is to be expected that at *zero temperature* the ground state of the fermionic system lies entirely in the physical spin-1/2 sector and that unphysical occupations are gapped excitations with an energy on the order of the exchange couplings. In Sec. 4.1.1 we will show that this is indeed the case, proving that at $T = 0$ the pseudo fermion constraint is automatically fulfilled without any further methodological adjustments. This proof will be based on the addition of level repulsion terms to the Hamiltonian. In our case our study will be based on Heisenberg like Hamiltonians of the form in Eq. (3.30), so the level repulsion term takes the form $-A \sum_i \mathbf{S}_i^2$. Since the eigenvalues of $\mathbf{S}_i^2$ are $S(S+1)$, where S is the spin length, this implies that, if A is positive, this term will shift the ground state energy of our Hamiltonian by a factor of $S(S+1)$. In our particular case the pseudofermions can generate two different spin lengths, total spin 1/2 or 0, and in turn the level repulsion term will lower the energy of the spin-1/2 sector with respect to the spin-0. What we expect is that, if our assumption is correct and indeed there is no pseudofermionic number fluctuation, then the inclusion of the level repulsion terms in the Hamiltonian should not affect the results obtained from it as the ground state would already be completely generated by spin-1/2. Please note that we assume this considering that the energy scale of the level repulsion terms, A, is positive (interesting results arise in the case of negative coupling as we will show in the next chapter) and that in general $A \ll J_{ij}$. If A would be of the order or bigger than the Heisenberg couplings, the overall physics of the Hamiltonian would change, for example, in the limit of $A \gg J_{ij}$ we could treat our Hamiltonian as the Hamiltonian of non interacting spin (arising from the extremely large level repulsion terms) perturbed by a small interaction (coming from the Heisenberg part) which is very far from the strongly interacting Heisenberg systems of interest.

3.3 PFFRG framework

3.3.1 General form of the PFFRG equations for spin systems

We will now explicitly derive the PFFRG equations for the spin-1/2 case. In the next chapter we will show a generalization to a Heisenberg model with spin operators of arbitrary length [8]. We will concentrate on non-magnetic phases, i.e. phases which do not break a symmetry of the Hamiltonian. To study long range ordered phases we would have to include infinitesimal symmetry breaking terms in the Hamiltonian (as has been done for superconductivity in Ref. [39]), which would increase the complexity of the equations. Please note that even though we cannot access magnetically ordered phases, we will still be able to detect magnetic instabilities as a breakdown of the flow.

Starting from the introduction of the pseudo fermions we see that without any quadratic terms in the pseudo-particle Hamiltonian the bare fermionic propagator in Matsubara space is simply given by

$$G_0(1';1) = \frac{1}{i\omega_1}\delta(\omega_1 - \omega_{1'})\delta_{i_{1'}i_1}\delta_{\alpha_1\alpha_{1'}}\,, \tag{3.37}$$

where the index "$1 = \{\omega_1, i_1, \alpha_1\}$" denotes a multi index containing the frequency variable ω_1, the site index i_1, and the spin index α_1. Also note that in the zero temperature limit considered here, the discrete Matsubara frequencies become continuous. The diagonal structure of Eq. (3.37) in the frequency, site, and spin variables is due to energy conservation, absence of any fermion hopping in the Hamiltonian, and isotropy in spin space (coming from the non-magnetic nature of the phases), respectively.

Within PFFRG, the singularity of the propagator at $\omega_1 = 0$ is regularized by introducing an artificial infrared cutoff Λ implemented via a Heaviside step-function,

$$G_0^\Lambda(1';1) = \Theta(|\omega_1| - \Lambda)G_0(1';1)\,. \tag{3.38}$$

This introduces a Λ-dependence in the self energy. Similarly as before, energy conservation, the absence of hopping, and isotropy in spin space gift the self energy with a diagonal structure

$$\Sigma^\Lambda(1';1) \equiv \Sigma^\Lambda_{i_1}(\omega_1)\delta(\omega_1 - \omega_{1'})\delta_{i_{1'}i_1}\delta_{\alpha_1\alpha_{1'}}\,, \tag{3.39}$$

which also extends to the single scale propagator S^Λ.

Here and in the following we will denote the two particle vertex by Γ^Λ (not to be confused with the generating functional $\Gamma^\Lambda(\bar{\phi}, \phi)$), and the self energy by Σ^Λ. As mentioned

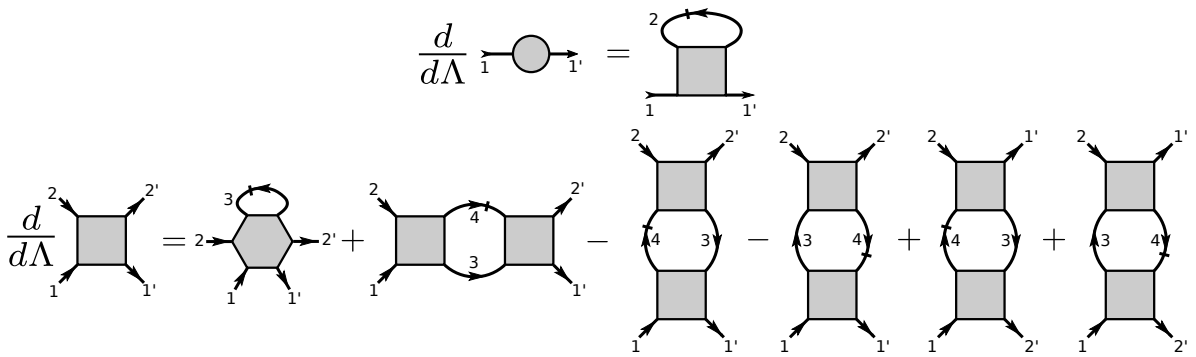

Figure 36: Diagrammatic illustration of the PFFRG flow equations for the self energy and the two-particle vertex, see also Eqs. (3.40) and (3.41). The thick black lines represent full propagators, G^Λ while the black crossed lines are identified with the single scale propagator S^Λ.

before, this modification generates a Λ dependence of all fermionic irreducible one particle vertex functions with m-legs, Γ^Λ_m, such as the self energy $\Sigma^\Lambda(1';1) \equiv \Gamma^\Lambda_1(1';1)$ and the two-particle vertex $\Gamma^\Lambda(1',2';1,2) \equiv \Gamma^\Lambda_2(1',2';1,2)$. Following the standard FRG framework we showed in the previous section (for more details please refer to [40, 41]), this dependence can be described by an infinite hierarchy of coupled integro-differential equations where the scale derivative $d\Gamma^\Lambda_m/d\Lambda$ couples to all vertices Γ^Λ_n with $n = 1,2,\ldots,m,m+1$. The equations for the self energy and the two-particle vertex take the form

$$\frac{d}{d\Lambda}\Sigma^\Lambda\left(1';1\right) = -\frac{1}{2\pi}\sum_{2'2}\Gamma^\Lambda\left(1',2';1,2\right)S^\Lambda\left(2,2'\right), \tag{3.40}$$

$$\begin{aligned}\frac{d}{d\Lambda}\Gamma^\Lambda\left(1',2';1,2\right) = &\frac{1}{2\pi}\sum_{3'3}\Gamma^\Lambda_3\left(1',2',3';1,2,3\right)S^\Lambda\left(3,3'\right)\\ &+\frac{1}{2\pi}\sum_{3'34'4}\Big[\Gamma^\Lambda\left(1',2';3,4\right)\Gamma^\Lambda\left(3',4';1,2\right)\\ &-\Gamma^\Lambda(1',4';1,3)\Gamma^\Lambda\left(3',2';4,2\right)-\left(3'\leftrightarrow 4',3\leftrightarrow 4\right)\\ &+\Gamma^\Lambda(2',4';1,3)\Gamma^\Lambda\left(3',1';4,2\right)+\left(3'\leftrightarrow 4',3\leftrightarrow 4\right)\Big]\\ &\times G^\Lambda(3,3')S^\Lambda(4,4'),\end{aligned} \tag{3.41}$$

where sums stand for $\Sigma_1 \equiv \int_{\omega_1} d\omega_1 \sum_{i_1} \sum_{\alpha_1=\uparrow,\downarrow}$ and Γ^Λ_3 is the three particle vertex. The diagrammatic form of these equations is depicted in Fig. 36. The right hand side of the equation for the two particle vertex contains six terms, the first one is the three particle vertex. The second is the particle-particle graph, and the remaining four represent particle-hole graphs.

As before, $G^\Lambda(\omega) = [(G_0^\Lambda(\omega))^{-1} - \Sigma^\Lambda(\omega)]^{-1}$ denotes the fully dressed propagator and

$$S^\Lambda(\omega) = G^\Lambda(\omega)^2 \frac{d}{d\Lambda} \left(G_0^\Lambda(\omega)\right)^{-1}, \tag{3.42}$$

is the single-scale propagator. This expression can be brought to a more convenient form noticing that G^Λ contains a step function $\Theta(|\omega| - \Lambda)$ and it's derivative gives a delta function $\delta(|\omega| - \Lambda)$. Morris' identity ([42]) tells us that if we use broadened functions $\delta_\epsilon(|\omega| - \Lambda) = \delta(|\omega| - \Lambda + \epsilon)$ and $\Theta_\epsilon(|\omega| - \Lambda) = \Theta(|\omega| - \Lambda + \epsilon)$ and take the limit $\epsilon \to 0$ it can be proven that

$$\delta_\epsilon(x - \Lambda) f(\Theta_\epsilon(x - \Lambda)) \to \delta(x - \Lambda) \int_0^1 f(t) dt\,. \tag{3.43}$$

This identity straightforwardly leads to an expression of the single scale propagator of the form

$$S^\Lambda(\omega) = \frac{\delta(|\omega| - \Lambda)}{i\omega - \Sigma^\Lambda(\omega)} \tag{3.44}$$

We mentioned previously that we chose a sharp frequency cutoff given that it would simplify the flow equations. This simplification is evident now looking at Eq. (3.44), given that due to energy conservation the Matsubara sums are greatly simplified, with only one sum remaining.

For a numerical evaluation of these equations, the infinite hierarchy needs to be truncated. The most straightforward truncation scheme amounts to treating the three-particle vertex Γ_3^Λ as zero. This, however, leads to an insufficient feedback of the self energy into the two-particle vertex flow such that all results effectively remain on a classical level. Particularly, quantum fluctuations needed for the description of magnetically disordered phases are almost completely neglected within such a scheme [35]. The key improvement is achieved by the so-called Katanin truncation [43] which neglects Γ_3^Λ in Eq. (3.41) but at the same time replaces the single-scale propagator by the total derivative of the full Green's function

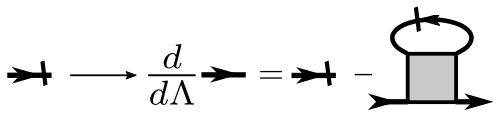

Figure 37: Diagrammatic expression of Eq. (3.45). A crossed line represents a Λ-derivative in the propagator.

$$S^\Lambda \longrightarrow -\frac{d}{d\Lambda} G^\Lambda = S^\Lambda - \left(G^\Lambda\right)^2 \frac{d}{d\Lambda} \Sigma^\Lambda\,, \tag{3.45}$$

where the last equality arises from simply applying the quotient rule and the first term of the utmost right hand side is the results of derivating G_0^Λ. The diagrammatic form of the replacement is shown in Fig. 37, where we have denoted by a crossed out propagator line the propagator that contains a Λ-derivative. When this replacement is inserted in the second flow equation, new terms arise.

This scheme effectively takes into account a certain subset of three-particle vertex contributions in Eq. (3.41), an example of one of these three particle contributions is shown in Fig. 38.

Most importantly, the modified single-scale propagator is given by the total derivative $-\frac{d}{d\Lambda}G^\Lambda$, such that the complete feedback of the self energy into the two-particle vertex is always ensured within the Katanin truncation. We can see the usefulness of this approach if we interpret the self energy as a pseudo fermion damping term in the full propagator. In this picture the contribution of the self energy plays a fundamental role as it can destroy magnetic order by suppressing the fermionic propagation. It seems then that this feedback is essential for the proper description of quantum fluctuations that lead to magnetically disordered phases. If the Katanin truncation were not to be implemented, one would expect that the results of our PFFRG scheme would be biased towards magnetically ordered phase, thankfully though, the Katanin truncation balances the different terms in such a way that all diagrams corresponding to magnetic order or disorder are accounted for with the same weight, leading to an *unbiased* calculation.

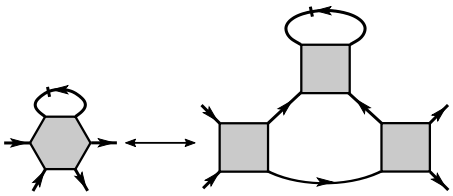

Figure 38: Part of the three particle contribution to the two particle vertex generated by the Katanin truncation (right hand side diagram). If we replace the single scale propagator in the particle-particle term by the self energy correction arising from the Katanin truncation (Eq.3.45) the right hand side term arises, which can be seen as of the same type as the three particle vertex as it has four external legs and one loop.

3.3.2 Initial conditions

The initial conditions are taken in the limit $\Lambda \to \infty$, where the free propagator vanishes identically. Hence, the only finite vertex function at $\Lambda \to \infty$ is the bare two-particle vertex given by

$$\begin{aligned}\Gamma^{\infty}(1',2';1,2) = &\frac{1}{4} J_{i_1 i_2} \sigma^{\mu}_{\alpha_{1'}\alpha_1} \sigma^{\mu}_{\alpha_{2'}\alpha_2} \delta_{i_{1'} i_1} \delta_{i_{2'} i_2} \\ &\times \delta(\omega_1 + \omega_2 - \omega_{1'} - \omega_{2'}) \\ &- (\omega_1 \leftrightarrow \omega_2, i_1 \leftrightarrow i_2, \alpha_1 \leftrightarrow \alpha_2)\,, \end{aligned} \tag{3.46}$$

where the factor $\sim 1/4\sigma^{\mu}\sigma^{\mu}$ results from the pseudo fermion representation (3.32) and a sum over μ is implicitly assumed. The last line guarantees that the fermionic antisymmetry condition under the exchange of variables $1 \leftrightarrow 2$ or $1' \leftrightarrow 2'$ is fulfilled. Furthermore note that due to the absence of any quadratic fermionic terms in the Hamiltonian, the self energy always vanishes identically at $\Lambda \to \infty$, but it will become non-zero as the flow progresses.

The flow equations can be brought into a more convenient form by exploiting the special site index structure of the two-particle vertex. Since all propagators $G^{\Lambda}(1',1)$, $S^{\Lambda}(1',1)$ are diagonal in $i_{1'}$, i_1 the spatial dependence of $\Gamma^{\infty}(1',2';1,2)$ as indicated in Eq. (3.46) is retained to all levels of diagrammatic approximations. This means that for each diagrammatic contribution with site indices $i_{1'}$ and $i_{2'}$ on two external fermion lines, the other two indices must either be given by $i_1 = i_{1'}$, $i_2 = i_{2'}$ or $i_1 = i_{2'}$, $i_2 = i_{1'}$. The spatial dependence of $\Gamma^{\Lambda}(1',2';1,2)$ can therefore be parametrized as

$$\begin{aligned}\Gamma^{\Lambda}(1',2';1,2) = &\tilde{\Gamma}^{\Lambda}_{i_1 i_2}(1',2';1,2) \delta_{i_{1'} i_1} \delta_{i_{2'} i_2} \\ &\times \delta(\omega_1 + \omega_2 - \omega_{1'} - \omega_{2'}) \\ &- (\omega_1 \leftrightarrow \omega_2, i_1 \leftrightarrow i_2, \alpha_1 \leftrightarrow \alpha_2)\,, \end{aligned} \tag{3.47}$$

where the new vertex $\tilde{\Gamma}^{\Lambda}$ fulfills the condition $\tilde{\Gamma}^{\Lambda}_{i_1 i_2}(1',2';1,2) = \tilde{\Gamma}^{\Lambda}_{i_2 i_1}(2',1';2,1)$. Note that the multi index "1" appearing in the argument of $\tilde{\Gamma}^{\Lambda}$ only stands for the frequency ω_1 and the spin α_1, while the site indices are written as a subscript. Furthermore, the δ-function in the frequencies in Eq. (3.47) guarantees that energy is conserved.

The initial conditions for $\tilde{\Gamma}^{\Lambda}$ takes the form

$$\tilde{\Gamma}^{\infty}_{i_1 i_2}(1',2';1,2) = \frac{1}{4} J_{i_1 i_2} \sigma^{\mu}_{\alpha_{1'}\alpha_1} \sigma^{\mu}_{\alpha_{2'}\alpha_2} \delta_{i_{1'} i_1} \delta_{i_{2'} i_2}\,. \tag{3.48}$$

3.3.3 Parametrization of the spin dependence

The parametrization of the vertices according to their spin dependences leads us to a clearer picture of the underlying structure of our equations, and is fundamental for their

numerical solution.

Considering the self energy, we know it is a local quantity in spin space, proportional to the unit matrix, and is related to the Green's function G^Λ via Dyson's equation. At the same time, G^Λ is related to the spectral function $\rho(\omega)$ via $G(\omega) = \int_{-\infty}^{\infty} \frac{\rho(\epsilon)}{(\omega-\epsilon)} d\epsilon$, where ω is a Matsubara frequency. Since the spectral function represents the distribution of probabilities of a particle having an energy ω, it has to be an even function in the presence of particle hole symmetry. Then G^Λ is an odd function with vanishing real part, and via Dyson's equation we find that the self energy also result as a purely imaginary odd function, $\Sigma^\Lambda = -i\gamma^\Lambda(\omega)$.

Furthermore, the rotational invariance of our system will be conserved during the flow. As a consequence, the two-particle vertex can be parametrized by spin-spin terms $\propto \sigma^\mu_{\alpha\beta}\sigma^\mu_{\gamma\delta}$. What it is perhaps not obvious, is that even though the initial conditions only contain spin-spin terms, the structure of our equations allow for the appearance of density-density terms $\propto \delta_{\alpha\beta}\delta_{\gamma\delta}$ at finite Λ, with the density term vanishing in the limit $\Lambda \to \infty$. This way the two particle vertex, $\tilde{\Gamma}^\Lambda_{i_1 i_2}(1',2';1,2)$ can be represented as in a similar form as Eq. (3.47):

$$\begin{aligned}\tilde{\Gamma}^\Lambda_{i_1 i_2}(1',2';1,2) = \big(&\tilde{\Gamma}^\Lambda_{\mathrm{s}i_1 i_2}(1',2':1,2)\sigma^\mu_{\alpha_{1'}\alpha_1}\sigma^\mu_{\alpha_{2'}\alpha_2} \\ &+\tilde{\Gamma}^\Lambda_{\mathrm{d}i_1 i_2}(1',2':1,2)\delta_{\alpha_{1'}\alpha_1}\delta_{\alpha_{2'}\alpha_2}\big) \\ &\times\delta_{i_{1'}i_1}\delta_{i_{2'}i_2}\delta(\omega_1+\omega_2-\omega_{1'}-\omega_{2'}) \\ &-(\omega_1 \leftrightarrow \omega_2, i_1 \leftrightarrow i_2, \alpha_1 \leftrightarrow \alpha_2),\end{aligned} \tag{3.49}$$

where s(d) correspond to spins (density) interactions, the δ-function ensures energy conservation, and the numbers now only represent a short hand notation for frequencies.

We can now re derive the flow equations for both the self energy, Σ^Λ, and the two particle vertex, Γ^Λ in terms of the parametrized vertices $\tilde{\Gamma}^\Lambda_{\mathrm{s(d)}}$.

We will derive the new flow equations in the conventional truncation scheme, where the single scale propagator adopts the form (3.44). Later on we will show that the Katanin truncation scheme just modifies a portion of the flow equations.

3.3.4 PFFRG equations for the self energy

For the self energy, inserting the parametrization Eq. (3.49) into (3.40) and using Eq.(3.39), we can see that evaluating the sum over spin variables becomes straightforward. At the same time the ω_2 integration is also simple to calculate since Eq.(3.49) contains a delta function on frequencies. Performing the above mentioned steps we obtain

$$\frac{d}{d\Lambda}\gamma^{\Lambda}(1) = \frac{1}{2\pi}\sum_{2=\pm\Lambda}\Big(-2\sum_{j}\tilde{\Gamma}^{\Lambda}_{\mathrm{d}i_1j}(1,2:1,2) + 3\tilde{\Gamma}^{\Lambda}_{\mathrm{s}i_1i_1}(1,2:2,1) + \tilde{\Gamma}_{\mathrm{d}i_1i_1}(1,2:2,1)\Big)\frac{1}{\omega_2+\gamma^{\Lambda}(2)}, \tag{3.50}$$

This equation can be rewritten by exploiting symmetries in frequency space. First, since energy conservation apply, we can write one of the frequencies in terms of the other three, which means we can rewrite the arguments of $\tilde{\Gamma}^{\Lambda}_{\mathrm{s}}$ and $\tilde{\Gamma}^{\Lambda}_{\mathrm{d}}$ as

$$\tilde{\Gamma}^{\Lambda}_{\mathrm{s(d)}i_1i_2}(1,2:3,4) \to \tilde{\Gamma}^{\Lambda}_{\mathrm{s(d)}i_1i_2}(1+2,1-3,1-4). \tag{3.51}$$

Please remember that the number notation now only represents frequencies. With this in mind, we can rename $s = \omega_{1'} + \omega_{2'}$, $t = \omega_{1'} - \omega_1$, and $u = \omega_{1'} - \omega_2$ such that $\tilde{\Gamma}^{\Lambda}_{\mathrm{s(d)}i_1i_2}(1+2,1-3,1-4) \to \tilde{\Gamma}^{\Lambda}_{\mathrm{s(d)}i_1i_2}(s,t,u)$. Naming $1 \to \omega$, and performing the explicit sum in Eq. (3.50) we thus arrive at the final equation for the self energy

$$\begin{aligned}\frac{d}{d\Lambda}\gamma^{\Lambda}(\omega) = \frac{1}{2\pi}\Big[&-2\sum_{j}(\tilde{\Gamma}^{\Lambda}_{\mathrm{d}ij}(\omega+\Lambda,0,\omega-\Lambda) - \tilde{\Gamma}^{\Lambda}_{\mathrm{d}ij}(\omega-\Lambda,0,\omega+\Lambda)) \\ &+ 3(\tilde{\Gamma}^{\Lambda}_{\mathrm{s}ii}(\omega+\Lambda,\omega-\Lambda,0) - \tilde{\Gamma}^{\Lambda}_{\mathrm{s}ii}(\omega-\Lambda,\omega+\Lambda,0)) \\ &+ \tilde{\Gamma}^{\Lambda}_{\mathrm{d}ii}(\omega+\Lambda,\omega-\Lambda,0) - \tilde{\Gamma}^{\Lambda}_{\mathrm{d}ii}(\omega-\Lambda,\omega+\Lambda,0)\Big]\frac{1}{\Lambda+\gamma^{\Lambda}(\Lambda)}\end{aligned} \tag{3.52}$$

3.3.5 PFFRG equation for the two particle vertex and Katanin contribution

The two particle vertex can be obtained via a similar process as we used for the self energy. The form of the fully parametrized equations is shown in Appendix . Here we will show the equations without parameterizing the spin dependence, and we will point out the explicit difference between the conventional and the Katanin truncation schemes. The two particle vertex flow equation is

$$\begin{aligned}\frac{d}{d\Lambda}\tilde{\Gamma}^{\Lambda}_{i_1 i_2}(1',2':1,2) = &\frac{1}{2\pi}\int_{-\infty}^{\infty} d\omega_4 \int_{-\infty}^{\infty} d\omega_3 \sum_{\alpha_3,\alpha_4} \\ &\Big[\tilde{\Gamma}^{\Lambda}_{i_1 i_2}(1',2':3,4)\tilde{\Gamma}^{\Lambda}_{i_1 i_2}(3,4:1,2)P^{\Lambda}_{i_1 i_2}(\omega_3,\omega_4) \\ &-\sum_j \tilde{\Gamma}^{\Lambda}_{i_1 j}(1',4:1,3)\tilde{\Gamma}^{\Lambda}_{j i_2}(3,2':4,2)P^{\Lambda}_{jj}(\omega_3,\omega_4) \\ &+\tilde{\Gamma}^{\Lambda}_{i_1 i_2}(1',4:1,3)\tilde{\Gamma}^{\Lambda}_{i_2 i_2}(3,2':2,4)P^{\Lambda}_{i_2 i_2}(\omega_3,\omega_4) \\ &+\tilde{\Gamma}^{\Lambda}_{i_1 i_1}(1',4:3,1)\tilde{\Gamma}^{\Lambda}_{i_1 i_2}(3,2':4,2)P^{\Lambda}_{i_1 i_1}(\omega_3,\omega_4) \\ &+\tilde{\Gamma}^{\Lambda}_{i_2 i_1}(4,2':1,3)\tilde{\Gamma}^{\Lambda}_{i_2 i_1}(1',3:4,2)P^{\Lambda}_{i_2 i_1}(\omega_3,\omega_4)\Big]\end{aligned} \tag{3.53}$$

where we have defined

$$P^{\Lambda}_{i_1 i_2}(\omega_1,\omega_2) = G^{\Lambda}_{i_1}(\omega_1)S^{\Lambda}_{i_2}(\omega_2) + G^{\Lambda}_{i_2}(\omega_2)S^{\Lambda}_{i_1}(\omega_1). \tag{3.54}$$

Depending on the truncation scheme in use, the form of $P^{\Lambda}_{i_1 i_2}(\omega_1,\omega_2)$ will be different. If the conventional scheme is used, in which the third particle vertex is completely disregarded, the single scale propagator has the form of Eq. (3.44) and we obtain

$$G^{\Lambda}(\omega_1)S^{\Lambda}(\omega_2) = \frac{\delta(|\omega_1|-\Lambda)}{\omega_1+\gamma^{\Lambda}(\omega_1)}\frac{\Theta(|\omega_2|-\Lambda)}{\omega_2+\gamma^{\Lambda}(\omega_2)}. \tag{3.55}$$

Within the Katanin truncation scheme, the replacement Eq. (3.45) is done only in the second flow equations, and it leads to

$$\begin{aligned}G^{\Lambda}(\omega_1)S^{\Lambda}(\omega_2) = &\frac{\delta(|\omega_1|-\Lambda)}{\omega_1+\gamma^{\Lambda}(\omega_1)}\frac{\Theta(|\omega_2|-\Lambda)}{\omega_2+\gamma^{\Lambda}(\Omega_2)} \\ &+\Big(\frac{d}{d\Lambda}\gamma^{\Lambda}(\omega_1)\Big)\frac{\Theta(|\omega_1|-\Lambda)}{(\omega_1+\gamma^{\Lambda}(\omega_1))^2}\frac{\Theta(|\omega_2|-\Lambda)}{\omega_2+\gamma^{\Lambda}(\omega_2)}.\end{aligned} \tag{3.56}$$

This means that within the Katanin truncation scheme the right hand side of the flow equation for the two particle vertex will contain a new term.

The five terms on the right-hand side of Eq. (3.53) can be easily distinguished according to their site-index structure, as illustrated in Fig. 39. The first term is a particle-particle term that generates ladder-type diagrams where the fermion lines have the same orientation (see arrows in Fig. 39). The second term is special as it contains an internal closed fermion loop associated with a site summation. This term

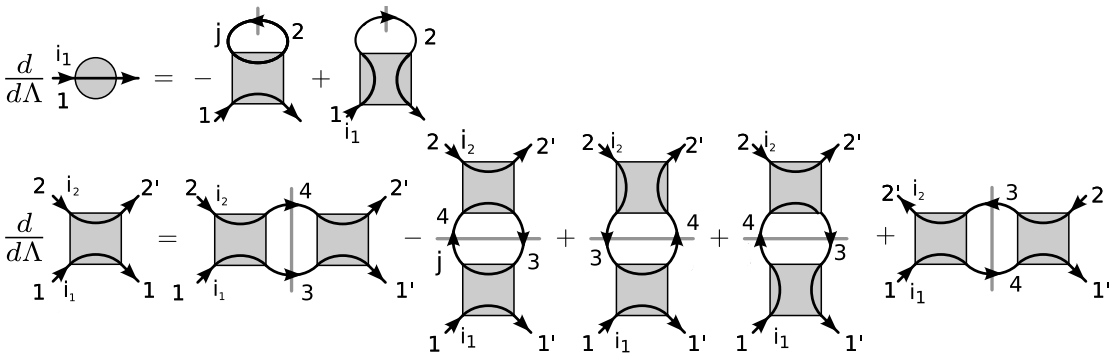

Figure 39: Diagrammatic illustration of the PFFRG flow equations for the self energy and the two-particle vertex, see also Eqs. (3.52) and (3.53). The gray lines crossing two fermion propagators denote the term $P^{\Lambda}_{i_1 i_2}(\omega_1,\omega_2) = G^{\Lambda}_{i_1}(\omega_1)S^{\Lambda}_{i_2}(\omega_2) + G^{\Lambda}_{i_2}(\omega_2)S^{\Lambda}_{i_1}(\omega_1)$ while slashes crossing only one line are the single scale propagators. Site indices i_1, i_2, j illustrate the real-space structure of the flow equations. The five terms on the right-hand side of the second equation are the particle-particle channel, the RPA term, two vertex correction terms and the crossed particle hole term in the same order as they appear in Eq. (3.53).

sums up RPA diagrams and will play an important role in the spin-S generalization described in the next chapter. Most importantly, this is the only term in the PFFRG equations where the vertex evolution $\frac{d}{d\Lambda}\tilde{\Gamma}^{\Lambda}_{i_1 i_2}$ does not only couple to the local vertex $\tilde{\Gamma}^{\Lambda}_{ii}$ or to itself, but also to any other vertex $\tilde{\Gamma}^{\Lambda}_{i_1 j}$ and $\tilde{\Gamma}^{\Lambda}_{j i_2}$. As a consequence, the RPA term generates long-range correlations between spins. The third and fourth terms in Eq. (3.53) are referred to as vertex corrections, while the fifth term is the crossed particle-hole channel summing up ladder diagrams with fermion lines of opposite orientation. In general, the non-local nature of the RPA term is responsible for the formation of magnetic long-range order. On the other hand, the ladder diagrams induce a strong short-range binding between nearby spins leading to spin-singlet formation and to an effective non-magnetic resonating-valence bond description. Given that in our approach the terms that contribute to magnetic order and those that induce quantum fluctuations are treated on the same level of approximation, magnetically ordered and disordered phases can be described on equal footing, which establishes the strength of the PFFRG method.

The last step of the derivation is straightforward though tedious, we show the final flow equations in Appendix . It regards the replacement of $\tilde{\Gamma}^{\Lambda}$ with $\tilde{\Gamma}^{\Lambda}_{\mathrm{s}}$ and $\tilde{\Gamma}^{\Lambda}_{\mathrm{d}}$ in Eq.3.53 and performing the spin sums over α_3 and α_4 with the subsequent introduction of the

frequencies s, t, and u. Comparing the contributions corresponding to the spin and density interactions on both sides we obtain flow equations for $\tilde{\Gamma}_{\mathrm{s}}^{\Lambda}$ and $\tilde{\Gamma}_{\mathrm{d}}^{\Lambda}$.

3.4 Technical aspects on the numerical solution

To numerically solve the PFFRG equations, several further steps of manipulating Eq. (3.53) need to be performed. In the following we treat the definition of boundary conditions for our real space dependence, as well as the appropriate approximation of the continuous frequency variables by a discrete grid. Finally we will briefly explain the numerical algorithm employed in the solution of the equations.

3.4.1 Treating the spatial dependence

Since our flow equations have summations which depend on the lattice sites, and the numerics require a finite set, we need to treat this spatial dependence in a way in which, for finite system sizes, we can distinguish between presence and absence of long range order, and where the finite size effects are minimized. At the same time, given the site summations involved, maintaining the translational invariance of our lattice intact will allow us to speed up the calculation. In our numerics we will treat this spatial dependence considering an infinite system where the spatial limit appears in the vertex functions. We will consider an infinite system in which $\Gamma^{\Lambda}_{i_1 i_2} \neq 0$ for i_1 and i_2 such that

$$|R^{\gamma}_{i_1} - R^{\gamma}_{i_2}| < L^{\gamma}, \tag{3.57}$$

where $\gamma = \{x, y, z\}$, $\mathbf{R}_i = (R^x_i, R^y_i, R^z_i)$ is the distance between sites i_1 and i_2, and $\mathbf{L} = (L_x, L_y, L_z)$, with $L_{x,y,z}$ the number of unit cells in (x, y, z) direction where the condition holds.

With condition (3.57), our effective system "size" will be defined in terms of $\mathbf{L}$. For example, for a simple cubic lattice we take $L_x = L_y = L_z = L$, and our system size will contain L^3 sites. With this constraint, translational invariance is preserved, so our site summations will be performed only over all the neighboring sites that fulfill the length constraint. Please note that in the case of the two particle each RPA bubble contains sums running over an index j, dealing with vertices between i_1 and j, and j and i_2, while the self energy only contains one. Further lattice symmetries will be employed to speed up the calculation.

3.4.2 Frequency dependence and numerical approximation

Once we resolved the spatial dependence, we can concentrate on the treatment of the frequencies.

First and foremost, the flow equations at zero temperature are formulated in terms of a continuous set of frequencies. To achieve a numerical solution we need to discretized the frequency dependence, i.e selecting our frequencies s, t, and u from an appropriate grid. In general we will use a linear grid for the frequencies corresponding to several orders of magnitude above the coupling strength, where the flow of the two particle vertex is small and shows little variation, and a logarithmic grid at energy scales of the order of the coupling strength and below, to obtain a good resolution of the small energy scales where the interesting behavior of the flow is located. In principle, the frequency arguments ω, ω_1, ω_2, and ω_3 that appear on the right hand side of the flow equations for $\tilde{\Gamma}^{\Lambda}_{\mathrm{s(d)}}$ and $\Sigma^{\Lambda}(\omega)$ will not coincide with grid points as they are given by combinations of s, t, and u as mentioned before Eq. (3.52). To choose one point from the grid for each one of these frequencies we use a linear interpolation based on the nearest grid point below ($\omega_<$) and above ($\omega_>$) our desired frequency. This way, our self energy results

$$\gamma^{\Lambda}(\omega) = [\gamma^{\Lambda}(\omega_<)(\omega_> - \omega) + \gamma^{\Lambda}(\omega_>)(\omega - \omega_<)]\frac{1}{\omega_> - \omega_<}. \tag{3.58}$$

and the two particle vertex

$$\begin{aligned}\Gamma^{\Lambda}_{\mathrm{s(d)}i_1i_2}(\omega_1,\omega_2,u) = \big[&\Gamma^{\Lambda}_{\mathrm{s(d)}i_1i_2}(\omega_{1<},\omega_{2<},u)(\omega_{1>}-\omega_1)(\omega_{2>}-\omega_2)\\ &+\Gamma^{\Lambda}_{\mathrm{s(d)}i_1i_2}(\omega_{1<},\omega_{2>},u)(\omega_{1>}-\omega_1)(\omega_2-\omega_{2<})\\ &+\Gamma^{\Lambda}_{\mathrm{s(d)}i_1i_2}(\omega_{1>},\omega_{2<},u)(\omega_1-\omega_{1<})(\omega_{2>}-\omega_2)\\ &+\Gamma^{\Lambda}_{\mathrm{s(d)}i_1i_2}(\omega_{1>},\omega_{2>},u)(\omega_1-\omega_{1<})(\omega_2-\omega_{2<})\big]\\ &\times\frac{1}{(\omega_{1>}-\omega_{1<})(\omega_{2>}-\omega_{2<})}.\end{aligned} \tag{3.59}$$

Finally, we point out that as we could use lattice symmetries to speed up the numerics, we can also use frequency symmetries[44]. The vertex $\Gamma^{\Lambda}_{\mathrm{s(d)}i_1i_2}(s,t,u)$ is invariant under $s \to -s$, $t \to -t$, and $u \to -u$. Furthermore, $\Gamma^{\Lambda}_{\mathrm{s}i_1i_2}(s,t,u)$ is invariant and $\tilde{\Gamma}^{\Lambda}_{\mathrm{d}i_1i_2}(s,t,u)$ changes sign under $s \leftrightarrow u$. These symmetries reduce the computational power by a factor of 16 since only 1/16 of the space spanned by the frequencies needs to be calculated.

3.4.3 Numerical algorithm

The equations that remain to be solved are ordinary first order (coupled) differential equations of the form

$$\frac{d}{d\Lambda}\Upsilon^{\Lambda} = f(\Upsilon^{\Lambda}, \Lambda) \tag{3.60}$$

where Υ represents the self energy and two particle vertex, and f is the right hand side of the flow equations.

The solutions of these equations can be found numerically via an iterative method, for this we chose a Runge Kutta algorithm. Furthermore, a Runge Kutta order one, otherwise known as the Euler method, is sufficient to solve it with minimal numerical error. The algorithm consists on replacing the boundary ∞ by a large value and splitting up the integration range into n small pieces, $[\Lambda_0, \infty) \rightarrow [\Lambda_0, \Lambda_1]$, $[\Lambda_1, \Lambda_2]$, ... , $[\Lambda_{n-1}, \Lambda_n]$. For the first step we get $\Upsilon = \Upsilon^{\Lambda_n}$, from then the algorithm proceeds by introducing in the integrand the previous values of Υ.

The pseudo code (ignoring the spatial dependence that only consists on nested "for" loops on the lattice indices) has the form:

Algorithm 1 Euler method for the flow equations.

```
Define f(Υ^Λ, Λ).
Input the initial conditions Υ^{Λ_n} and Λ_n.
Input the step size h, and the number of steps n.
for (j = 0; j < n+1) do
   m = f (Υ^{Λ_n}, Λ_n)
   Υ_{n-1} = Υ_n + h*m
   Λ_{n-1} = Λ_n + h
   Υ_n = Υ_{n-1}
   Λ_n = Λ_{n-1}
end for
```

Please note that certain care needs to be taken regarding the third step, since the step size, h, will change depending on the discretization of the continuous frequency Λ. The algorithm is in principle straightforward, but using every possible symmetry in the frequency and real space is essential, since the scaling with the different parameters can require several CPU hours/days per data point. We can estimate the scaling of the computation by looking at the most complex flow equation, the two particle vertex: for the spacial dependence of the scaling we notice that the two particle vertex $\tilde{\Gamma}^{\Lambda}_{i_1 i_2}$ depends

on two sites. This is due to the fact that the lattice is translation invariant and as such the two particle vertex will depend on the distance between the sites, but not the sites themselves. As such we can fix i_1 and calculate the two particle vertex for every site i_2. These scales with system size, N, as $\mathcal{O}(N)$. But at the same time the two particle vertex contains a site summation running over all the sites in the lattice, which transforms the scaling to $\mathcal{O}(N^2)$. For the frequencies, we have three frequencies discretized over a grid containing f points, which together with the Katanin truncation result in a scaling of the form $\mathcal{O}(f^4)$. Finally, our total computational scaling for a calculation consisting of N lattice sites, provided translational invariance is not broken, and f frequency grid points, results $\mathcal{O}(N^2 \times f^4)$.

For our results throughout this thesis we use a combination of a linear and logarithmic grid consisting of up to 60 discrete values for each frequency variable. For the Λ grid we will employ a scale in which $\Lambda_n = 0.95\Lambda_{n-1}$. Furthermore, the spatial dependence of the vertex functions is treated with $L = 10$ according to our spatial constraint.

3.5 Calculations of the static spin-spin correlator

Finally, from our approach we can calculate the static spin-spin correlation function, which gives us information on the magnetic properties related to two particle interactions. We can calculate this quantity via Kubo's formula. If we consider a small local magnetic field at site i , we can ask what the effect on a spin on another site j will be, and treat this as a perturbation to our Hamiltonian on site j. The response to this perturbation is given by

$$\chi_{ij}(\tau) = \theta(\tau)\langle\{\mathbf{S}_i(\tau)\mathbf{S}_j(0)\}\rangle\,. \tag{3.61}$$

For the static correlator we can write

$$\chi_{ij} = \int_0^\infty d\tau\, \langle T_\tau\{\mathbf{S}_i(\tau)\mathbf{S}_j(0)\}\rangle\ . \tag{3.62}$$

This has the form of a spin-spin correlator, which can also be interpreted as a local susceptibility. We can replace the spin operators for pseudofermions, and see that the form of the susceptibility resembles that of a two point Green's function with the superindices $1' = 1$ and $2' = 2$. We can expand the expectation value diagrammatically as we have done in previous sections for the Green's functions, and we find

(3.63) $\chi^{\Lambda}_{ij} =$ 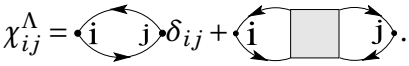

which in explicit form reads

$$\chi^{\Lambda}_{ij} = -\frac{1}{4\pi}\int d\omega G^{\Lambda}(\omega)G^{\Lambda}(\omega)\delta_{ij} - \frac{1}{8\pi^2}\int\int d\omega d\omega' G^{\Lambda}(\omega)G^{\Lambda}(\omega)G^{\Lambda}(\omega')G^{\Lambda}(\omega') \tag{3.64}$$
$$\times\left[2\Gamma^{\Lambda}_{\mathrm{s}ij}(\omega+\omega',0,\omega-\omega') + \Gamma^{\Lambda}_{\mathrm{s}ii}(\omega+\omega',\omega-\omega',0)\delta_{ij} - \Gamma^{\Lambda}_{\mathrm{d}ii}(\omega+\omega',\omega-\omega',0)\delta_{ij}\right].$$

Exploiting translation invariance of the lattice and transforming the site variables i_1 and i_2 into $\mathbf{k}$-space yields the spin susceptibility $\chi^{\Lambda}(\mathbf{k})$ as a function of the RG scale Λ. The magnetic properties of the system can be deduced from the Λ evolution of the susceptibility.

We have formulated our full PFFRG derivation considering that our system does not break time reversal symmetry. Furthermore, we have pointed out the increase in complexity if we were to add time reversal symmetry breaking terms to the Hamiltonian. This means that the flow equations will have a physical solution as long as time reversal is not broken, if this symmetry is broken then the results lack physical meaning and the flow of the studied quantity breaks down. This property is used in the analysis of our numerical results by studying the behavior of the maximum of the two point susceptibility in the reciprocal space at a given Λ, $\chi_{max}(\mathbf{k})$: In the case that our particular Hamiltonian presents magnetic long-range order (LRO) in the ground state, and this LRO appears with wave vector $\mathbf{k}$, the corresponding maximal susceptibility $\chi_{max}(\mathbf{k})$ will grow as Λ is decreased, until a peak or a kink indicates the magnetic instability breakdown of the RG flow as can be seen in Fig. 310. Please note that with a dense frequency grid and in the thermodynamic limit, i.e., without limiting the spatial extent of the two-particle vertex, these peaks would grow and eventually become divergences. Otherwise, if the system does not exhibit LRO in the ground state, a smooth flow of the susceptibility is expected, i.e. it does not show

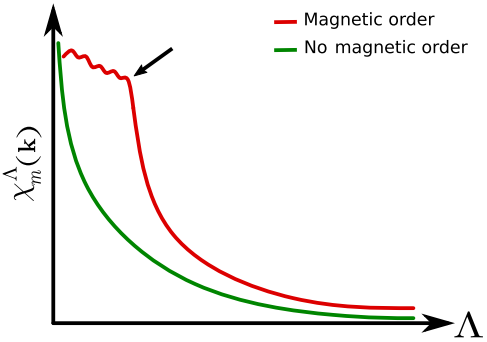

Figure 310: Sketch of the susceptibility's flow as a function of Λ for the cases of a magnetically disordered ground state (green curve) and another presenting LRO (red curve). We plot the maximum of the Fourier transform of the two particle susceptibility at the dominant wavevector $\mathbf{k}$ as a function of Λ.

signatures of an instability down to $\Lambda \to 0$, as shown by the green curve in Fig. 310. We have to be careful still with the interpretation of this analysis, as we are studying two point correlators. The absence of a magnetic instability is not a smoking gun proof of a disordered ground state without any type of symmetry breaking, as there might be an instability in a higher order correlator (for example, a chiral state is expected to present an instability in the three point correlator). It is worth noting that if the spatial constraint we mentioned before on the two particle vertex is too drastic, which would mean working with a lattice size too small, the signatures of magnetic instabilities cannot be clearly identified, as a relatively big system size is needed to identify LRO. In our experience, system sizes with a lattice size $L = 6$, which is equivalent in our honeycomb lattice benchmark to ~ 70 sites, is enough to detect a clear magnetic instability. As the size is increased the instability gets more pronounced, but the critical value at which it happens, Λ_{crit}, is not changed (please note that a good determination of Λ_{crit} requires a very dense discretization of the Λ scale).

CHAPTER 4

QUANTUM TO CLASSICAL CONNECTION
LARGE S GENERALIZATION FOR PFFRG

The part that is stable we are going to predict. And the part that is unstable we are going to control.

John von Neumann, 1948

In the following chapter, we will introduce a large S generalization for the pseudofermionic FRG framework. While this generalization might seem of pure academic interest, there is a growing number of spin systems, many of them with experimental realizations, where novel phases appear at higher spin lengths than 1/2.

The traditional recipe for maximizing the effects of quantum fluctuations has primarily involved spins of the smallest magnitude $S = 1/2$, but extremely interesting spin phases can likewise occur in the extreme opposite limit of classical spins, $S \to \infty$. For example, this limit is realized in pyrochlore materials known as spin-ices[45] which are characterized by an extensive ground state degeneracy[46] and effective monopole excitations[47], and in spiral spin liquid materials [48–50]. Furthermore, there are many novel types of quantum phases that appear at a specific intermediate value of S (see e.g. Refs [51–54]).

In the present chapter we will show how this generalization is obtained within the PFFRG framework, and later on, as a first test, we will apply this scheme to the

antiferromagnetic J_1-J_2 Heisenberg model on the honeycomb lattice with first (second) neighbor interactions J_1 (J_2). Due to the frustrating effect of the J_2 coupling, the system shows rich magnetic behavior as a function of S and J_2/J_1, where the spin-1/2 case has attracted particular attention.

4.1 Large S generalization

The first step of our approach to generalizing the $S = 1/2$ PFFRG method of the previous chapter to arbitrary spin lengths S, consists on generating spins of length S in our lattice sites. The most straightforward way in which we could do this is generalizing the Pauli matrix representation σ^μ in Eq. (3.32) to higher angular momenta, as described, e.g., in Ref. [55]. In such a scheme, the implementation of a spin-S degree of freedom requires the introduction of $2S+1$ fermions on each site with a pseudo fermion constraint fixing the particle number to either 1 or $2S$. This constraint could be implemented by introducing a non-zero chemical potential, but in situations as we are interested in, the problem of applying a chemical potential is that any finite μ will either deplete the system completely ($\mu > 0$) or induce the maximal fermion occupation ($\mu < 0$), as our Hamiltonians posses no hopping terms. To not deal with this complication, we will approach the problem from a different perspective: we will generate our spin S in a given site, by considering multiple copies of spin-1/2 degrees of freedom of different *flavors* on each site [56–58]. Thus the finite chemical potential problem is avoided since for each flavor κ a spin-1/2 degree of freedom is realized at half filling which corresponds to a chemical potential $\mu = 0$ as stated in the previous chapter.

To achieve the arbitrary S formulation, we have to rewriting our pseudo-fermionic approach considering the different flavors. In our definition (3.32) we now add a sum over the M spin flavors, i.e.

$$\mathbf{S}_i \to \sum_{\kappa=1}^{M} \mathbf{S}_{i\kappa}\,, \tag{4.1}$$

where κ denotes the new "flavor" index. Inserting into the Hamiltonian (3.30) we obtain

$$\mathscr{H} = \sum_{(ij)} J_{ij} \left(\sum_{\kappa=1}^{M} \mathbf{S}_{i\kappa} \right) \cdot \left(\sum_{\kappa'=1}^{M} \mathbf{S}_{j\kappa'} \right). \tag{4.2}$$

Please note that all flavors κ on site i interact with all flavors κ' on site j via the same coupling J_{ij}, but there is no coupling between spins of different flavors in the same site. A coupling between different flavors in the same site can be added, this is what we will reference in the next sections as *level repulsion terms*.

The question that arises when one introduces the different flavors is related to the total spin our combination of pseudofermions of different flavors will generate. If we study the modified pseudo-fermionic representation in Eq. (3.32) we see that in this case, if we aim to set up a generalized spin-S PFFRG scheme, the pseudo-fermions acquire an extra flavor index, and the representation takes the form

$$S^{\mu}_{i\kappa} = \frac{1}{2}\sum_{\alpha\beta} f^{\dagger}_{i\alpha\kappa}\sigma^{\mu}_{\alpha\beta}f_{i\beta\kappa}\,, \tag{4.3}$$

where the operators $f_{i\alpha\kappa}$ fulfill the standard fermionic anti-commutation relation

$$\{f_{i\alpha\kappa}, f^{\dagger}_{i'\alpha'\kappa'}\} = \delta_{ii'}\delta_{\alpha\alpha'}\delta_{\kappa\kappa'}\,. \tag{4.4}$$

As mentioned in the previous chapter, the operators $f^{(\dagger)}_{i\uparrow\kappa}$, $f^{(\dagger)}_{i\downarrow\kappa}$ for a given site i (and now also for a particular flavor κ) will generate sectors in our Hilbert space which correspond to spins of total length 0 and 1/2. This means that if we sum up M of these operators we essentially are generating subspaces that correspond to net spin lengths ranging from $M/2$ to 0. The main problem is that, a priori, we cannot state which spin length will correspond to the ground state. Since we aim to use this approach to study the ground state of spin models with a certain fixed spin $S = M/2$, we need to find out whether the subspace corresponding to our desired spin length S is the one in which the ground state of

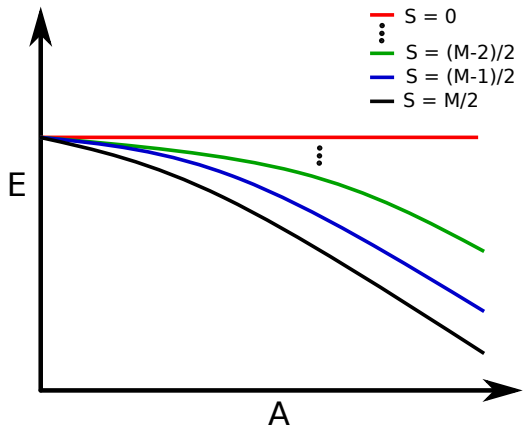

Figure 41: Scheme representing the energy of the different spin sectors as a function of the on-site level repulsion term strength. We show the energy as a function of a ferromagnetic coupling A for different values of the total spin length S. A ferromagnetic level repulsion term will strongly reduce the energy of the higher spin sector.

Eq. (4.2) is realized or whether the ground state has contributions from different sectors. We can gain an intuitive understanding of which spin length will correspond to the ground state if we think about Hund's first rule. This rules states that for a given electron configuration, the term with maximum multiplicity has the lowest energy. The multiplicity being equal to $2S+1$, where S is the total spin angular momentum for all electrons. This means that according to this rule, the term with lowest energy is also the term with maximum total spin S. In our particular case, given that the largest angular momentum eigenvalues corresponds to $S = M/2$, it is natural to assume that the ground state will be constructed from states with $S = M/2$ on each site.

We will show in Sec. 4.1.1 that this is indeed the case. We will do this by explicitly adding the aforementioned level repulsion terms, of the form $A(\sum_{\kappa=1}^{M} \mathbf{S}_{i\kappa})^2$, with a ferromagnetic coupling, A. Since the eigenvalues of $\mathbf{S}_i^2$ are $S(S+1)$ then a ferromagnetic A will shift the ground state energy of our Hamiltonian by a factor of $S(S+1)$ as shown in Fig. 41. What we expect is that, if the ground state is indeed composed exclusively from $S = M/2$ states, then the inclusion of the level repulsion terms should not affect the results obtained from PFFRG. This would be a clear indication that the ground state of the modified Hamiltonian in Eq. (4.2) with M spin flavors is identical to the ground state of the model (3.30) with spin length $S = M/2$.

To see how this modified pseudofermionic representation affects the flow equations, we set up a diagrammatic theory with the new flavor indices κ. This is a straightforward process since we already know what the building blocks of our theory are. In the diagrammatic theory with new flavor indices we obtain the bare propagator $G_0(1';1)$ (analogous to that in Eq. (3.37)

$$G_0(1';1) = \frac{1}{i\omega_1}\delta(\omega_1 - \omega_{1'})\delta_{i_{1'}i_1}\delta_{\alpha_1\alpha_{1'}}\delta_{\kappa_{1'}\kappa_1}\,, \tag{4.5}$$

where the δ-function on the flavor indices arises from the anticommutation relations in Eq. (4.4). With this in mind we see that the bare interaction $\Gamma^{\infty}(1',2';1,2)$ (i.e., the two-particle vertex at $\Lambda \to \infty$, analogous to Eq. (3.46) also has a δ-function in the flavor indices,

$$\begin{aligned}\Gamma^{\infty}(1',2';1,2) =& J_{i_1 i_2}\sigma^{\mu}_{\alpha_{1'}\alpha_1}\sigma^{\mu}_{\alpha_{2'}\alpha_2}\delta_{i_{1'}i_1}\delta_{i_{2'}i_2}\delta_{\kappa_{1'}\kappa_1}\delta_{\kappa_{2'}\kappa_2} \\ &\times \delta(\omega_1+\omega_2-\omega_{1'}-\omega_{2'}) \\ &-(\omega_1 \leftrightarrow \omega_2, i_1 \leftrightarrow i_2, \alpha_1 \leftrightarrow \alpha_2, \kappa_1 \leftrightarrow \kappa_2)\,.\end{aligned} \tag{4.6}$$

where the multi indices also include the κ variables, i.e. "$1 = \{\omega_1, i_1, \alpha_1, \kappa_1\}$". By simple inspection we notice that the index structure in Eqs. (4.5) and (4.6) is identical for the indices κ and i. This simply means that the flavor index can be understood as an extra site variable, and as such the sums can be dealt with exactly the same way as for site indices. Furthermore, since the bare couplings J_{ij} do not depend on the flavor indices, and the number of flavors is finite, the treatment of the multiple flavors is even simpler than the case for the sites. A depiction of this process is shown in figure 42.

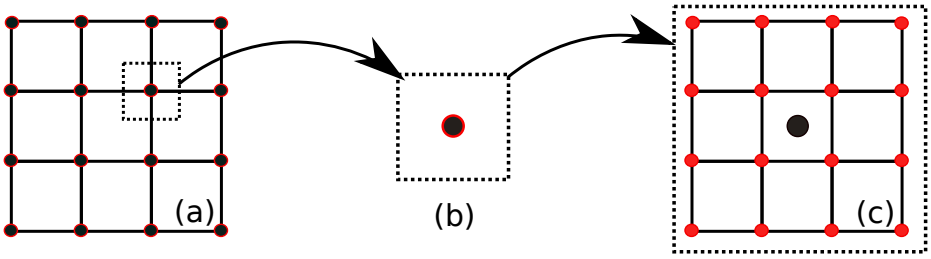

Figure 42: Scheme depicting the equivalence between different flavor pseudofermions and site indices. (a) Each site here is a real space site where an spin lives. A red and black dot represents a spin-S. (b) One spin-S site contains 2M pseudofermions corresponding to M different flavors. (c) According to Eqs. (4.5) and (4.6) the flavor index can be considered as a site index. As such the sum between flavors can be dealt in exactly the same way as a sum between real space indices, which can be depicted as each flavor corresponding to the sites of an underlying lattice (red dots).

With this equivalence, the analog of Eq. (3.47) is immediately given by

$$\begin{aligned}\Gamma^{\Lambda}(1',2';1,2) =& \tilde{\Gamma}^{\Lambda}_{i_1 i_2 \kappa_1 \kappa_2}(1',2';1,2)\delta_{i_{1'} i_1}\delta_{i_{2'} i_2}\delta_{\kappa_{1'}\kappa_1}\delta_{\kappa_{2'}\kappa_2} \\ & -(\omega_1 \leftrightarrow \omega_2, i_1 \leftrightarrow i_2, \alpha_1 \leftrightarrow \alpha_2, \kappa_1 \leftrightarrow \kappa_2)\,. \end{aligned} \tag{4.7}$$

As noted earlier, the exchange couplings $J_{i_1 i_2}$ in Eq. (4.6) do not depend on the flavor variables such that there is no explicit κ dependence in the scheme. Consequently, the couplings $J_{i_1 i_2}$ also remain independent of the flavor index yielding $\tilde{\Gamma}^{\Lambda}_{i_1 i_2 \kappa_1 \kappa_2}(1',2';1,2) \equiv \tilde{\Gamma}^{\Lambda}_{i_1 i_2}(1',2';1,2)$.

With this, the modifications of the PFFRG scheme are rather simple. If we look at Eq. (3.40) and (3.41) we see that we will obtain a very similar equation, but where now the sums stand for $\Sigma_1 \equiv \int_{\omega_1} d\omega_1 \sum_{i_1} \sum_{\alpha_1=\uparrow,\downarrow} \sum_{\kappa_1}$. Following the exact same procedure as described in the previous section we can obtain the flow equations for the self energy

$$\begin{aligned}\frac{d}{d\Lambda}\gamma^{\Lambda}(\omega) = \frac{1}{2\pi}\Big[&-2M\sum_j(\tilde{\Gamma}^{\Lambda}_{\mathrm{d}ij}(\omega+\Lambda,0,\omega-\Lambda)-\tilde{\Gamma}^{\Lambda}_{\mathrm{d}ij}(\omega-\Lambda,0,\omega+\Lambda))\\ &+3(\tilde{\Gamma}^{\Lambda}_{\mathrm{s}ii}(\omega+\Lambda,\omega-\Lambda,0)-\tilde{\Gamma}^{\Lambda}_{\mathrm{s}ii}(\omega-\Lambda,\omega+\Lambda,0))\\ &+\tilde{\Gamma}^{\Lambda}_{\mathrm{d}ii}(\omega+\Lambda,\omega-\Lambda,0)-\tilde{\Gamma}^{\Lambda}_{\mathrm{d}ii}(\omega-\Lambda,\omega+\Lambda,0)\Big]\frac{1}{\Lambda+\gamma^{\Lambda}(\Lambda)}\end{aligned} \tag{4.8}$$

and the two particle vertex.

$$\begin{aligned}\frac{d}{d\Lambda}\tilde{\Gamma}^{\Lambda}_{i_1i_2}(1',2':1,2) = \frac{1}{2\pi}\int_{-\infty}^{\infty}d\omega_4\int_{-\infty}^{\infty}d\omega_3\sum_{\alpha_3,\alpha_4}&\\ \Big[\tilde{\Gamma}^{\Lambda}_{i_1i_2}(1',2':3,4)\tilde{\Gamma}^{\Lambda}_{i_1i_2}(3,4:1,2)P^{\Lambda}_{i_1i_2}(\omega_3,\omega_4)&\\ -2M\sum_j\tilde{\Gamma}^{\Lambda}_{i_1j}(1',4:1,3)\tilde{\Gamma}^{\Lambda}_{ji_2}(3,2':4,2)P^{\Lambda}_{jj}(\omega_3,\omega_4)&\\ +\tilde{\Gamma}^{\Lambda}_{i_1i_2}(1',4:1,3)\tilde{\Gamma}^{\Lambda}_{i_2i_2}(3,2':2,4)P^{\Lambda}_{i_2i_2}(\omega_3,\omega_4)&\\ +\tilde{\Gamma}^{\Lambda}_{i_1i_1}(1',4:3,1)\tilde{\Gamma}^{\Lambda}_{i_1i_2}(3,2':4,2)P^{\Lambda}_{i_1i_1}(\omega_3,\omega_4)&\\ +\tilde{\Gamma}^{\Lambda}_{i_2i_1}(4,2':1,3)\tilde{\Gamma}^{\Lambda}_{i_2i_1}(1',3:4,2)P^{\Lambda}_{i_2i_1}(\omega_3,\omega_4)\Big]&\end{aligned} \tag{4.9}$$

The extra flavor sum that needs to be performed on the process only appear in the site summations, as these are the RPA terms that couple spins, and thus flavors, on different sites. Performing the sum over flavors explicitly, and using the anticommutation relations, we find that this leads to the prefactors of M in front of the site summations. Please note that there is no further modification of the flow equations. The Katanin truncation can be implemented as before, as well as the vertex parametrization and the numerical treatment of the resulting equations.

We see then that all terms in Eqs. (3.52) and (3.53) that contain a site summation $\sum_j$ now also acquire a flavor sum $\sum_{\kappa=1}^{M}$ producing an extra factor M in these terms. In this fashion we see that (provided the above assumption about the angular momentum subspace of the ground state is correct) a spin-S generalization of the PFFRG only requires an additional prefactor $M = 2S$ in the first term on the right-hand side of Eq. (3.52) (the new version of the equation is shown in Eq (4.8)) and $2M$ in the site summation of Eq. (3.53) (i.e. the second term on the right-hand side of this equation, now in Eq. (4.9). This is a somewhat expected result from a phenomenological point of view: since the site summation lead to the RPA-like terms in the diagrammatic expansion, and these are responsible for the onset of magnetic order, is no surprise that increasing the spin length reinforces this term. Even though the bare couplings J_{ij} are independent of the spin length, the RPA terms are reinforced the bigger $S = M/2$ is and thus the

spin-spin interaction will be enhanced, as a consequence, the system will tend towards some form of magnetic order. In other words, increasing the spin length makes the ladder terms weaker, which is equivalent to decreasing the quantum fluctuations. Since quantum fluctuations are responsible for the existence of disordered ground states in clean quantum systems, we expect that for Heisenberg type systems, there will be a critical value of S at which the possible disordered states are lost and magnetic order appears. We will show how this can happen when we study the honeycomb lattice.

Though these results are expected, it is also remarkable from the numerical point of view. We have shown that arbitrary spin lengths S can be easily implemented in the PFFRG scheme, and that the implementation amounts to a multiplicative factor in the equations. This factor does not change the computational scaling with system size, and as such, any arbitrary spin length can be implemented without additional numerical efforts.

Regarding the numerical solution, one more point needs to be clarified. As prefactors of M appear in front of the RPA terms, it is expected that in the limit of big spin, $S \to \infty$, the equations would contain divergences. Furthermore, the energy scale would change with varying M since

$$\tilde{\Gamma}^{\Lambda\to\infty} \propto \frac{J}{M}. \tag{4.10}$$

Then, to ensure a correct numerical convergence and normalize the energy scales for different spin lengths we define

$$\bar{\Gamma}^{\Lambda} = M\tilde{\Gamma}^{\Lambda}. \tag{4.11}$$

Rewriting the flow equations in terms of $\bar{\Gamma}^{\Lambda}$, and rescaling the bare couplings as $J_{ij} \to J_{ij}/M$, we see that this would be equivalent to "exchanging" the factors proportional to M in the RPA terms for factors proportional to $1/M$ in the rest of the terms. Furthermore,

$$\bar{\Gamma}^{\Lambda\to\infty} \propto J, \tag{4.12}$$

thus the energy scales are automatically rendered equal for every spin length.

4.1.1 Level repulsion terms

Above we have claimed that the ground state of the spin model in Eq. (4.2) featuring M copies of spin-1/2 degrees of freedom on each site is constructed from states in the highest

angular momentum sector, and we proposed an analogy with Hund's first rule. To check that these statements are correct we will consider additional level repulsion terms of the form $A(\sum_{\kappa=1}^{M}\mathbf{S}_{i\kappa})^2$, and we will study the effect of this term on a known model. We will study the Heisenberg honeycomb lattice with nearest neighbor interactions (see Fig. 46) where the resulting Hamiltonian takes the form

$$\mathscr{H} = \sum_{(ij)} J_{ij}\left(\sum_{\kappa=1}^{M}\mathbf{S}_{i\kappa}\right)\cdot\left(\sum_{\kappa'=1}^{M}\mathbf{S}_{j\kappa'}\right) + A\sum_{i}\left(\sum_{\kappa=1}^{M}\mathbf{S}_{i\kappa}\right)^2 . \tag{4.13}$$

The eigenvalues of the operator $(\sum_{\kappa=1}^{M}\mathbf{S}_{i\kappa})^2$ present in the level repulsion term are given by $S(S+1)$ where the total angular momentum quantum number S can, in principle, take all values $0, 1/2, \ldots, (M-1)/2, M/2$. When A is chosen negative, the expected effect of the level repulsion terms it to shift down in energy the angular momentum sectors. This reduction will be more pronounced for the highest angular momentum eigenvalue $S = M/2$. If our assumption is correct, and indeed the ground state of our Hamiltonian without the level repulsion term is given by the biggest total angular momentum, then we expect that further reducing the energy of that subspace with respect to the other ones should have no effects on our results.

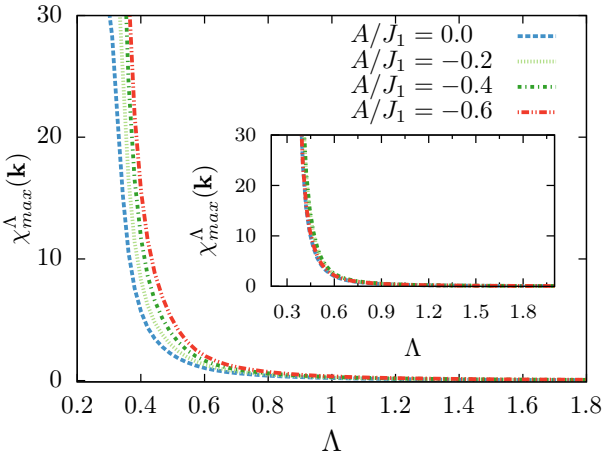

Figure 43: Flowing PFFRG susceptibility for the nearest neighbor honeycomb Heisenberg antiferromagnet with onsite level repulsion terms at $S = 3/2$, and varying negative values of A (due to almost diverging susceptibilities, the RG flow is not shown below the critical Λ scale)

We tested this assumption for the honeycomb Heisenberg antiferromagnet with nearest neighbor interactions $J_1 > 0$. We will present plots showing the maximum of the susceptibility $\chi^{\Lambda}(\mathbf{k})$, which is the Fourier transform of the spin-spin correlator calculated according to Eq. (3.62), as a function of the cutoff parameter Λ. As mentioned before the susceptibility's RG flow breaks down whenever there exists an onset of magnetic order, and we shall call the Λ value at which this breakdown happens *critical*, Λ_c. The breakdown is observed as a change in the slope of the susceptibility curves, accompanied by oscillations arising from the discretization of the continuous frequencies (as a clear

example of this breakdown please look at Fig.44). The model studied here presents long range Neel order, as such, the flow of the two particle correlator will break down. This will appear as a kink in the slope of the susceptibility's flow. Studying how this kink and the overall behavior of the flow changes in the presence of the level repulsion terms, we will explore whether our assumptions about the angular momentum corresponding to the ground state are correct.

In Fig. 43 we show the flow behavior for the case of $S = 3/2$. We present different susceptibilities corresponding to different values of the level repulsion term strength A, normalized with the exchange coupling J_1. It can be seen that the susceptibility's flow behavior remains qualitatively unchanged as A is decreased from zero, except for an overall shift of the curves towards higher values of Λ. This shift is not surprising, as A and Λ both have the dimension of an energy, and subsequently the energy scale is modified when the values of A change. Increasing $|A|$ while keeping J_1 fixed increases the overall energy scale of the system such that the parameter Λ becomes renormalized. To account for these effects, we repeated the calculations for rescaled values of A and J_1. Phenomenologically, we find that for fixed $\sqrt{A^2 + J_1^2}$ such artifacts are largely removed, yielding an approximate collapse of all curves, see inset in Fig. 43. In the rest of the plots in this section the susceptibility $\chi^{\Lambda}(\mathbf{k})$ (RG scale Λ) is given in units of $1/J_1$ (J_1). In the insets, energy scales are in units of $\sqrt{A^2 + J_1^2}$ to compensate for energy renormalization effects in Λ.

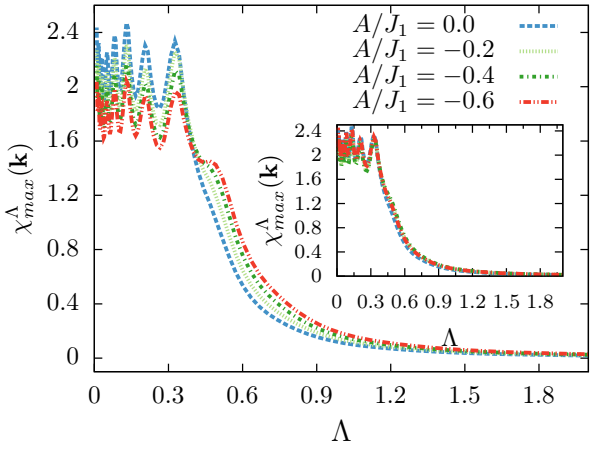

Figure 44: Flowing PFFRG susceptibility for the nearest neighbor honeycomb Heisenberg antiferromagnet with onsite level repulsion terms at $S = 1/2$, and varying negative values of A

We also studied the effect of level repulsion terms for the case of spin-1/2 systems. In this case the level repulsion terms will change the energy of the two sectors mentioned in section 3.2: the unphysical spin-zero sector, representing occupations such as singly or doubly occupied sites, and the spin-1/2 sector. Our initial assumption was that the spin-0 sector is energetically suppressed in the ground state given that fluctuations of the pseudofermionic number are forbidden at zero temperature. If this is indeed the case,

then we should see no qualitative difference in the behavior of the susceptibility's RG flow, as was the case for the spin-3/2 system. We show in Fig. 44 the RG flow behavior of the susceptibility for the nearest neighbor honeycomb Heisenberg antiferromagnet for $S = 1/2$. In analogy to the spin-3/2 case, the flow remains qualitatively unchanged and shifts in Λ can again be compensated by keeping $\sqrt{A^2 + J_1^2}$ constant (inset in Fig. 44). These results indeed shows that our initial assumption was correct, and that no unphysical subspaces contribute to the flow.

Additional calculations also confirm the absence of any qualitative changes in the RG flow for finite second neighbor interactions J_2 and varying S. In particular, phase boundaries between different magnetic phases or melting transitions into non-magnetic phases are never found to be affected by A. We therefore conclude that at least for the honeycomb Heisenberg model our assumptions about the angular momentum sector in which the ground state is located are correct. Furthermore, we anticipate that also a wider class of spin models shares this property within the PFFRG framework.

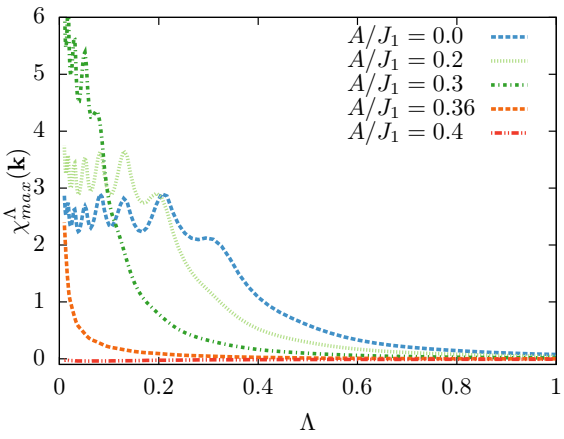

Figure 45: Flowing PFFRG susceptibility for the nearest neighbor honeycomb Heisenberg antiferromagnet with onsite positive level repulsion terms [see Eq. (4.13)]. Susceptibility for $J_2/J_1 = 0.1$, $S = 1/2$, and positive level repulsion terms $A \geq 0$.

It can also be studied what the effect of an antiferromagnetic level repulsion term will be. In this case, the energy levels in the highest angular momentum sector undergo the largest relative *increase*, until above a certain threshold of A, lower subspaces should become energetically preferred. It is expected that the subspace with the *smallest* net spin (the unphysical spin-0 sector) will be preferred after the threshold is reached.

The situation for $J_2/J_1 = 0.1$ and $S = 1/2$ is depicted in Fig. 45, where the absolute value of A is varied within similar ranges as in Figs. 43 and 44 but with a positive sign. Upon increasing A we first observe a decrease of the critical Λ, followed by a sudden drop of the susceptibility at $A \approx 0.35$, and almost vanishing responses above this value. We interpret this behavior as a consequence of promoting the unphysical zero or doubly occupied states. These results can be qualitatively understood with a simple analogy:

if we promote total spin-0 states, what we are basically doing is diluting our system by replacing the magnetic ions with non-magnetic ones. The states carrying $S = 0$ are equivalent to having vacancies in the magnetic lattice, as such the bigger A is, the more magnetic ions are missing, the more diluted our system is, drastically changing the behavior of the magnetic susceptibility. When A is sufficiently large, the ground state resides entirely in the unphysical sector of the Hilbert space, which can be seen as no magnetic ions living in the lattice anymore, leading to a vanishing susceptibility.

4.2 Antiferromagnetic J_1-J_2 Heisenberg model on the honeycomb lattice

To study how this method can be employed to understand the role of quantum fluctuations in different magnetic systems, we apply this scheme to the antiferromagnetic J_1-J_2 Heisenberg model on the honeycomb lattice with first (second) neighbor interactions J_1 (J_2) (see Fig. 46), the Hamiltonian is given by

$$H = J_1 \sum_{\langle ij \rangle} \mathbf{S}_i \mathbf{S}_j + J_2 \sum_{\langle\langle ij \rangle\rangle} \mathbf{S}_i \mathbf{S}_j \,, \tag{4.14}$$

where $\langle ij \rangle$ denotes a pair of nearest neighbor sites while $\langle\langle ij \rangle\rangle$ indicates second neighbor sites. We are interested in the antiferromagnetic version of the system, so the corresponding exchange couplings are $J_1 > 0$ and $J_2 \geq 0$, respectively. The ratio of the two couplings is denoted by $g = J_2/J_1$.

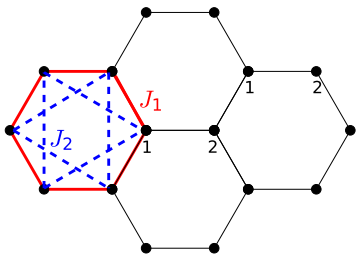

Figure 46: Illustration of the honeycomb lattice where J_1 nearest neighbor (J_2 second neighbor) interactions are highlighted by red (dashed blue) lines. The two sublattices are indicated by numbers and the nearest neighbor distance is assumed to be one.

Plenty of studies have been performed on this particular variant of the Heisenberg honeycomb model. It is known that while the quantum system, $S = 1/2$, remains antiferromagnetically ordered up to $J_2/J_1 \approx 0.2$, an abundance of numerical studies indicate an intermediate magnetically disordered phase above this value [59–73]. The precise nature of this phase is still debated, but there is growing numerical evidence

that it might again be split up into a potential plaquette valence bond solid (a state in which pairs of spins couple into spin-0 singlets, and where these singlets order in a plaquette fashion in the honeycomb lattice, thus preserving the lattice rotational invariance) at smaller J_2/J_1, and a staggered dimer crystal phase at larger J_2/J_1 (also known as lattice nematic, a state in which there is also dimerization present, but the dimers order in a staggered fashion, breaking the rotational invariance of the lattice)[64, 66, 67, 70].

Concerning the opposite, classical, limit $S \to \infty$[74] it has early been realized that above the classical antiferromagnetic phase (which is stable up to $J_2/J_1 = 1/6$) the system features a continuous set of degenerate incommensurate spiral ground states[60, 75] where it is known that quantum fluctuations at large S select a certain finite subset of these states[60] via an order by disorder mechanism. We will not concentrate on a detailed study of the different phases in the $S = 1/2$ case, as it has previously been studied with PFFRG[59]. We will actually concentrate on the effect finite spin lengths, $S > 1/2$, have on the different phases, and in how the presence of quantum fluctuations affect the phase diagram. For sake of completeness we mention that with the PFFRG framework it has been shown for the $S = 1/2$ case that there indeed exists a magnetically disordered phase within the range $J_2/J_1 \approx 0.15 \ldots 0.6$ [59]. Probing this regime with respect to the formation of different types of valence-bond crystals, strong staggered dimer responses are found near the upper boundary of this phase, in agreement with other numerical studies[64, 66–70]. Near the lower phase boundary ($J_2 \sim 0.2$) the PFFRG dimer responses are small, possibly pointing at the existence of a spin liquid phase.

We will show that at relatively large spin lengths the phase diagram quickly resembles the classical one. In particular, already at $S = 1$, PFFRG shows no indication of a magnetically disordered phase (it is worth noting that numerical investigations based on coupled cluster and DMRG approaches indicate the possibility of a small non-magnetic phase in the $S = 1$ case[76, 77]). Instead, the system exhibits two regimes with different types of incommensurate magnetic spiral phases. At $S = 3$ the magnetic phase diagram is almost indistinguishable from the one at $S \to \infty$ except that, as mentioned before, quantum fluctuations select specific states from a continuous set of degenerate classical states via an order by disorder mechanism. This selection is found to be in agreement with earlier semiclassical studies of the system.[60]. At the end of this chapter we will also prove that at $S \to \infty$, when the PFFRG equations can be solved analytically, we exactly reproduce the known classically ordered states. More generally, we will also demonstrate that for arbitrary lattices the PFFRG becomes identical to the Luttinger-Tisza method in this limit.

4.2.1 Phase diagram in the J_2/J_1-S plane via PFFRG

We now apply the spin-S generalization of the PFFRG method discussed in the last section to the antiferromagnetic J_1-J_2 Heisenberg model on the honeycomb lattice as illustrated in Fig. 46.

We will work with a lattice size consisting of 10 unit cells in each direction, i.e $L = 10$, and we will take advantage of the rotational invariance of the lattice to speed up the numerics. The Hamiltonian is given by Eq.4.14.

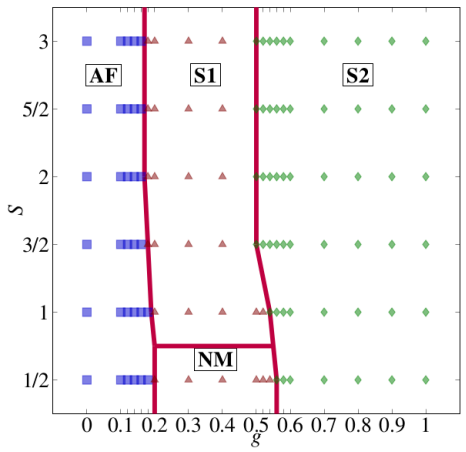

Figure 47: Phase diagram in the g-S plane. We find a non-magnetic (NM) phase at $S = 1/2$ and three magnetically ordered phases: an antiferromagnetic (AF) state represented by blue squares, and two spiral phases S1 (red triangles), and S2 (green diamonds).

Numerically solving the PFFRG equations for varying parameters in the g-S plane we obtain the phase diagram shown in Fig. 47. For $S = 1/2$ we reproduce the phases that have previously been found within PFFRG (see Ref. [59]): An extended non-magnetic phase at $g \approx 0.2 \ldots 0.6$ is framed by an antiferromagnetic phase at $0 \leq g \lesssim 0.2$ and an incommensurate spiral phase at $g \gtrsim 0.6$. When quantum fluctuations are slowly suppressed, meaning, when S is increased, the phase diagram changes drastically.

Already at $S = 1$, the tendency towards magnetic order is strong enough that the non-magnetic phase is completely eaten up by magnetic long-range order presenting incommensurate wavevectors (See Fig. 49). This leads, in total, to three magnetically ordered phases at $S = 1$: an antiferromagnetically ordered regime at $0 \leq g \lesssim 0.19$ and two spiral phases we will name "S1", and "S2" at $0.19 \lesssim g \lesssim 0.53$ and $g \gtrsim 0.53$, respectively.

While this sequence of phases persists for larger values of S, the locations of the two phase transitions shift towards the classical values 1/6 (for the boundary between the antiferromagnetic phase and the S1 spiral), and 0.5 (between S1 and S2), see Fig. 47. This implies that for intermediate values of the spin length, $1/2 < S \leqq 3/2$ quantum fluctuations are suppressed enough as to destroy the non magnetic states, but not enough that the boundaries of the phases will coincide with those in the classical limit.

To demonstrate how the onset of magnetic long-range order for all spin lengths $S \geq 1$ appears within our framework, we show in Fig. 48 the PFFRG flow of the susceptibility

for the highly frustrated case $g = 0.3$ and varying values of S. While at $S = 1/2$ we do not observe an instability feature as Λ is decreased, hinting at a magnetically disordered phase, for all values $S \geq 1$ we find pronounced kinks at $\Lambda \approx 0.2$ associated with the onset of magnetic order. With increasing S the susceptibility grows and the kink becomes more pronounced, signaling an increase in the tendency towards magnetic order. The point at which the kink appears does not change with different spin length, as we have rescaled the equations following the discussion at the end of section 4.1. We will use the point at which the kink appears in $\mathbf{k}$ space to identify the type of magnetic order.

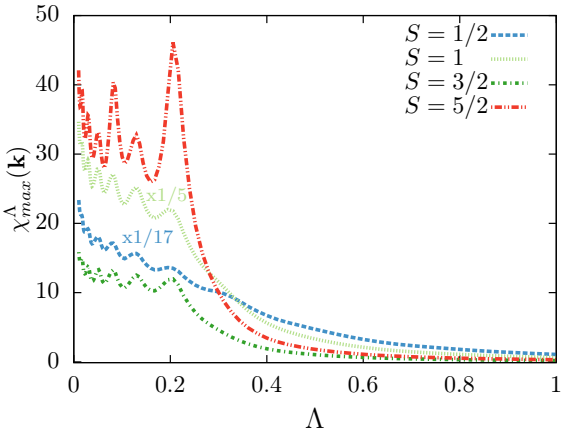

Figure 48: Λ flow of the maximal $\mathbf{k}$ space component of the susceptibility $\chi^{\Lambda}(\mathbf{k})$ for $g = 0.3$ and increasing values of S. While the flow for $S = 1/2$ does not show signatures of an instability, for $S \geq 1$ we find a kink in the susceptibility at $\Lambda \approx 0.2$ that gets more pronounced with increasing S.

To study in more detail the types of magnetic orders detected in the system, we plot in Fig. 49 the $\mathbf{k}$ space resolved susceptibilities at $S = 3/2$ within the three ordered phases, along with real space illustrations of the spin patterns. In the antiferromagnetic phase (Fig. 49(a)) magnetic Bragg peaks are located at the corners of the extended Brillouin zone. As g is increased the system first establishes planar incommensurate spiral order of S1 type, which is characterized by magnetic wave vectors residing at the edges of the extended Brillouin zone, as shown in Fig. 49(b). In the S1 phase the susceptibility presents a ring-like shape. Along these rings the susceptibility is actually not uniform in $\mathbf{k}$ space, but small maxima of the form $\mathbf{k}_{max} = (q, q')$ at the edges of the Brillouin zone can be detected.

This can be contrasted with the selection of wavevectors via quantum fluctuations described in Ref. [60]. Please note that in the classical limit, where the quantum fluctuations disappear, the selection effect is not present, and we obtain a continuous set of degenerate ground states. To sketch the spin pattern of this phase in real space (Fig. 49(b)) we extract the maximum wavevector from our PFFRG susceptibility and construct a planar spiral which – upon Fourier transformation – yields a dominant Bragg peak in $\mathbf{k}$ space at exactly the same position. As a characteristic feature of this state,

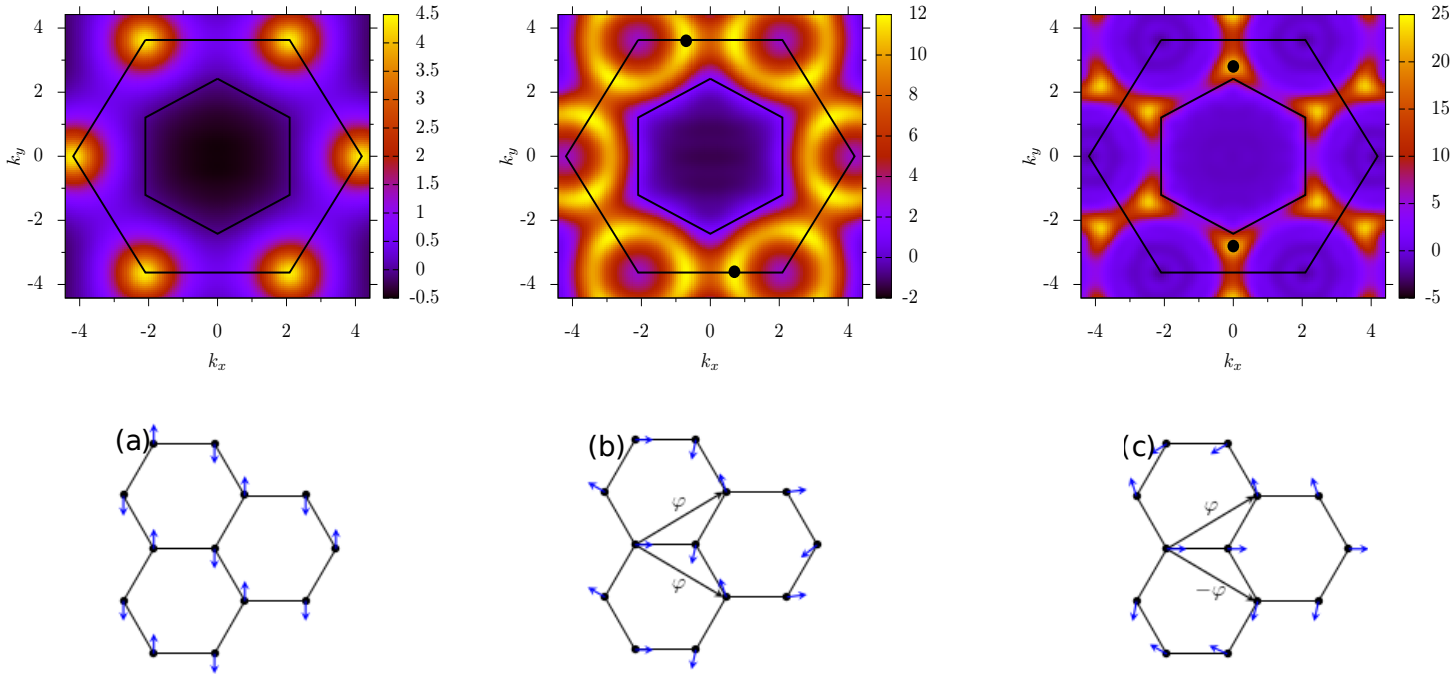

Figure 49: *Upper panel*: Susceptibility $\chi^{\Lambda}(\mathbf{k})$ in reciprocal space for the three magnetically ordered phases at $S = 3/2$. (a) antiferromagnetic state at $g = 0$, (b) S1 spiral at $g = 0.3$, and (c) S2 spiral at $g = 0.9$. All plots correspond to Λ values right above the instability feature during the RG flow. Outer (inner) hexagons indicate the boundaries of the extended (first) Brillouin zone. *Lower panel*: Below each susceptibility profile we depict the corresponding real space spin patterns which yield magnetic Bragg peaks in $\mathbf{k}$ space at the marked positions (black dots). Arrows illustrate the unit vectors of the honeycomb lattice and indicate the pitch angles of the spiral state along these directions.

the spiral pitch angles along the lattice vectors indicated in Fig. 49(b) are identical, while the angle between spins in the two sublattices is almost 90^o. Further increasing g the system enters the S2 spiral phase, which shows magnetic Bragg peaks at the $k_x = 0$ line (or symmetry related positions), see Fig. 49(c) ($\mathbf{k}_{max} = (0, q)$) . These peaks correspond to a planar spiral with pitch angles of opposite signs but same absolute value. Furthermore, along one of the three nearest neighbor directions, pairs of spins are in parallel orientation.

The overall movement of the magnetic wave vectors in $\mathbf{k}$ space upon increasing g can be tracked. We illustrate it in Fig. 410 for $S = 3/2$. In the antiferromagnetic phase the magnetic Bragg peaks remain at the corner position of the extended Brillouin zone (black dots in Fig. 410) and start moving along the Brillouin zone boundary as the system enters the S1 phase. At the transition between the S1 and S2 spirals, the peaks reside exactly at the midpoints of the edges (purple squares). Further increasing g they move

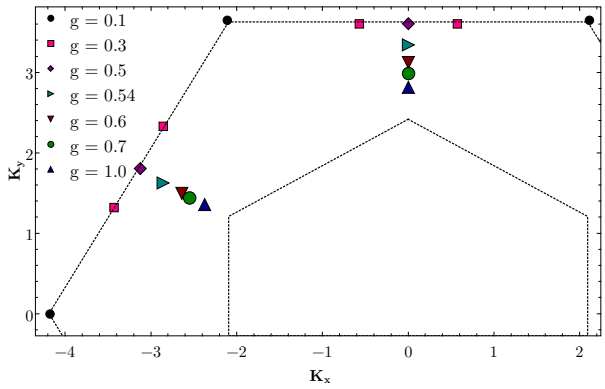

Figure 410: Position of the magnetic wave vectors in reciprocal space at $S = 3/2$ for increasing values of g: While the antiferromagnetic state is characterized by susceptibility peaks at the corners of the extended Brillouin zone, in the S1 (S2) spiral the maxima move along the Brillouin zone edges (radial $k_x = 0$ direction or symmetry related directions

towards the center, in the limit $g \to \infty$ these points should reside at the corners of the first Brillouin zone, as this limit corresponds to the 120° Néel order. In this limit, the nearest neighbor coupling can be neglected, and as such the honeycomb lattice decouples into two triangular lattices with 120° Néel order each.

4.3 Classical Limit, $S \to \infty$

4.3.1 RPA solution

To shed more light on the spin-S generalization of the PFFRG method and the approximations associated with it, we now consider the classical limit $S \to \infty$ where the flow equations can be solved analytically. Starting from the PFFRG equations (4.8) and (4.9), we have argued that an arbitrary spin length S can be implemented via a simple multiplicative factor $M = 2S$ in the internal closed fermion loops. In the limit $S \to \infty$ these terms are the only ones that remain, and the classical limit is effectively recovered. In this limit, the flow equations have the form

$$\frac{d}{d\Lambda}\gamma^{\Lambda}(\omega) = \frac{1}{2\pi}\Big[\sum_j (\tilde{\Gamma}^{\Lambda}_{\mathrm{d}ij}(\omega+\Lambda,0,\omega-\Lambda) - \tilde{\Gamma}^{\Lambda}_{\mathrm{d}ij}(\omega-\Lambda,0,\omega+\Lambda))\Big]\frac{1}{\Lambda+\gamma^{\Lambda}(\Lambda)}\,, \tag{4.15}$$

and

$$\frac{d}{d\Lambda}\tilde{\Gamma}^{\Lambda}_{i_1 i_2}(1',2';1,2) = -\frac{1}{2\pi}\sum_{34}\sum_j \tilde{\Gamma}^{\Lambda}_{i_1 j}(1',4;1,3)\tilde{\Gamma}^{\Lambda}_{j i_2}(3,2';4,2)P^{\Lambda}_{jj}(\omega_3,\omega_4)\,. \tag{4.16}$$

Here, we have omitted the prefactors M to avoid diverging terms at $S \to \infty$, and used the notation where sums stand for $\Sigma_1 \equiv \int_{\omega_1} d\omega_1 \sum_{\alpha_1=\uparrow,\downarrow}$. Furthermore, for the equation corresponding to the self energy, we have performed the frequency integration and spin sum implicitly, as shown in the previous chapter. For the following argument, it will be useful not to look at Eq. (4.15) in it's present form, but to study the analogous of Eq. (3.50). In this case, the flow equation for the self energy takes the form

$$\frac{d}{d\Lambda}\gamma^{\Lambda}(1) = -\frac{1}{2\pi}\left(\sum_{2}\sum_{j}\tilde{\Gamma}^{\Lambda}_{\mathrm{d}i_1 j}(1,2:1,2)\right)\frac{1}{\omega_2+\gamma^{\Lambda}(2)}, \tag{4.17}$$

Due to the special spin-index structure of Eq. (4.16), the property $\tilde{\Gamma}^{\infty}_{i_1 i_2}(1',2';1,2) \propto \sigma^{\mu}_{\alpha_{1'}\alpha_1}\sigma^{\mu}_{\alpha_{2'}\alpha_2}$ of the initial conditions [see section (3.3.2)] is retained during the entire RG flow. This can be seen remembering that the full PFFRG scheme at finite S also contains density terms of the form $\delta_{\alpha_{1'}\alpha_1}\delta_{\alpha_{2'}\alpha_2}$ (see Eq. (3.49)). If we introduce Eq. (3.49) in the the right hand side of Eq. (4.16) we can see that the density terms vanish identically. Furthermore, if the density terms are zero throughout the flow, we see that Eq. (4.17) contains all spin sums of the form $\sum_{\alpha_2}\sigma^{\mu}_{\alpha_1\alpha_1}\sigma^{\mu}_{\alpha_2\alpha_2} = 0$ and thus the self energy is identically zero throughout the full RG flow. As the self energy is contained in the Katanin contribution [see Eq. (3.56)], this term in the single scale propagator also remains identically zero.

In the following we will concentrate on a static PFFRG approach, which consists on only taking into account the zero-frequency components of the vertex functions. This approach is not suitable for the full PFFRG scheme, as it leads to a self energy identical to zero during the full RG flow. This can be seen putting all frequencies to zero in Eq.(3.52) and employing the symmetric relations in frequency space mentioned in section 3.4.2. In our case, since in the limit $S \to \infty$ the self energy identically vanishes, we can look at the frequency arguments in Eq. (4.16) and concentrate only on the static component, $\omega_{1'} = \omega_{2'} = \omega_1 = \omega_2 = 0$, of the two-particle vertex. In this approach, such component completely decouples from all other components thanks to the delta function in the parametrization of the two particle vertex. This allows us to perform the frequency integration analytically, given that the explicit form of $P^{\Lambda}_{jj}(\omega_3,\omega_4)$ (Eq. (3.55)) contains a term of the form

$$\frac{\delta(|\omega_3|-\Lambda)}{\omega_3}\frac{\Theta(|\omega_4|-\Lambda)}{\omega_4} + \frac{\delta(|\omega_4|-\Lambda)}{\omega_4}\frac{\Theta(|\omega_3|-\Lambda)}{\omega_3} \tag{4.18}$$

and the two particle vertex has a frequency structure of the form $\tilde{\Gamma}^{\Lambda}_{i_1 i_2}(1',2';1,2) \propto \delta(\omega_1+\omega_2-\omega_{1'}-\omega_{2'})$ (Eq. (3.49)). Using $P^{\Lambda}_{jj}(\omega_3,\omega_4)$ explicit form, and employing Eq. (3.49) we can perform the integration over ω_3 and ω_4 and will obtain a term proportional to $2/\Lambda^2$ in the static case. At the same time, the spin sums are straightforward to perform, using Eq. (3.49) and the identity between Pauli matrices $\sigma^{\mu}\sigma^{\mu'} = \delta_{\mu\mu'}I + i\varepsilon_{\mu\mu'\nu}\sigma^{\nu}$ we obtain after some algebra a term proportional to $-\sigma^{\mu}_{\alpha_{1'}\alpha_1}\sigma^{\mu}_{\alpha_{2'}\alpha_2}$. All this combined yields a flow equation of the form

$$\frac{d}{d\Lambda}\tilde{\Gamma}^{\Lambda}_{i_1 i_2} = \frac{2}{\pi\Lambda^2}\sum_j \tilde{\Gamma}^{\Lambda}_{i_1 j}\tilde{\Gamma}^{\Lambda}_{j i_2} \tag{4.19}$$

where the prefactor $1/\Lambda^2$ is the result of the frequency integration and $\tilde{\Gamma}^{\Lambda}_{i_1 i_2}$ (without arguments "1", "2", ...) parametrizes the static two-particle vertex component via

$$\tilde{\Gamma}^{\Lambda}_{i_1 i_2}(1',2';1,2)\big|_{\omega_{1'}=\omega_{2'}=\omega_1=\omega_2=0} = \tilde{\Gamma}^{\Lambda}_{i_1 i_2}\sigma^{\mu}_{\alpha_{1'}\alpha_1}\sigma^{\mu}_{\alpha_{2'}\alpha_2}\,. \tag{4.20}$$

This vertex is initially given by $\tilde{\Gamma}^{\infty}_{i_1 i_2} = \frac{1}{4}J_{i_1 i_2}$.

To simplify the remaining spatial dependence of Eq. (4.19) we Fourier-transform $\Gamma^{\Lambda}_{i_1 i_2}$ using

$$\tilde{\Gamma}^{\Lambda}_{a(i)b(j)}(\mathbf{k}) = \sum_{\Delta\mathbf{R}=\mathbf{R}_i-\mathbf{R}_j} e^{-i\mathbf{k}(\mathbf{R}_i-\mathbf{R}_j)}\tilde{\Gamma}^{\Lambda}_{ij}\,. \tag{4.21}$$

Here, $a(i)=1,2$ denotes a function that returns the sublattice index of site i on the honeycomb lattice ($b(j)$ is defined in the same way) and $\mathbf{R}_i$ is the position of the two-site unit cell that contains site i. If we Fourier transform the right hand side of Eq. (4.19)

$$\begin{aligned}\sum_j \tilde{\Gamma}^{\Lambda}_{i_1 j}\tilde{\Gamma}^{\Lambda}_{j i_2} &\to \sum_{\mathbf{R}_j b(j)}\sum_{\mathbf{R}_{i_1}-\mathbf{R}_j}\sum_{\mathbf{R}_j-\mathbf{R}_{i_2}} e^{-i\mathbf{k}(\mathbf{R}_{i_1}-\mathbf{R}_j)}e^{-i\mathbf{k}'(\mathbf{R}_j-\mathbf{R}_{i_2})}\tilde{\Gamma}^{\Lambda}_{\mathbf{R}_{i_1}a(i_1)\mathbf{R}_j b(j)}\tilde{\Gamma}^{\Lambda}_{\mathbf{R}_j b(j)\mathbf{R}_{i_2}a(i_2)} = \\ &= \sum_{\mathbf{R}_j b(j)}\sum_{\mathbf{R}_{i_1}-\mathbf{R}_j}\sum_{\mathbf{R}_{i_1}-\mathbf{R}_{i_2}} e^{-i\mathbf{R}_j(\mathbf{k}-\mathbf{k}')}e^{-i\mathbf{k}\mathbf{R}_{i_1}}e^{i\mathbf{R}_{i_2}}\tilde{\Gamma}^{\Lambda}_{\mathbf{R}_{i_1}a(i_1)\mathbf{R}_j b(j)}\tilde{\Gamma}^{\Lambda}_{\mathbf{R}_j b(j)\mathbf{R}_{i_2}a(i_2)},\end{aligned} \tag{4.22}$$

Carrying our the sum over $\mathbf{R}_j$ we obtain a delta function $\delta_{\mathbf{k}\mathbf{k}'}$. Furthermore, noticing that $\tilde{\Gamma}^{\Lambda}_{\mathbf{R}_{i_1}a(i_1)\mathbf{R}_j b(j)}\tilde{\Gamma}^{\Lambda}_{\mathbf{R}_j b(j)\mathbf{R}_{i_2}a(i_2)}$ can be written as a matrix element $[\tilde{\Gamma}^{\Lambda}\times\tilde{\Gamma}^{\Lambda}]_{\mathbf{R}_{i_1}a(i_1)\mathbf{R}_{i_2}a(i_2)}$ we obtain

$$\sum_j \tilde{\Gamma}^{\Lambda}_{i_1 j}\tilde{\Gamma}^{\Lambda}_{j i_2} \to \sum_{\mathbf{R}_{i_1}-\mathbf{R}_{i_2}} e^{-i\mathbf{k}}[\tilde{\Gamma}^{\Lambda}\times\tilde{\Gamma}^{\Lambda}]_{\mathbf{R}_{i_1}a(i_1)\mathbf{R}_{i_2}a(i_2)} = [\tilde{\Gamma}^{\Lambda}\times\tilde{\Gamma}^{\Lambda}]_{a(i_1)a(i_2)}(\mathbf{k}). \tag{4.23}$$

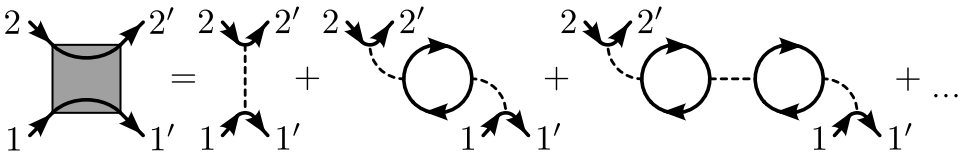

Figure 411: Fermionic two-particle vertex in RPA approximation: Dashed lines denote bare exchange couplings $J_{i_1 i_2}$ and arrows illustrate free fermion propagators.

This shows that since the Fourier-transform is only performed with respect to the unit-cell coordinates without involving the sublattice positions, different $\mathbf{k}$ components in the flow equations decouple. Writing the Fourier transform of Eq. (4.19) in matrix form we find,

$$\frac{d}{d\Lambda}\tilde{\Gamma}^{\Lambda}(\mathbf{k}) = \frac{2}{\pi\Lambda^2}\left[\tilde{\Gamma}^{\Lambda}(\mathbf{k})\right]^2. \tag{4.24}$$

Given that there is more than one atom per unit cell, the vertex $\Gamma^{\Lambda}(\mathbf{k})$ in this equation is understood as a 2×2 matrix in the sublattice indices, and the square on the right-hand side is a standard matrix product. The analytical solution of Eq. (4.24) is given by the ansatz

$$\tilde{\Gamma}^{\Lambda}(\mathbf{k}) = \left[\frac{2}{\pi\Lambda}\mathbb{1}_{2\times 2} + \left(\tilde{\Gamma}^{\infty}(\mathbf{k})\right)^{-1}\right]^{-1}, \tag{4.25}$$

where $\tilde{\Gamma}^{\infty}(\mathbf{k})$ is the Fourier-transform of the bare exchange couplings $\frac{1}{4}J_{ij}$, using Eq. (4.21), and $\mathbb{1}_{2\times 2}$ denotes the two dimensional identity matrix. It can be straightforwardly shown that the ansatz is a solution of Eq. (4.24)

$$\begin{aligned}\frac{d}{d\Lambda}\tilde{\Gamma}^{\Lambda}(\mathbf{k}) = &\frac{d}{d\Lambda}\left[\frac{2}{\pi\Lambda}\mathbb{1}_{2\times 2} + \left(\tilde{\Gamma}^{\infty}(\mathbf{k})\right)^{-1}\right]^{-1} = \\ &-\left(\frac{d}{d\Lambda}\left[\frac{2}{\pi\Lambda}\mathbb{1}_{2\times 2} + \left(\tilde{\Gamma}^{\infty}(\mathbf{k})\right)^{-1}\right]\right)\left[\frac{2}{\pi\Lambda}\mathbb{1}_{2\times 2} + \left(\tilde{\Gamma}^{\infty}(\mathbf{k})\right)^{-1}\right]^{-2}\end{aligned} \tag{4.26}$$

Since $\tilde{\Gamma}^{\infty}$ does not depend on Λ we obtain,

$$\frac{d}{d\Lambda}\tilde{\Gamma}^{\Lambda}(\mathbf{k}) = \frac{2}{\pi\Lambda^2}\mathbb{1}_{2\times 2}\left[\frac{2}{\pi\Lambda}\mathbb{1}_{2\times 2} + \left(\tilde{\Gamma}^{\infty}(\mathbf{k})\right)^{-1}\right]^{-2} = \frac{2}{\pi\Lambda^2}\left[\tilde{\Gamma}^{\Lambda}(\mathbf{k})\right]^2. \tag{4.27}$$

This equation has the form of an RPA solution. Illustrated in Fig. 411 is the diagrammatic expansion of 4.25 in terms of the exchange couplings $\Gamma^{\infty}(\mathbf{k})$. The equivalence

of the PFFRG and the pseudo fermion RPA in the limit $S \to \infty$ can be seen from the diagrammatic expansion. If we expand the RPA equation (Eq. (4.25)) for the two particle vertex we obtain a Dyson-like equation

$$\tilde{\Gamma}^{\Lambda}(\mathbf{k}) = \tilde{\Gamma}^{\infty}(\mathbf{k}) + \tilde{\Gamma}^{\infty}(\mathbf{k})\frac{2}{\pi\Lambda}\mathbb{1}_{2\times 2}\tilde{\Gamma}^{\infty}(\mathbf{k}) + \tilde{\Gamma}^{\infty}(\mathbf{k})\frac{2}{\pi\Lambda}\mathbb{1}_{2\times 2}\tilde{\Gamma}^{\infty}(\mathbf{k})\frac{2}{\pi\Lambda}\mathbb{1}_{2\times 2}\tilde{\Gamma}^{\infty}(\mathbf{k}) + \ldots \tag{4.28}$$

Where $\frac{2}{\pi\Lambda}\mathbb{1}_{2\times 2}$ takes the place of a fermion bubble. For each given order in the exchange couplings expansion, J, the RPA terms are those diagrams with the maximal number of closed fermion loops (in Fig. 411, this means that the n-th term on the right hand side is of n-th order in J and contains $n-1$ loops), as in the classical limit the RPA terms contain a prefactor of $2S$, these terms are the only ones that remain when we take the limit $S \to \infty$.

We can think about this solution from a classical mean field perspective. In this case, the RPA approximation relates the susceptibility to the inverse of a function that contains the temperature and the Fourier transform of the exchange couplings. In our case the form is the same, specially since the Fourier transform of our couplings is encoded in $\Gamma^{\Lambda\to\infty}(\mathbf{k})$, but Λ takes the place of the temperature. Even though our scale Λ cannot be considered a temperature, since we have derived our formulation at $T = 0$, both Λ and T set the cutoff energy scale of the problem, and as such have a similar effect over the susceptibility in this limit.

The key outcome of Eq. (4.25) is the wave vector $\mathbf{k}_{\mathrm{RPA}}$ at which the two-particle vertex diverges first as Λ is decreased. We mentioned before that the wavevector corresponding to the maximum susceptibility determines the type of magnetic order the system presents at the critical Λ. In the classical limit, unlike the full PFFRG scheme, instabilities appear as real divergences, nonetheless taking the Λ point at which this divergence occurs as our critical Λ and studying the wavevector corresponding to the maximum susceptibility, $\mathbf{k}_{\mathrm{RPA}}$, we can also determine the type of magnetic order the system develops. Interestingly, Eq. (4.25) implies that in order to find $\mathbf{k}_{\mathrm{RPA}}$, we need to minimize the eigenvalues of the initial interaction matrix $\Gamma^{\infty}(\mathbf{k})$. Such a minimization procedure is, in turn, a well known method for finding the classical magnetic order of a spin system. We will denote the eigenvalues of $\Gamma^{\infty}(\mathbf{k})$ by $\lambda_m(\mathbf{k})$ below and we generalize the discussion to arbitrary lattices with n sites per unit cell. All relations in Eqs. (4.21)-(4.25) then become $n \times n$ matrix equations.

We first denote the eigenvalues of the matrix $\frac{2}{\pi\Lambda}\mathbb{1}_{n\times n} + [\Gamma^{\infty}(\mathbf{k})]^{-1}$ by $\lambda'_m(\mathbf{k})$. It follows that the eigenvalues of $[\Gamma^{\infty}(\mathbf{k})]^{-1}$ are given by $1/\lambda_m(\mathbf{k})$ (with $m = 1, \ldots, n$).

(4.29) $$\lambda'_m(\mathbf{k}) = \frac{2}{\pi\Lambda} + \frac{1}{\lambda_m(\mathbf{k})} .$$

where the constant term originates from $\frac{2}{\pi\Lambda}\mathbb{1}_{n\times n}$.

From Eq. (4.25) we can see that the two-particle vertex $\Gamma^\Lambda(\mathbf{k})$ will diverge when the matrix $\frac{2}{\pi\Lambda}\mathbb{1}_{n\times n} + [\Gamma^\infty(\mathbf{k})]^{-1}$ has a vanishing eigenvalue $\lambda'_m(\mathbf{k})$ at some wave vector $\mathbf{k}$. Then we obtain

(4.30) $$\Lambda = -\frac{2}{\pi}\lambda_m(\mathbf{k}) .$$

It follows that each negative eigenvalue $\lambda_m(\mathbf{k}) < 0$ can cause a diverging vertex $\Gamma^\Lambda(\mathbf{k})$ when Eq. (4.30) is fulfilled. This condition also indicates that as Λ is decreased from infinity, the *first* divergence occurs when the *smallest* (negative) eigenvalue $\lambda_m(\mathbf{k})$ satisfies Eq. (4.30) (here, the term "*smallest*" refers to a minimization with respect to $\mathbf{k}$ and m). This proves that the classical magnetic order found within an RPA scheme occurs at the wave vector $\mathbf{k}_{\mathrm{RPA}}$ that minimizes the eigenvalues of $\Gamma^\infty(\mathbf{k})$.

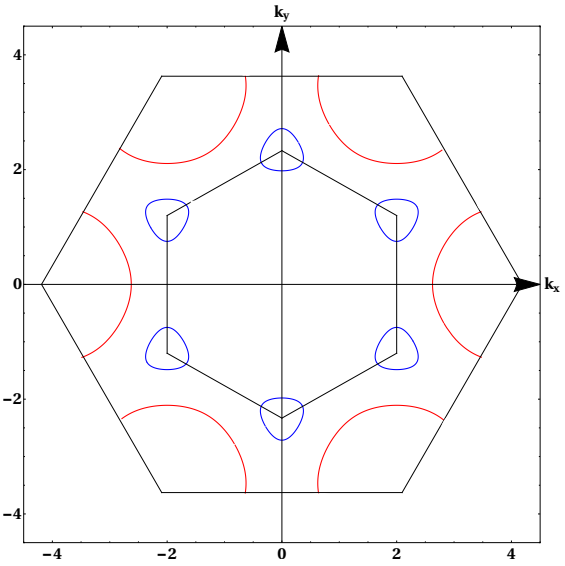

Figure 412: Degenerate spiral magnetic wave vectors of the classical antiferromagnetic J_1-J_2 honeycomb Heisenberg model in reciprocal space. At $1/6 < g < 1/2$ the degenerate states form contours around the corners of the extended Brillouin zone, see red ring for $g = 0.3$. For $g > 0.5$ the contours are around the corners of the first Brillouin zone, see blue ring for $g = 0.9$.

We calculated the wave vectors $\mathbf{k}_{\mathrm{RPA}}$ for arbitrary g by minimizing the wavevectors of the interaction matrix, and compared the results with Ref. [60], where the exact phase diagram is determined via a direct minimization of the classical energy. Throughout the phase diagram we find perfect agreement of the two approaches demonstrating that for the J_1-J_2 honeycomb Heisenberg model the spin-S generalization of the PFFRG approach becomes exact (see Fig. 412). For small g the system shows antiferromagnetic order which remains stable up to $g = 1/6$. At $1/6 < g < 1/2$ one finds contours of degenerate classically ordered states forming rings in $\mathbf{k}$ space around the antiferromagnetic order position (red rings in Fig. 412). With increasing g the rings become larger, merge at $g = 0.5$ and then form new rings-like features around the corners of the first Brillouin zone (blue lines in Fig. 412).

4.3.2 Equivalence to the Luttinger-Tisza method

Previously we mentioned that the wavevector that determines the magnetic order, $\mathbf{k}_{\mathrm{RPA}}$, can be obtained via a minimization of the eigenvalues of the interaction matrix. Coincidentally, this approach is identical to the Luttinger-Tisza (LT) approximation[78, 79] for arbitrary classical spin models. LT method provides a simple framework to construct approximate classical ground states[80–83]. Instead of minimizing the classical energy under the hard constraint $|\mathbf{S}_i|^2 = S$, normalizing the spin length on each site i separately, the minimization is done subject to a weak constraint of the form

$$\sum_i |\mathbf{S}_i|^2 = N\,, \tag{4.31}$$

where N is the total number of lattice sites.

We will now show that with this condition the LT method reduces to the same minimization of eigenvalues $\lambda_m(\mathbf{k})$ of $\tilde{\Gamma}^{\infty}(\mathbf{k})$ that yields the RPA solution. We will start with a brief description of the LT method as was shown in Ref. [80].

For a generic system in a lattice that can be separated in different sublattices, we start by defining our exchange couplings J_{ij} in terms of a function $\alpha(i)$ which indicates which spins are in which sublattice

$$J_{ij} = J_{\alpha(i)\beta(j)}(\mathbf{R}_{ij})\,, \tag{4.32}$$

where $\mathbf{R}_{ij}$ is the distance vector between spins in sublattices α and β in sites i and j. Now we can define the Fourier transform of our spin components

$$\tilde{\mathbf{S}}_{\alpha}(\mathbf{q}) = \frac{1}{\sqrt{N_{sub}}} \sum_{i\in\alpha} \mathbf{S}_i e^{-i\mathbf{q}.\mathbf{r}_i}\,, \tag{4.33}$$

where N_{sub} is the number of lattice sites in sublattice α, $\mathbf{q}$ is a wavevector in the Brillouin zone. Fourier transforming the exchange couplings

$$\tilde{J}_{\alpha\beta} = \frac{1}{2} \sum_{j\neq i} J_{\alpha(i)\beta j}(\mathbf{R}_{ij}) e^{i\mathbf{q}\mathbf{R}_{ij}}\,, \tag{4.34}$$

where $\tilde{J}_{\alpha\beta}$, if our system consists of n sublattices, are the elements of an $n \times n$ matrix. Further substituting in the Hamiltonian, which we will regard as that of the standard Heisenberg model, we find

$$H = \sum_{\mathbf{q}} \sum_{\alpha\beta} \tilde{J}_{\alpha\beta}(\mathbf{q}) \tilde{\mathbf{S}}_{\alpha}(\mathbf{q}) \tilde{\mathbf{S}}_{\beta}(-\mathbf{q}) \tag{4.35}$$

Now, let's regard $\lambda_{\mu}(\mathbf{q})$ as the eigenvalues of this coupling matrix at wavevector $\mathbf{q}$, and $u^{\mu}_{\alpha}(\mathbf{q})$ to the corresponding eigenvector. Then we can write

$$\tilde{\mathbf{S}}_{\alpha}(\mathbf{q}) = \sum_{\alpha} \tilde{\mathbf{w}}_{\mu} u^{\mu}_{\alpha}(\mathbf{q}), \tag{4.36}$$

where $\tilde{\mathbf{w}}_{\mu}$ are three dimensional coefficients. The total energy will be given by

$$H = \sum_{\mathbf{q}} \sum_{\mu} \lambda_{\mu}(\mathbf{q}) |\tilde{\mathbf{w}}_{\mu}(\mathbf{q})|^2 . \tag{4.37}$$

It's easy to see now that, if λ_{min} is the minimum eigenvalue of the matrix $\tilde{J}(\mathbf{q})$ and Q_{LT} is the wavevector that minimizes λ_{min}, then $H \geq N\lambda_{min}(Q_{LT})$.

We have shown that the Luttinger-Tisza method reduces to the same minimization as our $S \to \infty$ case. But a caveat needs to be taken into account: in the context of the LT method, the wave vector $\mathbf{Q}_{\mathrm{LT}} \equiv \mathbf{k}_{\mathrm{RPA}}$ that minimizes $\lambda_{min}(\mathbf{Q})$ is referred to as "optimal" LT eigenmode. If there exists a degenerate set of these modes (as is the case for the J_1-J_2 honeycomb Heisenberg model), classical ground states can be constructed by linear superpositions of the corresponding plane waves. Whether these states are the actual ground state of the system depends on whether it fulfills not only the weak constraint, but the strong constraint too. If this is the case, such a configuration represents the exact solution of the classical problem. It can be proven that a normalized spin state can always be created with the eigenmodes $\mathbf{Q}_{\mathrm{LT}}$ for Bravais lattices. When the lattices are non Bravais, the modes $\mathbf{Q}_{\mathrm{LT}}$ are not always sufficient to obtain a spin state[80, 82] that satisfied the strong constraint. If we want to obtain the true ground state we need to add extra modes to our constructions which do not correspond to the absolute minimum of $\lambda_m(\mathbf{q})$. While in such situations the LT method is no longer exact, the wave vectors $\mathbf{Q}_{\mathrm{LT}}$ still allow to construct phase diagrams of classical spin models which typically closely resemble the exact ones.

Now, one would notice that the J_1-J_2 honeycomb model discussed here is an example where the LT method still works, and gives the exact result for a non-Bravais lattice. The reason why this is the case can be traced back to the equivalence of the two sublattices. The initial two-particle vertex $\tilde{\Gamma}^{\infty}(\mathbf{k})$ for this Hamiltonian is of the form

$$\tilde{\Gamma}^{\infty}(\mathbf{k}) = \begin{bmatrix} \gamma^0 & \gamma^x - i\gamma^y \\ \gamma^x + i\gamma^y & \gamma^0 \end{bmatrix} \tag{4.38}$$

with

$$\begin{aligned} \gamma^0(\mathbf{k}) &= \frac{J_2}{2}\left(\cos k_+ + \cos k_- + \cos\sqrt{3}k_y\right), \\ \gamma^x(\mathbf{k}) &= \frac{J_1}{4}(1 + \cos k_+ + \cos k_-), \\ \gamma^y(\mathbf{k}) &= \frac{J_1}{4}(\sin k_+ + \sin k_-), \end{aligned} \tag{4.39}$$

and

$$k_\pm = \frac{3k_x}{2} \pm \frac{\sqrt{3}k_y}{2}. \tag{4.40}$$

Where the nearest neighbor lattice distance is set to one and the sublattice structure follows the convention of Fig. 46. From the form of the interaction matrix we see that all eigenvectors $u^m(\mathbf{k})$ of $\Gamma^{\infty}(\mathbf{k})$ will have have sublattice components with equal norm, i.e., $|u_1^m(\mathbf{k})|^2 = |u_2^m(\mathbf{k})|^2$. The explicit form of these eigenvectors is

$$u^{\alpha}(\mathbf{k}) = \beta\{\pm\frac{\gamma^x(\mathbf{k}) - i\gamma^y(\mathbf{k})}{\sqrt{\gamma^x(\mathbf{k})^2 + \gamma^y(\mathbf{k})^2}}, 1\}, \tag{4.41}$$

where $\alpha = 1,2$ and β is a normalization constant. Calculating the norm of the different sublattice components we find $|u_1^m(\mathbf{k})|^2 = |u_2^m(\mathbf{k})|^2 = \beta$. Since the Luttinger-Tisza method works if one can find a normalized spin configuration composed of eigenmodes of the $\mathbf{k}_{\mathrm{RPA}}$ (and of symmetry related wavevectors) we can see that in this case it is possible to write the spins as a superposition of plane waves

$$\{\mathbf{S}(\mathbf{R})_a, \mathbf{S}(\mathbf{R})_b\} = \sum_{\mathbf{k}_{RPA} = \pm\mathbf{Q}_{\mathrm{RPA}}} e^{i\mathbf{k}_{\mathrm{RPA}}\mathbf{R}} u^{\alpha}(\mathbf{Q}_{\mathrm{RPA}}) \tag{4.42}$$

Since all sublattices components of the eigenvectors have equal norm, then spins on both sublattices can be normalized simultaneously, thus fulfilling the strong constraint.

Finally, one important point needs to be clarified, we mentioned that the LT method is not exact for non Bravais lattices, and we have proven that RPA is equivalent to the

LT approach. But RPA includes all possible pseudo-fermion Feynman diagrams in the classical limit, reason for which one would expect the RPA result is always exact, which in turn would mean the LT approach is also always exact. This contradiction can be clarified by noting that FRG schemes yield physical results only in the limit $\Lambda = 0$. In every discussion here, the instabilities occur at a finite critical $\Lambda = \Lambda_c$ such that the RG flow has to be stopped before the physical limit $\Lambda = 0$ is reached. Therefore, any result obtained at a finite RG scale may still be subject to errors. While proposals to track the FRG flow into symmetry broken phases exist and reach the physical limit (for example for superconductivity in a BCS model[39]) in out PFFRG approach this implies an enormous complication of the method. In such type of generalization the self energy would no longer vanish at $S \to \infty$ but the loop term in Eq. (4.15) would contribute which would increase the complexity of the equations and a numerically precise solution is, in principle, not ensured.

In conclusion, we developed a general framework that allows one to study in detail the effect of quantum fluctuations on spin systems. Starting from the classical limit, $S \to \infty$ we can study how quantum fluctuations modify the classical ground state of a system. We implemented a systems with $S > 1/2$ considering M copies of spin-1/2 degrees of freedom on each lattice site. Using onsite level-repulsion terms we showed that in our framework spin systems tend to realize the largest possible local spin magnitude $S = M/2$ in the ground state. Furthermore we showed that this property survives when the onsite level-repulsion terms are excluded, such that no further projection is necessary to fix the spin length. Finally, we show that for the case of $S = 1/2$ the constraint of having single pseudo fermion occupancy is automatically satisfied in the ground state, justifying the treatment of the particle constraint in previous PFFRG studies.

To test this method we studied the antiferromagnetic J_1-J_2 honeycomb Heisenberg model, exploring the phase diagram as a function of $g = J_2/J_1$ and S. Studying the effect of the quantum fluctuations induced by the presence of a frustrating J_2 interaction we show that they are strong enough to melt down the magnetic order at $0.2 \lesssim g \lesssim 0.6$. When the quantum fluctuations are diminished, i.e, when the spin length is increased, the phase diagram quickly resembles the classical one. In particular, already at $S = 1$ we find no evidence of non magnetic states, instead finding two spiral phases at $g \gtrsim 0.2$, and an antiferromagnetic phase at $g \lesssim 0.2$. We observe that these spin spiral phases exhibit a set of maxima in the momentum resolved spin susceptibility, which are located along rings enclosing either the corners of the first, or extended, Brillouin zone. At a finite spin length quantum fluctuations induce an order by disorder mechanism which selects

a particular wavevector from these rings. Increasing S (or equivalently, decreasing quantum fluctuations) the signal becomes more evenly distributed along these rings until in the limit $S \to \infty$ we obtain an continuous degeneracy of states along these rings. This means that the spiral states are degenerated for all wave vectors along rings in $\mathbf{k}$ space, in agreement with the solutions found for the classical states. More generally, we prove that for $S \to \infty$ the PFFRG method becomes identical to the LT approach.

Comparing our results with other methods (the $S = 1/2$ case has already been discussed in detail in an earlier PFFRG work[59]) we note that the existence of a non-magnetic intermediate phase is supported by the vast majority of previous studies[60–73]. However, there is an ongoing debate regarding the nature of this non magnetic state [64, 66–70]. Comparing results in the opposite limit $S \to \infty$, the continuous set of degenerate classical states as well as the selection of states out of this manifold[60] by a quantum order by disorder mechanism are correctly captured within our approach.

In the case of intermediate spin magnitudes S, and to the best of our knowledge, there are few works to compare with, two of them investigating the $S = 1$ case [76, 77] and one studying the $S \geq 1$ case [84]. The detailed studied for $S = 1$ find indications for a narrow non-magnetic phase around $g = 0.3$, whereas our approach and the study performed by Li *et. al*[84] detects magnetic order throughout the phase diagram. Since the pfFRG study is unbiased towards any form of magnetic order or disorder, and since we proved that there are no contributions from spurious admixtures of spin subspaces which can increase quantum fluctuations, we believe in the accuracy of our results in this limit, despite the differences observed with other methodologies.

Finally we note that another difference with know results appears when one studies large enough J_2. Refs. [76] and [77] both find stripy order while we detect incommensurate spiral phases. In the quantum limit, $S = 1/2$, the ground state has been a topic of debate. Some methods identify spiral order[59, 61, 69] while others find a stripy state [62, 71, 72]. The stripy order usually comes together with a quantum locking of the magnetic wavevector, where the wavevector is localized at a high-symmetry point. However, when quantum fluctuations are decreased the strength of this quantum locking becomes weaker, hence strengthening spiral order tendencies. The origin of this differences can arise from particular properties of each study. The coupled cluster method applied in Ref. [77] did not probe the system with respect to spiral order, which could be the reason while they are not detected. In the case of the DMRG studies in Ref. [76], they report conflicting spin patterns in this parameter regime when extrapolating the results to the thermodynamic limit. In this case the reason for not detecting incommensurate order

can arise from the fact that these type of studied restrict the lattice to cylinder. This is, periodic boundary conditions are applied in one direction. Since periodic boundary conditions are incompatible with incommensurate order, then they might mask spiral order states in the DMRG study. Since PFFRG is not implemented on a finite system, commensurate and incommensurate types of magnetism can both be described on equal footing within this approach. Which lead us to rely on the quality of our results.

CHAPTER 5

NUMERICAL METHODS FOR CLASSICAL MAGNETISM

Monte Carlo originated as a form of emergency first aid, in answer to the question: What do we do until the mathematician arrives?

George Dyson, 2012

At the beginning of this thesis we concentrated on the study of quantum frustrated spin models and their quantum fluctuations. We also mentioned that the study of frustrated quantum many body systems is not trivial at all, since most of the time there is not an exact solution, and numerical methods that can treat these systems efficiently are lacking. As a way to attack the latter problem we developed an FRG formalism that would work not only in the quantum but also in the purely classical limit. And we showed how in the classical limit FRG provides exact results within the RPA approximation for a certain class of systems . Considering the classical limit of our frustrated spin systems an interesting question arises: is there a way in which these systems can be computationally studied without having to resort to FRG (or it's associated RPA limit)? Furthermore, is there a way to extract further information, besides the correlation function, regarding the classical Hamiltonian? The answer to both these questions is yes, in fact, many methods, approximate or otherwise, exist to treat classical spin systems, independently of whether they are frustrated or not. The study of the frustrated part of the spin system's family is far from trivial even in the classical case,

the competing interactions produce a rough landscape of energies that has to be dealt with carefully. But what is remarkable is that for many years, the study of classical spin systems has been an extremely active field of research, not only because of the academic interest in the classical version of certain Hamiltonians, but also since for many systems the results obtained within the classical description match the experimental evidence extremely well.

One of the most prominent numerical methods to study classical spin systems is the Monte Carlo method. Many Monte Carlo studies have proven invaluable for the understanding of many condensed matter phenomena. Among others, it has been employed in the theoretical description of multiferroic behavior in different materials (see for example Refs. [85–87]), and in the description of thermodynamic properties of spin ice systems [15, 20, 88, 89], paved the way to the understanding of spin ice most famous low energy fluctuations, the magnetic monopoles [90, 91], and has been the chosen method to study classically disordered systems and their associated properties (look at Ref. [92] for a brief overview on Monte Carlo methods applied to glassy systems written by the fathers of the field).

In the next chapter we will employ large scale Monte Carlo simulations to study continuous spin systems, in particular we will study a particular Kitaev material for which exciting experimental results have been recently published but Monte Carlo studies have not yet been performed. We will show how the classical description reproduces the latest experiments with a high degree of accuracy, and contrast our results to other, not so robust, numerical methods. As such, in the present chapter we will give an introduction to the Monte Carlo method, paying particular attention to the implementation on continuous spin variables, and we will show in detail how our algorithm was developed. Furthermore, we will introduce the parallel tempering and iterative minimization algorithms as a way to improve the convergence of the method in the presence of many competing interactions.

5.1 Equilibrium thermal Monte Carlo method

Monte Carlo (MC) methods are part of a broad family of stochastic simulation methods. Simply put, MC probes the phase space of a statistical problem stochastically, taking into account the random thermal fluctuations of the system that appear from state to state. Its aim is to estimate the thermal expectation value of a given quantity $\mathcal{O}$ (this can be a magnetization, correlation function, etc). In these type of simulations we

create a model system and evolve it through a variety of states in such a way that the probability of the system being in a particular state m, at a given simulation time t, is equal to the probability weight $\omega_m(t)$ that the state would have in a real system. We will concentrate on systems governed by a Hamiltonian H at constant temperature, which will be implemented in the form of a thermal reservoir (please note that even though the formulation of the method relies on a constant temperature, we are still able to study thermal phase transitions with it). The effects of this reservoir in our simulations can basically be considered as gifting the system with dynamics. In the particular case of classical spin systems, the dynamics are governed by a Boltzmann distribution. Effectively, what we are doing with MC is taking our Hamiltonian H, setting it into an initial random state, choosing a temperature T that will remain constant throughout the simulations, and letting time pass (this does not mean real time dynamics, the system is evolved to reach equilibrium and the time being referred here is a time given in simulation steps, also called *Monte Carlo time*), during this time the system will evolve through a set of thermal states until it reaches equilibrium, ideally this equilibrium corresponds to the minimal energy state at that given temperature.

5.1.1 Principles of Monte Carlo simulations

In the present section, we will detail the fundamentals of Monte Carlo (MC) techniques. The simplest implementation of MC to solve spin systems was formulated by Metropolis *et.al.* in 1953 [93, 94](here we will use a modified version called *Metropolis-Hastings* algorithm [95]). In this implementation, the simulation generates configurations following a Markovian chain, i.e, at each step a new configuration of the system will be generated from the immediately previous one. In accordance with *importance sampling*, we will choose the transition probability rate from one state to the other over a certain time, $W_{i\to j}$, as dependent on the energy difference between the initial and final state according to a Boltzmann distribution, $e^{-\beta\Delta E}$.

$$W_{i\to j} = W_{ij} = \min\left(1, e^{-\beta\Delta E}\right) \tag{5.1}$$

Metropolis' implementation is extremely effective for two reasons: first, it can be proven that whatever the initial state, a Markov chain in the Metropolis implementation will eventually sample the full phase space associated to our statistical ensemble at a given temperature. This is an extremely important point given that we want to ensure an *ergodic* simulation. If the implementation of the simulation results to be path dependent

then the simulation is non ergodic, as there might exist states that cannot be reached, as such our simulation would be biased and, in principle, uncontrolled. This would mean that there exist a non zero probability of equilibrating the system in a state that is not the real equilibrium state of the system just because the real equilibrium state was rendered unreachable by an unfortunate and somewhat fortuitous selection of path. Or what might be even worse, our simulation might never reach equilibrium. On the other hand, we could avoid the memory dependence by randomly sampling the phase space every time, and weighting the contribution of the selected state with a Boltzmann factor. While this completely rules out any kind of history dependence, the configurations generated in this fashion will contribute very little to the real evolution of the system towards an energy minimum, especially in cases where a specific state is expected, as is the case of the Ising model below the critical temperature. We can see now that a Markovian process in which the steps are random, but connected to the evolution of the system without depending on it's history, while at the same time sampling a Boltzmann distribution is the optimal choice for our unbiased simulations.

We will now show that a Metropolis type implementation [96], based on a Markov chain, fulfills the detailed balance condition ensuring that the Boltzmann distribution is the equilibrium distribution of the chain, and thus leading to the transition probability of the form 5.1.

We define a stochastic process at discrete times $\{t_1, t_2, ...\}$ for a system with a finite set of states $\{S_1, S_2, ...\}$. If the system is in state X_t at time t then we can consider the conditional probability of the system being in a state $X_{t_n} = S_{i_n}$ as:

$$P(X_{t_n} = S_{i_n} | X_{t_{n-1}} = S_{i_{n-1}}, X_{t_{n-2}} = S_{i_{n-2}}, ..., X_{t_1} = S_{i_1}). \tag{5.2}$$

If the system follows a Markovian process, the previous expression reduces to

$$P(X_{t_n} = S_{i_n} | X_{t_{n-1}} = S_{i_{n-1}}), \tag{5.3}$$

and this expression can be considered a transition probability from state $S_{i_{n-1}}$ to S_{i_n} in a time interval $\Delta t = t_n - t_{n-1}$. At the same time we can study the probability transition rate from one state to the other in the limit $\Delta t = t_n - t_{n-1} = 0$ as

$$W_{ij} = W(S_i \to S_j) = \lim_{\Delta t \to 0} \frac{P(X_{t_n} = S_j | X_{t_{n-1}} = S_i)}{\Delta t}, \tag{5.4}$$

with the usual requirements for transition probabilities

$$W_{ij} \geq 0 \quad \forall i,j, \quad \text{and} \quad \sum_j W_{ij} = 1. \tag{5.5}$$

With this we can construct the total probability of the system being in state S_j at time t_n:

$$P(X_{t_n} = S_j) = \sum_i P(X_{t_n} = S_j | X_{t_{n-1}} = S_i) P(X_{t_{n-1}} = S_i). \tag{5.6}$$

The master equation determining the evolution of the probability with time can be obtained from the Chapman-Kolmogorov equation which states that the probability of being in a give state S_3 at time $t_3 = t_1 + 2$ while we where at S_1 at time t_1 is given by

$$P(X_{t_3} = S_3 | X_{t_1} = S_1) = \sum_{S_2} P(X_{t_3} = S_3 | X_{t_2} = S_2) P(X_{t_2} = S_2 | X_{t_1} = S_1). \tag{5.7}$$

Which simply states that, knowing the initial an final state, the probability of jumping from one to the other is given by the sum of the probabilities of jumping to all possible intermediate states. We can now take the transition probability $P(X_{t_3} = S_3 | X_{t_2} = S_2)$ and expand it in a Taylor series around zero for small time steps $\Delta t = t_3 - t_2$

$$P(X_{t_3} = S_3 | X_{t_2} = S_2) = (1 - \alpha \Delta t)\delta(S_3 - S_2) + \Delta t W_{23} + \mathcal{O}(\Delta t)^2, \tag{5.8}$$

the δ-function represents the probability of staying in the same state after no time has passed is one. The correction factor in front stems from the fact that the probability needs to be normalized, and as such we need to consider the case in which no transition occurs at all in Δt, which equals to $(1 - \alpha \Delta t)$, where

$$\alpha(S_2) = \sum_{S_3} W_{32}, \tag{5.9}$$

i.e. the probability rate of transition from any state S_3 towards state S_2.

Introducing Eq. (5.8) into Eq. (5.7),

$$
\begin{aligned}
P(X_{t_3}=S_3|X_{t_1}=S_1) = \sum_{S_2}\Big[& P(X_{t_2}=S_2|X_{t_1}=S_1)\delta(S_3-S_2) \\
& -\Delta t\alpha\delta(S_3-S_2)P(X_{t_2}=S_2|X_{t_1}=S_1) \\
& +\Delta t W_{23}P(X_{t_2}=S_2|X_{t_1}=S_1)\Big],
\end{aligned} \tag{5.10}
$$

using Eq. (5.9)

$$
\begin{aligned}
P(X_{t_3}=S_3|X_{t_1}=S_1) = P(X_{t_2}=S_3|X_{t_1}=S_1) & \\
-\sum_{S_2}\Big[& \Delta t W_{32}P(X_{t_2}=S_3|X_{t_1}=S_1) \\
& +\Delta t W_{23}P(X_{t_2}=S_2|X_{t_1}=S_1)\Big],
\end{aligned} \tag{5.11}
$$

dividing by Δt, and taking the limit $\Delta t \to 0$ we find the differential form of the Chapman-Kolmogorov equation, also called the *master equation*

$$
\begin{aligned}
& \frac{d}{dt}P(X_{t_3}=S_3|X_{t_1}=S_1) = \\
& = \sum_{S_2}\left(W_{23}P(X_{t_2}=S_2|X_{t_1}=S_1) - W_{32}P(X_{t_3}=S_3|X_{t_1}=S_1)\right)
\end{aligned} \tag{5.12}
$$

We notice that all the transition probabilities are for a given S_1 at a time t_1, then we can recast this equation in terms of the probability of the system to be in state S_3 simply by multiplying both sides by $P(X_{t_1}=S_1)$ and summing over S_1. Then we find

$$
\frac{d}{dt}P(X_{t_3}=S_3) = \sum_{S_2}\left(W_{23}P(X_{t_2}=S_2) - W_{32}P(X_{t_3}=S_3)\right). \tag{5.13}
$$

This is the master equation. If the system is in equilibrium, and for arbitrary states S_i and S_j, then we can see that $\frac{dP(X_{t_n}=S_j)}{dt}=0$ and consequently

$$
\sum_i W_{ji}P(X_{t_n}=S_j) = \sum_i W_{ij}P(X_{t_n}=S_i). \tag{5.14}
$$

This expression takes a stronger form when we ask not that the sum of all the terms are equal, but that for each pair i,j the condition holds. This is the *Detailed balance* condition.

$$W_{ji}P(X_{t_n} = S_j) = W_{ij}P(X_{t_n} = S_i)\,. \tag{5.15}$$

This means that if we choose a probability rate that respects detailed balance we can ensure that this probability is the equilibrium distribution of our Markov chain, as we have proven that detailed balance is a sufficient condition to ensure the stationary nature of our master equation. However, if we expect that the equilibrium probability of the system to be in a given state with energy E_j at time t follows a Boltzmann distribution,

$$P(X_{t_n} = S_j) = \frac{e^{-E_j\beta}}{Z}\,, \tag{5.16}$$

where Z is the partition function, then we can see that this probability is not usually known, since we lack knowledge about Z. We can avoid this problem if we generate a Markov chain of states, which produces the j-th state from state i-th, then the transition probability of producing state j from i is the ratio of the probabilities of being in state S_i and S_j. This means that our transition rate can be chosen as

$$\begin{aligned} W_{ij} &= e^{-\Delta E\beta} \quad \text{when} \quad \Delta E > 0 \\ W_{ij} &= 1 \quad \text{when} \quad \Delta E < 0 \end{aligned} \tag{5.17}$$

which is precisely condition 5.1. We see now that Eq. (5.15) is respected, and as such we can choose a probability of the form $P_j(t) = e^{-E_j\beta}$.

In essence, any transition rate of a Markovian process that satisfies detailed balance is acceptable and it will lead to the equilibration of an unbiased simulation after a certain Monte Carlo time t_{eq}. The desired Boltzmann distribution being the equilibrium distribution in our case.

In the language of the Ising model, given in Eq. (5.18) (in the presence of an external magnetic field h)

$$H = J\sum_{ij}\sigma_i\sigma_j - h\sum_i \sigma_i \quad \text{with} \quad \sigma_i = \pm 1\,. \tag{5.18}$$

generating a new state following an importance sampling Markovian process amounts to, in principle, flipping a random spin from $+1$ to -1 (or vice versa). Calculating the energy difference ΔE of the system with and without the spin flip (please note that the

process of flipping the spin is the so called "update algorithm" in the literature) we can determine if the flip will be accepted or not. We iterate this process until convergence is reached. We show the pseudo-code for the Importance sampling Metropolis-Hastings in Algorithm 2.

Algorithm 2 Importance sampling Metropolis-Hastings algorithm

```
Generate an initial state with spins in random ±1 orientations.
for (j = 0; j < Monte Carlo steps) do
  for (p=0; p < System size) do
    Choose a site i at random
    Flip that spin
    Calculate ΔE
    if ΔE ≤ 0 then
      accept the move
    else if ΔE > 0 then
      Generate a random number r / 0 < r < 1
      if r < e^{-ΔEβ} then
        accept the move
      else
        discard the move
      end if
    end if
  end for
end for
```

Importance sampling is the crucial part of the previous algorithm, given that it accounts for the proper entropic contributions. Even if a new configuration has higher energy, it can still be accepted given that at finite temperature and in thermal equilibrium the free energy ($F = U - TS$ with $U =< H >$) is minimum. We could always accept the spin flip following an uniform distribution, i.e accept if $\Delta E < 0$ and discard otherwise, and this would indeed minimize the energy, but is only at $T = 0 \leftrightarrow \beta \rightarrow \infty$ that the transition probability to states of higher energy tends to zero and this simple minimization is physically feasible.

Please note that having a convergence in the simulation doesn't necessarily mean we are in the minimal energy state of the system at temperature T, as we might have landed on a local energy minimum. In general, depending on the system the global minimum is not ensured within this simple algorithm. For systems with simple energy landscapes is relatively easy to detect if the system is in a local minima or not, but as we shall see in the next section, for systems with a rough energy landscape, as is the case for simulation of Heisenberg Hamiltonians, the algorithm needs to be further modified and

extra diagnostics need to be performed on the final state to asses whether it is the global minimum or not.

Once the simulation reaches equilibrium, it is continued for a certain amount of time to calculate statistical averages. One of the strengths of MC methods reside in the ability to accumulate the spin configurations at different times and thus calculate statistical quantities from one single simulation. While a certain amount of statistical noise is expected, this can always be reduced by performing several different simulations and averaging the results. In this context, the order parameters of different phases can be calculated after equilibration via a statistical average. For example, the ferromagnetic order parameter for an Ising model, i.e, the magnetization in the $z-$ direction, can be calculated after equilibrium as

$$\langle m \rangle = \frac{1}{NM} \sum_{i=0}^{M} \sum_{m=0}^{N} S_i^z \tag{5.19}$$

where N is the number of Monte Carlo steps in the simulation, and M is the number of sites. The sum over N in the above expression is the statistical average, i.e the average of the quantity S_i at different steps of the simulation. We define one Monte Carlo step, also called Monte Carlo sweep, as M spin flips, meaning, we will choose as many spins at random to flip as spins there are in our system (second loop in Algorithm 2). This is a way to be able to consider every spin in the system on one iteration of the algorithm. Note that since the spins are chosen at random nothing ensures that we will choose different spins every time. This way, if the simulations employs N Monte Carlo steps, we randomly choose a spin to flip $N \times M$ times.

From the fluctuations of the energy, E, and different order parameters we can extract the associated susceptibilities, e.g. the specific heat of the ferromagnetic order parameter

$$C_v = \frac{1}{T^2} \left(\langle E^2 \rangle - \langle E \rangle^2 \right), \tag{5.20}$$

while the magnetic susceptibility has the form

$$\chi = \frac{1}{T} \left(\langle m^2 \rangle - \langle m \rangle^2 \right). \tag{5.21}$$

Finally, from the stored spin configuration we can calculate the correlation function as

$$C_{ij} = \langle \mathbf{S}_i \cdot \mathbf{S}_j \rangle - \langle \mathbf{S}_i \rangle \langle \mathbf{S}_j \rangle \,, \tag{5.22}$$

where the average stands for statistical average. One point needs to be further clarified: Since the update algorithm flips one spin at a time, then consecutive states will be highly correlated to each other. If we calculate a given observable $\mathscr{A}$ with correlated configurations, we can end up with biased results. To avoid this problem it is important that for each system we measure the autocorrelation time of our simulation, τ, this time describes the time it takes for two measurements to be decorrelated. As such, the statistical averages in our MC simulation, after the system has been thermally equilibrated, can only be taken every τ steps. If a thermal phase transition is studied, the divergence of the correlation length induces longer relaxation times, thus slowing down the simulation. Different methods have been proposed to deal with this effect (Wolff cluster method [97] and Swendsen-Wang [98] to name a few) that involve cluster moves or worm updates. We will not deal with these modifications in this thesis since they are in general not applicable to frustrated systems.

5.1.2 Boundary conditions and finite size effects

Throughout this thesis we will be interested in bulk properties of different materials, but our systems will, understandably, be finite. This is the reason for which it is necessary to explore the different types of boundary conditions that we could apply in our simulation. The choice will depend on the type of system and states we want to study. In principle, since we want to work with bulk properties it would be tempting to choose periodic boundary conditions (PBC), since this represents bulk physics extremely well. While the finite size effects do not disappear (and in some cases this is good as it leads to estimates of critical exponents), they are minimized with PBC, and this has the fundamental advantage that the studied sizes can be reduced and as such the simulation will speed up. The introduction of PBC needs to be done with care, as there are cases in which the ordered state of the system has a special configuration which does not coincide with an arbitrary choice of PBCs.

This last point will become relevant in the next section: if we expect that the ground state of our system will be incommensurate to the lattice, meaning that the real space period of the state is an irrational number in units of the lattice spacing, then PBCs are not the right choice of boundary conditions. They would implicitly make the system adopt a commensurate state, which would lead to the miss-identification of the phases,

or to a lack of convergence in our code. In that case we need to completely forgo PBCs and instead employ free edge boundary conditions (FEBCs). In this case the spins on the edges of the lattice see no neighbors where PBCs would introduce one. This choice of boundary condition is less than ideal, as it introduces heavy finite size effects and surface and corner effects. To obtain a representative physical system in the presence of FEBC, system sizes have to be considerably bigger than for PBCs, and we need to limit our study to the bulk of the lattice (i.e. away from the edges). Everything is not lost though, as even though we lose some much needed computation time studying bigger sizes, we not only gain the possibility of studying incommensurate states, but also the appearance of domain walls and small energy fluctuations can be representative of the behavior of real materials, and as such interesting to study on themselves.

5.2 Implementation for continuous spin variables

For systems with continuous degrees of freedom things can change drastically, not in terms of the algorithm (the modification to Algorithm 2 will be straightforward) but in terms of performance and data analysis. In these cases, the spins do not take discrete values as in Ising or Potts models, but vary continuously on a circle (as is the case for XY models) or on a sphere (for Heisenberg models). As such, several complications arise: while in systems with discrete degrees of freedom the elementary excitations (spin flips) cost a finite amount of energy, systems with continuous spins will have excited states that cost an infinitesimal amount of energy. This implies that the spectrum of elementary excitations in continuous spin systems will be gapples at low temperatures, which leads to an energy landscape that contains multiple energy minima, as creating a defect or domain wall costs an infinitesimally small amount of energy, and once is created it can move through the lattice without further energy cost. This makes the determination of the true minimal energy equilibrium state much more complicated than for e.g. Ising models. At the same time, thermal fluctuations are more prominent in continuous models which smears out the different phases and transitions.

Metropolis algorithm (Algorithm 2) can still be employed to study continuous spin systems, but with some caveats. We need to define a way to chose a random orientation for our spins, we cannot simply flip the spin between two positions as in the Ising model, which brings complications of it's own: first, how does one choose the spin orientation in such a way that the distribution of possible directions is uniform? The most straightforward way would be to choose new random orientations of the spin components (in

Cartesian coordinates) and normalizing the total spin length to unity. Implementing this would translate into selecting a real random number in the range $[-0.5, 0.5]$ for each component and then normalizing to unity, but this would not give a uniform distribution in a unit sphere since spins will tend to point towards the corners of a cube more often. While other such proposals that provide uniform distributions of spin components in Cartesian coordinates exist, we will opt to track the coordinates of our spins in polar coordinates. As we will work with large system sizes, we need to keep in check our memory usage. An efficient code that can deal with heavy memory requirements is fundamental if we aim to surpass finite size effects brought by our implementation of FEBC. In this case polar coordinates are a good choice since we have to keep track of two numbers instead of three (since the vector is always on unit length). To choose the angles such that we obtain a uniform distribution on a sphere we choose two random variables u and v in $(0,1)$ and define the polar angles as

$$\theta = 2\pi u \quad \phi = \cos^{-1}(2v-1), \tag{5.23}$$

this is enough to ensure a uniform distribution of spin coordinates. Of course, we still need to transform to Cartesian coordinates to calculate the energy and one would think that this is an extremely time consuming process. We have performed benchmarks of our code comparing many different ways to chose our spins (Marsaglia's algorithm [99] among them) and the polar coordinates selection, and reached the conclusion that the update in terms of polar coordinates is the most efficient one. Once we know how to choose random spin orientations, the second caveat appears, in a system with continuous degrees of freedom at low temperature, simply choosing a random new orientation of our spin will generally produce large energy changes, which will decrease the acceptance ratio considerably and require extensive simulation time. As such, an update algorithm that chooses random spin orientations in the sphere is inefficient. The ratio can be increased via a modification of the update algorithm that we can extract from one of

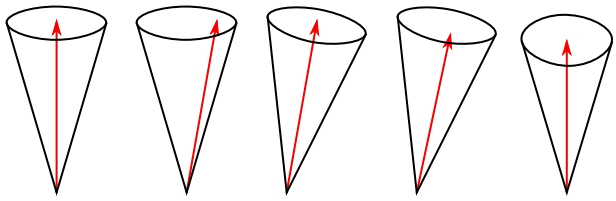

Figure 51: Sketch of the update algorithm for continuous spin variables. For a given spin, only a new configuration within the cone can be chosen. Once the spin is moved to the new orientation, a new cone is generated from which the new orientation will be chosen.

the fundamental property of classical spin systems at low temperature: in these cases the excitations can be considered spin waves, where the spins precess around a fix axis, it is then not expected that small temperatures will produce a big deviation of the spins from their original position, as such, we can restrict the space of random spin orientations from which we will select the new one to a cone around the original position (see Fig. 51). The size of the cone has to be carefully chosen, since a choice too narrow will again slow down the dynamics considerably. Careful initial trials where performed for the codes used in this thesis to ensure the optimal size. Please note that this does not mean that the ground state will be close to the original random state. With this update algorithm ergodicity is preserved, as spins can still change position drastically after enough sweeps.

5.2.1 Parallel tempering

Up to now Metropolis-Hastings algorithm has not been modified (except for a more sophisticated update algorithm), and in principle it needs no further modification. Once the new random orientation is chosen the process stays unaltered, we calculate ΔE and accept the move according to our detailed balance condition.

As we mentioned previously, we are interested in the study of Hamiltonians with continuous spins, and furthermore, with many competing interactions as we are searching for the low temperature properties of frustrated systems. This in turn means that the energy landscape is increasingly complicated, with multiple energy minima, where these minima might be states consisting of only one stable phase which is higher in energy than the ground state, and separated from the ground state by a large energy barrier which cannot be surpassed at low temperatures. Or it many consist on many domains separating domains of the same state (please note that as we have previously stated creating domains cost a certain energy, but moving them around the lattice does not provided the area of the domain does not change). We will see in the next chapter that the closer we are to a phase boundary the local energy minima multiply and the tendency to form magnetic domains is increased. To ensure we reach the true energy minima of the system we will implement two modifications to the Metropolis' algorithm, one of them, *parallel tempering*, is aimed at avoiding local energy minima altogether, the other one we will define in the next section, called *iterative minimization*, and will be employed in an attempt to reduce the magnetic domains that might remain.

Parallel tempering was first devised [100] as means of speeding up the equilibration process of systems presenting quenched disorder and glassy behavior. This algorithm relies on the replica trick, simultaneously simulating N identical copies of the system,

the replicas, at a range of temperatures $\{T_1, T_2, ...T_N\}$. After a certain number of Monte Carlo sweeps has taken place a swap move is performed. A swap move consists of N iterations of the following: two replicas at neighboring temperatures T_i and $T_{i\pm1}$ are randomly chosen and exchanged. The time evolution of all replicas will still follow a Boltzmann distribution, but with different β values, as such, if we make the exchange $\beta \leftrightarrow \beta'$, then there will be an energy difference given by

$$\Delta\mathscr{E} = (\beta E + \beta' E') - (\beta' E + \beta E') = (\beta - \beta')(E - E') = \Delta\beta\Delta E\,. \tag{5.24}$$

Employing this $\Delta\mathscr{E}$ we find that our transition probability now takes the form

$$W_{ij} = \min\left(1, e^{\Delta\beta\Delta E}\right) \tag{5.25}$$

and this exchange will be accepted or rejected according to a Metropolis algorithm. We present the pseudo code for the swap move in Algorithm 3

Algorithm 3 Parallel tempering

```
Randomly select a given replica i at temperature T_i
Randomly select a neighboring replica i' with T_{i'} = T_{i+1} or T_{i'} = T_{i-1}
Calculate ΔE
if ΔE ≤ 0 then
    Exchange temperatures T_{i'} ↔ T_i
else if ΔE > 0 then
    Generate a random number r / 0 < r < 1
    if r < e^{ΔE} then
        Exchange temperatures T_{i'} ↔ T_i
    else
        do nothing
    end if
end if
```

We can see now that if both temperatures where equal, the move would always be accepted and if, on the other hand, the temperatures are close together, the chance of acceptance is also high. In short, when the temperatures are similar then the corresponding Boltzmann distributions will overlap substantially. In a manner of speaking, if both temperatures are close to each other then there will be thermal states that belong to both replicas, and as such the energy change upon exchanging them will not be so drastic and the acceptance rate will increase.

For a given replica, the swap moves induce a random walk through temperature space, with the replicas diffusing to a high temperature region, where the equilibration is rapid, and back to a low temperature region where the simulation naturally slows down. This way the simulation efficiently explores complex energy landscapes and surmounts local energy minima in which it might get stuck. With this in mind we aim at maximizing the number of round trips one replica performs (how many times the lowest temperature replica visits the highest temperature region and returns to it's original position), this will depend on the choice of the given temperature set for our simulation. One would in principle consider that, given the appropriate conditions for a large scale parallel simulation, the more temperatures one uses the better as the temperatures can be closer and closer together thus increasing the acceptance rate considerably. But, since the movement of the replicas in temperature space is diffusive, the time scale for round-trips scales approximately as the square of the number of temperatures. Following the work in Ref. [101] we will chose a temperature set such that the probability for a swap at neighboring temperatures is flat. This is a good choice provided the specific heat of the system is constant, i.e no phase transition occurs at the studied temperatures. If this is the case then a good approximation is given by a geometric progression of temperatures:

$$T_i = T_1 \prod_{i=1}^{i-1} R \quad \text{with} \quad R = \left(\frac{T_N}{T_1}\right)^{1/(N-1)}, \tag{5.26}$$

where T_1 is the minimum temperature, T_N is the maximum, and T_i are the $N-2$ intermediate temperatures. As we will explore low temperature properties away from thermal phase transitions, we will implement this temperature set, if thermal excitations and associated transitions are of interest then the algorithm needs to be modified as proposed by Katzgraber *et.al.* [102].

5.2.2 Iterative minimization

As mentioned before, within the implementation of FEBCs the appearance of domain walls cannot be avoided. If our system is in a state that possesses any sort of degeneracy the domains will consist of different versions of the same state, e.g in a ferromagnetic Ising model the ordered state has a two fold degeneracy, as such the system can induce magnetic domains where the total magnetization has two different orientations. In cases where the phase diagram is more complex, if we choose exchange couplings which locate us close to a phase boundary, the magnetic domains can consist of two different phases,

one type of domain will be formed by the expected ground state for the selected exchange couplings, while the other will be given by the phase we are close to. This is another way in which our simulation gets trapped in a local minima. In principle parallel tempering will not always get rid of this problem, as higher temperatures can induce the appearance of domain walls that cannot be broken at low temperature.

To solve this problem, we will use an iterative minimization (IM) algorithm[103, 104]. In this method, a local field is calculated, $\mathbf{h}^{\text{loc}}$ for a given spin at site i,

$$\mathbf{h}_i^{\text{loc}} = -\sum_{j \neq i} J_{ij} \mathbf{S}_i \,, \tag{5.27}$$

in a sense, we calculate an effective local field generated by all the spins which whom the spin at site i interacts via the Hamiltonian H. In this way, the Hamiltonian can be written as

$$H = -\sum_i \mathbf{h}_i^{\text{loc}} \cdot \mathbf{S}_i \,. \tag{5.28}$$

The method selects one spin at random, and aligns it with the local field, this is iterated N times, where N is the number of spins in the system. Later on we calculate the average energy change (between the system with the original spin orientation and the system with the spin aligned with it's local field) of all the moves and if it is lower than a certain threshold (we chose this threshold as $\Delta E < 10^{-20}$) the algorithm ends. In principle this method can be used as a stand alone method to find the ground state of different classical Hamiltonians at $T = 0$ as it completely disregards thermal fluctuations. In that case we would start our simulation on a random state, and orient random spins with their local field until the threshold is reached. We chose to employ it instead as an improvement algorithm of our MC method since IM comprises a very slow relaxation time, if a long wavelength magnetic excitation is present in the system, it will take the IM method a considerably longer simulation time to make it disappear than MC, which constrains the system size greatly. As we have stated, we aim at studying incommensurate states which require extensive system sizes, then the IM method alone is out of the question. We show the pseudo code for the IM method in Algorithm 4.

One would be worried that employing IM as a further equilibration algorithm of a MC simulation would drastically change the observed physics, as MC is based on thermal excitations driving the dynamics while IM completely disregards them. And indeed this would be a problem if we where studying high temperature phases and

Algorithm 4 Iterative Minimization

```
input the low T state obtained from MC
while Δℰ > 10^−20 do
  for p = 0, p <(N +1) do
    Randomly select a spin S_i
    Calculate the local field h_i^loc
    Calculate the energy change for this move
    Update the spin S_i = h_i^loc
    accumulate the energy change ΔE
  end for
  Δℰ = ΔE/N
end while
```

their transitions. In our case, we will focus on low temperature properties well below the smallest energy scale of the Hamiltonian ($T \sim 0.01 J_{\min}$, where $J_{\min}$ is the smallest exchange coupling in the system), and as such a final minimization via IM will not affect the ground state obtained via MC, but it will reduce the domain walls that might appear in it. Furthermore, since the energy of the system is minimal in the ground state (at $T = 0$), then all spins are aligned with their local field, which justifies the use of IM to study ground state properties.

In conclusion: we have implemented a Metropolis algorithm for continuous spins to treat Heisenberg like Hamiltonians with an arbitrary number of interactions. Focusing on the study of incommensurate states of the next chapter we explained the need to implement free edge boundary conditions and the associated difficulties. Furthermore, we implemented two extra algorithms to ensure a proper equilibration of the low temperature states and to deal with the effects of the FEBCs. When everything is taken into consideration, the final code used to map the phase diagram of continuous spin systems consisting of N spins reduces to: M Metropolis Monte Carlo sweeps interlaced with P parallel tempering swaps. Once the low T state was equilibrated we employed iterative minimization with a threshold E. While the number of iterations for every step vary for system to system, for the different models studied thought this thesis we employed (unless stated otherwise) $N = 2400$ or 5400 sites, $M = 10^6$ with 10^5 used for equilibration and the rest to calculate the averages. The parallel tempering swaps where performed with either 16 or 32 replicas, every 100 MC sweeps, as such is $P = 16$ or 32 , finally $E = 10^{-20}$.

CHAPTER 6

MAGNETISM IN THE CLASSICAL LIMIT
PHYSICS OF α–Li_2IrO_3

Perhaps the material is the simulation approaching your computer's results.

Daniel Litinski, 2018

Now that we have shown how our Monte Carlo method works, we can employ it in the study of low temperature properties of classical magnets. In particular, since the algorithms don't change when different Heisenberg like or anisotropic interactions are employed, we will concentrate in models that present bond dependent interactions. In particular, we will study a compound belonging to the broad family of Kitaev materials.

In 2006 Alexei Kitaev put forward an exactly solvable model [9], the now called Kitaev honeycomb model, which belongs to a wider range of quantum compass Hamiltonians [105]. The distinguishing feature of the quantum compass models is that the spin-spin interactions along each bond are anisotropic, and depend on the orientation of the bond. We show the spin Hamiltonian corresponding to Kitaev interactions in equation 6.1.

$$\mathcal{H} = K \sum_{<ij>} \sum_{\gamma} S_i^{\gamma} S_j^{\gamma}, \tag{6.1}$$

where $\gamma = \{x, y, z\}$, and where different bonds couple different components of the spin. We show in Fig. 61 the different bond interactions in the honeycomb lattice. One of the most relevant features of Kitaev's honeycomb model consists on the fact that it can be solved exactly. Reformulating the spin operators in terms of Majorana fermions the Kitaev-honeycomb model can be mapped onto a $\mathbb{Z}_2$ gauge theory with static flux excitations describing a spin liquid ground state.

A detailed study of quantum compass models or of the particular Kitaev model is beyond the scope of this chapter, but it suffices to say that Kitaev's model is special in the sense that for spins 1/2 it harbors both gapped and gappless spin liquids. This proposal kick-started a quest for experimental realizations of model 6.1, and since then many materials have been synthesized that have been proposed to realize Kitaev interactions (Na_2IrO_3[106], Li_2IrO_3[107–109], $RuCl_3$[110], $Ba_3IrTi_2O_9$[111]).

Until now, though, these materials not only present Kitaev interactions but also are accompanied by Heisenberg and other bond dependent exchanges, we will call these models *extended Kitaev models*. These perturbing interactions have a strong effect on the ground state of the these materials. Even though Kitaev interactions give rise to spin liquid states, the perturbation are so strong that in the experiments they give rise to classical magnetic order. One of the materials in which we will be interested in this chapter is α–Li_2IrO_3. While the quest for materials which *only* realize a Hamiltonian of the form 6.1 is still ongoing, the theoretical understanding of extended Kitaev models remains challenging. These extended models are in principle not exactly solvable, and as such approximate analytical methods, or numerical simulations need to be employed. In particular, the question of which minimal model α-Li_2IrO_3 realizes has not been settled. We aim in this chapter to give an overview of the physics of this material, and study the different proposed Hamiltonians via large scale Monte Carlo simulations to compare the different models with the accepted experimental evidence. Furthermore, we will go one step beyond and study the magnetization processes of the different models, with the intention of predicting their behavior in an experimentally reproducible way.

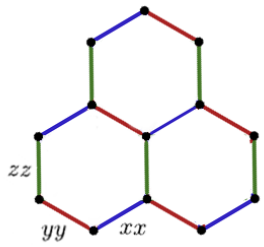

Figure 61: Color coded honeycomb lattice showing the Kitaev exchanges $S_i^x S_j^x$ (blue), $S_i^y S_j^y$ (red), and $S_i^z S_j^z$ (green) for nearest neighbor interactions.

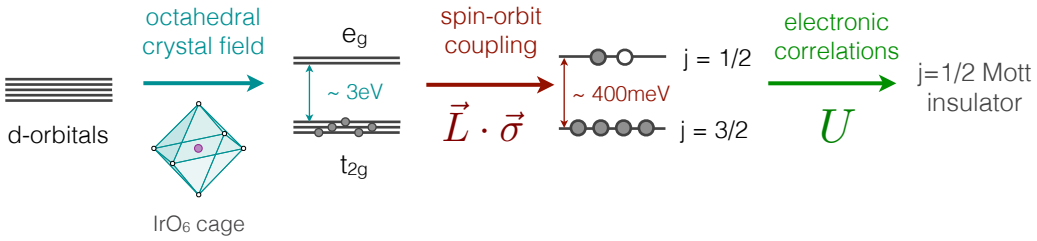

Figure 62: Diagram showing the formation of spin-orbit entangled $j = 1/2$ local moments arising from ions in a d^5 electronic configuration. A canonical example of this process is the Ir^{4+} ions in α–Li_2IrO_3. Figure adopted from [112].

This chapter is structured in the following way: First we will present the current understanding of the generation of bond dependent interactions in real materials, focusing on α–Li_2IrO_3. Following we will study extended Kitaev models based on symmetry allowed interactions, that will lead us to a minimal model that accurately reproduces the low temperature experimental signatures of this material. We will also study a model put forward in Ref. [1] based on DFT calculations. Finally we will make predictions on the magnetization behavior of both models.

6.1 Bond dependent interactions

We will start this chapter by briefly describing the main properties of materials like α-Li_2IrO_3 composed of transition metal oxides with partially filled $5d$ shells in an octahedral environment (in α–Li_2IrO_3 the $5d$ transition metal Ir^{4+} are the magnetic ions). Materials such as this present a rich behavior arising from the combinations of electronic correlations, spin orbit entanglement, and crystal field effects [113]. In the presence of both strong electronic correlations and spin orbit coupling, it can be shown that these materials form spin orbit entangled Mott insulators. We will be interested in the particular class of Mott insulators in which the local moments are spin-orbit entangled $j = 1/2$ Kramers doublets arising from a d^5 electronic configuration in an octahedral environment. The environment around the magnetic ion (please see Fig. 63 for the crystal structure of α–Li_2IrO_3) contains six O atoms that form an octahedron around the metal ion. In these cases the d-orbital splits, thanks to the crystal field of the ligands, into a high energy empty e_g pair and a lower energy, three-fold degenerated, t_{2g} level containing one hole. This way five electrons, with a total $s = 1/2$, are located in the t_{2g} levels, each one realizing an effective $l = 1$ orbital moment. The strong spin orbit coupling also affects the elec-

tronic levels, splitting the t_{2g} into two bands with corresponding $j_{eff} = 3/2$ and $j_{eff} = 1/2$. Furthermore one hole is localized in each metal ion in such a way that the $j_{eff} = 3/2$ band is full and the remaining $j_{eff} = 1/2$ band is half-filled. This process if schemed in Fig. 62.

One important point needs to be clarified before moving on: in chapter 4 we mentioned that the classical limit of our spin system is given by $S \to \infty$. And we mentioned that increasing the spin length can be interpreted as decreasing the quantum fluctuations. Theoretically this can be proven by studying the overlap of coherent spin states as the spin length is increased [115] and noticing that the overlap vanishes in the classical limit. The experimental reason for why a system composed of atomic spins 1/2 (that in principle are quantum objects) can be studied classically, as we will do in this chapter, is related to the experimental evidence suggesting that the ground state of α–Li_2IrO_3 is a magnetically ordered phase. In cases such as this, a good first approach is to completely neglect quantum fluctuations and study the purely classical case. Please note that previously, in chapter 4 we studied another model, in which the classical limit moves the boundaries between different phases, but does not change the nature of the magnetic long range orders present in the quantum limit. As such, in this particular model we could also in principle neglect quantum fluctuations and proceed with a classical treatment as a first approach in the parts of the phase diagram showing LRO.

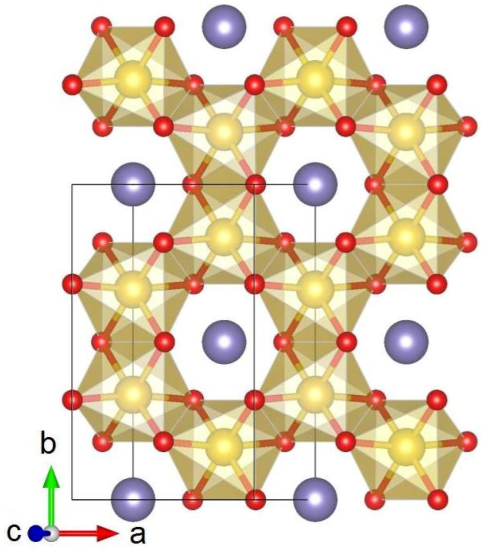

Figure 63: Refined crystal structure of α–Li_2IrO_3, showing unit cell as a black outline. Here we present the basal plane layer showing the honeycomb of edge-sharing IrO_6 octahedron. The Ir ions are represented by gold spheres, Li as purple, and O as red. Figure extracted from Ref. [114].

One more detail needs to be pointed out, for the material we will study in this chapter the crystal field presents no easy axis (easy plane) anisotropy that could force the local moments to point in a particular direction (plane). As such we will model our system of spins as vectors living on a sphere. It has to be noted that there are cases where the crystal field not only splits the energy levels but also selects particular directions (planes) for the movement of the local moments. This is the mechanism by which spin ices [45]

(XY models) can be considered as classical spins pointing only in a particular direction (taking values in one particular plane).

With this in mind, now we can study where the particular interactions that will be used to model α–Li_2IrO_3 arise from. Jackeli and Khaliullin [116] realized that the geometric orientation of the octahedron affects the exchange paths between magnetic ions located at the center of these octahedra. If the IrO_6 octahedron share a corner, as in the case of Sr_2IrO_4 [117], there is one single Ir-O-Ir exchange path with the bond in a 180^o configuration. It can be calculated in a similar way as was done in Chapter 1, that in this case the dominant super-exchange interaction is of Heisenberg type between the two $j_{eff} = 1/2$ moments. On the other hand, if the octahedron share an edge (as in the case of α–Li_2IrO_3) there are two possible Ir-O-Ir exchange paths with a 90^o geometry. In this case, when considering hopping only between the p-orbitals we see that, for the symmetric Heisenberg exchange, both paths interfere destructively if we only consider paths arising only from the $j_{eff} = 1/2$ bands, and that this path is significantly reduced when considering the full multi-orbital model. Further calculations including hopping between d-orbitals (which in $4d$ and $5d$ elements are diffuse which leads to a bigger direct overlap between them) arrive at more significant deviations from the pure Kitaev model. What is consistent is that, even in the case where all hopping paths are taken into account, the dominant interaction is of Kitaev type, and bond dependent couplings enter into play.

The bond directionality stems from the fact that a pair of Ir are linked between two neighbor octahedra sharing an edge, which induces different orientations of the t_{2g} orbitals, as their lobes point exactly along the axis of the Ir-O-Ir bonds, and these bonds are not the same for all Ir-O-Ir triads. Many works have shown that these bond dependent interactions are of Ising type, between the two $j_{eff} = 1/2$ moments, with a magnetic easy axis perpendicular to the plane spanned by the two exchange paths[118–120]. If we represent these two local 1/2 moments by vectors of the SU(2) spin 1/2 Pauli matrices algebra, $\mathbf{S}_1$ and $\mathbf{S}_2$, it can be calculated that this bond geometry naturally couples only one component of the spin, which is precisely the Kitaev exchange in equation 6.1.

With these considerations in mind a generic model for the magnetic interactions between spin-orbit entangled $j = 1/2$ moments was determined [120, 121],

$$\mathscr{H} = J\sum_{ij}\mathbf{S}_i\mathbf{S}_j + \sum_{ij\in\gamma-\text{bonds}}\left(KS_i^{\gamma}S_j^{\gamma} + \Gamma(S_i^{\alpha}S_j^{\beta} + S_i^{\beta}S_j^{\alpha})\right), \tag{6.2}$$

where $\gamma = \{x, y, z\}$, and where α and β indicate the two spin components perpendicular

to γ. J represents a Heisenberg coupling, while the bond dependent terms contain Kitaev interactions coupled by K, and a Γ exchange that couples two orthogonal spin components, α and β, along the bond with Kitaev interactions in the γ spin component. In this class of materials the specific model may vary, not always been exactly of the form 6.2 or including interactions of different ranges, but it is a distinguishing feature of most Kitaev materials that the dominant interaction has been proposed to be of Kitaev type, $K \gg J, K$.

For α–Li_2IrO_3 many experimental studies have been performed, and up to the moment the consensus is that the ground state of this material is a long range ordered state, in which spins form incommensurate counterotating spirals with a tilted rotation plane [14]. Different variations of model 6.2 have been proposed for α–Li_2IrO_3, in particular Kimchi *et. al.* have proposed [122] a slightly different model where the bond dependent interaction is allowed by the crystallographic symmetry. This model was studied by the authors in a toy model consisting of 1D zig-zag chains, and it can be seen that the Hamiltonian can be taken to a similar form as Eq. 6.2, but the coupling strength, their respective signs, and the symmetries, change drastically. We will study the model proposed by [122], but we will employ large scale Monte Carlo in the precise crystallographic configuration of α–Li_2IrO_3 instead of the 1D toy model. We will also study a variant of the model shown in Eq. 6.2 with coupling strengths obtained via DFT calculations, and other further models which might present a similar ordered ground state as the one expected for α–Li_2IrO_3.

6.2 Characteristics of $\alpha - Li_2IrO_3$

As mentioned before, we will concentrate on the study of a particular material believed to be representative of extended Kitaev models, $\alpha - Li_2IrO_3$. This material, isostructural to Na_2IrO_3, possesses a layered crystal structure where the Ir^{4+}, surrounded by an octahedral cage of oxygens, form a honeycomb lattice (see Fig. 63). This lattice resides in the [111] Cartesian plane, with one bond parallel to the $[\bar{1}10]$ direction.

Both compounds, Na_2IrO_3 and $\alpha - Li_2IrO_3$, present long range order [107], showing anomalies in the specific heat and in the magnetic susceptibility at a critical temperature $T_c \sim 15K$ (experimental data extracted from [107] is shown in Fig. 64), with a Curie-Weiss temperature of $\Theta = -125(6)K$ and $\Theta = -33(3)K$ respectively. Na_2IrO_3 presents a zig-zag ordered state and it would be expected that, given the similarities in the thermodynamic anomalies, $\alpha - Li_2IrO_3$ would also present a zig-zag order. While the

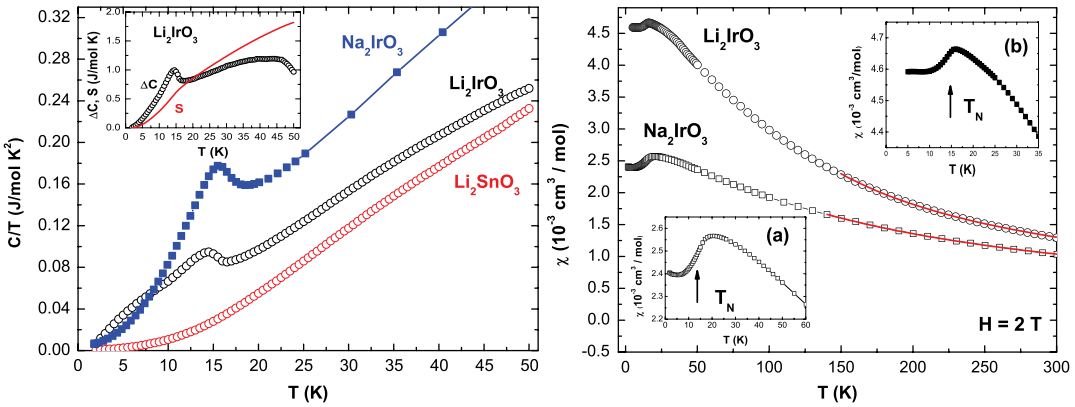

Figure 64: *Top*: Specific heat as a function of temperature for NA_2IrO_3 (blue), $\alpha - Li_2IrO_3$ (black), and the nonmagnetic compound Li_2SnO_3. Inset shows the difference heat capacity ΔC and the difference entropy ΔS for the Li compound. *Bottom*: Zero field magnetic susceptibility as a function of temperature for the Na and Ir compounds. The red curve represents a fit by the Curie-Weiss expression $\chi = \chi_0 + C/(T - \Theta)$. The insets (a) and (b) show the anomaly at T_c for NA_2IrO_3 and $\alpha - Li_2IrO_3$, respectively. In both cases, a clear peak corresponding to the transition towards long range order is seen at $T_c \sim 15K$. Figures extracted from [107].

thermodynamics show similarities in the behavior of the Na and Li compound, recent studies performed on single crystals and powder samples of $\alpha - Li_2IrO_3$ have shown that the magnetic order present in this material is not of zig-zag type, but of spiral nature. Magnetic resonant X-ray diffraction (MRXD) together with magnetic powder neutron diffraction determine a magnetic structure composed of counterrotating incommensurate coplanar spin spirals [14], with a propagation wavevector $\mathbf{q} = (0.32(1), 0, 0)$. At the same time they are able to determine that the plane of rotation of the spirals is uniform between the different sublattices and tilted with respect to the lattice plane by 80^o. In their studies they see that the MRXD, at a temperature of $5K$, present satellite peaks at positions $\tau + \mathbf{q}$, where τ are the positions of allowed structural reflections $\tau = (h, k, l)$, with $h + k$ =even. We show a scan of the magnetic diffraction along the $[h, 0, 6]$ plane in Fig. 65(b).

Similarities have been found between the ground state of $\alpha - Li_2IrO_3$ and the two structural polytypes, $\beta - Li_2IrO_3$ and $\gamma - Li_2IrO_3$, which correspond to hyper-honeycomb and stripy-honeycomb magnetic lattices respectively. All three of these polytypes are members of the "harmonic honeycomb" structural series, and the similarities in their magnetic ordering have lead to proposals of universality between the members of the family of harmonic honeycomb Iridates [122].

It has been shown previously that the magnetic ordering of the β and γ structures are well described by a dominant antiferromagnetic Kitaev interaction, combined with

other smaller exchange terms, like Heisenberg or bond dependent terms, [122–125], in particular the counterrotating spirals can be modeled via a bond dependent interaction in the $zz-$bonds. Furthermore, these materials present an alternating tilt of the rotation plane that can be reproduced via a change in the sign of the Kitaev interaction along the zz-bonds. [122].

Given the similarities between the different polytypes we predict that the model which correctly describes the magnetic structure of α–Li_2IrO_3 will be composed of dominant Kitaev interactions, supplemented by weaker Heisenberg and bond dependent terms. While in principle this proposal is in agreement with what is known of the β and γ polytypes, the particularities of the minimal model have not yet been defined. Many models have been proposed which reproduce some characteristics of the α polytype, but which have been tested only in toy models, or by a Luttinger-Tisza (LT) approximation, which are not ensure to succeed at the detection of incommensurate states. In the following we will study the models that have been proposed until now, and propose some of our own, under the light of a common method, a Monte Carlo simulation. We aim at exploring the possible ground states of the different models via a method which is not biased towards any type of magnetic order, and which can deal with the incommensurate nature of the expected ground state appropriately. At the same time, we will go one step beyond and study the magnetization properties of the different models whose ground state match the experimental signatures of the material. Our aim is that the differences in the magnetization processes with different field directions can provide an efficient experimental route to probe which of

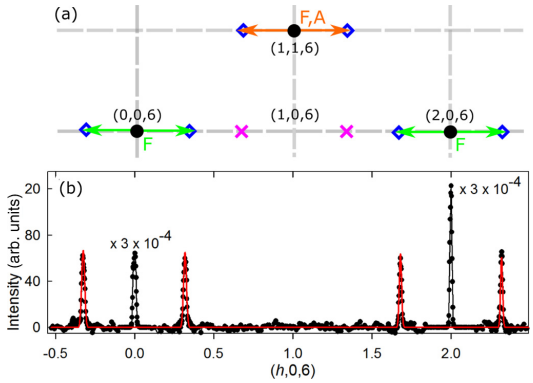

Figure 65: *(a)* Schematic diagram for the [hk6] reciprocal plane of $\alpha - Li_2IrO_3$ showing structural peaks (black circles), measured magnetic peaks (blue diamonds), and the absence of peaks (pink crosses). The lattice points are indexed by their magnetic basis vectors. *(b)* Intensity of the magnetic resonant X-ray diffraction scanned along the (h,0,6) direction. Structural peaks appear at integer $h = 0,\ 2$ (points rescaled by 3×10^{-4}) with their magnetic satellite points at positions $h = 0 \pm q,\ 2 \pm q$. The red line indicates the calculated magnetic scattering intensity for a magnetic structure corresponding to incommensurate counterotating spin spirals with a tilted plane of rotation and a magnetic wavevector $q = 0.32$. Figure extracted from [14].

the proposed models is the more feasible one.

6.3 Models

We will classify the different models according to the range of their interactions, into nearest, second, and third neighbor models. All the models we will study here are variations of the extended Kitaev-Heisenberg model shown in Eq. 6.2. Here we will show some of their basic common features. More information regarding the particularities of each model will be given as the results are shown, as the construction of some of these models heavily rely on the results found for others.

The nearest and second neighbor models are based on the following Hamiltonian

$$\mathscr{H} = \sum_n \left[J_n \sum_{<ij>_n} \mathbf{S}_i \cdot \mathbf{S}_j + K_n \sum_{<ij>_n} \sum_{\gamma} S_i^{\gamma} S_j^{\gamma} + I_c \sum_{<ij>} S_i^{r_{ij}} S_j^{r_{ij}} + I_d \sum_{<ij>} S_i^{r_{ij}} S_j^{r_{ij}} \right] \tag{6.3}$$

where $<ij>_n$ denote a sum over n-th neighbors, $\gamma = x, y, z$ indicates the bond in which the Kitaev coupling acts, and $\mathbf{S}_i = (S_i^x, S_i^y, S_i^z)$ denotes the classical spin operator acting on site i. The terms containing the couplings I_c and I_d are Ising terms that couple the spins components parallel to the bond orientation, i.e $\mathbf{S}^{r_{ij}} = \mathbf{S} \cdot \hat{\mathbf{r}}_{ij}$, where $\hat{\mathbf{r}}_{ij}$ is the unit vector connecting the spins in sites i and j. In the real material, the octahedral cage enclosing the Ir atoms is not perfect, and presents deformations. This deformations induce a bond anisotropy on the interactions, where the couplings of the Ising terms is not the same on the zz-, and xx- and yy-bonds. For this, we choose I_c to be active only on the zz-bonds, while I_d acts on the rest of them (zig zag bonds). A diagram of the lattice and the Kitaev interactions is shown in Fig. 66

Please note that the Kitaev model has a particular symmetry in the bond isotropic case, where a 60^o rotation in real space and spin space leave the ground state invariant.

We will work with two nearest neighbor models, the model we will name "I_c-model" will contain dominant ferromagnetic Kitaev interactions $K_1 < 0$ as well as small antiferromagnetic Heisenberg terms $J_1 > 0$, the Ising term is ferromagnetic as well, $I_c < 0$. The "$I_c I_d$-model" will also include terms with $I_d < 0$. For the second neighbor models we will have the "$2N$-model" with $J_1 > 0$, $J_2 < 0$, $K_1 < 0$, and $K_2 > 0$, while "$2NI_c$-model" will include terms with $I_c < 0$. The different models with their respective interactions are shown in Table 61.

For the third neighbor case we will use the model proposed by Winter *et.al.* based on DFT calculations [1]. The Hamiltonian, for the zz-bonds takes the form

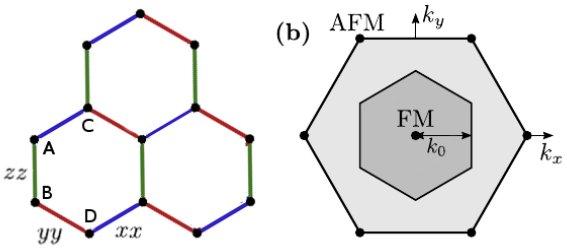

Figure 66: (a) Color coded honeycomb lattice showing the Kitaev exchanges $S_i^x S_j^x$ (blue), $S_i^y S_j^y$ (red), and $S_i^z S_j^z$ (green) for nearest neighbor interactions. The I_c terms act on the the zz-bonds which in this figure correspond to the vertical bonds. The I_d term acts on the remaining zig-zag bonds, xx and yy. (b) Extended Brillouin zone of the honeycomb lattice (inner hexagon is the first Brillouin zone). Ferromagnetic (FM) order presents peaks in the center of the first Brillouin zone, while antiferromagnetic (AFM) order resides at the corner of the extended zone scheme.

Model	J_1	K_1	I_c	I_d	J_2	K_2	J_3
I_c	>0	<0	<0	-	-	-	-
$I_c I_d$	>0	<0	<0	<0	-	-	-
$2N$	>0	<0	-	-	<0	>0	-
$2NI_c$	>0	<0	<0	-	<0	>0	-
	J_1	K_1	Γ_1	J_2	K_2	Γ_2	J_3
W	Yes	Yes	Yes	Yes	Yes	Yes	Yes

Table 61: Different interactions present in each model, together with the names we will assign to each model throughout this thesis. While I_c- and $I_c I_d$-models are nearest neighbor models, $2N$- and $2NI_c$-models are second neighbors. The more extended model we will study is Winter's model ("W-model") which contains interactions up to third neighbors (see text). The double lines separate the nearest, second, and third neighbor interactions.

$$\mathcal{H} = \sum_n \left[J_n \sum_{<ij>_n} \mathbf{S}_i \cdot \mathbf{S}_j + K_n \sum_{<ij>_n} S_i^\gamma S_j^\gamma - \Gamma_n \sum_{<ij>_n} (S_i^\alpha S_j^\beta + S_i^\beta S_j^\alpha) \right] \tag{6.4}$$

where $(\alpha, \beta, \gamma) = (x, y, z)$. In this model the Γ-exchange term couple the spin components that are perpendicular to the spin component coupled via the Kitaev terms. For this model, that we will name "W-model", we will study the bond isotropic version of the Hamiltonian in Eq. 6.4, but also a version which introduces large bond anisotropies in the nearest neighbors interactions. Defining the bond anisotropy constant by δ we obtain

$$
\begin{aligned}
J_1^{XY} = J_1 - \delta \quad J_1^Z = J_1 + \delta \\
K_1^{XY} = K_1 - \delta \quad K_1^Z = K_1 + \delta \\
\Gamma_1^{XY} = \Gamma_1 - \delta \quad \Gamma_1^Z = \Gamma_1 + \delta \\
\Gamma_2^{XY} = \Gamma_1 - \delta \quad \Gamma_1^Z = \Gamma_1 + \delta \,,
\end{aligned} \tag{6.5}
$$

where the quantities J_1, K_1, Γ_1, and Γ_2 are understood as bond averaged interactions. In Table.62 we show the bond average value of the different couplings together with the anisotropic component δ that reproduce the experimental results.

	δ_W	Bond average W	Anisotropic interactions
J_1	0.14	0.2	$J_1^{XY} = 0.06 \quad J_1^Z = 0.34$
K_1	0.34	-1	$K_1^{XY} = -1.34 \quad K_1^Z = -0.66$
Γ_1	0.195	1	$\Gamma_1^{XY} = 0.805 \quad \Gamma_1^Z = 1.195$
K_2	0	-0.275	$K_2^{XY} = -0.275 \quad K_2^Z = -0.275$
Γ_2	-0.06	0.275	$\Gamma_2^{XY} = 0.335 \quad \Gamma_2^Z = 0.215$
J_3	0	0.3	$J_3^{XY} = 0.3 \quad J_3^Z = 0.3$

Table 62: Values that reproduce the experimental results with the corresponding bond anisotropies for the W-model. All values are given in terms of $|K_1|$.

6.3.1 Method

The numerical simulation consist on a Monte Carlo simulations implementing a Metropolis-Hastings algorithm. As mentioned in the previous chapter, even though we want to study ground state properties of the bulk, some of these ground states are incommensurate phases which, to the effect of the algorithm, means that our system will need free edge boundary conditions (FEBs). The presence of FEBs carries some added effects, and as such the system will exhibit edge modes that are, in principle, not relevant to the study of the ground state, plus it will enhance the appearance of domain walls. We show in Appendix B that the edge modes do not affect the bulk properties of the data, provided the lattice sizes are sufficiently big. We achieve this via a benchmark of our code implementing FEBs against the results of Ref. [126] for the Kitaev-Heisenberg model ($J_1 \neq 0$, $K_1 \neq 0$) with periodic boundary conditions.

To minimize the creation of domain walls, and to increase the acceptance rate, we will implement an iterative minimization and parallel tempering algorithms respectively, with system sizes ranging from 2400 up to 5400 sites. To identify the different states in the phase diagram we will rely on the study of the Fourier transform of the spin-spin correlation function

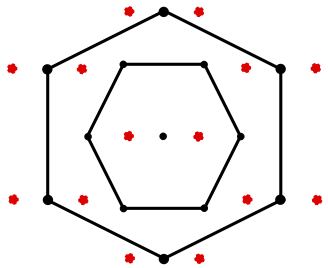

Figure 67: Reciprocal space diagram of the honeycomb lattice showing in red the positions of the magnetic Bragg peaks corresponding to the ground state of α–Li_2IrO_3. The black dots correspond to the allowed structural Bragg peaks τ, while the red stars correspond to the satellite peaks $\tau + \mathbf{q}$. The inner hexagon is the first Brillouin zone, while the outer hexagon is the extended Brillouin zone.

$$C_{ij} = \langle \mathbf{S}_i \cdot \mathbf{S}_j \rangle - \langle \mathbf{S}_i \rangle \langle \mathbf{S}_j \rangle , \tag{6.6}$$

where the average is taken over different Monte Carlo sweeps. For the ground state of α–Li_2IrO_3 we expect to find peaks at positions indicated by the red stars in Fig. 67 in accordance with the results of [14], in particular with their results shown here in Fig. 65. We can determine the propagation wavevector of the magnetic spirals from the maxima of the Fourier transform of Eq. 6.6, as they will be located at the points $\tau \pm \mathbf{q}$, with $\mathbf{q} = (\pm q, 0)$ the propagation wavevector. At the same time, and since Monte Carlo produces the spin pattern of the state, we confirm our results by calculating the relative angle between nearest neighbor spins in one spiral.

To study the magnetization processes we will be interested in the ferromagnetic order parameter,

$$|\mathbf{FM}_{OP}| = \frac{1}{N} |\sum_i \langle \mathbf{S}_i \rangle| , \tag{6.7}$$

where the average is taken over different Monte Carlo sweeps, the magnetization in the direction of an externally applied field,

$$M_H = \mathbf{M}.\mathbf{H} = \frac{1}{N}(FM_{OPx}H_x + FM_{OPy}H_y + FM_{OPz}H_z) , \tag{6.8}$$

where N is the number of sites, $\mathbf{S}_i$ represent the spin at site i, and FM_{OPi} is the i-th component of the ferromagnetic order parameter. Please note that while $\mathbf{FM}_{OP}$ probes the existence of a ferromagnetic state in the system, it does so without taking into account the possible directions of the magnetic polarization. To probe the existence of a ferromagnetic order with a particular polarization the ferromagnetic order parameter

has to be projected onto this direction. As we will include magnetic fields, we choose to study the projection of $\mathbf{FM}_{OP}$ in the direction of the field, as we know that at high enough intensities the system will polarize in that direction. To estimate critical fields we will also employ the associated response function of the ferromagnetic order parameter, the magnetic susceptibility

$$\chi = \frac{d\mathbf{FM}_{OP}}{dH} = \frac{1}{N}\frac{1}{T}\sum_i \left(\langle \mathbf{S}_i^2 \rangle - \langle \mathbf{S}_i \rangle^2\right) \tag{6.9}$$

where H is the magnitude of the applied magnetic field, and T is the temperature of the simulation.

6.4 Nearest neighbor models

6.4.1 Heisenberg-Kitaev-I_c model (I_c-model)

We begin the study of our different models by analyzing a nearest neighbor model which qualitatively captures the features of the spin spirals along the harmonic honeycomb family of Li_2IrO_3 compounds. Both β and γ polytypes suffer from a phase transition to a LRO state at $T_c = 38K$, magnetic X-ray diffraction experiments show that both materials order in a spin spiral state with counterrotating magnetic spirals propagating with a $(q,0)$ wavevector, where $q = 0.57(1)$ in units of 2π. As mentioned before, the α polytype also shares the same groundstate properties as its sibling compounds. For this reason Kimchi *et. al.* proposed [122] a nearest neighbor Hamiltonian that is capable of capturing the qualitative features of the ground state properties common to these three compounds. The Hamiltonian, corresponding to the I_c-model, takes the form of Eq. 6.3 with $I_d = 0$,

$$\mathscr{H} = J\sum_{<ij>} \mathbf{S}_i \cdot \mathbf{S}_j + K\sum_{<ij>_\gamma}\sum_{\gamma} S_i^\gamma S_j^\gamma + I_c \sum_{<ij>_{zz}} S_i^{r_{ij}} S_j^{r_{ij}}. \tag{6.10}$$

where $< ij >_\gamma$ indicates the bonds in which the interactions acts. This Hamiltonian contains terms that are symmetry allowed by the microscopic structure of the materials, and in their paper[122] Kimchi and collaborators studied it via a reduction to a 1D chain model and a subsequent solution employing an LT approximation. While the results they have obtained are in good qualitative agreement with what is known for these materials, the methods used are approximate. The 1D toy model relies on the reduction of the Hamiltonian in Eq. 6.10 to that of decoupled zig-zag chains by taking the I_c term

to zero and introducing a second neighbor Heisenberg interactions. This Hamiltonian is solved by proposing an ansatz for the spin components and then the interchain coupling arising from the I_c terms is slowly introduced. They subsequently solve the perturbed Hamiltonian by an LT approximation. They find that even when the second neighbor interactions is zero and the I_c term is completely introduced, the spin spirals survive in the phase diagram. As such, we opt for studying the model in Eq. 6.10 exactly, via Monte Carlo simulations. This gives us the chance to test whether the appearance of spin spiral states in this model exist without recurring to approximations given that LT is an approximation, that cannot ensure the correct ground state when treating non-Bravais lattices and incommensurate states, while MC methods are exact up to stochastic noise.

In the following we will show the obtained phase diagram for the I_c-model, and the properties of the spiral phases present in it.

6.4.1.1 Phase diagram

Employing large scale Monte Carlo simulations we are able to map the phase diagram of the I_c-model in the phase space of the J and I_c couplings. In all the models we will study, the dominant coupling is the Kitaev exchange, which we consistently set to -1. The obtained phase diagram can be seen in Fig. 68. This diagram shows evidence of the strong Kitaev interactions present, displaying a broad region where the stripy phase lives, which is a prominent feature of the Kitaev-Heisenberg model as shown in Appendix. B.

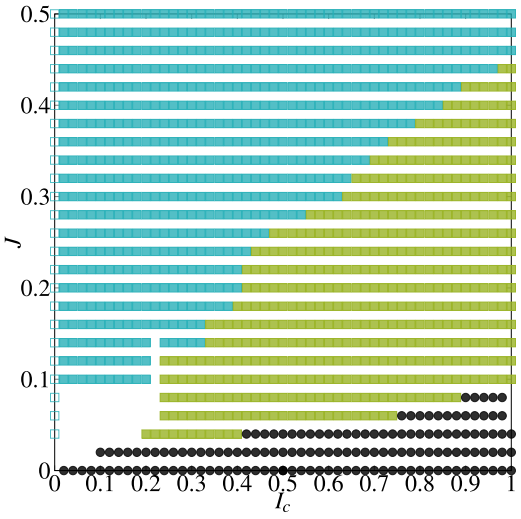

Figure 68: Phase diagram for model shown in Eq. 6.10. Blue squares represent the st-Z order (see text), green squares the spiral phase, and black dots correspond to ferromagnetic order

At the boundary $I_c = 0$ ($J \neq 0$) we recover the Kitaev Heisenberg model, which presents a stripy phase for these values of J and K. A stripy phase is such that one pair of spins on nearest neighbors are aligned ferromagnetically, while the other two are aligned antiferromagnetically. This order is three fold degenerated in this case, with the spins orienting themselves along one of the Cartesian spin directions, i.e the spins will all have one component equal ± 1

and the other two equal 0. For example in Fig. 69 we see green (red) dots representing spins pointing in the $(0,0,-1)$ ($(0,0,1)$) direction. Furthermore, this state is affected by a spin locking effect. This mechanism is that by which the neighbors in which the spins are ferromagnetically aligned are correlated to the spin direction in which the spins aligned, in the sense that if our spins are aligning in the z direction, then the neighbors which will align ferromagnetically are those coupled by the zz-bonds. The name of this state comes from the fact that it can be seen as stripes of spins propagating along the lattice (In Fig. 69 we show the propagation direction by a blue arrow).

As soon as we set $I_c \neq 0$ the degeneracy of the stripy phase is broken, and a stripy in the z direction is chosen (we will name this phase st-Z), which we show in the phase diagram by blue squares. This break down of the degeneracy is not surprising, as the I_c terms reinforce ferromagnetic order over the zz-bonds.

On the other limit, when $J = 0$ and $I_c \neq 0$ the model in Eq. 6.10 reduces to two ferromagnetic couplings, which produces a large ferromagnetic phase which survives up to finite J (black dots in Fig. 68). The case $I_c = 0$ and $J = 0$ is special, as this point reduces to the Kitaev model, which is a macroscopically degenerate state without LRO. For finite J and I_c we find an incommensurate spiral phase (green squares in Fig. 68) which we will study in detail in the next section. It is worth noting that Kimchi *et.al* report the existence of a small area where the st-X and st-Y phases should be present, and they locate it at the intersection of the spiral and st-Z phase.

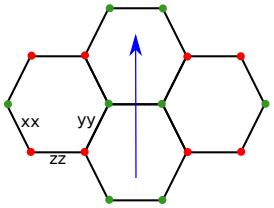

Figure 69: Sketch of the stripy order in the z-direction. Red (green) dots represent spins oriented in the $+z$ ($-z$) direction. The blue arrow indicates the propagation direction of the stripe, and the kitaev coupling on each bond is indicated.

6.4.1.2 Spiral properties

The incommensurate order present in the phase diagram (green squares in Fig. 68) exhibits signatures of incommensurate counterotating spirals. This spiral phase propagates in the horizontal direction according to Fig. 66 (the direction perpendicular to the zz-bonds), with a wavevector that varies from 0.5 to 0.30 in units of 2π. The phase of rotation tilted with respect to the lattice plane remains constant throughout the phase diagram at $\theta = 54^o$, i.e, the rotation plane is oriented parallel to the XY-Cartesian plane. This phase mostly reproduces the experimental structure determined from neutron

diffraction except for the tilt of the rotation plane (we find a tilt of 54^o and the expected value for the tilt angle is 80^o). For this reason we will postpone further discussions regarding this phase until the next section, where we analyze in detail the I_cI_d-model, which reproduces the experimental results fully, and is derived from the present model.

6.4.2 Heisenberg-Kitaev-I_c-I_d model (I_cI_d model)

6.4.2.1 Phase diagram

We study the model described in Eq. 6.3 setting fixed values for the Heisenberg and Kitaev interactions $J/|K| = 0.2$, $K/|K| = -1$, which we know from the previous section show the presence of a stripy and an incommensurate phase at finite I_c. To analyze the effect of bond dependent interactions we allow the couplings I_c and I_d to move in the range $\{-1,...0\}$. Studying both the real space configuration of the spins, as well as the correlation function in reciprocal space we are able to map the phase diagram for finite I_c and I_d. We show this phase diagram in Fig. 610. We observe a rich behavior, with different commensurate-incommensurate transitions. The experimentally relevant phase corresponds to the green squares.

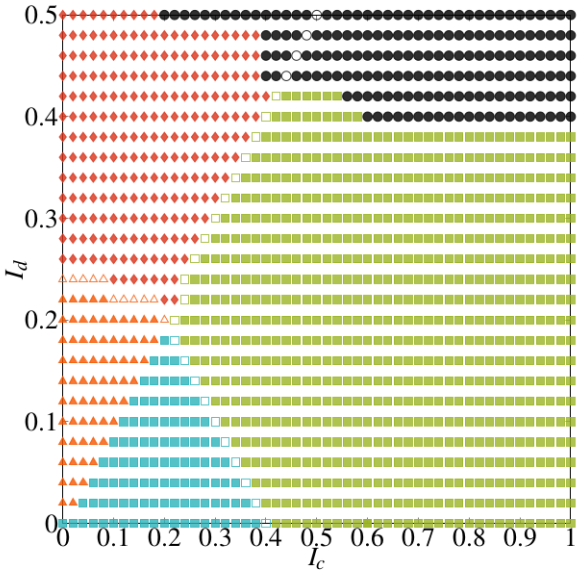

Figure 610: Phase diagram for the I_cI_d-model. Blue squares represent the st-Z order, orange triangles are st-XY, red diamonds the 120^o, green squares the spiral, and black dots correspond to ferromagnetic order. The open marks show the zone boundaries between the st-XY, st-Z, 120^o, and incommensurate phases. The line of open circles in the ferromagnetic phase indicates the line along which a U(1)-like behavior appears.

The regime $I_d = 0$ was shown in the previous section, and it corresponds to a cut along the line $J = 0.2$ in Fig. 68. All our results in this limit are consistent with what we have found for the I_c model. In the $I_c = 0$ regime: for moderate values of I_d ($I_d > -0.25$) we observe a degenerate stripy phase, that we denote st-XY (orange triangles), while for smaller I_d we obtain a 120^o order (red diamonds). This latter state was previously studied via a soft spin approximation, and identified as an incommensurate

spin spiral propagating in the vertical direction of Fig. 66.

While the Fourier transform of the correlation function present maxima close to the first Brillouin zone, Fig. 611(top), which would indicate a spiral-like state that is approaching the 120^o order, the spin pattern in the real space shows that the state is that of a distorted 120^o.

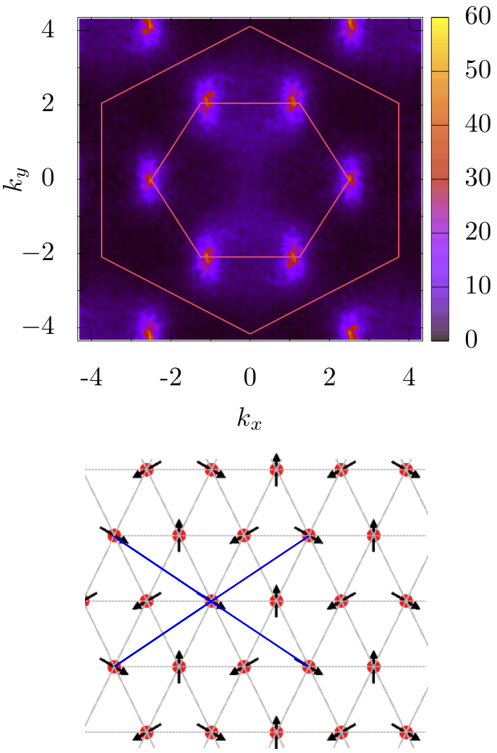

Figure 611: *Top*: Fourier transform of the correlation function for the order present in the $I_c = 0$ regime, for $I_d = 0.5$. The maxima are located close to the corners of the first Brillouin zone. *Bottom*: 120^o order in the triangular lattice. Blue lines indicate the neighbors which lie parallel to each other.

The distortion can be understood if we think of the origin of the 120^o order in the honeycomb lattice. This state can be constructed with a pure second neighbor Heisenberg Hamiltonian, in this case both triangular sublattices decouple, and each presents a 120^o states. A depiction of the spin pattern of this state in the triangular lattice is shown in Fig. 611(bottom). In this case, we see that second neighbors in the underlying triangular lattice are parallel to each other. In our model we see that, for high enough $|I_d|$, the distortion present in the 120^o order can be understood as long wavelength spin spirals propagating over the second neighbors. In the language of spin spirals, the 120^0 state can be seen as a spin spiral state with wavevector 0.33 in units of 2π, the distortion here appears as a small deviation from this wavevector, on the order of 10%. This deviation can be observed in the Fourier transform of the pseudo-120^0 state present in our model (Fig. 611(top)). While in the 120^o state the maxima lie on the corners of the first Brillouin zone, here they appear slightly away from them. For smaller $|I_d|$ and non zero $|I_c|$ the distortion becomes more pronounced, with the wavevector deviating more from 0.33. We expect that in the limit $I_d \to \infty$ we recover the exact 120^o order.

The stripy phase in the $I_c = 0$ regime arise as a superposition of st-X and st-Y phases. We will call it, st-XY phase, according to the literature. The appearance of this

superposition can be understood remembering that previously we have mentioned that the Heisenberg-Kitaev model stabilizes a triple degenerated stripy phase (see appendix B and [126]), each of which we denote as st-X, st-Y, and st-Z respectively. As we have also seen in the case of the I_c model, the inclusion of a small bond dependent interaction strengthening one particular bond, breaks the degeneracy of the stripy phase. In the case of the I_c model (where the I_c terms strengthen the ferromagnetic ordering over the zz-bonds) we saw that, as expected, the stripy phase selected is that which has spins over the zz-bond coupled ferromagnetically. Is then easy to understand why, in the case where $I_c = 0$ and $I_d \neq 0$, the selection happens in the x- and y-bond, as the I_d terms strengthen the ferromagnetic interaction equally in them.

When both I_c and I_d are non-zero, we see a clear separation of phases through the line $I_c = I_d$. For the stripy phases this is again intuitive, as we expect a different selection of stripes based on which coupling is dominant. It is expected, and indeed observed, that throughout this line, and where the stripy phases are located, there is a superposition of st-X, st-Y, and st-Z states.

Beyond the line $I_c = I_d$ a counterrotating spiral state dominates the phase diagram. This phase reproduces well the experimental results for $\alpha - Li_2IrO_3$ and will be studied in detail in the next section.

Finally, we note that, at high enough values of $|I_c|$ and $|I_d|$ the model adopts an in plane ferromagnetic order. This order lives on both sides of the $I_c = I_d$ line, presenting a ferromagnetic order with a net magnetization in the direction of the zz-bonds when $|I_c| > |I_d|$, and perpendicular to it in the $|I_c| < |I_d|$ case.

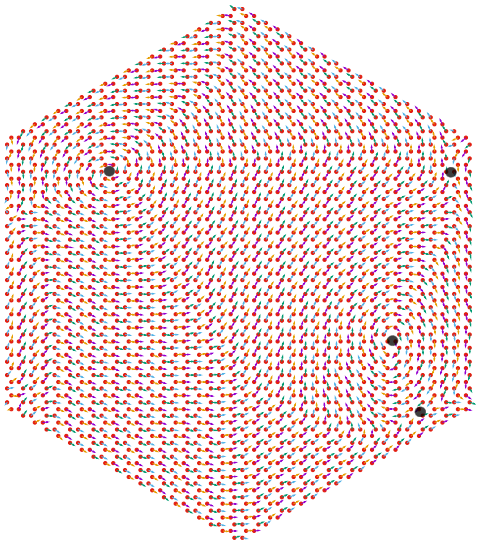

Figure 612: Ferromagnetic order for the model shown in Eq. 6.11 with parameters $I_c = 0.5$ and $I_d = 0.5$.

Understanding the behavior of the ferromagnetic phase will be crucial to understand the magnetization plots given that the experimentally representative point is close to this phase. In Fig. 610 we observe a ferromagnetic phase (full black dots) which is separated in two by the line $I_c = I_d$ (line with open black dots). On the left side of this line ($I_d > I_c$) we encounter ferromagnetic polarization on the direction perpendicular to

the zz-bonds. On the other side ($I_c > I_d$) the magnetic vector is also in plane but parallel to the zz-bonds. Both cases posses the same type of low energy fluctuations, these being domain walls separating different orientations of the magnetic polarization. The line in the phase diagram separating both polarization is of special interest given that the low energy fluctuations of the system are of a different nature. All over the line $I_c = I_d$ the low energy fluctuations are vortex-antivortex pairs, where antivortices are extended over a number of unit cells. An example of a spin pattern presenting this behavior is shown, for a calculation over 2400 sites, in Fig. 612.

These vortex fluctuations where studied in systems ranging from 24 to 5400 lattice sites, and they consistently appear in all the studied system sizes over this particular line in the phase diagram, which rules out this behavior as a finite size effect. This low energy behavior reminds us (though it is not necessarily the same physics) of the behavior of XY-models when $I_c = I_d$ and $I_c \geq 0.46$.

This behavior can be understood following a symmetry argument. The I_c (I_d) term posses a rotational invariance along the Z Cartesian axis (XY plane). When $I_c = I_d$, there is no preferred symmetry axis or plane, instead the preferred orientation is the lattice plane, and, as both these off-diagonal terms are of the same strength, there is no preferred bond direction, which implies that an on-plane XY-like behavior could emerge.

6.4.2.2 Spiral properties

A big part of the phase diagram on Fig. 610 is dominated by an incommensurate phase (green squares). This state represents an incommensurate counter-rotating spiral which propagates in the horizontal direction according to Fig. 66 (the direction perpendicular to the zz-bonds). In the regime $I_d = 0$ the wavevector varies between 0.5 and 0.4 (in units of 2π) and the plane of rotation is tilted with respect to the lattice plane by 54^o, i.e, the rotation plane is oriented parallel to the XY-Cartesian plane. This coincides with what it is found for the I_c model when a cut on the phase diagram over the line $J = 0.2$ is performed.

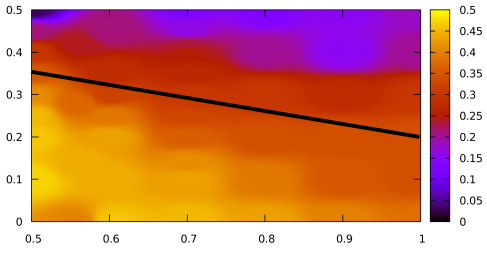

Figure 614: Heat map of the wavevector for the regime $I_c/K > 0.5$. The black like represents the line of wavevector $q = 0.32$, in units of 2π.

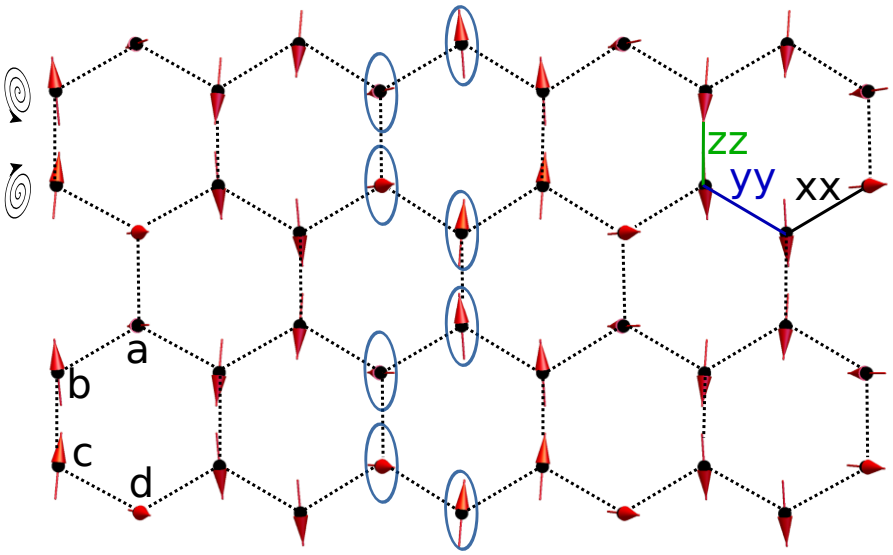

Figure 613: Spiral structure obtained from Monte Carlo simulations for the couplings $I_c = -0.5$ and $I_d = -0.35$. The wavevector and tilt angle coincide with the experimental results $q = 0.31(1)$ and $\theta \sim 80^o$. The circular drawings on the upper right indicate the rotation direction of two neighboring spirals. Blue circles show the plane of rotation, with the plane tilt. By a, b, c, and d we mean to label the four spirals that appear in one single slab of hexagons, with spins of each sublattice forming one spiral along the slab. Finally, and for the sake of completeness we indicate the bonds that correspond to the Kitaev interaction as defined in the model.

In the regime where both $I_c \neq 0$ and $I_d \neq 0$ the commensurate phases mentioned previously survives for values of I_d down to -0.4 and for values of I_c such that $|I_c| > |I_d| - 0.4$ for $|I_d| < 0.2$, and $|I_c| > |I_d|$ for $0.2 < |I_d| < 0.4$. We show in Fig. 613 a real space pattern of the spin spiral, at a point in the phase diagram which reproduces the experimental results. In this regime some properties of the spiral phase are modified. As I_c and I_d are varied the wavevector changes, but in this case it changes between 0.5 and 0 (wavevector 0 correspond to the onset of ferromagnetic order). The rotation plane's tilt now also varies along the phase diagram, between $\sim 50^o$ (consistent with the spin spiral known to appear at $I_d = 0$) and $\sim 90^o$.

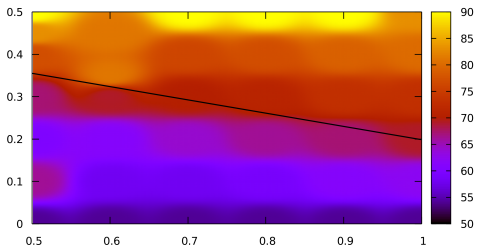

Figure 615: Heat map of the rotation plane's tilt for the SP phase in the regime $I_c/K > 0.5$. The black like represents the experimental value obtained for the wavevector, $q = 0.32$ in units of 2π.

In Fig.614 and 615 we show two heat maps, one for the wavevector and another for the tilt angle of the rotation plane, respectively. We can clearly see the variation of these quantities in the phase diagram. In the heat map corresponding to the wavevector (Fig. 614) we indicate with a black line the zone of wavevector $q = 0.32$ (in units of 2π) and superimpose this line over the tilt angle heat map (Fig. 615). Please note that this mark is a guide to the eye, it does not arise from a fit to the data.

Further confirming the existence of counterrotating spin spirals reproducing the experimental results, we show the Fourier transform of the correlation function in Fig. 616. This figure was calculated for the parameters $I_c = -0.5$ and $I_d = -0.35$, which reproduce the wavevector and rotation plane tilt found in experiments. The correlation function presents maxima at the experimentally expected positions. They appear as satellites of the Γ point, with positions $\tau + \mathbf{q}$, where τ indicates the location of the Γ points and $\mathbf{q} = (\pm 0.32(1), 0)$ in units of 2π, which coincide with the experimental results discusses in section 6.2, and in particular, with the findings shown in Fig. 65.

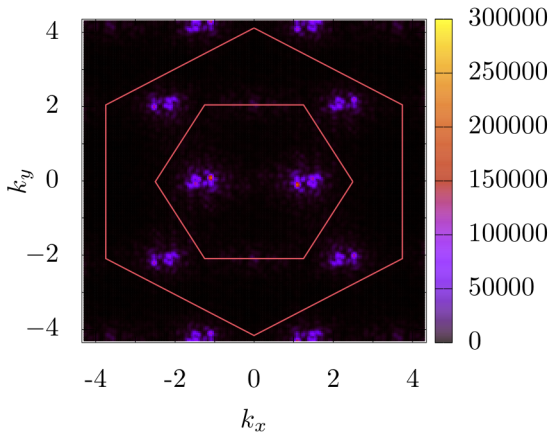

Figure 616: Correlation function for the incommensurate spin spiral state at $I_c = -0.5$ and $I_d = -0.35$. We observe maxima as satellite points of the Γ point, and secondary maxima as satellites of the K points.

6.5 Second neighbor models

6.5.1 Next Nearest Neighbors Heisenberg-Kitaev model ($2N$-model)

We proceed now to study the $2N$ model, which consists of first and second Heisenberg and Kitaev interactions. We show in Fig. 617 the exchange couplings in the honeycomb lattice for this model. The Hamiltonian corresponding to the $2N$ model is given by Eq. 6.11.

$$\mathscr{H} = J_1 \sum_{<ij>} \mathbf{S}_i \cdot \mathbf{S}_j + K_1 \sum_{<ij>} \sum_{\gamma} S_i^{\gamma} S_j^{\gamma} + J_2 \sum_{<<ij>>} \mathbf{S}_i \cdot \mathbf{S}_j + K_2 \sum_{<<ij>>} \sum_{\gamma} S_i^{\gamma} S_j^{\gamma} \tag{6.11}$$

This model was previously studied in the context of the Li_2IrO_3 family via PFFRG [127]. In their paper, Reuther *et. al* parametrize the different couplings via two angles, P_1 and P_2, as $J_1 = \cos(\pi P_1/2)$, $K_1 = -\sin(\pi P_1/2)$, $J_2 = -g\cos(\pi P_2/2)$, $K_2 = g\sin(\pi P_2/2)$, and map the phase diagram of 6.11 for $P_1 \in (0,1)$ and $P_2 \in (0,1)$.

They find two incommensurate spiral phases for $P_2 \gtrsim 0.5$, the spirals SP1 and SP2, while for values below 0.5 they find a ferro and antiferromagnet. Studying the maximum of the susceptibility they find that the state SP1 corresponds to maxima outside of the first Brillouin zone, while the SP2 has maxima inside the first zone. We will employ Monte Carlo simulations to study the classical equivalent of this model, and we will restrict ourselves to the value $g = 0.8$, as according to the evidence in Ref.[127] the phase diagram does not change drastically for different values of g.

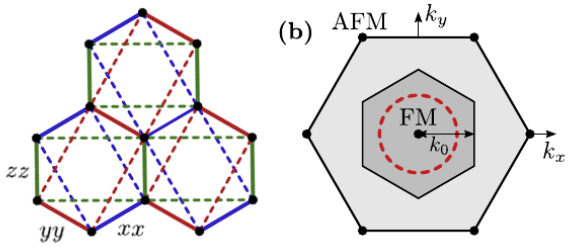

Figure 617: (a) Color coded honeycomb lattice showing the Kitaev exchanges $S_i^x S_j^x$ (blue), $S_i^y S_j^y$ (red), and $S_i^z S_j^z$ (green) for nearest (full lines) and second (dotted lines) neighbor interactions.

6.5.1.1 Phase diagram

The phase diagram for model $2N$ is shown in Fig. 618. Please note that since the aim of this study is to identify the nature of the spiral phases, we have not gone to great lengths mapping the boundary in between the phases in this model. While it is expected that the boundaries between the quantum and classical phase diagram will shift, we have previously seen cases in this thesis where the quantum to classical limit affects the

position of the boundaries but not the nature of the phases when LRO is expected. For this reason, we leave the study of the precise boundaries for future work, as we don't anticipate fundamental differences between those of the quantum and classical phase diagram. In the phase diagram shown in Fig. 618 the phase boundaries will be located somewhere over the white spaces.

The phase diagram presents two commensurate and two incommensurate phases. Pink dots represent antiferromagnetic order, black ones indicate the onset of ferromagnetic order. We indicate by red diamonds the incommensurate spiral phase SP1, and by green squares the phase SP2. We will study these phases in detail in the next section.

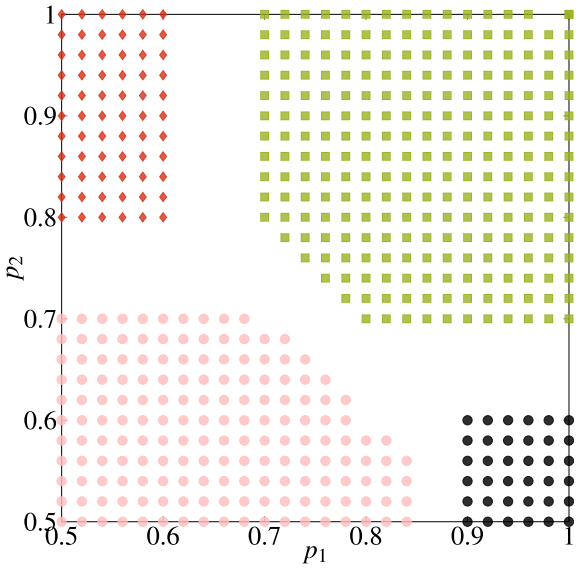

Figure 618: Phase diagram for the $2N$-model. Pink dots represent antiferromagnetic order, black dots correspond to ferromagnetic order, red diamonds to a spiral phase SP1, and green squares to another spiral phase SP2.

The ferro and antiferromagnetic phases exhibit clear features in the correlation function which confirms their nature. However, when we study the real space pattern of the spins we find that these phases come together with domain walls as well as with vortex-like defects. As our numerical calculations have been performed at low temperature, and the iterative minimization algorithm probes ground state properties, we are lead to believe that this vortices are ground state properties of the Hamiltonian. In Fig. 619 *left* we show a magnification of the real space spin pattern of the ferromagnetic state for $P_1 = 1$ and $P_2 = 0.6$. We show the zone in which a vortex like structure is present viewed directly from above the lattice plane. While in Fig. 619 *right* we show the associated Fourier transform of the correlation function for this state, calculated with the same spin pattern that is shown in the left side. The maxima resides at the Γ point, as it is expected for a ferromagnet. Furthermore, secondary maxima are present in the corners of the extended Brillouin zone.

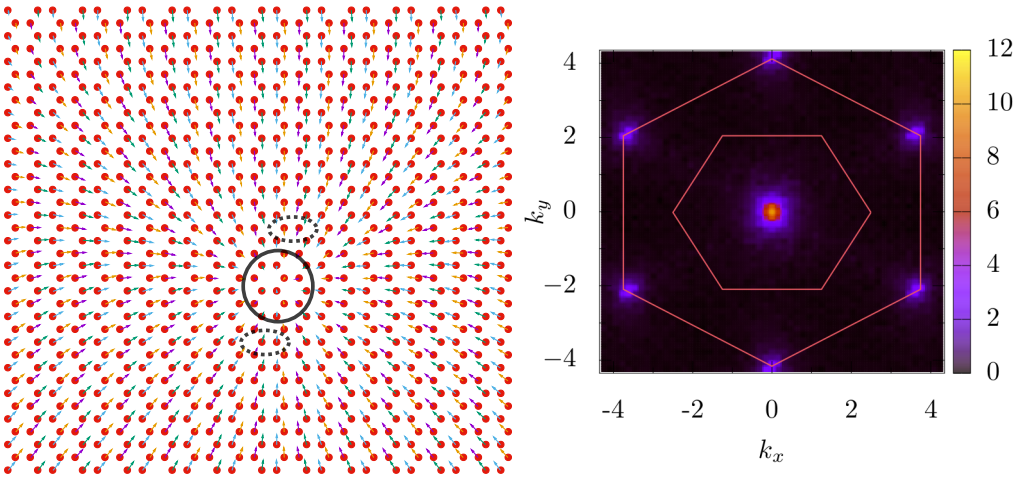

Figure 619: *Left*: real space spin pattern for the ferromagnetic state at $P_1 = 1$ and $P_2 = 0.6$ showing a vortex-like defect in the center. The filled circle indicates the center of the defect. *Right*: Fourier transform of the correlation function for the same ferromagnetic state.

6.5.1.2 Spiral properties

The two incommensurate spin spiral phases we find correspond to the red diamonds in Fig. 618 (SP1), and to the green squares (SP2). Upon examination of the correlation function (Fig. 620) we see that the SP1 phase present maxima outside of the first Brillouin zone, while the maxima corresponding to the SP2 phase are contained within the first Brillouin zone.

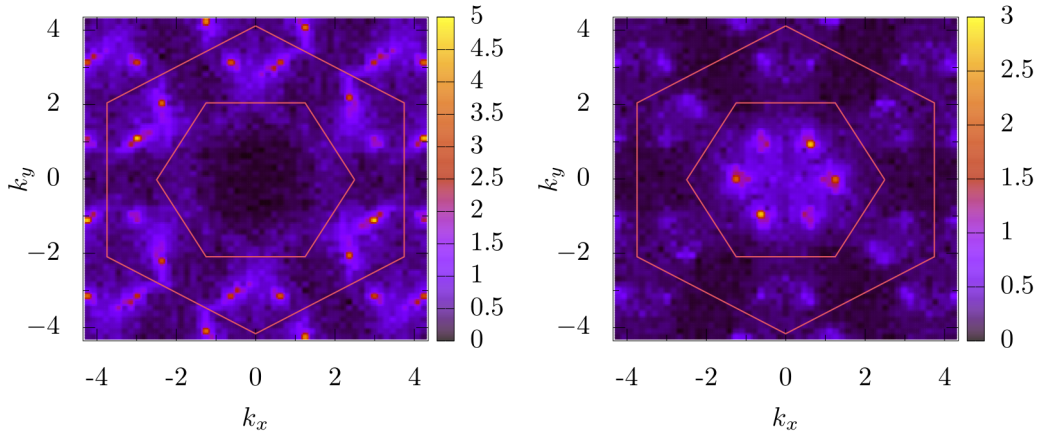

Figure 620: Fourier transform of the correlation function for the $2N$-model shown in Eq. 6.11 with parameters $P_1 = 0.6$ and $P_2 = 0.8$ (SP1 phase, *left*) and $P_1 = 1$ and $P_2 = 0.7$ (SP2 phase, *right*).

The structure factor for the SP2 phase resembles that of $\alpha - Li_2IrO_3$, with satellites

around the Γ point and very faint secondary maxima around the K points. However, unlike the expected signal for the Iridate material, an degeneracy is present, in which the maxima appear in the three symmetry related positions, which would indicate that the spin spirals propagate in the three directions allowed by the Kitaev symmetry. On the other hand, the spiral phase SP1 presents only maxima as satellite peaks around the K points.

Upon a closer inspection of the real space spin pattern we see that for both the SP1 and SP2 phases, the actual spiral present in this model does not coincide with that of $\alpha-Li_2IrO_3$. In the experimental case one observes co-planar spirals, where the plane of rotation can be defined by $(\mathbf{S}_1\times\mathbf{S}_2)\cdot\mathbf{S}_3$, where S_x (with $x=\{1,2,3\}$) are consecutive spins on a single spiral (this type of spiral was observed in both nearest neighbor models). However, the $2N$-model exhibits a non-coplanar helimagnet, where a plane of rotation cannot be defined. This is not strange, as there are different types of spin spirals, all belonging to the family of helimagnets [128], and indeed some of these are non-coplanar. For example, a non-coplanar case are conic spin spirals which rotate not in plane, but in a cone, and are relevant to the study of multiferroic behavior [129, 130].

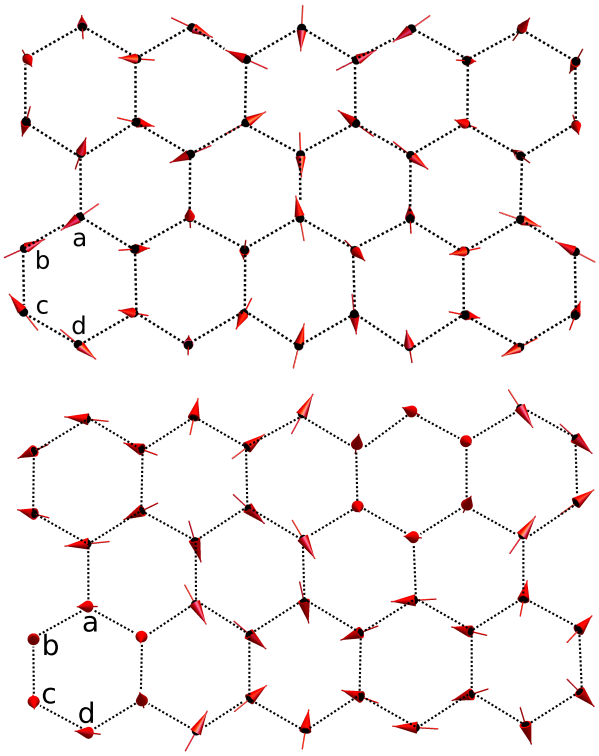

Figure 621: Spiral structure obtained for the model shown in Eq. 6.11 within the phase SP1, i.e. parameters $P_1=0.6$ and $P_2=0.8$. (*top*) and within phase SP2, $P_1=1$ and $P_2=0.t$. (*bottom*).

While both spirals are non-coplanar, we can further distinguish them by studying their nearest neighbor correlations. Calculating the correlation function up to nearest neighbors, and Fourier transforming it, we obtain Fig. 622. From here we see that the main distinguishing feature between both non-coplanar spirals resides in the nature of the nearest neighbor correlations. While the maxima are broadened, we see that for phase SP1 we find maxima in the corners of the extended Brillouin, which indicates antiferromagnetic nearest neighbor correlations. On the other hand, SP2 has a maximum

in the Γ point, which coincides with ferromagnetic correlations.

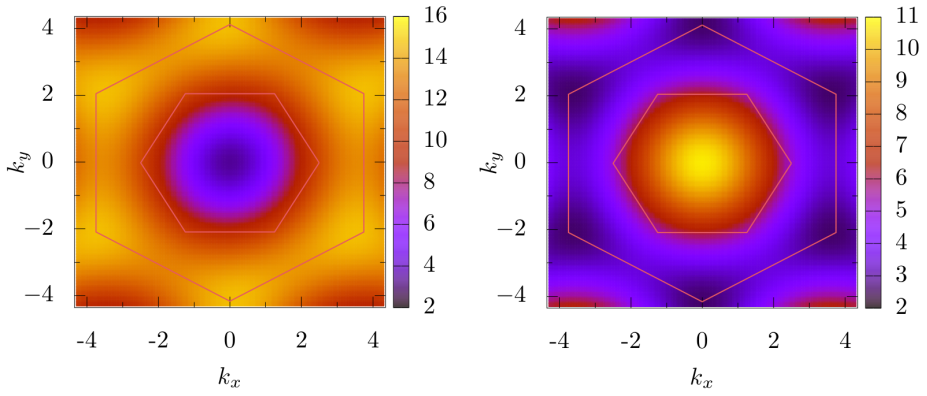

Figure 622: Fourier transform of the nearest neighbor correlation function for the $2N$-model shown in Eq. 6.11 with parameters $P_1 = 0.6$ and $P_2 = 0.8$ (SP1 phase, *left*) and $P_1 = 1$ and $P_2 = 0.7$ (SP2 phase, *right*).

6.5.2 $2NI_c$ model

Since $\alpha - Li_2IrO_3$ presents bond dependent interactions, a question that arises after studying the $2N$ model is what the effect of other symmetry allowed interactions are in this model. It is not absurd to think that an I_c-like term could break the degeneracy and perhaps induce a coplanar spiral. For this purpose we will now study a modification of the $2N$ model, where we introduce an I_c term of the same form as used in the I_c- and I_cI_d-models. The Hamiltonian results.

(6.12)
$$\mathscr{H} = J_1 \sum_{<ij>} \mathbf{S}_i \cdot \mathbf{S}_j + K_1 \sum_{<ij>} \sum_{\gamma} S_i^{\gamma} S_j^{\gamma} + J_2 \sum_{<<ij>>} \mathbf{S}_i \cdot \mathbf{S}_j + K_2 \sum_{<<ij>>} \sum_{\gamma} S_i^{\gamma} S_j^{\gamma} + I_c \sum_{<ij>} S_i^{r_{ij}} S_j^{r_{ij}}$$

As before we parametrize the different couplings via two angles, P_1 and P_2, as $J_1 = \cos(\pi P_1/2)$, $K_1 = -\sin(\pi P_1/2)$, $J_2 = -g\cos(\pi P_2/2)$, $K_2 = g\sin(\pi P_2/2)$, and set $g = 0.8$. The coupling I_c will take values in the range $\{-1, -0.9, ..., 0\}$. We run Monte Carlo simulations for the pairs $\{P_1 = 0.5, P_2 = 0.5\}$, $\{P_1 = 0.5, P_2 = 1\}$, $\{P_1 = 1, P_2 = 0.5\}$, $\{P_1 = 1, P_2 = 1\}$, and $\{P_1 = 0.9, P_2 = 0.9\}$ as a way to probe the effect of the I_c term at different points in the phase diagram.

6.5.2.1 $p_1 = 0.5$, $p_2 = 0.5$

For the limit $I_c = 0$ an antiferromagnetic state is realized, as shown in Fig. 618. This state is degenerate, with spins able to point in different symmetry allowed directions. For $I_c > -0.5$ the state remains an antiferromagnet, but now the degeneracy disappears and the ground state selects the state with spins pointing in plane and perpendicular to the zz-bonds, as shown in Fig. 623. For $I_c < -0.5$ the state changes slightly, maintaining its antiferromagnetic nature, but with the staggered magnetization in a direction perpendicular to the lattice plane.

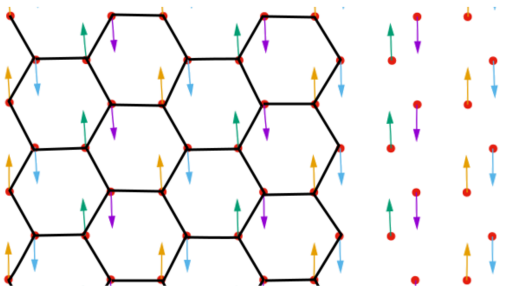

Figure 623: Stripy phase in the $2NI_c$-model, for $I_c = 1$.

This selection of states from a degenerate set is not surprising since the effect of the I_c term is that of destroying the discrete symmetry arising from the Kitaev interactions (please remember that this symmetry is such that, without the I_c term, the Hamiltonian remains invariant on a 60^o rotation on spin and real space).

6.5.2.2 $p_1 = 1$, $p_2 = 0.5$

For these set of parameters, a ferromagnetic state is realized, where vortex-like defects appear. When the value of I_c is non zero, the vortex defects disappear, and we find a ferromagnetic state with a net magnetization in the direction of the zz-bonds. This configuration is reached for the smallest values of I_c studied and remains unchanged through the whole range. Here, two possible orientations of the net magnetization are possible, and they appear through the simulation separated by extended domain walls expanding through the system.

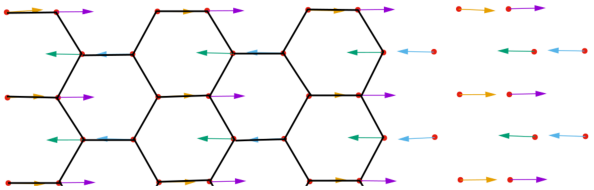

Figure 624: Stripy phase in the $2NI_c$-model, for $I_c = 1$. The spins are colored according to the conventions in Fig. 623.

6.5.2.3 $p_1 = 0.5$, $p_2 = 1$

In the case of the $2N$ model, i.e, the case for $I_c = 0$ realized a helimagnetic state, which was studied in detail in the previous section. The inclusion of a finite $I_c > -0.2$ breaks the degeneracy of the spin spiral states, and spirals only propagate in the direction

perpendicular to the zz-bonds. The nature of the spin spiral also changes with respect to the case $I_c = 0$, the spirals are still non-coplanar, but the nearest neighbor correlations are not purely antiferromagnetic, as the I_c term introduces a ferromagnetic binding in the zz- bonds. For $I_c < -0.2$ domains of stripy order appear, growing in size and overpowering the phase diagram as I_c decreases. For $I_c = -0.3$ the stripy phase already dominates the phase diagram, with domain walls separating different orientations of the spins. In this stripy phase, the spins are in plane, aligned in the direction of the zz-bonds. We show in Fig. 624 the resulting stripy phase for the case $I_c = 1$.

6.5.2.4 $p_1 = 1$, $p_2 = 1$, and $p_1 = 0.9$, $p_2 = 0.9$

For the limit $I_c = 0$ we observed a spin spiral state which we analyzed in the previous section. When $I_c > 0$ the non-coplanar nature of the spin spiral disappears, the anisotropy along the zz-bonds introduced by the ferromagnetic I_c term enforces a ferromagnetic in plane alignment of the spins in this bond, which transforms the spin spiral into an antiferromagnetic state. As I_c decreases the state remain unchanged.

6.6 Third neighbor model

Until now we have been studying models that were devised with symmetric considerations in mind. The atomic structure of $\alpha - Li_2IrO_3$ induces bond dependent interactions, of which Kitaev exchange is the dominant one. Furthermore the symmetry of the material allows for longer range interactions and other bond dependent exchanges beyond Kitaev exchange. In the following we will study a model which was obtained via DFT calculations performed by Winter, *et al* [1]. In their work, they propose a model with Heisenberg, Kitaev, and other bond dependent interactions, some of them ranging up to third neighbors. The effective Hamiltonian obtained results in

$$\begin{aligned}\mathscr{H} =& J_1 \sum_{<ij>_1} \mathbf{S}_i \cdot \mathbf{S}_j + K_1 \sum_{<ij>_1} S_i^\gamma S_j^\gamma + \Gamma_1 \sum_{<ij>_1} (S_i^\alpha S_j^\beta + S_i^\beta S_j^\alpha) \\ &+ K_2 \sum_{<ij>_2} S_i^\gamma S_j^\gamma + \Gamma_2 \sum_{<ij>_2} (S_i^\alpha S_j^\beta + S_i^\beta S_j^\alpha) + J_3 \sum_{<ij>_3} \mathbf{S}_i \cdot \mathbf{S}_j \end{aligned} \tag{6.13}$$

Where X_n, with $X = J, K$, or Γ, represent the exchange coupling for an interaction between nth-neighbors, $\sum_{<ij>_n}$ represents a sum over nth-neighbors, and $\{\alpha, \beta, \gamma\} = \{x, y, z\}$ indicate the spin component.

Ref. [1] report strong bond anisotropies in the model, an observation which coincides with previous proposals for this material [122]. To gain an intuitive understanding of such a complex Hamiltonian we will proceed to study the isotropic case, in which the exchange couplings for each interaction are the same for each bond. Afterwards we will introduce bond anisotropies based on Ref. [1].

6.6.1 Isotropic W-model

6.6.1.1 Phase diagram

We will start by mapping part of the phase diagram of the isotropic case for the model shown in Eq. 6.13. In their work they show that this model has the peculiarity of the Kitaev and Γ exchanges to be equal in magnitude and opposite in sign, i.e $K_i = -\Gamma_i$. The isotropic case was already studied by Winter and collaborators employing the LT method. For this reason we can constrain ourselves to the parts of the phase diagram which indicate in the soft spin approximation to contain incommensurate phases. We will employ a dominant Kitaev coupling $K = -1$ supported by (here and in the following, all exchange couplings are given in units of $|K_1|$) $K_2 = -0.275$, $\Gamma_1 = 1$, $\Gamma_2 = 0.275$, $J_1 \in (-0.1, ..., 0.4)$, and $J_3 \in (0, ..., 0.4)$.

The phase diagram is shown in Fig. 625. We observe three commensurate phases, and an incommensurate one. In the limit $J_3 = 0$ we observe a transition from a ferromagnetic to a stripy phase at $J_1 \sim 0.15$. Since our model contains two dominant interactions, K_1 and Γ_1, it is not surprising to observe that many of the states that appear in the phase diagram are on the lattice plane. For example, the ferromagnetic state is one in which spins are ordered in the lattice plane. The presence of off diagonal bond dependent terms in the Hamiltonian can induce the appearance of vortex-like defects when the ground state (as we have seen in the previous sections) is collinear. In this case the

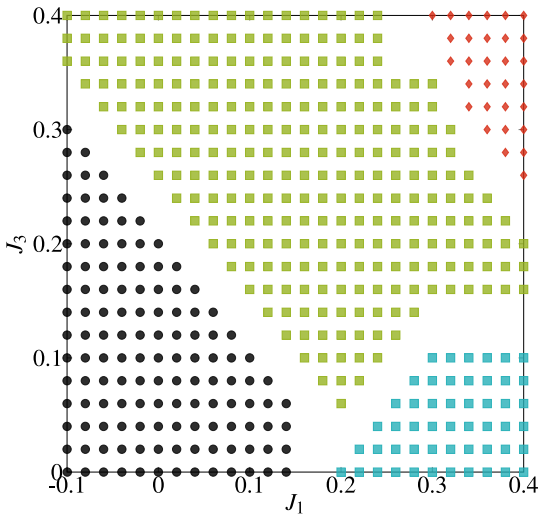

Figure 625: Phase diagram for the isotropic case of the Hamiltonian shown in Eq. 6.13. Black dots correspond to ferromagnetic order, light blue squares to stripy order. The incommensurate states are represented by green squares, and the Neel state by red diamonds.

ferromagnetic state presents vortex-like
defects which increase in number as we
increase the interaction strength. For example, we show in Fig. 626 two spin patterns obtained at $J_3 = 0.1$, $J_1 = 0.1$ and $J_1 = 0.15$. We notice that as J_1 is increased the number of defects increases.

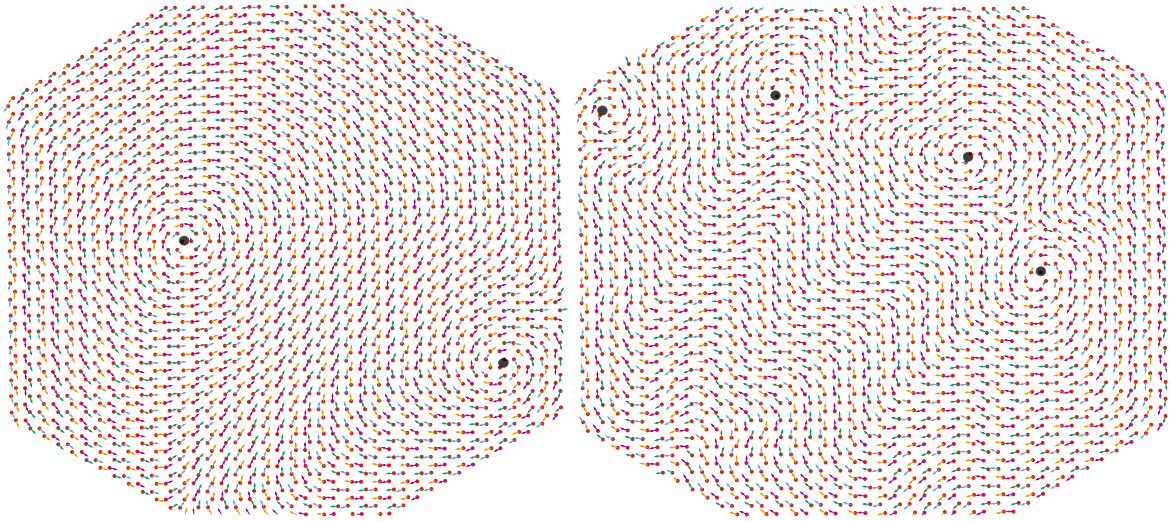

Figure 626: Ferromagnetic spin patterns for the ferromagnetic state of the isotropic W-model obtained at $J_3 = 0.1$, $J_1 = 0.1$ (left) and $J_1 = 0.15$ (right).

At a critical value of J_1 (which depends on the value of $J_3 \gtrsim 0.05$) the defects dominate the ground state and the system enters into a spiral phase (green squares in Fig. 625. If J_1 is further increased the system can enter a stripy phase ($J_3 \lesssim 0.1$), an antiferromagnetic phase ($J_3 \gtrsim 0.25$), or remains in the spiral phase. Both antiferromagnetic and stripy phases have spins oriented perpendicular to the lattice plane. This means that the stripy phase is a st-Z phase. Both phases are two fold degenerated, and this is seen in the spin pattern as domains separating these degenerate states. We have confirmed the existence of these phases via a LT minimization, which also confirms the results of Ref. [1].

6.6.1.2 Spiral properties

The incommensurate order present in this model exhibits the signatures of a coplanar counterrotating spin spiral. The fundamental difference between these spirals and the ones appearing in α-Li_2IrO_3 is that in this case, the spirals are degenerate. Since the model is bond isotropic, the spin spirals can propagate in three symmetry allowed directions, i.e. The propagation direction can be perpendicular to the x-, y- or z bonds. This means that our state will contain domain walls separating spin spirals propagating in one of the three allowed directions. This can be seen in Fig. 627 where we show the Fourier transform of the correlation function. Here we see that indeed, we obtain maxima inside the first Brillouin zone, and that these are three fold degenerated. The study of the wavevector and nature of the spirals confirm that these spirals are the same ones we obtain with the I_cI_d-model, except for the fact that there is a degeneracy in the state.

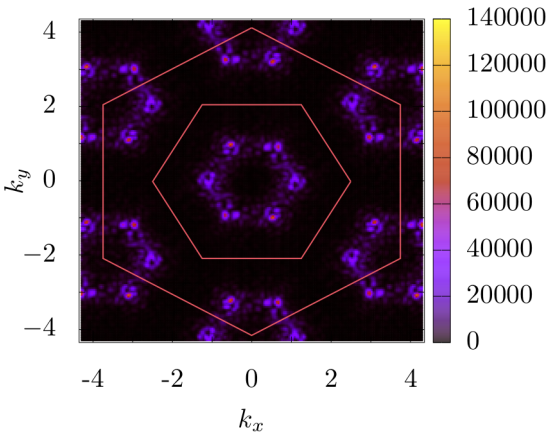

Figure 627: Correlation function for the spiral phase found in the isotropic W-model. We observe a degenerate set of maxima inside the first Brillouin zone

The material we are interested does not seem to show any type of degeneracy of the ground state in the powder MRXD measurements, which point to the fact that, since Winter *et. al.* [1] have found strong bond anisotropies in their work, these anisotropies need to be included in the model to break the degeneracy. In the following we will include these anisotropies and study what their effect is on the phase diagram and the spiral properties of the system.

6.6.2 Anisotropic W-model

To study the anisotropic W-model we first need to determine what there anisotropies are. In their work, Winter *et. al.* [1] determined (via a combination of DFT and exact diagonalization on a small cluster of hexagons) that the model presents large anisotropies in various parameters. The values of the exchange parameters are shown in table 63.

Studying this table it becomes clear that an analysis considering that the model is

Bond	J_n	K_n	Γ_n
X_1, Y_1	$\mathbf{-1.0}$	$\mathbf{-13.0}$	$\mathbf{+6.6}$
Z_1	$\mathbf{-4.6}$	$\mathbf{-4.2}$	$\mathbf{+11.6}$
X_2, Y_2	$+0.9$	$\mathbf{-2.9}$	$\mathbf{+3.0}$
Z_2	-0.9	$+0.1$	$\mathbf{+1.5}$
X_3, Y_3	$\mathbf{+4.7}$	-0.2	0
Z_3	$\mathbf{+4.4}$	$+0.4$	-0.1

Table 63: Values of the anisotropic interactions as obtained in Ref. [1]. All interactions are given in meV. For the study of the anisotropic model we have selected those interactions which are greater than one (bold).

bond isotropic is an excessive simplification, if we aim at modeling the material, there anisotropies need to be taken into account. We will introduce them in our model (where we will also only consider those who are greater than one) in the following way: we will first express every coupling in terms of $|K_1|$. Next, for a given coupling α (which now is expressed in units of $|K_1|$) we have an anisotropy which differentiates the X and Y bond (α_{XY}) from the Z bond (α_Z).

We will define α_m as the bond average of the exchange coupling α, and δ as the anisotropy constant (with an appropriate sign) such that (for a direct comparison please look at Eqs. 6.5)

$$\alpha_{XY} = \alpha_m - \delta \quad \alpha_Z = \alpha_m + \delta \tag{6.14}$$

This way, calculating the bond average from Table 63 we can determine what the anisotropy for each exchange is. The values obtained for the anisotropy constants are given in Table. 64

	δ_W
J_1	0.14
K_1	0.34
Γ_1	0.195
K_2	0
Γ_2	-0.06
J_3	0

Table 64: Values of the anisotropy constants for the W-model, extracted from Ref. [1] following the process described in the text. All values are given in terms of $|K_1|$.

If we were to study the bond isotropic model in Table. 63, we would obtain a a zig-zag type of order. In the phase diagram shown in the previous section, no zig-zag order is present, as we have concentrated in mapping a part of the phase diagram which exhibits incommensurate spirals. If we were to map the full phase diagram we would see (and we have confirmed this via numerical simulations) that for $J_3 \gtrsim 0.4$ a zig zag phase is present. In the bond anisotropic case, where the interaction couplings reduce to those shown in Table. 63, we again obtain a zig zag state. By changing the

bond averages but maintaining the anisotropic parameters δ constant, we can map a phase diagram including anisotropies. Please note that changing the bond averages is not a radical idea, since the values obtained by Winter, *et. al.* [1], have been obtained via diagonalizations on small clusters. Furthermore, the uncertainty in the crystal structure which has been resolved until this point indicates that while the nature of the interactions might not change, their couplings could.

6.6.2.1 Phase diagram

The phase diagram of the anisotropic W-model is shown in Fig. 628. We map the phase diagram for various values of J_1 and J_3, we do this by maintaining the anisotropy values constant and varying the bond average. The phase diagram presents two dominant phases, a ferromagnetic state (black dots) and an incommensurate state (green squares). At the bottom right corner a small stripy phase is observed (blue squares). A comparison with the the phase diagram for the isotropic model (Fig. 625) indicates that both the ferromagnetic phase and the spin spiral state are displacing the rest of the phases. Furthermore, the ferromagnetic phase also eats away part of the spin spiral phase.

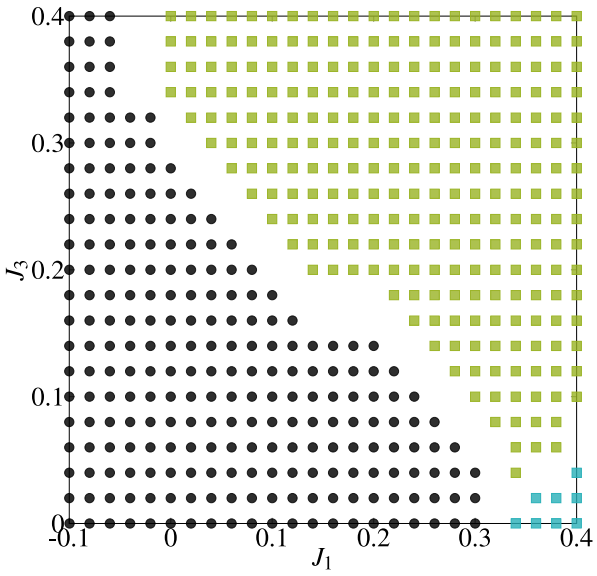

Figure 628: Phase diagram for the anisotropic case of the Hamiltonian shown in Eq. 6.13. Black dots correspond to ferromagnetic order, light blue squares to stripy order. The incommensurate states are represented by green squares.

The ferromagnetic phase present in this model contains an in plane net magnetization, in the direction perpendicular to the nearest neighbors zz-bonds (Fig. 617). Domain walls separate the two domains containing the two possible orientations of the polarization. Furthermore these domain walls are given by spins aligned antiferromagnetically. As J_1 and J_3 are increased the domains multiply, until the system enters the spiral phase.

To understand how this transition happens we can look at Fig. 629. In this figure we sketch the projected spin pattern on the lattice [111] plane for a cut though a fixed value of J_3, where the system suffers a phase transition from a ferromagnetic state to

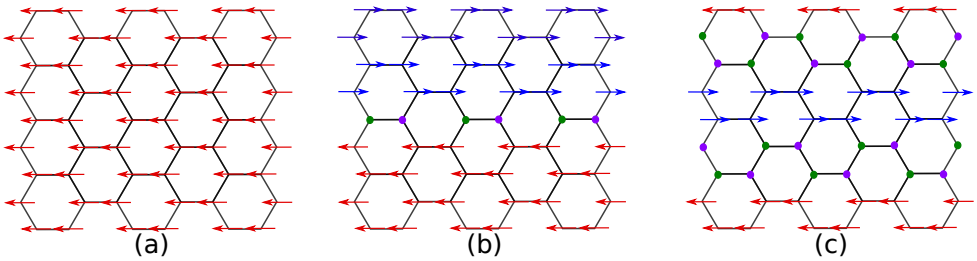

Figure 629: Sketch depicting the commensurate/incommensurate transition in the anisotropic W-model projected on the [111] plane for $J_3 = 0.2$. *(a)* Ferromagnetic state at $J_1 = -0.1$. *(b)* When J_1 is increased (here we show $J_1 = 0$) ferromagnetic domains are separated by antiferromagnetic domain walls (green dots depict spins pointing outside the page, and purple are spins pointing inside the page). *(c)* at a critical value of $J_1 \sim 0.15$ the system enters the spiral phase which can be depicted in the [111] plane as alternating ferromagnetic/antiferromagnetic domains.

a spiral state. To simplify the argument we have assumed for this discussion that the angles between the resulting spirals is 45^o and there is no tilt angle in the rotation plane. But careful study of the numerical results shows that this picture is still valid for arbitrary wavevector and rotation plane tilt. [1] Then, for this particular example, we see that at small values of J_1 the state presents no domain walls (Fig. 629(a)). As J_1 is increased domain walls start to span the length of the system, separating big domains of ferromagnetic order (Fig. 629(b)). For even bigger J_1 the system now contains ferromagnetic and antiferromagnetic domains spanning two sites in the vertical direction, each. This is seen in Fig. 629(c), which corresponds to spin spirals of a wavevector such that the angle between spins is 45^o.

6.6.2.2 Spiral properties

As can be seen from Fig. 628, a big part of the phase diagram is dominated by an incommensurate state. These spirals are of the same nature of those found for the I_cI_d model. In essence, the state is such that planar spirals propagate in the direction perpendicular to the zz-bond. Furthermore, the spirals counterotate, with those formed by spins on sublattice a and c rotating with opposite chirality to those formed by the spins of sublattices b and d (see Fig. 630). A real space pattern of the spirals can be observed in Fig. 630, where we show a spiral which coincides with the experimental

[1] The reason for choosing this particular example is that of convenience, given that at this angle and plane tilt, the spin spiral can be seen as alternating ferromagnetic/antiferromagnetic domains of size two. For another wavevector there would also be ferromagnetic and antiferromagnetic domains but the size of these regions would not be the same.

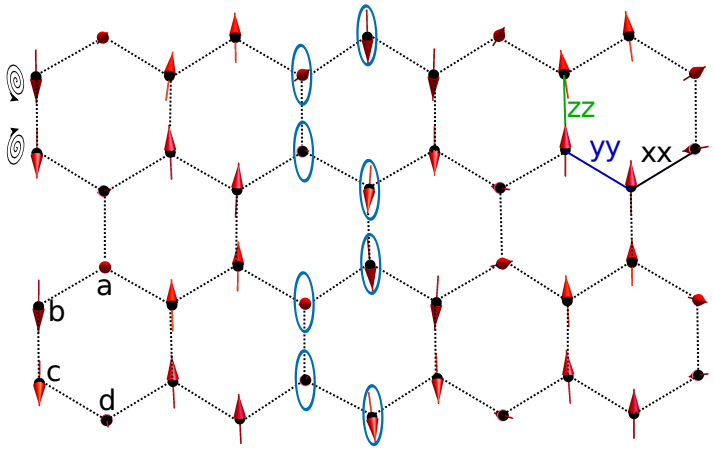

Figure 630: Spin pattern for the spiral phase found in the bond anisotropic W-model. We observe incommensurate couterotating spirals propagating in the direction perpendicular to the zz-bonds. The wavevector and plane of rotation of this phase coincide with those found in the MXRD experiments.

results for α-Li_2IrO_3, exhibiting a wavevector $(q,0)$ where $q = 0.32$ in units of 2π, and a tilt of the rotation plane of $\sim 80^0$.

Comparing this spiral with that found for the bond isotropic model, it is not surprising to notice that the effect of the anisotropies was that of destroying the degeneracy of the spiral phase. Recall that in the bond isotropic model our spirals were planar spirals, but also degenerate, where the degeneracy came from the fact that the Hamiltonian retained the discrete Kitaev symmetry, and as such the spirals were free to propagate in three possible direction. In the anisotropic case this degeneracy is destroyed, a fact which can already be observed in the ferromagnetic phase, where the spins are ordered in only one particular direction. Throughout the phase diagram, we notice that the wavevector and tilt angle change. In

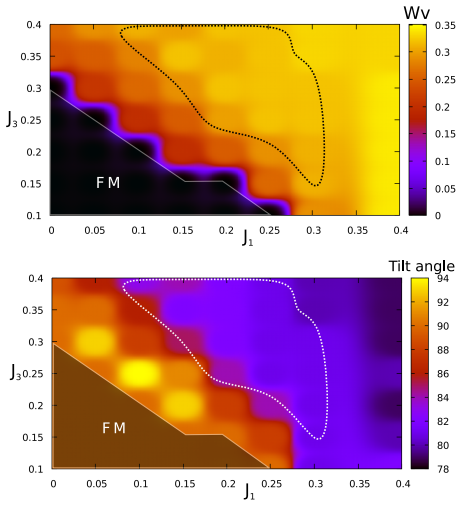

Figure 631: Heat map of the wavevector (top) and rotation plane's tilt (bottom) for the spiral phase in the anisotropic W-model. The dotted line represents the calculated wavevector, $q = 0.32(1)$ in units of 2π.

Fig. 631 we show a heat map of the variation of the wavevector (Fig. 631 top) of the tilt angle (Fig. 631 bottom) as the exchanges J_1 and J_3 are modified.

The dotted line indicates the region of the wavevector map where the wavevector coincides with the experimental value $q = 0.32(1)$. Superimposing this dotted line on the tilt angle heat map we show there is a broad region of the phase diagram where the experimental results are reproduced. Please note that this heat maps and the dotted lines are a guide to the eye, where an interpolation has been performed between the points obtained from our simulations. Non the less our simulations clearly show an extended region where the experimental values are recovered.

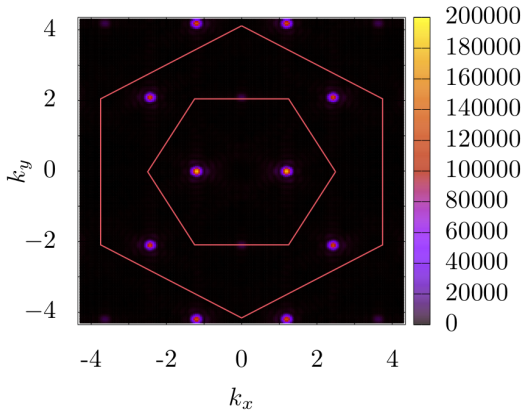

Figure 632: Fourier transform of the correlation function for the spiral phase ($J_1 = 0.3$, $J_3 = 0.3$). This state reproduces the experimental features: wavevector $(q,0)$ with $q = 0.32$, and tilt of the plane of rotation of 80^o.

In Fig. 632 we show the Fourier transform of the spin pattern shown in Fig. 630. From this we observe that the maxima are located inside the Brillouin zone as satellite peaks of the Γ point, and secondary maxima appear as satellite points of the K points. From this Fourier transform we can further extract a wavevector $(q,0)$, $q = 0.31$ in units of 2π, which coincides with the analysis performed on the real space spin pattern. Furthermore, these results are consistent with the experimental results shown in Section 6.2.

6.7 Magnetization process

Up to this point, we have performed an analysis, based on Monte Carlo simulations, of the possible minimal models for α-Li_2IrO_3. All these models where proposed either on the basis of symmetry allowed interactions, or on DFT studied. Having compared the results for all the models we have determined that only two of those reproduce the experimental features of the material. While all models present incommensurate spin spiral phases, only the I_cI_d- and anisotropic W-models reproduce not only the counterotating nature and wavevector of the spirals present in α-Li_2IrO_3, but also the tilt of the rotation plane.

Now, if any of these two models is indeed the minimal model of α-Li_2IrO_3, we want

to predict what the behavior of these models would be in a way which can be verifiable experimentally. For this we have chosen to study the magnetization processes of the different models by applying an external magnetic field in different directions. Given the strong bond anisotropy of both models, the behavior in the presence of external magnetic fields will be different depending on the direction of the field. As we will see, the magnetization processes of the I_cI_d- and anisotropic W-models are radically different, which indicates an experimentally feasible way of reducing the number of possible minimal models further. It can be that the magnetization processes of α-Li_2IrO_3 coincide with one of these two models, which would be evidence of the validity of one of them, or that it is different from both of them, which would mean a different model needs to be put forwards.

6.7.1 I_cI_d-model

We will study the magnetization processes of the I_cI_d-model (Eq. 6.3) for magnetic fields in three different directions: $H \parallel [111]$, $H \parallel [\bar{1}10]$, and $H \parallel [11\bar{2}]$. Of these three directions, [111] corresponds to the direction perpendicular to the lattice plane, while $[\bar{1}10]$ is the direction parallel to the zz- bonds and $[11\bar{2}]$ the direction perpendicular to those bonds.

We will concentrate on the point of the phase diagram that reproduces the experimental results: $I_c = -0.5$ and $I_d = -0.35$, in units of the Kitaev coupling, $|K|$. Fig. 633 shows the magnetization curves for the different directions of the field. We observe that for field directions in the lattice plane ($H \parallel [\bar{1}10]$, $H \parallel [11\bar{2}]$) the critical field is much lower than for the out of plane direction ($H \parallel [111]$). This indicates the existence of an easy plane anisotropy. The origin of this easy plane can be seen from the position of the experimentally relevant point in the phase diagram. This point is close to the phase boundary between the spiral and the ferromagnetic phase.

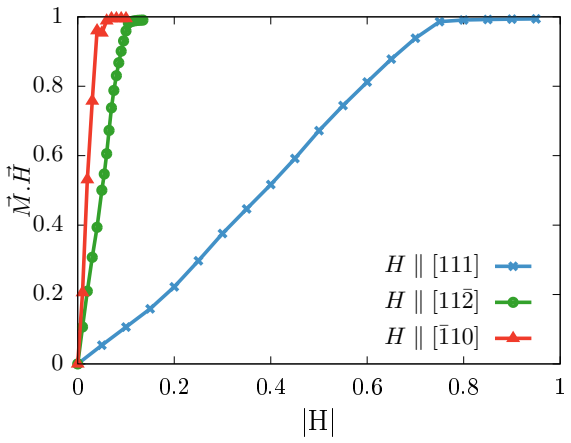

Figure 633: Magnetization in the direction of the field as a function of field intensity for three different field directions.

We have seen before that the ferromagnetic phase is such that the spins point in plane, in a direction that depends on the values of I_c and I_d. Since our spiral phase is so close to the boundary with a ferromagnetic phase, a small reinforcement of one of the bond dependent terms will drive the system towards a ferromagnetic state. Applying a magnetic field in the direction of one of the bonds then is equivalent to reinforcing one of the Ising terms, and as such the magnetization in these directions is easy. Furthermore, we also compare the magnetization in the direction of the field ($M.H$) with the ferromagnetic order parameter (FM_{OP}) and analyze the susceptibility, χ/H, of the ferromagnetic order parameter (FM_{OP}) to determine the critical field at which ferromagnetic order is realized. (FM_{OP}) will probe the system for the presence of a ferromagnetic state, while $M.H$ will probe whether the polarization vector is in the direction of the field or not.

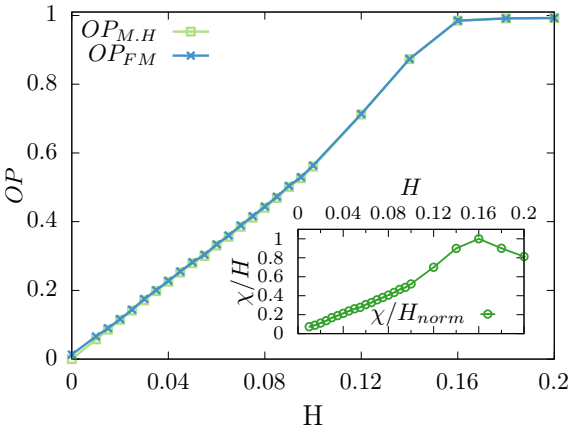

Figure 634: Magnetization in the global [11$\bar{2}$] direction (green) and ferromagnetic order parameter (blue) as a function field intensity. *Inset:* susceptibility of FM_{OP} as a function of field.

For both in plane direction, [11$\bar{2}$] and [$\bar{1}$10] (Figs. 634 and 635), we observe the same behavior in both the FM_{OP} and $M.H$. The magnetization monotonically increases until saturation is reached at rather small critical fields (in comparison with the relevant couplings of the model). The susceptibility curves show a peak that indicates a phase transition towards the fully polarized state. The transition towards saturations for all field directions resembles the well know paramagnetic/ferromagnetic transition of many magnets, in which small domains showing ferromagnetic correlations form at small

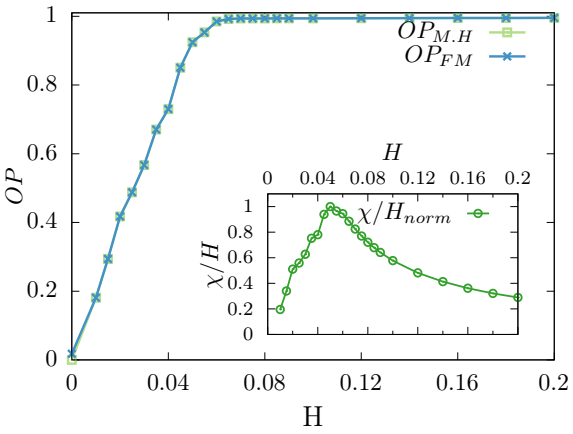

Figure 635: $M.H$ in the global [$\bar{1}$10] direction (green) and FM_{OP} (blue) as a function field intensity. *Insets:* susceptibility of FM_{OP} as a function of field.

fields, and whose size grows with increasing intensity of the external field until they dominate the system.

In the case of the field in the [111] direction the behavior between $M.H$ and FM_{OP} is rather different. Both curves increase monotonically up to $H = 0.5$ (unless stated otherwise, the magnetic fields are given in units of $|K|$), at this point they separate into two different behaviors. While $M.H$ keeps slowly growing until saturation at approximately $H = 0.8$, the ferromagnetic order parameter suddenly reaches saturation at $H = 0.6$. This indicates a stable intermediate state in which the ferromagnetic state is realized in a direction not parallel to the applied field. The resulting ferromagnetic state is a state where the spins are out of plane, their z-component aligned parallel to the external field, while their x- y-component are aligned along the zz-bonds.

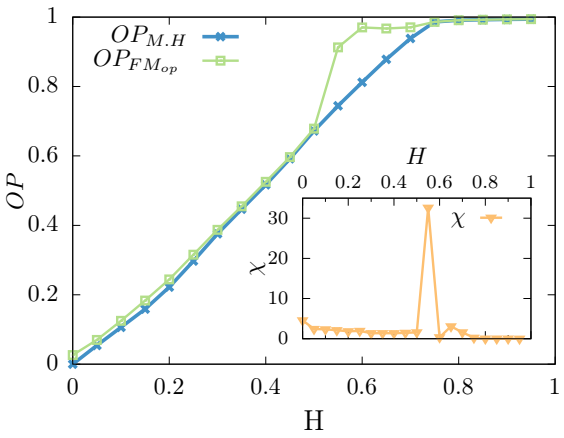

Figure 636: $M.H$ in the global [111] direction (blue) and FM_{OP} (green) as a function field intensity. *Inset:* susceptibility of FM_{OP} as a function of field.

We determine the critical fields consistent with the susceptibility simulations. We obtain a critical field $H_{crit} = 0.05$ (in units of the Kitaev exchange coupling) for a field direction $[\bar{1}10]$, $H_{crit} = 0.1$ for the magnetic field in the $[11\bar{2}]$ direction, and $H_{crit} = 0.8$ for the field in the [111] direction.

6.7.2 Anisotropic W-model

Now, we will study the magnetization processes for the anisotropic W-model with the same field directions as for the I_cI_d model, this is $H \parallel [111]$, $H \parallel [\bar{1}10]$, and $H \parallel [11\bar{2}]$. As we shall see, the magnetization processes change drastically from those in the I_cI_d model, given the strong off-diagonal and further neighbor interactions present in the model.

In Fig. 637 we show the magnetization in the direction of the field for the three field directions studied. We observe that the polarized state is reached at $H \sim 0.25$ in the $[\bar{1}10]$ direction, while for the magnetic field in the $[11\bar{2}]$ direction the critical field is $H \sim 1.5$ and $H \sim 4$ for the field in the [111] direction. This behavior points towards the

existence of an easy axis anisotropy in the $[\bar{1}10]$ direction (please remember that the $[\bar{1}10]$ direction is the direction parallel to the zz-bonds). Note that we have dedicated a big part of the numerical effort to fields $H \lesssim 1.5$, which correspond to experimentally realizable fields.

We show in Fig. 638(top) the magnetization curve for an applied magnetic field in the $[\bar{1}10]$ direction. We observe that the magnetization monotonically increases with an increasing slope at small fields up to $H \sim 0.25$ (unless stated otherwise all fields are in units of $|K_1|$), at which point it suddenly reaches saturation. This behavior, and the associated presence of an easy axis anisotropy can be understood following the argument developed in section 6.6.2.1 for the ferromagnetic/spiral phase transition. In this case we stated that, in the spiral phase, the spin pattern projected over the [111] plane, is that of alternating ferromagnetic and antiferromagnetic domains, where the ferromagnetic domains are oriented in the direction parallel to the zz-bonds, this is, in the $[\bar{1}10]$ or $[11\bar{2}]$ directions. If we introduce a small magnetic field in one of these two direction, the effect of it is of decreasing the wavevector of the magnetic spiral, which is evidenced in the projection on the [111] plane as the increase on the size of the ferromagnetic domains, until they overpowerd the system. In Fig. 638(bottom) we show the change in the spiral wavevector, calculated from the resulting spin pattern obtained from Monte Carlo, as a function of field. It can be seen that at small fields, $H < 0.15$ the change in the wavevector is not pronounced, ranging from $q = 0.31$ to $q = 0.25$ (in units of 2π). On the other hand, for $H < 0.15$, the wavevector decreases rapidly, reaching $q = 0$ at $H \sim 0.3$, a vanishing wavevector would then be interpreted as a ferromagnetic state. It is also at $H \sim 0.3$ that we observe the maxima in the susceptibility of the ferromagnetic parameter (inset of Fig. 638(top)). The maxima of the susceptibility, together with the decreasing wavevector and the saturation point of both $OP_{M.H}$ and OP_{FM}, show that the critical field for this field direction is $H_{\text{crit}} \sim 0.3$.

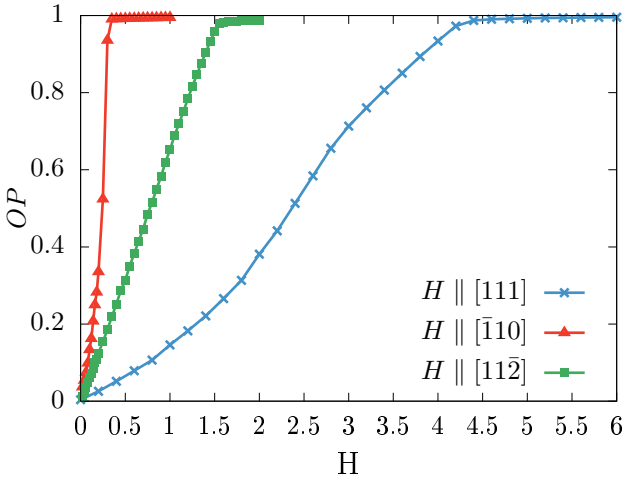

Figure 637: Magnetization in the direction of the field as a function of field intensity for three different field directions, $H \parallel [111]$, $H \parallel [\bar{1}10]$, $H \parallel [11\bar{2}]$

For the other in plane direction, $H \parallel [11\bar{2}]$ (the direction perpendicular to the zz-bonds) the behavior at small fields is radically different. In Fig. 639(top) we show that the magnetization grows monotonically with a constant slope, reaching saturation at $H \sim 1.5$. At $H = 0$ the state is a planar counterrotating spiral as shown in the previous section, but for $H > 0$ a continuous transition between a counterotating planar spiral and a counterotating conical spiral is realized.

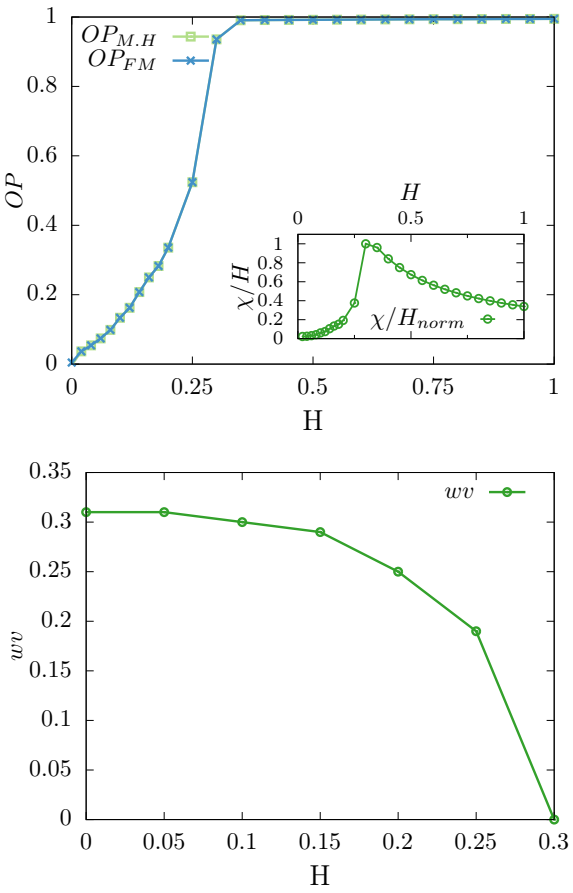

Figure 638: *Top, main figure*: Magnetization in the global $[\bar{1}10]$ (green curve) and ferromagnetic order parameter (blue curve). *Top, inset:* susceptibility of the ferromagnetic order parameter as a function of field. *Bottom*: change in the associated spiral wavevector (q) as a function field intensity

As the name indicates, a conic spiral is a helimagnetic state in which the spiral does not rotate in a plane but in a cone around a certain common direction, which in this case is the propagation direction of the spiral. Since the magnetic field is applied in the direction parallel to the propagation direction, at moderate fields the spins cant in that direction, which transform the plane of rotation into a cone. We show in Fig. 639(bottom) a scheme of this process. We indicate the direction of propagation (which coincides with the direction of the applied field, $[11\bar{2}]$) as well as the direction perpendicular to it ($[\bar{1}10]$). At low fields the canting in the spins induces the transition from a rotation plane to a rotation cone. As the field increases the cone gets narrower, until at high fields the spins point in the direction of the field, thus reaching saturation.

Since the model contains strong in plane interactions, saturation is only achieved at strong magnetic fields for out of plane directions. In the case of a magnetic field in the [111] direction (direction perpendicular to the lattice plane) the saturation is reached at $H \sim 4$ (in units of the Kitaev coupling) as can be observed in Fig. 640(left). In this case,

as well as in the I_cI_d-model, both order parameters saturate at different field intensities. Both the ferromagnetic order parameter and the magnetization in the direction of the field have to saturate at high enough fields, but while the ferromagnetic order parameter saturates at $H \sim 0.4$, the magnetization in the direction of the field does not completely saturate up to the biggest calculated fields.

A magnetic field in the [111] direction tilts the spins in this direction, producing a net magnetization, up to the biggest calculated field, which is deviated from the magnetic field direction. The magnetization process can be understood recalling Fig. 629. Here we mentioned that the spin spiral state can be considered as arrangements of ferromagnetic/antiferromagnetic domains of spin in the [111] plane. When a magnetic field is applied in perpendicular to the direction of the ferromagnetic domain's polarization (as is the case here, since the [111] plane is the lattice plane), the spins of the ferromagnetic domains will be tilted in the direction of the field. The same will happen to the spins in the antiferromagnetic domains which are not already pointing parallel to the field, but the tilt angle will not be the same as the one in the ferromagnetic domains. In Fig. 640(right) we show the spin pattern at $H = 0.35$, where the tilt in the direction of the field can be observed.

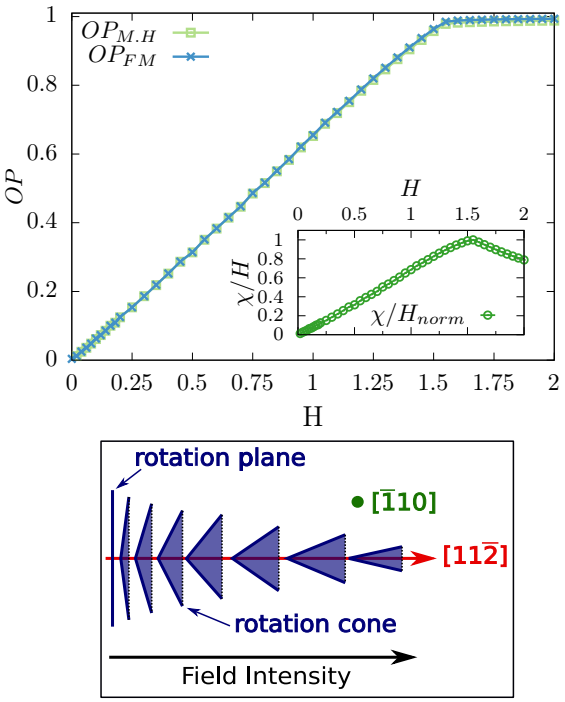

Figure 639: *Top*: Magnetization in the global [11$\bar{2}$] direction (green curve) and ferromagnetic order parameter (blue curve) as a function field intensity. *Inset:* susceptibility of the ferromagnetic order parameter as a function of field. *Bottom:* scheme showing the change from a rotation plane towards a rotation cone (see text).

6.8 Discussion

We have studied a variety of extended Kitaev Hamiltonians as minimal models of α-Li_2IrO_3. The experimental studies of this material indicate a strong bond anisotropy, which led us to study models which contain strong anisotropic bond dependent interac-

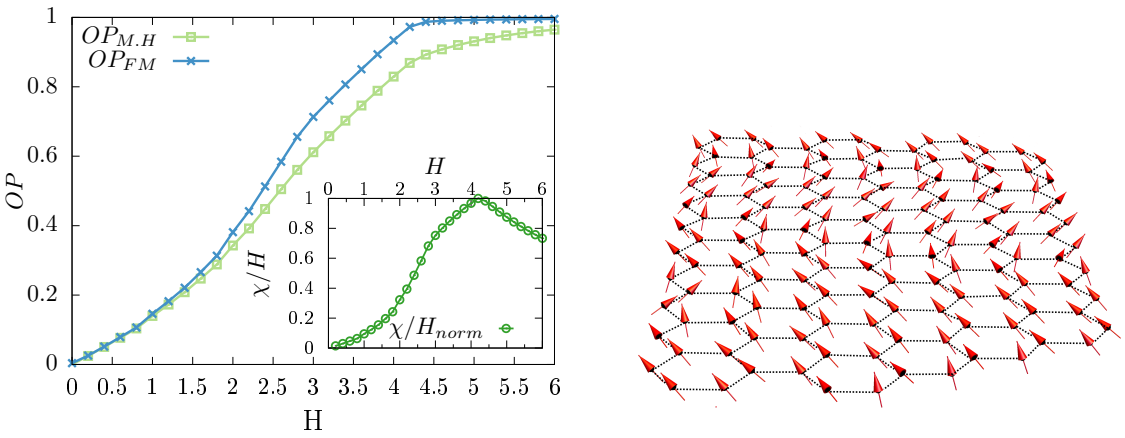

Figure 640: *Left*: Magnetization in the global [111] direction (green curve) and ferromagnetic order parameter (blue curve) as a function field intensity. *Right:* real space spin pattern at $H = 0.325$

tions beyond Kitaev interactions. Furthermore we have considered interactions ranging from nearest to third neighbor models. While all models share similarities with each other, we have shown that the range of the interactions can produce radical differences in the behavior of the system.

Our nearest neighbor models (I_c- and I_cI_d-models) exhibit a phase diagram where a big part of it presents an incommensurate counterrotating coplanar spiral state. For the I_c model we encounter a spiral state whose wavevector coincides with that of α-Li_2IrO_3 on a section of the phase diagram. However, whether in the Iridate material the plane of rotation is tilted away from the lattice plane by $\sim 80^o$, in this model the plane of rotation is parallel to the XY Cartesian plane (54^o tilt with respect to the lattice plane). This can be understood realizing that a Hamiltonian only containing the I_c term is equivalent to and XY model, where in this case the model posses a U(1) symmetry around the Cartesian z-axis. This mean that in a Hamiltonian only containing the I_c term the spins are constraint to take values on a circumference, and this circumference is parallel to the XY plane. When the Kitaev and Heisenberg terms are included, the U(1) symmetry is broken, but there is a residue of this symmetry, which is exhibited in the rotation plane of the spin spiral state. The introduction of a small term of the same nature as the I_c but over the xx- and yy-bonds (I_cI_d-model) will induce a tilt of the rotation plane, and we have shown that the I_cI_d model reproduces all the experimental features of α-Li_2IrO_3.

When a second neighbor Heisenberg-Kitaev model is considered ($2N$-model) also two spiral states are present in the phase diagram, but these spirals are non-coplanar. We

expected that the introduction of an I_c term, inducing a ferromagnetic alignment over the zz-bonds would modify the spiral states into coplanar spirals. We do not see this in any part of the phase diagram. Furthermore, one would expect that the introduction of an I_d term would modify the plane of rotation, but not the wavevector, as we have shown in the nearest neighbor model that only an I_c term is enough to generate incommensurate counterotating spirals, so a further modification of the $2NI_c$- model was not attempted. We can conclude then, that the $2N$- and $2NI_c$-models are not minimal models for α-Li_2IrO_3.

While the introduction of second neighbor interactions do not reproduce the experimental results, recent DFT calculations [1] have put forward a model, the W-model, which indicate that further neighbor interactions are needed. We tested this model, in both its bond isotropic and anisotropic forms. Given that the experiments performed on α-Li_2IrO_3 indicate strong bond anisotropy, is no surprise that the model which reproduced the experimental features of the material is the bond anisotropic W-model. While the isotropic third neighbor model presents incommensurate spirals, they do not propagate on only one direction, but can propagate in three symmetry allowed directions. Unsurprisingly, the introduction of anisotropies destroy the degeneracy by selecting a preferred propagation direction.

In the third neighbor models, the interactions are slightly different than in the models previously studied. We modeled the bond dependent interactions in the nearest and second neighbor models as $I_{c/d}\sum_{<ij>} S_i^{r_{ij}} S_j^{r_{ij}}$, with $S_i^{r_{ij}} = \mathbf{S}_i \cdot \mathbf{r}_{ij}$, where r_{ij} is the bond between sites i and j. This in turn takes the form, for the zz-bonds (the expression for the remaining bonds is analogous)

$$I_c \sum_{<ij>} S_i^{r_{ij}} S_j^{r_{ij}} = I_c(S_i^x S_j^x + S_i^y S_j^y + S_i^x S_j^y + S_j^x S_i^y) = I_c(S_i^x S_j^x + S_i^y S_j^y) + I_c \Gamma^{xy}, \tag{6.15}$$

which has the form of the Γ terms included in the W-model, supplemented by two Heisenberg terms. This expression indeed shows that the connection between the nearest neighbor and the anisotropic W-model could be achieved by adding further interactions in the $I_c I_d$ model and finely tuning the bond anisotropy parameters in the W model.

Since both $I_c I_d$- and anisotropic W-models reproduce the experimental features of the specific heat, we proceed to calculate the Curie-Weiss temperature within a mean field approach. For the $I_c I_d$-model we find an anisotropic susceptibility $\chi = (\chi_{xx}, \chi_{yy}, \chi_{zz})$ arising from the I_c and I_d terms, where the associated Curie-Weiss temperatures are given by

$$\Theta_{xx} = \Theta_{yy} = \frac{S(S+1)}{3K_b}(-3J - I_c - I_d - K), \tag{6.16}$$

$$\Theta_{zz} = \frac{S(S+1)}{3K_b}(-3J - 2I_d - K). \tag{6.17}$$

At the point of interest ($I_c = -0.5$ and $I_d = -0.35$), where experimental results are reproduced, we obtain positive Curie-Weiss temperatures: $\Theta_{xx} = \Theta_{yy} = 16.35K$ and $\Theta_{zz} = 14.38K$ in units of the Kitaev coupling.

In the case of the W-model we also find an anisotropic susceptibility, in this case arising from the anisotropy of the nearest neighbor Heisenberg and Kitaev interactions

$$\Theta_{xx} = \Theta_{yy} = \frac{S(S+1)}{3K_b}(-3J_1^{XY} - K_1^{XY} - 2K_2 - 3J_3), \tag{6.18}$$

$$\Theta_{zz} = \frac{S(S+1)}{3K_b}(-3J_1^{Z} - K_1^{Z} - 2K_2 - 3J_3), \tag{6.19}$$

Evaluated at the experimentally relevant point shown in Table. 62 we obtain $\Theta_{xx} = \Theta_{yy} = 20.15K$ and $\Theta_{zz} = -17.17K$.

The experimentally measured Curie-Weiss temperature [107] was obtained from a fit to the high temperature magnetic susceptibility for polycrystalline samples, $\Theta_{\text{exp}} = -33(3)K$. Since the experiments have been performed on a polycrystalline sample, the Curie-Weiss temperature obtained is the average of the anisotropic Curie-Weiss temperatures. In the case of the I_cI_d- and anisotropic W-models we obtain an averaged Curie-Weiss temperature $\Theta_{av}^{I_cI_d} = 15.7K$ and $\Theta_{av}^{W} = 7.58K$. As previously shown, a considerable part of the phase diagram for the anisotropic W-model reproduces the experimental results. This would indicate that a different selection of coupling strengths could modify the averaged Curie-Weiss temperature of the model as to obtain the experimental value, while maintaining the overall behavior of the system to be the same as in the neutron diffraction experiments. For example, for coupling strengths such that the bond averages are $J_1 = 0.2$ and $J_3 = 0.5$ we obtain a averaged susceptibility $\Theta_{av}^{W} = -7.41K$. In this case, the behavior of the model still reproduces the neutron diffraction results, but now the sign of the calculated Curie-Weiss temperature coincides with that of the experiments. While we could do a similar analysis for the I_cI_d-model the region of the

phase diagram that reproduces the results in much more reduced, and as such the variation of the exchange parameters is not enough to change the sign of the Curie-Weiss temperatures. Given that the experiments where performed at high temperature the comparison between our ground state calculations and the experimental results are not sufficient to determine if the anisotropic W-model is the minimal model of α-Li_2IrO_3. Furthermore, extra thermodynamic studies on single crystals would prove useful at determining the anisotropic susceptibilities and the respective signs of the associated Curie-Weiss temperatures.

We also studied the magnetization processes for both I_cI_d- and W-models. In both cases we find a strong anisotropy in the magnetic response, with different behaviors for different directions of the applied field. For the I_cI_d-model we find a strong easy plane anisotropy, arising from the off diagonal terms of the Hamiltonian. Since these terms favor in plane orderings, the tendency to order ferromagnetically when an in-plane magnetic field is applied is strong, which presents in our study as a lower critical field for in-plane rather than out of plane directions of the external field. Furthermore, since the experimentally representative point of this phase is close to an in-plane ferromagnetic phase with polarization in the $[\bar{1}10]$ direction, small fluctuations favoring this type of in-plane ferromagnetic state quickly drive the system towards this phase, which explains the difference in the critical fields for the external field in the $[\bar{1}10]$ and $[11\bar{2}]$ directions. The tendency to in-plane ordering is also observed in the magnetization behavior when a field in the [111] plane is applied, as there exist an intermediate state where the magnetization has a net component in the direction of the field, but also a component in the lattice plane direction. For increasing field strength the lattice plane component decreases in magnitude until full saturation in the direction of the field is reached. For intermediate fields the three directions show similar magnetic behavior, which resembles that of a ferromagnetic/paramagnetic transition, where ferromagnetic domains with polarization parallel to the direction of the external field are induced, and which grow in size as the field is increased. Finally, we mention that, since the magnetic field are expressed in terms of K, we can extract the value in Tesla since $H = 1$ in units of $|K|$ is equivalent to $g\mu_B H/|K| = 1$. The gyromagnetic factor is believed to be anisotropic, given the deformations of the octahedral cage of Oxygens, but the exact value is not known. Recent calculations [131] show that the g factor can drastically change depending on the octahedral deformation, with values ranging from ~ 1.5 to ~ 4 for the parallel component of the gyromagnetic factor (the component in the lattice plane), and from ~ 2.5 to ~ 0.5 for the out of plane component. Given the strong variation of this parameter and the

lack of experimental data, we employ an isotropic factor $g = 2$. Finally, if we assume the interaction strength of the Kitaev interaction to be -4.5meV (as proposed in Ref. [14]), we obtain the critical fields of ~ 31T for the [111] field direction, ~ 6T for $[11\bar{2}]$, and ~ 2.7T for $[\bar{1}10]$.

For the case of the anisotropic W-model the behaviors is quite different. While the system also exhibits an anisotropic magnetic response, in this case it possesses a strong easy axis anisotropy. Additionally, assuming that the overall energy scale of the couplings determined by DFT is correct we find that the critical field for an external field in the [111] direction results ~ 200T, while it is ~ 111T for the $[11\bar{2}]$ direction, and ~ 22T for $[\bar{1}10]$. While such high fields are hard to achieve in experiments (for continuous field the world record is at approximately 45T), the low field regime already exhibits a high anisotropy which can be probed experimentally. This anisotropy can be traced back to the Hamiltonian of the model, where strong off diagonal terms are present. In particular the nearest neighbor Γ exchange, which induces an in-plane configuration of spins, is equal in magnitude to the nearest neighbor Kitaev exchange, which makes these two interactions the dominant ones in the model. Equally, the anisotropy drastically changes the magnetic behavior at intermediate fields. For fields in the $[\bar{1}10]$ direction, the magnetization suddenly increases at $|H| \sim 0.25$ (in units of the nearest neighbor Kitaev coupling) indicating the possible discontinuity of the transition, while for fields in the $[11\bar{2}]$ and [111] directions the transition is continuous, exhibiting a continuous transformation of the spin pattern (in the case of the $[11\bar{2}]$ field direction, from a planar spiral towards a conical spiral).

The similarities in the ground states found for both systems indicate that one of them could prove to be the minimal model of α-Li_2IrO_3. The differences in specific heat as well as different magnetization behaviors indicate that further experimental studies are needed to decide which one, if any, is the model corresponding to this material. While the Curie-Weiss temperature for the I_cI_d-model does not reproduce the sign found from the calorimetric experiments, the nature of the experiments (the powder average and the high temperature measures) could obscure further details which could help clarify the discrepancy. Furthermore, studies on single crystals would prove valuable as in these cases the different crystallographic directions could be probed to assert the existence of anisotropic susceptibilities. In the case of the anisotropic W-model, we find that for a careful choice of parameters we can reproduce the sign of the Curie-Weiss temperature. While Ref. [1] proposes a set of values for all couplings (which were chosen as the starting point for our study), in both isotropic and anisotropic cases these values

do not correspond to spiral phases. By changing the couplings of the nearest and third neighbor Heisenberg exchanges we find a range of values where the experimental results are obtained. This indicates that further studies regarding the quantum chemistry as well as the crystal structure of the material are necessary to further determine the strength of the couplings.

To further distinguish the models, magnetization measurements can be fruitful. While the critical field for W-model are far beyond current capabilities, interesting studies can be performed at low field. In particular, for the I_cI_d-model the calculated critical fields are within the possibility of experimental realization, while for the W-model, the anisotropy present at low fields can be measured experimentally (we remind the reader that the critical field measured for a field in the $[\bar{1}10]$ direction in W-model is 22T, which is reachable experimentally). In particularly, the low field behavior, which is different for the different field directions, could be observed in single crystals.

We conclude then, pointing out that questions remain open regarding the minimal model of α-Li_2IrO_3. We have reduced the number of possible models and explored the different magnetization behavior of those models which reproduce the experimental signatures of the material. We expect that magnetization measurements can point in the direction of one these models being correct in the low temperature limit. However, we recommend further studies: We expect that electronic structure calculations could clarify the current situation in which the obtained exchange couplings do not lead to the experimentally measured spin pattern. On the other hand, as pointed out in Ref. [1], the crystal structure of the material is not well understood. The recent growth of single crystals could help refine the crystal structure. Furthermore, our study of the W-model suggest that modest long-range interactions can stabilize the counterotating spirals found in α-Li_2IrO_3, but that anisotropy is crucial to obtain a non degenerate state. Since materials realizing Kitaev interactions show strong bond anisotropy, it cannot be discarded that perhaps a different combination of interactions with a different combination of anisotropies could also reproduce the experimental results and be relevant in real materials. We further mention that also more Monte Carlo studies can be beneficial. By studying the finite temperature magnetization curves, we might encounter lower critical magnetizations and interesting intermediate states which could be easier to realize experimentally (as it was recently done for β-Li_2IrO_3 [132]). Furthermore, a study of the full phase diagram in the presence of different external magnetic fields could help model future materials which could be realized. Finally, we mentioned that both models could also reproduce the observed behavior in β-Li_2IrO_3 and γ-Li_2IrO_3, which

indicated that further numerical studies of both models in three dimensional lattice as hyper-honeycomb and stripy-honeycomb are necessary.

CHAPTER 7

CONCLUSIONS AND OUTLOOK

The awesome splendor of the universe is much easier to deal with if you think of it as a series of small chunks.

Terry Pratchett

We have studied frustrated magnetic systems in their quantum and classical version. We extended the pfFRG scheme shown in Chapter 3 to include arbitrary spin lengths (Chapter 4), and showed that this formalism can be employed to study the effect of quantum fluctuations on a given model. We showed how this approach can be used, by employing it to study the nearest and next nearest antiferromagnetic Heisenberg honeycomb model, and we proved that in the limit of infinite spin length, when we recover the classical limit, pfFRG reduces to the Luttinger-Tisza approach.

The large-S extension of pfFRG has had great success at studying the effects of quantum fluctuations in several different systems. Buessen [133] *et. al.* employed it to study the classical to quantum transition and the subsequence appearance of spin liquids in diamond lattices, Iqbal and collaborators studied the effect of different spin lengths on the pyrochlore lattice [134] and the stability of spiral states on $MnSc_2S_4$[135]. At the same time the large-S expansion has recently been complemented by a large-N extension where the flow equations are formulated now with a pseudofermionic approach based on a $SU(N)$ spin representation [136, 137].

pfFRG for spin systems is a new technique, and it is still currently being developed. Nevertheless, the present state of the technique makes it very versatile for the study of different systems without the need to modify the basic formulation. Plenty of materials can be modeled as Heisenberg Hamiltonians with competing interactions, and pfFRG is a technique designed to study the phase diagram of models which cannot be accessible with other techniques. Furthermore, pfFRG is not constrained to particular lattices or low dimensionality, and does not suffer from a sign problem. The large-S implementation is straight forward, as it amounts to adding a multiplicative factor to some terms in the flow equations, which extends the strength of the method now including all spin lengths and, as a consequence, both the purely quantum and classical limit, with the added benefit of recovering an exact solution within the classical limit.

Many questions remain open which can be addressed with pfFRG. For example, long ranged interactions can be treated with relative ease, as has been shown in Refs. [138, 139] for the case of Coulomb interactions. With both the large-S and the dipolar interactions implementations many interesting phenomena can be studied. In many frustrated magnets Coulomb phases emerge (as in Heisenberg kagome or spin ice systems), whose properties can be very different in the presence or absence of dipolar interactions. These phases are heavily studied in the classical limit and become particularly interesting when quantum fluctuations are included. The effect of quantum fluctuations on Coulomb phases in the presence of Coulomb interactions has not been fully studied, and pfFRG offers a good numerical first approach to deal with this particular topic.

A particular interesting problem resides on the fact that, at the moment, the algorithm relies on the translational invariance of the lattice, but that many interesting phenomena can be studied, both in the classical and quantum limits, when translational invariance is broken. The introduction of hard boundaries in the system induces edge defects, whose behavior in a quantum spin liquid state is not well understood. pfFRG provides a framework in which (assuming a good code parallelization and sufficient CPU power is provided) analyzing the properties of the edge states in spin liquids can be straightforwardly obtained. Translational invariance can be broken in many different ways. A natural question that arises is what would happen if the reason the translational invariance is broken is not due to edges, but due to defects in the magnetic lattice. Disorder arising from dilution or stuffing of the magnetic ions can also be studied within pfFRG. In the classical limit it has long been known that frustration and disorder are the two main ingredients of spin glass states, and are a topic of intense research up to date. In the quantum limit, the effects of atomic disorder in a spin liquid state

have not been studied in detail giving the lack of methodology available to tackle this problem. Furthermore a detailed pfFRG study of how edge states change in the presence of disorder could help discern between spin glasses and spin liquids in the quantum limit.

We have shown that the classical limit can be exactly recovered within pfFRG, but we have also mentioned that in the classical case many powerful methods exist which can treat these systems and provide further information beyond the zero temperature two point correlation function. To this end we have shown how Monte Carlo simulations can be employed to study effective models for continuous (spin space) frustrated magnetism (Chapter. 5). We showed how the introduction of open boundary conditions can be an asset to study incommensurate phases, and showed that a modified update algorithm together with parallel tempering and iterative minimization schemes are extremely useful to study magnetic insulators that exhibit strong spin orbit coupling.

We studied one material in particular, α-Li_2IrO_3 (Chapter. 6), where the most recent experiments indicate the presence of an incommensurate spin spiral ground state. The many minimal models that were proposed for this material had not been studied under the light of a common framework. Employing large scale Monte Carlo we performed a comparative analysis of the models, and determined that only two out of six models reproduce the full set of experimental results. These two models belong to the same category of Hamiltonians, both presenting strong ferromagnetic Kitaev couplings and secondary Heisenberg and off diagonal terms. They differ, though, on the extent of these interactions. One of the models is a purely nearest neighbor model, while the other presents interactions ranging up to third neighbors. This elevates the question of how minimal a minimal model needs to be. While we would be tempted to select the nearest neighbor model as the minimal one (given the reduced number of interactions) there cannot be discarded that the actual material allows for longer range interactions which would modify the results of further experiments. To resolve this issue we studied the magnetization processes of the two models which reproduce the known experimental results up to date. The two studied models show a very different behavior at both the high and low magnetic field regimes. The nearest neighbor model exhibits an anisotropic magnetization for different field directions, but the magnetization process is consistently the same for all the studied directions. In the case of the third neighbor model, an anisotropic magnetization behavior is also detected, but the magnetization processes are different for the different directions. We proposed that a low field study of α-Li_2IrO_3 with the field in the directions studied in this work could help discern which one of the

studied models belongs to the material, or if another model needs to be put forward. Furthermore, we proposed x-Ray diffraction experiments and pointed out the need for further quantum chemical studies to determine the exchange couplings of the model with higher accuracy.

It needs to be pointed out that there is a proposal of universality between the three members of the Li_2IrO_3 family, given that they share similar ground state properties. Furthermore, it has been shown that a nearest neighbor model (the I_c-model) can reproduce some of the ground state properties common to all of these materials. Therefore, the next question to answer would be whether the nearest and third neighbor models also reproduce the ground state of all these materials. We would expect that the minimal models for the three of them are extremely similar. A good test of universality, which would help determine which minimal model is the correct one, will be to check how the nearest and third neighbor models perform in the lattices corresponding to the β and γ members of the family (hyper- and stripy-honeycomb lattices respectively).

Besides that test, the door is now open to the study of thermal phase transitions in these materials. While we know that in the absence of an external field α-Li_2IrO_3 orders at a critical temperature below $15K$, we have not studied the effect of thermal fluctuations on the magnetization processes. This can be a fruitful endeavor, since thermal fluctuations can decrease the critical fields, or induce exotic intermediate states which can be accessed experimentally. While we are a step closer to defining what the minimal model of α-Li_2IrO_3 is, the previous discussion indicates that a lot of work remains to be done. Within the Monte Carlo framework developed in this thesis, the proposed studies are straightforward to resolve, and these will be the next steps in our study of the Li_2IrO_3 family.

APPENDIX A

FLOW EQUATIONS FOR THE TWO PARTICLE VERTEX

Here we present the FRG flow equations for the simetrized two particle vertex Γ_s^Λ and Γ_d^Λ. This can be obtained by replacing $\tilde{\Gamma}^\Lambda$ with $\tilde{\Gamma}_{\mathrm{s}}^\Lambda$ and $\tilde{\Gamma}_{\mathrm{d}}^\Lambda$ in Eq.3.53 and performing the spin sums over α_3 and α_4 with the subsequent introduction of the frequencies s, t, and u. Comparing the contributions corresponding to the spin and density interactions on both sides we obtain the following flow equations for the two particle vertex,

$$
\begin{aligned}
\frac{d}{d\Lambda}\Gamma^\Lambda_{\mathrm{s}\,i_1i_2}(s,t,u) = \frac{1}{2\pi}\int_{-\infty}^{\infty} d\omega' \Big\{ & \\
& \big[-2\Gamma^\Lambda_{\mathrm{s}\,i_1i_2}(s,-\omega_{2'}-\omega',\omega_{1'}+\omega')\Gamma^\Lambda_{\mathrm{s}\,i_1i_2}(s,\omega_2+\omega',\omega_1+\omega') \\
& \quad +\Gamma^\Lambda_{\mathrm{s}\,i_1i_2}(s,-\omega_{2'}-\omega',\omega_{1'}+\omega')\Gamma^\Lambda_{\mathrm{d}\,i_1i_2}(s,\omega_2+\omega',\omega_1+\omega') \\
& \quad +\Gamma^\Lambda_{\mathrm{d}\,i_1i_2}(s,-\omega_{2'}-\omega',\omega_{1'}+\omega')\Gamma^\Lambda_{\mathrm{s}\,i_1i_2}(s,\omega_2+\omega',\omega_1+\omega') \\
& \quad -2\Gamma^\Lambda_{\mathrm{s}\,i_1i_2}(s,\omega_{1'}+\omega',-\omega_{2'}-\omega')\Gamma^\Lambda_{\mathrm{s}\,i_1i_2}(s,-\omega_1-\omega',-\omega_2-\omega') \\
& \quad +\Gamma^\Lambda_{\mathrm{s}\,i_1i_2}(s,\omega_{1'}+\omega',-\omega_{2'}-\omega')\Gamma^\Lambda_{\mathrm{d}\,i_1i_2}(s,-\omega_1-\omega',-\omega_2-\omega') \\
& \quad +\Gamma^\Lambda_{\mathrm{d}\,i_1i_2}(s,\omega_{1'}+\omega',-\omega_{2'}-\omega')\Gamma^\Lambda_{\mathrm{s}\,i_1i_2}(s,-\omega_1-\omega',-\omega_2-\omega') \big] \\
& \quad \times P^\Lambda(\omega',s+\omega')
\end{aligned}
$$

$$
\begin{aligned}
&+\Big[\quad 2\sum_j \Gamma^{\Lambda}_{\mathrm{s}\,i_1 j}(\omega_{1'}+\omega',t,\omega_1-\omega')\Gamma^{\Lambda}_{\mathrm{s}\,j i_2}(\omega_2+\omega',t,-\omega_{2'}+\omega') \\
&\quad +2\sum_j \Gamma^{\Lambda}_{\mathrm{s}\,i_1 j}(\omega_1-\omega',t,\omega_{1'}+\omega')\Gamma^{\Lambda}_{\mathrm{s}\,j i_2}(\omega_{2'}-\omega',t,-\omega_2-\omega') \\
&\qquad +\Gamma^{\Lambda}_{\mathrm{s}\,i_1 i_2}(\omega_{1'}+\omega',t,\omega_1-\omega')\Gamma^{\Lambda}_{\mathrm{s}\,i_2 i_2}(\omega_2+\omega',-\omega_{2'}+\omega',t) \\
&\qquad -\Gamma^{\Lambda}_{\mathrm{s}\,i_1 i_2}(\omega_{1'}+\omega',t,\omega_1-\omega')\Gamma^{\Lambda}_{\mathrm{d}\,i_2 i_2}(\omega_2+\omega',-\omega_{2'}+\omega',t) \\
&\qquad +\Gamma^{\Lambda}_{\mathrm{s}\,i_1 i_2}(\omega_1-\omega',t,\omega_{1'}+\omega')\Gamma^{\Lambda}_{\mathrm{s}\,i_2 i_2}(\omega_{2'}-\omega',-\omega_2-\omega',t) \\
&\qquad -\Gamma^{\Lambda}_{\mathrm{s}\,i_1 i_2}(\omega_1-\omega',t,\omega_{1'}+\omega')\Gamma^{\Lambda}_{\mathrm{d}\,i_2 i_2}(\omega_{2'}-\omega',-\omega_2-\omega',t) \\
&\qquad +\Gamma^{\Lambda}_{\mathrm{s}\,i_1 i_1}(\omega_{1'}+\omega',\omega_1-\omega',t)\Gamma^{\Lambda}_{\mathrm{s}\,i_1 i_2}(\omega_2+\omega',t,-\omega_{2'}+\omega') \\
&\qquad -\Gamma^{\Lambda}_{\mathrm{d}\,i_1 i_1}(\omega_{1'}+\omega',\omega_1-\omega',t)\Gamma^{\Lambda}_{\mathrm{s}\,i_1 i_2}(\omega_2+\omega',t,-\omega_{2'}+\omega') \\
&\qquad +\Gamma^{\Lambda}_{\mathrm{s}\,i_1 i_i}(\omega_1-\omega',\omega_{1'}+\omega',t)\Gamma^{\Lambda}_{\mathrm{s}\,i_1 i_2}(\omega_{2'}-\omega',t,-\omega_2-\omega') \\
&\qquad -\Gamma^{\Lambda}_{\mathrm{d}\,i_1 i_i}(\omega_1-\omega',\omega_{1'}+\omega',t)\Gamma^{\Lambda}_{\mathrm{s}\,i_1 i_2}(\omega_{2'}-\omega',t,-\omega_2-\omega')\Big] \\
&\qquad\quad \times P^{\Lambda}(\omega',t+\omega') \\
&-\Big[\quad 2\Gamma^{\Lambda}_{\mathrm{s}\,i_1 i_2}(\omega_{2'}-\omega',-\omega_1-\omega',u)\Gamma^{\Lambda}_{\mathrm{s}\,i_1 i_2}(\omega_2-\omega',\omega_{1'}+\omega',u) \\
&\qquad +\Gamma^{\Lambda}_{\mathrm{s}\,i_1 i_2}(\omega_{2'}-\omega',-\omega_1-\omega',u)\Gamma^{\Lambda}_{\mathrm{d}\,i_1 i_2}(\omega_2-\omega',\omega_{1'}+\omega',u) \\
&\qquad +\Gamma^{\Lambda}_{\mathrm{d}\,i_1 i_2}(\omega_{2'}-\omega',-\omega_1-\omega',u)\Gamma^{\Lambda}_{\mathrm{s}\,i_1 i_2}(\omega_2-\omega',\omega_{1'}+\omega',u) \\
&\qquad +2\Gamma^{\Lambda}_{\mathrm{s}\,i_1 i_2}(\omega_1+\omega',-\omega_{2'}+\omega',u)\Gamma^{\Lambda}_{\mathrm{s}\,i_1 i_2}(\omega_{1'}+\omega',\omega_2-\omega',u) \\
&\qquad +\Gamma^{\Lambda}_{\mathrm{s}\,i_1 i_2}(\omega_1+\omega',-\omega_{2'}+\omega',u)\Gamma^{\Lambda}_{\mathrm{d}\,i_1 i_2}(\omega_{1'}+\omega',\omega_2-\omega',u) \\
&\qquad +\Gamma^{\Lambda}_{\mathrm{d}\,i_1 i_2}(\omega_1+\omega',-\omega_{2'}+\omega',u)\Gamma^{\Lambda}_{\mathrm{s}\,i_1 i_2}(\omega_{1'}+\omega',\omega_2-\omega',u)\Big] \\
&\qquad\quad \times P^{\Lambda}(\omega',u+\omega')\Big\},
\end{aligned}
\tag{A.1}
$$

$$
\begin{aligned}
\frac{d}{d\Lambda}\Gamma^{\Lambda}_{\mathrm{d}\,i_1 i_2}(s,t,u) = \frac{1}{2\pi}\int_{-\infty}^{\infty} d\omega' \Big\{ & \\
&\Big[\quad 3\Gamma^{\Lambda}_{\mathrm{s}\,i_1 i_2}(s,-\omega_{2'}-\omega',\omega_{1'}+\omega')\Gamma^{\Lambda}_{\mathrm{s}\,i_1 i_2}(s,\omega_2+\omega',\omega_1+\omega') \\
&\quad +\Gamma^{\Lambda}_{\mathrm{d}\,i_1 i_2}(s,-\omega_{2'}-\omega',\omega_{1'}+\omega')\Gamma^{\Lambda}_{\mathrm{d}\,i_1 i_2}(s,\omega_2+\omega',\omega_1+\omega') \\
&\quad +3\Gamma^{\Lambda}_{\mathrm{s}\,i_1 i_2}(s,\omega_{1'}+\omega',-\omega_{2'}-\omega')\Gamma^{\Lambda}_{\mathrm{s}\,i_1 i_2}(s,-\omega_1-\omega',-\omega_2-\omega') \\
&\quad +\Gamma^{\Lambda}_{\mathrm{d}\,i_1 i_2}(s,\omega_{1'}+\omega',-\omega_{2'}-\omega')\Gamma^{\Lambda}_{\mathrm{d}\,i_1 i_2}(s,-\omega_1-\omega',-\omega_2-\omega')\Big] \\
&\qquad \times P^{\Lambda}(\omega',s+\omega')
\end{aligned}
$$

$$
\begin{aligned}
+\Big[\quad & 2\sum_j \Gamma^{\Lambda}_{\mathrm{d}\,i_1 j}(\omega_{1'}+\omega',t,\omega_1-\omega')\Gamma^{\Lambda}_{\mathrm{d}\,j i_2}(\omega_2+\omega',t,-\omega_{2'}+\omega') \\
& +2\sum_j \Gamma^{\Lambda}_{\mathrm{d}\,i_1 j}(\omega_1-\omega',t,\omega_{1'}+\omega')\Gamma^{\Lambda}_{\mathrm{d}\,j i_2}(\omega_{2'}-\omega',t,-\omega_2-\omega') \\
& -3\Gamma^{\Lambda}_{\mathrm{d}\,i_1 i_2}(\omega_{1'}+\omega',t,\omega_1-\omega')\Gamma^{\Lambda}_{\mathrm{s}\,i_2 i_2}(\omega_2+\omega',-\omega_{2'}+\omega',t) \\
& -\Gamma^{\Lambda}_{\mathrm{d}\,i_1 i_2}(\omega_{1'}+\omega',t,\omega_1-\omega')\Gamma^{\Lambda}_{\mathrm{d}\,i_2 i_2}(\omega_2+\omega',-\omega_{2'}+\omega',t) \\
& -3\Gamma^{\Lambda}_{\mathrm{d}\,i_1 i_2}(\omega_1-\omega',t,\omega_{1'}+\omega')\Gamma^{\Lambda}_{\mathrm{s}\,i_2 i_2}(\omega_{2'}-\omega',-\omega_2-\omega',t) \\
& -\Gamma^{\Lambda}_{\mathrm{d}\,i_1 i_2}(\omega_1-\omega',t,\omega_{1'}+\omega')\Gamma^{\Lambda}_{\mathrm{d}\,i_2 i_2}(\omega_{2'}-\omega',-\omega_2-\omega',t) \\
& -3\Gamma^{\Lambda}_{\mathrm{s}\,i_1 i_1}(\omega_{1'}+\omega',\omega_1-\omega',t)\Gamma^{\Lambda}_{\mathrm{d}\,i_1 i_2}(\omega_2+\omega',t,-\omega_{2'}+\omega') \\
& -\Gamma^{\Lambda}_{\mathrm{d}\,i_1 i_1}(\omega_{1'}+\omega',\omega_1-\omega',t)\Gamma^{\Lambda}_{\mathrm{d}\,i_1 i_2}(\omega_2+\omega',t,-\omega_{2'}+\omega') \\
& -3\Gamma^{\Lambda}_{\mathrm{s}\,i_1 i_1}(\omega_1-\omega',\omega_{1'}+\omega',t)\Gamma^{\Lambda}_{\mathrm{d}\,i_1 i_2}(\omega_{2'}-\omega',t,-\omega_2-\omega') \\
& -\Gamma^{\Lambda}_{\mathrm{d}\,i_1 i_1}(\omega_1-\omega',\omega_{1'}+\omega',t)\Gamma^{\Lambda}_{\mathrm{d}\,i_1 i_2}(\omega_{2'}-\omega',t,-\omega_2-\omega')\Big] \\
& \quad \times P^{\Lambda}(\omega',t+\omega') \\
-\Big[\quad & 3\Gamma^{\Lambda}_{\mathrm{s}\,i_1 i_2}(\omega_{2'}-\omega',-\omega_1-\omega',u)\Gamma^{\Lambda}_{\mathrm{s}\,i_1 i_2}(\omega_2-\omega',\omega_{1'}+\omega',u) \\
& +\Gamma^{\Lambda}_{\mathrm{d}\,i_1 i_2}(\omega_{2'}-\omega',-\omega_1-\omega',u)\Gamma^{\Lambda}_{\mathrm{d}\,i_1 i_2}(\omega_2-\omega',\omega_{1'}+\omega',u) \\
& +3\Gamma^{\Lambda}_{\mathrm{s}\,i_1 i_2}(\omega_1+\omega',-\omega_{2'}+\omega',u)\Gamma^{\Lambda}_{\mathrm{s}\,i_1 i_2}(\omega_{1'}+\omega',\omega_2-\omega',u) \\
& +\Gamma^{\Lambda}_{\mathrm{d}\,i_1 i_2}(\omega_1+\omega',-\omega_{2'}+\omega',u)\Gamma^{\Lambda}_{\mathrm{d}\,i_1 i_2}(\omega_{1'}+\omega',\omega_2-\omega',u)\Big] \\
& \quad \times P^{\Lambda}(\omega',u+\omega')\Big\}. \qquad \text{(A.2)}
\end{aligned}
$$

The frequencies ω_1', and ω_2' are related to the s, t, and u frequencies by

$$\omega_1' = \frac{1}{2}(s+t+u) \quad \omega_2' = \frac{1}{2}(s-t-u) \qquad \text{(A.3)}$$

while for ω_1', and ω_2' we have the relations

$$\omega_1 = \frac{1}{2}(s-t+u) \quad \omega_2 = \frac{1}{2}(s+t-u). \qquad \text{(A.4)}$$

APPENDIX B

HEISENBERG-KITAEV MODEL

To fully comprehend the physics of the models studied in this thesis, we need to carefully analyze what the effects of the free edge boundary conditions (FEBs) are on our system since, as mentioned in Chapter 5, we will be studying incommensurate phases, which imply that periodic boundary conditions (PBCs) cannot be implemented. To this end, we will benchmark our code by studying the Heisenberg-Kitaev model on the honeycomb lattice,

$$\mathscr{H} = J \sum_{<ij>} \mathbf{S}_i \cdot \mathbf{S}_j + K \sum_{<ij>} \sum_{\gamma} S_i^{\gamma} S_j^{\gamma}. \tag{B.1}$$

This model contains exactly solvable points and has been studied in detail by Price *et. al* [126] via Monte Carlo simulations employing PBCs. We will reproduce some of the results in Ref. [126], to show how (in the case of FEBs), at big enough system sizes we recover the bulk behavior expected from a simulation employing PBCs.

We perform Monte Carlo simulations on the Hamiltonian shown in Eq. B.1, for sizes ranging from 24 to 5400 sites. The temperature of the simulations is consistently chosen as $T = 0.001$. We employ 2×10^5 Monte Carlo sweeps from which 1×10^5 are used as equilibration steps. The runtime for 2400 sites comprised 1.5 days of CPU time on a single node, as the Metropolis algorithm cannot be parallelized. We concentrate here in the behavior of a simple Metropolis-Hastings algorithm, without recurring to parallel tempering or iterative minimization schemes, to test the effectiveness of the Monte Carlo code. In this thesis further modifications of the code were performed to reduce the effects of domain walls and of rough energy landscapes as mentioned in chapter 5.

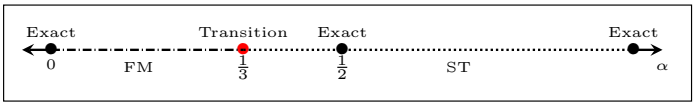

Figure B1: Phase diagram for the Heisenberg-Kitaev model. We observe a phase transition from a ferromagnetic state to a stripy phase occurring at $\alpha = 1/3$. The points $\alpha = 0$, $\alpha = 0.5$, and $\alpha \to \infty$ are exactly solvable, where $\alpha = 0.5$ presents an emergent SU(2) symmetry.

We have mapped the phase diagram for the Heisenberg-Kitaev model. We parametrized the exchange couplings as $K = 2\alpha$ and $J = 1-\alpha$ and calculated the ground state for values between $\alpha = 0$ and $\alpha = 1$. We show the phase diagram in Fig. B1.

The phase diagram exhibits two phases, at $\alpha < 1/3$ we obtain a ferromagnetic state, while for $\alpha > 1/3$ the state is a triple degenerated stripy phase. We have described the stripy phase in Chapter 6. This phase is degenerated owing to the symmetries of the Kitaev interaction, allowing for the three possible stripy phases, st-X, st-Y, and st-Z.

B.1 Real space configuration

Since the Heisenberg-Kitaev model does not contain bond dependent interactions, we will select the lattice plane as the Cartesian XY-plane, and observe the real space spin pattern on the YZ plane where both Néel and stripy phases are easy to distinguish. We will choose to show phases where the spins are oriented maximally in the z-direction to ease the comparison, but states where spins are aligned in other directions are also possible, and have been also obtained within our approach.

We study the real space configurations for different values of α to compare with the low temperature results of [126]. We show the results for $\alpha = 0$, $\alpha = 0.5$, and $\alpha = 0.75$ obtained from a calculation employing 216 sites.

For the case $\alpha = 0$ we recover the antiferromagnetic Heisenberg model. In Fig B2 we show one of the simulations performed, in which the system exhibits a Neel order, where (in this case) the spins are ordered ferromagnetically on the z directions. In this case the lattice can be partitioned into two sublattices where the spins in one sublattice points in the [001] direction (red arrows) while on the other sublattice the spins points in the $[00\bar{1}]$ direction (pink arrows).

For the stripy phases,we show the spin pattern for $\alpha = 0.75$ (Fig. B3). In this case we observe that in the center of the system, the spins point in two directions forming stripes that span the system. In this case we separate the system in four sublattices, two with spins pointing in the $+z$ directions (red and pink spins), and two in the $-z$ (blue

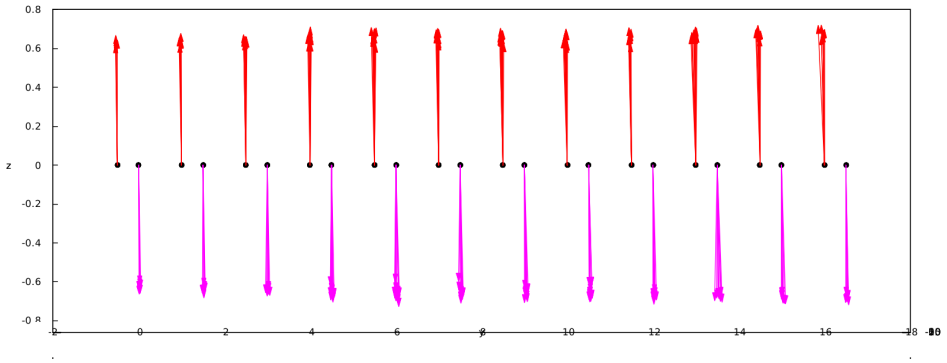

Figure B2: YZ plane of the real space configuration for the $\alpha = 0$ case.

and green). The finite size effects are noticeable here, where the spins deviate from the $\pm z$ orientation, and where this deviation is more pronounced at the boundaries of the system. Even for this small system size, where the finite size effects are considerable, the simulation already reproduces the known results for the Heisenberg-Kitaev model for these parameters.

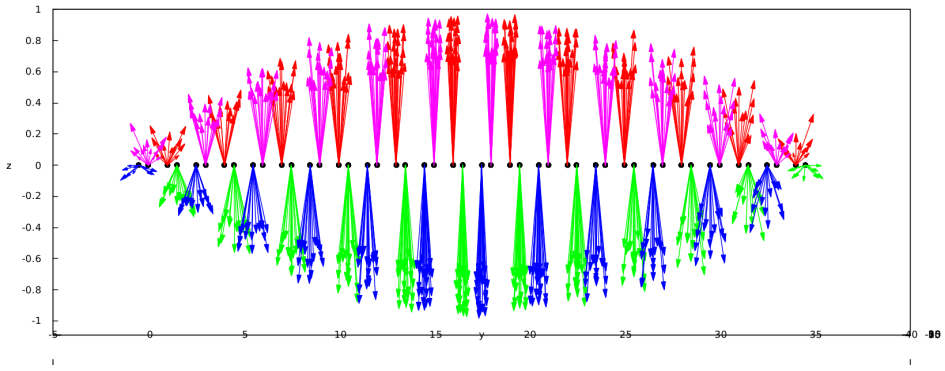

Figure B3: YZ plane of the real space configuration for the $\alpha = 0.75$ case.

For the stripy an important point needs to be mentioned. The point $\alpha = 0.5$ is special, since at this point the obtained stripy phase becomes and exact ground state of the system, which can be seen as a ferromagnetic state in a rotated basis. It can be proven also that in this case the system exhibits a SU(2) symmetry [126]. In Fig.B4 we show a spin pattern for this case. The ground state realizes a stripy phase, but in this particular case the spins are not arranged along only one direction, owing to the emergent symmetry of the state. While in the $\alpha = 0.5$ case some disorder in the state can be seen, these finite size effects are not as pronounced as in the rest of the stripy state.

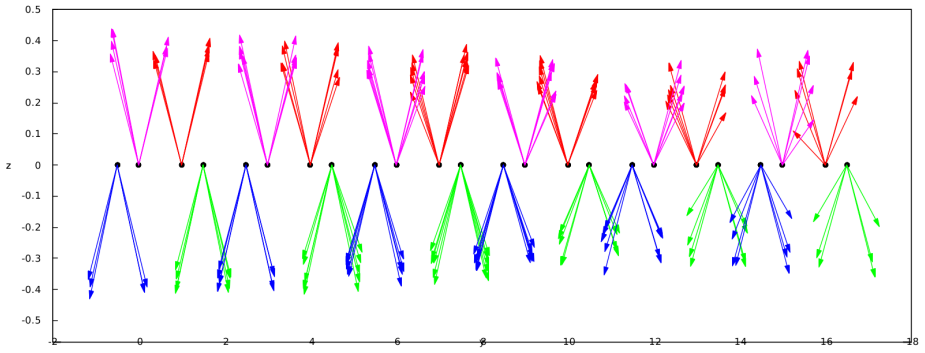

Figure B4: YZ plane of the real space configuration for the case $\alpha = 0.5$ which presents an emergent SU(2) symmetry.

These findings coincide with what was reported in Ref. [126] for the full phase diagram. We have purposefully showed results for a relatively small system size (216 sites), to exemplify the effect of FEBs. In the following we will calculate the Fourier transform of the correlation function and study in detail how the finite size effects shown here for small systems could affect bigger system sizes.

B.2 Correlation function

We proceed to show in Fig. B5 the Fourier transform of the correlation function for both the antiferromagnetic and stripy phases, obtained from simulations on 2400 sites.

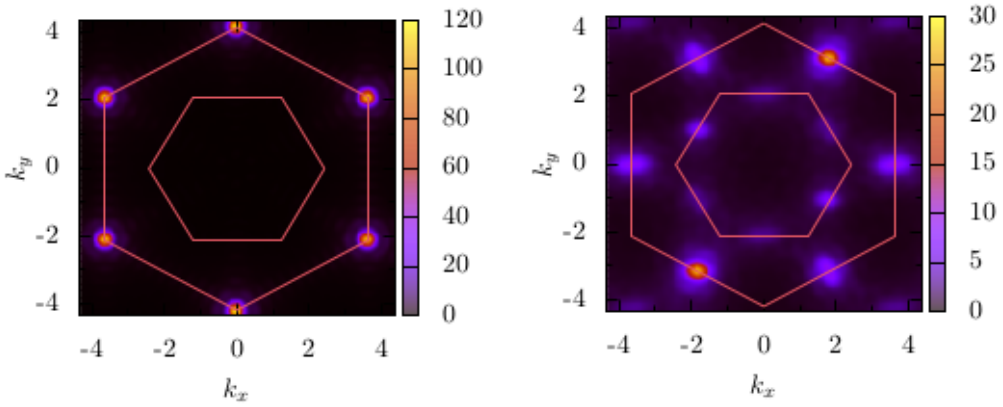

Figure B5: Fourier transform of the correlation function. *Left*: AF state for $\alpha = 0$. *Right*: Stripy phase for $\alpha = 0.75$

Fig. B5(left) shows the Fourier transform for the antiferromagnetic state. We observe the distinct features of the Néel phase, presenting maxima at the corners of the extended Brillouin zone. On the other hand, the stripy phase (Fig. B5, right) presents two maxima as well as secondary maxima on the sides of the extended Brillouin zone. This maxima indicate that, in this particular simulation, the state is dominated by a st-Y phase. The secondary maxima on the sides of the extended Brillouin are effects arising from the FEBs, where small regions of the system realize the other two degenerate stripy phase. These regions can take the form of magnetic domains, or can be generated by the presence of a domain wall as we will see in the following section.

B.3 FEBs effect on big system sizes

Even though the effect of FEBs is still noticeable in system sizes as big as 2400 sites, the behavior of the system is not radically affected by them. While the presence of FEBs has the tendency to generate domain walls where the ground state might be degenerate, the simulations consistently converge to states that correspond the true behavior of the system.

In the following, we show the results of two identical simulations, run with different stochastic seeds, for the case $\alpha = 0.75$ and 5400 sites. In this case, both simulations converge to the stripy phase on the z-direction. Fig. B6 shows the stripy phase for a simulation in which no domain walls have been generated. In this case, away from the bulk the spins deviate from their $\pm z$ orientation, but it is only close to the edges of the system where the effects of FEBs destroy the stripy order. Furthermore, these deviations do not take any form. When the spins deviate from the $\pm z$ direction, they do it by inducing a non-zero x- and/or y-spin components arranged according to the st-X and st-Y phases.

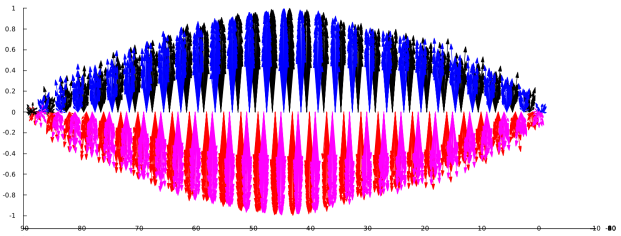

Figure B6: Real space snapshot of the XZ plane for the ground state of the case $\alpha = 0.75$ case using 5400 sites.

On the other hand, Fig. B7 shows a spin pattern where a domain wall has been generated in the middle of the system. In this case, both sides of the domain wall present a stripy order, but the orientation of the sublattices is flipped. In this case, the domain wall also generate non-zero x- y-spin components which are arranged accordingly to the st-X and st-Y phases.

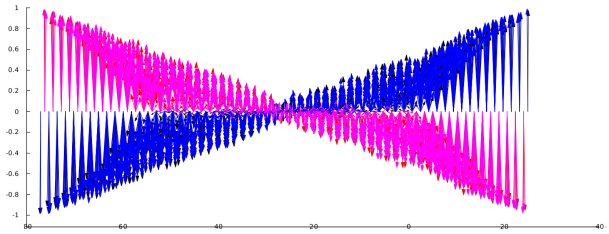

Figure B7: Real space snapshot of the XZ plane for a local minima spin configuration for the $\alpha = 0.75$ case using 5400 sites.

While in Fig B7 the effects of FEBs seem to be more noticeable than in Fig.B6, the correlations for both states are the same, i.e, the Fourier transform of the correlation function presents the same characteristics as Fig. B5.

In this thesis we will implement further algorithms to minimize the effect of FEBs, but while their effect can be minimized, they cannot be eliminated eliminated. To eliminate them entirely, we would have to implement periodic boundary conditions, which are not compatible with the incommensurate states we wish to study.

With this in mind, and the comparison of our results to the work in Ref. [126], we are ensured that while FEBs will induce domains (when the ground state is degenerated) and edge defects in the systems, these effects will not modify the nature of the studied system nor their correlations. If the simulations is able to converge to a low temperature state (please note that here we are not considering other effects such as local minima or critical slowing down of dynamics which would mean the simulation might never converge) then we are confident that this state will be a low temperature state of the studied Hamiltonian.

BIBLIOGRAPHY

[1] S. M. Winter, Y. Li, H. O. Jeschke, and R. Valentí, "Challenges in design of kitaev materials: Magnetic interactions from competing energy scales," *Phys. Rev. B*, vol. 93, p. 214431, Jun 2016.

[2] K. Yosida, "Magnetic properties of cu-mn alloys," *Phys. Rev.*, vol. 106, pp. 893–898, Jun 1957.

[3] J. Kondo, "Resistance minimum in dilute magnetic alloys," *Progress of Theoretical Physics*, vol. 32, no. 1, pp. 37–49, 1964.

[4] W. Heisenberg, "Zur theorie des ferromagnetismus," *Zeitschrift für Physik*, vol. 49, pp. 619–636, Sep 1928.

[5] P. W. Anderson *Materials Research Bulletin*, vol. 8, p. 153, 1973.

[6] P. W. ANDERSON, "The resonating valence bond state in la2cuo4 and superconductivity," *Science*, vol. 235, no. 4793, pp. 1196–1198, 1987.

[7] Y. Saito and K. Igeta, "Antiferromagnetic ising model on a triangular lattice," *Journal of the Physical Society of Japan*, vol. 53, no. 9, pp. 3060–3069, 1984.

[8] M. L. Baez and J. Reuther, "Numerical treatment of spin systems with unrestricted spin length s: A functional renormalization group study," *Phys. Rev. B*, vol. 96, p. 045144, Jul 2017.

[9] A. Kitaev, "Anyons in an exactly solved model and beyond," *Annals of Physics*, vol. 321, no. 1, pp. 2 – 111, 2006.
January Special Issue.

[10] J. M. Kosterlitz and D. J. Thouless, "Ordering, metastability and phase transitions in two-dimensional systems," *Journal of Physics C: Solid State Physics*, vol. 6, no. 7, p. 1181, 1973.

[11] S. M. A. Tabei, M. J. P. Gingras, Y.-J. Kao, P. Stasiak, and J.-Y. Fortin, "Induced random fields in the $liho_xy_{1-x}f_4$ quantum ising magnet in a transverse magnetic field," *Phys. Rev. Lett.*, vol. 97, p. 237203, Dec 2006.

[12] T.-H. Han, J. S. Helton, S. Chu, D. G. Nocera, J. A. Rodriguez-Rivera, C. Broholm, and Y. S. Lee, "Fractionalized excitations in the spin-liquid state of a kagome-lattice antiferromagnet," *Nature*, vol. 492, pp. 406 EP –, Dec 2012.

[13] A. Banerjee, J. Yan, J. Knolle, C. A. Bridges, M. B. Stone, M. D. Lumsden, D. G. Mandrus, D. A. Tennant, R. Moessner, and S. E. Nagler, "Neutron scattering in the proximate quantum spin liquid α-$rucl_3$," *Science*, vol. 356, no. 6342, pp. 1055–1059, 2017.

[14] S. C. Williams, R. D. Johnson, F. Freund, S. Choi, A. Jesche, I. Kimchi, S. Manni, A. Bombardi, P. Manuel, P. Gegenwart, and R. Coldea, "Incommensurate counterrotating magnetic order stabilized by kitaev interactions in the layered honeycomb $\alpha-li_2iro_3$," *Phys. Rev. B*, vol. 93, p. 195158, May 2016.

[15] S. T. Bramwell and M. J. P. Gingras, "Spin ice state in frustrated magnetic pyrochlore materials," *Science*, vol. 294, no. 5546, pp. 1495–1501, 2001.

[16] Z. Zhu, P. A. Maksimov, S. R. White, and A. L. Chernyshev, "Disorder-induced mimicry of a spin liquid in $ybmggao_4$," *Phys. Rev. Lett.*, vol. 119, p. 157201, Oct 2017.

[17] L. D. C. Jaubert and P. C. W. Holdsworth, "Magnetic monopole dynamics in spin ice," *Journal of Physics: Condensed Matter*, vol. 23, no. 16, p. 164222, 2011.

[18] S. R. Dunsiger, R. F. Kiefl, K. H. Chow, B. D. Gaulin, M. J. P. Gingras, J. E. Greedan, A. Keren, K. Kojima, G. M. Luke, W. A. MacFarlane, N. P. Raju, J. E. Sonier, Y. J. Uemura, and W. D. Wu, "Muon spin relaxation investigation of the spin dynamics of geometrically frustrated antiferromagnets $y_2mo_2o_7$ and $tb_2mo_2o_7$," *Phys. Rev. B*, vol. 54, pp. 9019–9022, Oct 1996.

[19] D. A. Garanin and B. Canals, "Classical spin liquid: Exact solution for the infinite-component antiferromagnetic model on the kagome lattice," *Phys. Rev. B*, vol. 59, pp. 443–456, Jan 1999.

[20] M. L. Baez and R. A. Borzi, "The 3d kasteleyn transition in dipolar spin ice: a numerical study with the conserved monopoles algorithm," *Journal of Physics: Condensed Matter*, vol. 29, no. 5, p. 055806, 2017.

[21] Z.-X. Li, Y.-F. Jiang, and H. Yao, "Majorana-time-reversal symmetries: A fundamental principle for sign-problem-free quantum monte carlo simulations," *Phys. Rev. Lett.*, vol. 117, p. 267002, Dec 2016.

[22] N. Onishi, K. Oka, M. Azuma, Y. Shimakawa, Y. Motome, T. Taniguchi, M. Hiraishi, M. Miyazaki, T. Masuda, A. Koda, K. M. Kojima, and R. Kadono, "Magnetic ground state of the frustrated honeycomb lattice antiferromagnet $bi_3mn_4o_{12}(no_3)$," *Phys. Rev. B*, vol. 85, p. 184412, May 2012.

[23] M. Heinrich, H.-A. Krug von Nidda, A. Loidl, N. Rogado, and R. J. Cava, "Potential signature of a kosterlitz-thouless transition in $bani_2v_2o_8$," *Phys. Rev. Lett.*, vol. 91, p. 137601, Sep 2003.

[24] S. Okubo, F. Elmasry, W. Zhang, M. Fujisawa, T. Sakurai, H. Ohta, M. Azuma, O. A. Sumirnova, and N. Kumada, "High-field esr measurements of s =3/2 honeycomb lattice antiferromagnet bi 3 mn 4 o 12 (no 3)," *Journal of Physics: Conference Series*, vol. 200, no. 2, p. 022042, 2010.

[25] N. Rogado, Q. Huang, J. W. Lynn, A. P. Ramirez, D. Huse, and R. J. Cava, "$bani_2v_2o_8$: a two-dimensional honeycomb antiferromagnet," *Phys. Rev. B*, vol. 65, p. 144443, Apr 2002.

[26] P. W. Anderson, "Antiferromagnetism. theory of superexchange interaction," *Phys. Rev.*, vol. 79, pp. 350–356, Jul 1950.

[27] P. W. Anderson, "New approach to the theory of superexchange interactions," *Phys. Rev.*, vol. 115, pp. 2–13, Jul 1959.

[28] I. Nándori, "Bosonization and functional renormalization group approach in the framework of qed_2," *Phys. Rev. D*, vol. 84, p. 065024, Sep 2011.

[29] M.-F. Li and M. Luo, "Functional renormalization flow and dynamical chiral symmetry breaking of qcd," *Phys. Rev. D*, vol. 85, p. 085027, Apr 2012.

[30] B. J. Schaefer and J. Wambach, "Renormalization group approach towards the qcd phase diagram," *Physics of Particles and Nuclei*, vol. 39, pp. 1025–1032, Dec 2008.

[31] T. Yokota, T. Kunihiro, and K. Morita, "Functional renormalization group analysis of the soft mode at the qcd critical point," *Progress of Theoretical and Experimental Physics*, vol. 2016, no. 7, p. 073D01, 2016.

[32] D. Benedetti and V. Lahoche, "Functional renormalization group approach for tensorial group field theory: a rank-6 model with closure constraint," *Classical and Quantum Gravity*, vol. 33, no. 9, p. 095003, 2016.

[33] A. Eichhorn and T. Koslowski, "Continuum limit in matrix models for quantum gravity from the functional renormalization group," *Phys. Rev. D*, vol. 88, p. 084016, Oct 2013.

[34] A. Codello, *A novel functional renormalization group framework for gauge theories and gravity*.
PhD thesis, Mainz U., Inst. Phys., 2010.

[35] J. Reuther and P. Wölfle, "J_1-J_2 frustrated two-dimensional heisenberg model: Random phase approximation and functional renormalization group," *Phys. Rev. B*, vol. 81, p. 144410, Apr 2010.

[36] P. Kopietz, L. Bartosch, and F. Schütz, *Introduction to the functional renormalization group*.
Springer, 2010.

[37] A. A. Abrikosov *Physics (Long Island City, NY)*, vol. 2, p. 5, 1965.

[38] V. Popov and S. A. Fedotov, "The functional-integration method and diagram technique for spin systems," *Zh. Eksp. Teor. Fiz.*, vol. 94, 1988.

[39] M. Salmhofer, C. Honerkamp, W. Metzner, and O. Lauscher, "Renormalization group flows into phases with broken symmetry," *Progress of Theoretical Physics*, vol. 112, no. 6, pp. 943–970, 2004.

[40] W. Metzner, M. Salmhofer, C. Honerkamp, V. Meden, and K. Schönhammer, "Functional renormalization group approach to correlated fermion systems," *Rev. Mod. Phys.*, vol. 84, pp. 299–352, Mar 2012.

[41] C. Platt, W. Hanke, and R. Thomale, "Functional renormalization group for multi-orbital fermi surface instabilities," *Advances in Physics*, vol. 62, no. 4-6, pp. 453–562, 2013.

[42] T. R. MORRIS, "The exact renormalization group and approximate solutions," *International Journal of Modern Physics A*, vol. 09, no. 14, pp. 2411–2449, 1994.

[43] A. A. Katanin, "Fulfillment of ward identities in the functional renormalization group approach," *Phys. Rev. B*, vol. 70, p. 115109, Sep 2004.

[44] J. Reuther and P. Wölfle, "J_1–J_2 frustrated two-dimensional heisenberg model: Random phase approximation and functional renormalization group," *Phys. Rev. B*, vol. 81, p. 144410, Apr 2010.

[45] S. T. Bramwell and M. J. P. Gingras, "Spin ice state in frustrated magnetic pyrochlore materials," *Science*, vol. 294, no. 5546, pp. 1495–1501, 2001.

[46] A. P. Ramirez, A. Hayashi, R. J. Cava, R. Siddharthan, and B. S. Shastry, "Zero-point entropy in /'spin ice/'," *Nature*, vol. 399, pp. 333–335, 05 1999.

[47] C. Castelnovo, R. Moessner, and S. L. Sondhi, "Magnetic monopoles in spin ice," *Nature*, vol. 451, pp. 42–45, 01 2008.

[48] D. Bergman, J. Alicea, E. Gull, S. Trebst, and L. Balents, "Order-by-disorder and spiral spin-liquid in frustrated diamond-lattice antiferromagnets," *Nature Physics*, vol. 3, pp. 487 EP –, May 2007.
Article.

[49] T. Suzuki, H. Nagai, M. Nohara, and H. Takagi, "Melting of antiferromagnetic ordering in spinel oxide coal 2 o 4," *Journal of Physics: Condensed Matter*, vol. 19, no. 14, p. 145265, 2007.

[50] N. Tristan, J. Hemberger, A. Krimmel, H.-A. Krug von Nidda, V. Tsurkan, and A. Loidl, "Geometric frustration in the cubic spinels $m\mathrm{al_2o_4}$ (m = Co, fe, and mn)," *Phys. Rev. B*, vol. 72, p. 174404, Nov 2005.

[51] I. Affleck, T. Kennedy, E. H. Lieb, and H. Tasaki, "Rigorous results on valence-bond ground states in antiferromagnets," *Phys. Rev. Lett.*, vol. 59, pp. 799–802, Aug 1987.

[52] H. Yao, S.-C. Zhang, and S. A. Kivelson, "Algebraic spin liquid in an exactly solvable spin model," *Phys. Rev. Lett.*, vol. 102, p. 217202, May 2009.

[53] T.-C. Wei, I. Affleck, and R. Raussendorf, "Affleck-kennedy-lieb-tasaki state on a honeycomb lattice is a universal quantum computational resource," *Phys. Rev. Lett.*, vol. 106, p. 070501, Feb 2011.

[54] T. Picot and D. Poilblanc, "Nematic and supernematic phases in kagome quantum antiferromagnets under the influence of a magnetic field," *Phys. Rev. B*, vol. 91, p. 064415, Feb 2015.

[55] Z.-X. Liu, Y. Zhou, and T.-K. Ng, "Fermionic theory for quantum antiferromagnets with spin $s > \frac{1}{2}$," *Phys. Rev. B*, vol. 82, p. 144422, Oct 2010.

[56] I. Affleck and F. D. M. Haldane, "Critical theory of quantum spin chains," *Phys. Rev. B*, vol. 36, pp. 5291–5300, Oct 1987.

[57] A. Singh, "Quantum corrections in an antiferromagnet: A systematic diagrammatical treatment of the hubbard model," *Phys. Rev. B*, vol. 43, pp. 3617–3625, Feb 1991.

[58] J. Brinckmann and P. Wölfle, "Auxiliary-fermion approach to critical fluctuations in the two-dimensional quantum antiferromagnetic heisenberg model," *Phys. Rev. B*, vol. 70, p. 174445, Nov 2004.

[59] J. Reuther, D. A. Abanin, and R. Thomale, "Magnetic order and paramagnetic phases in the quantum J_1-J_2-J_3 honeycomb model," *Phys. Rev. B*, vol. 84, p. 014417, Jul 2011.

[60] A. Mulder, R. Ganesh, L. Capriotti, and A. Paramekanti, "Spiral order by disorder and lattice nematic order in a frustrated heisenberg antiferromagnet on the honeycomb lattice," *Phys. Rev. B*, vol. 81, p. 214419, Jun 2010.

[61] J. Oitmaa and R. R. P. Singh, "Phase diagram of the $J_1 - J_2 - J_3$ heisenberg model on the honeycomb lattice: A series expansion study," *Phys. Rev. B*, vol. 84, p. 094424, Sep 2011.

[62] A. F. Albuquerque, D. Schwandt, B. Hetényi, S. Capponi, M. Mambrini, and A. M. Läuchli, "Phase diagram of a frustrated quantum antiferromagnet on the honeycomb lattice: Magnetic order versus valence-bond crystal formation," *Phys. Rev. B*, vol. 84, p. 024406, Jul 2011.

[63] J. B. Fouet, P. Sindzingre, and C. Lhuillier, "An investigation of the quantum j_1-j_2-j_3 model on the honeycomb lattice," *Eur. Phys. J. B*, vol. 20, no. 2, pp. 241–254, 2001.

[64] H. Mosadeq, F. Shahbazi, and S. A. Jafari, "Plaquette valence bond ordering in a j_1-j_2 heisenberg antiferromagnet on a honeycomb lattice," *Journal of Physics: Condensed Matter*, vol. 23, no. 22, p. 226006, 2011.

[65] X.-L. Yu, D.-Y. Liu, P. Li, and L.-J. Zou *Physica E: Low-dimensional Systems and Nanostructures*, vol. 59, p. 41, 2014.

[66] Z. Zhu, D. A. Huse, and S. R. White, "Weak plaquette valence bond order in the s=1/2 honeycomb J_1–J_2 heisenberg model," *Phys. Rev. Lett.*, vol. 110, p. 127205, Mar 2013.

[67] R. Ganesh, J. van den Brink, and S. Nishimoto, "Deconfined criticality in the frustrated heisenberg honeycomb antiferromagnet," *Phys. Rev. Lett.*, vol. 110, p. 127203, Mar 2013.

[68] S.-S. Gong, D. N. Sheng, O. I. Motrunich, and M. P. A. Fisher, "Phase diagram of the spin-$\frac{1}{2}$ J_1-J_2 heisenberg model on a honeycomb lattice," *Phys. Rev. B*, vol. 88, p. 165138, Oct 2013.

[69] H. Zhang and C. A. Lamas, "Exotic disordered phases in the quantum J_1-J_2 model on the honeycomb lattice," *Phys. Rev. B*, vol. 87, p. 024415, Jan 2013.

[70] R. F. Bishop, P. H. Y. Li, and C. E. Campbell *Journal of Physics: Condensed Matter*, vol. 25, no. 30, p. 306002, 2013.

[71] P. H. Y. Li, R. F. Bishop, D. J. J. Farnell, and C. E. Campbell, "Phase diagram of a frustrated heisenberg antiferromagnet on the honeycomb lattice: The J_1-J_2-J_3 model," *Phys. Rev. B*, vol. 86, p. 144404, Oct 2012.

[72] F. Mezzacapo and M. Boninsegni, "Ground-state phase diagram of the quantum $J_1 - J_2$ model on the honeycomb lattice," *Phys. Rev. B*, vol. 85, p. 060402, Feb 2012.

[73] R. F. Bishop, P. H. Y. Li, D. J. J. Farnell, and C. E. Campbell *Journal of Physics: Condensed Matter*, vol. 24, no. 23, p. 236002, 2012.

[74] E. Rastelli, A. Tassi, and L. Reatto *Physica B*, vol. 97, p. 1, 1979.

[75] S. Katsura, T. Ide, and T. Morita, "The ground states of the classical heisenberg and planar models on the triangular and plane hexagonal lattices," *Journal of Statistical Physics*, vol. 42, no. 3, pp. 381–404, 1986.

[76] S.-S. Gong, W. Zhu, and D. N. Sheng, "Quantum phase diagram of the spin-1 J_1-J_2 heisenberg model on the honeycomb lattice," *Phys. Rev. B*, vol. 92, p. 195110, Nov 2015.

[77] P. H. Y. Li and R. F. Bishop, "Ground-state phases of the spin-1J_1-J_2 heisenberg antiferromagnet on the honeycomb lattice," *Phys. Rev. B*, vol. 93, p. 214438, Jun 2016.

[78] J. M. Luttinger and L. Tisza, "Theory of dipole interaction in crystals," *Phys. Rev.*, vol. 70, pp. 954–964, Dec 1946.

[79] J. M. Luttinger, "A note on the ground state in antiferromagnetics," *Phys. Rev.*, vol. 81, pp. 1015–1018, Mar 1951.

[80] M. F. Lapa and C. L. Henley *arXiv:1210.6810*, unpublished.

[81] I. Kimchi and A. Vishwanath, "Kitaev-heisenberg models for iridates on the triangular, hyperkagome, kagome, fcc, and pyrochlore lattices," *Phys. Rev. B*, vol. 89, p. 014414, Jan 2014.

[82] S. R. Sklan and C. L. Henley, "Nonplanar ground states of frustrated antiferromagnets on an octahedral lattice," *Phys. Rev. B*, vol. 88, p. 024407, Jul 2013.

[83] S. Nishimoto, V. M. Katukuri, V. Yushankhai, H. Stoll, U. K. Rößler, L. Hozoi, I. Rousochatzakis, and J. van den Brink, "Strongly frustrated triangular spin lattice emerging from triplet dimer formation in honeycomb li2iro3," *Nature Communications*, vol. 7, pp. 10273 EP –, 01 2016.

[84] P. H. Y. Li, R. F. Bishop, and C. E. Campbell, "Frustrated heisenberg antiferromagnet on the honeycomb lattice with spin quantum number $s \geqslant 1$," *Journal of Physics: Conference Series*, vol. 702, no. 1, p. 012001, 2016.

[85] S. Dong, R. Yu, S. Yunoki, J.-M. Liu, and E. Dagotto, "Origin of multiferroic spiral spin order in the $r\mathrm{mno}_3$ perovskites," *Phys. Rev. B*, vol. 78, p. 155121, Oct 2008.

[86] X. Yao and Q. Li, "Monte carlo simulation on rotation of ferroelectric polarization by rotating magnetic field in conical-spin–ordered multiferroics," *EPL (Europhysics Letters)*, vol. 88, no. 4, p. 47002, 2009.

[87] M. Lilienblum, T. Lottermoser, S. Manz, S. M. Selbach, A. Cano, and M. Fiebig, "Ferroelectricity in the multiferroic hexagonal?manganites," *Nature Physics*, vol. 11, pp. 1070 EP –, Sep 2015.

[88] T. Fennell, P. P. Deen, A. R. Wildes, K. Schmalzl, D. Prabhakaran, A. T. Boothroyd, R. J. Aldus, D. F. McMorrow, and S. T. Bramwell, "Magnetic coulomb phase in the spin ice ho2ti2o7," *Science*, vol. 326, no. 5951, pp. 415–417, 2009.

[89] J. G. Rau and M. J. P. Gingras, "Spin slush in an extended spin ice model," *Nature Communications*, vol. 7, pp. 12234 EP –, Jul 2016.

[90] C. Castelnovo, R. Moessner, and S. L. Sondhi, "Magnetic monopoles in spin ice," *Nature*, vol. 451, Jan 2008.

[91] C. Paulsen, M. J. Jackson, E. Lhotel, B. Canals, D. Prabhakaran, K. Matsuhira, S. R. Giblin, and S. T. Bramwell, "Far-from-equilibrium monopole dynamics in spin ice," *Nature Physics*, vol. 10, pp. 135 EP –, Jan 2014.

[92] J.-S. Wang and R. H. Swendsen, "Replica monte carlo simulation (revisited)," *Progress of Theoretical Physics Supplement*, vol. 157, pp. 317–323, 2005.

[93] N. Metropolis and S. Ulam, "The monte carlo method," *Journal of the American Statistical Association*, vol. 44, no. 247, pp. 335–341, 1949.
PMID: 18139350.

[94] N. Metropolis, A. W. Rosenbluth, M. N. Rosenbluth, A. H. Teller, and E. Teller, "Equation of state calculations by fast computing machines," *The Journal of Chemical Physics*, vol. 21, no. 6, pp. 1087–1092, 1953.

[95] W. K. HASTINGS, "Monte carlo sampling methods using markov chains and their applications," *Biometrika*, vol. 57, no. 1, pp. 97–109, 1970.

[96] G. Haag, *Derivation of the Chapman–Kolmogorov Equation and the Master Equation*, pp. 39–61.
Cham: Springer International Publishing, 2017.

[97] U. Wolff, "Collective monte carlo updating for spin systems," *Phys. Rev. Lett.*, vol. 62, pp. 361–364, Jan 1989.

[98] R. H. Swendsen and J.-S. Wang, "Nonuniversal critical dynamics in monte carlo simulations," *Phys. Rev. Lett.*, vol. 58, pp. 86–88, Jan 1987.

[99] G. Marsaglia, "Choosing a point from the surface of a sphere," *Ann. Math. Statist.*, vol. 43, pp. 645–646, 04 1972.

[100] R. H. Swendsen and J.-S. Wang, "Replica monte carlo simulation of spin-glasses," *Phys. Rev. Lett.*, vol. 57, pp. 2607–2609, Nov 1986.

[101] C. Predescu, M. Predescu, and C. V. Ciobanu, "The incomplete beta function law for parallel tempering sampling of classical canonical systems," *The Journal of Chemical Physics*, vol. 120, no. 9, pp. 4119–4128, 2004.

[102] H. G. Katzgraber, S. Trebst, D. A. Huse, and M. Troyer, "Feedback-optimized parallel tempering monte carlo," *Journal of Statistical Mechanics: Theory and Experiment*, vol. 2006, no. 03, p. P03018, 2006.

[103] L. R. Walker and R. E. Walstedt, "Computer model of metallic spin-glasses," *Phys. Rev. Lett.*, vol. 38, pp. 514–518, Feb 1977.

[104] S. R. Sklan and C. L. Henley, "Nonplanar ground states of frustrated antiferromagnets on an octahedral lattice," *Phys. Rev. B*, vol. 88, p. 024407, Jul 2013.

[105] Z. Nussinov and J. van den Brink, "Compass models: Theory and physical motivations," *Rev. Mod. Phys.*, vol. 87, pp. 1–59, Jan 2015.

[106] Y. Singh and P. Gegenwart, "Antiferromagnetic mott insulating state in single crystals of the honeycomb lattice material na_2iro_3," *Phys. Rev. B*, vol. 82, p. 064412, Aug 2010.

[107] Y. Singh, S. Manni, J. Reuther, T. Berlijn, R. Thomale, W. Ku, S. Trebst, and P. Gegenwart, "Relevance of the heisenberg-kitaev model for the honeycomb lattice iridates A_2iro_3," *Phys. Rev. Lett.*, vol. 108, p. 127203, Mar 2012.

[108] T. Takayama, A. Kato, R. Dinnebier, J. Nuss, H. Kono, L. S. I. Veiga, G. Fabbris, D. Haskel, and H. Takagi, "Hyperhoneycomb iridate $\beta-li_2iro_3$ as a platform for kitaev magnetism," *Phys. Rev. Lett.*, vol. 114, p. 077202, Feb 2015.

[109] K. A. Modic, T. E. Smidt, I. Kimchi, N. P. Breznay, A. Biffin, S. Choi, R. D. Johnson, R. Coldea, P. Watkins-Curry, G. T. McCandless, J. Y. Chan, F. Gandara, Z. Islam, A. Vishwanath, A. Shekhter, R. D. McDonald, and J. G. Analytis, "Realization of a three-dimensional spin-anisotropic harmonic honeycomb iridate," *Nature Communications*, vol. 5, pp. 4203 EP –, Jun 2014.
Article.

[110] K. W. Plumb, J. P. Clancy, L. J. Sandilands, V. V. Shankar, Y. F. Hu, K. S. Burch, H.-Y. Kee, and Y.-J. Kim, "$\alpha - \mathrm{rucl}_3$," *Phys. Rev. B*, vol. 90, p. 041112, Jul 2014.

[111] T. Dey, A. V. Mahajan, P. Khuntia, M. Baenitz, B. Koteswararao, and F. C. Chou, "Spin-liquid behavior in $J_{\mathrm{eff}} = \frac{1}{2}$ triangular lattice compound $\mathrm{ba_3irti_2o_9}$," *Phys. Rev. B*, vol. 86, p. 140405, Oct 2012.

[112] S. Trebst, "Kitaev Materials," *ArXiv e-prints*, Jan. 2017.

[113] D. Pesin and L. Balents, "Mott physics and band topology in materials with strong spin-orbit interaction," *Nature Physics*, vol. 6, pp. 376 EP –, Mar 2010.

[114] F. Freund, S. C. Williams, R. D. Johnson, R. Coldea, P. Gegenwart, and A. Jesche, "Single crystal growth from separated educts and its application to lithium transition-metal oxides," *Scientific Reports*, vol. 6, pp. 35362 EP –, Oct 2016.

[115] A. Auerbach, *Interacting Electrons and Quantum Magnetism*.
Springer-Verlag, 1994.

[116] G. Jackeli and G. Khaliullin, "Mott insulators in the strong spin-orbit coupling limit: From heisenberg to a quantum compass and kitaev models," *Phys. Rev. Lett.*, vol. 102, p. 017205, Jan 2009.

[117] F. Ye, S. Chi, B. C. Chakoumakos, J. A. Fernandez-Baca, T. Qi, and G. Cao, "Magnetic and crystal structures of $\mathrm{sr_2iro_4}$: A neutron diffraction study," *Phys. Rev. B*, vol. 87, p. 140406, Apr 2013.

[118] G. Khaliullin, "Orbital order and fluctuations in mott insulators," *Progress of Theoretical Physics Supplement*, vol. 160, pp. 155–202, 2005.

[119] G. Chen and L. Balents, "Spin-orbit effects in $\mathrm{na_4ir_3o_8}$: A hyper-kagome lattice antiferromagnet," *Phys. Rev. B*, vol. 78, p. 094403, Sep 2008.

[120] J. G. Rau, E. K.-H. Lee, and H.-Y. Kee, "Generic spin model for the honeycomb iridates beyond the kitaev limit," *Phys. Rev. Lett.*, vol. 112, p. 077204, Feb 2014.

[121] J. G. Rau, E. K.-H. Lee, and H.-Y. Kee, "Spin-orbit physics giving rise to novel phases in correlated systems: Iridates and related materials," *Annual Review of Condensed Matter Physics*, vol. 7, no. 1, pp. 195–221, 2016.

[122] I. Kimchi, R. Coldea, and A. Vishwanath, "Unified theory of spiral magnetism in the harmonic-honeycomb iridates α, β, and γ li$_2$iro$_3$," *Phys. Rev. B*, vol. 91, p. 245134, Jun 2015.

[123] A. Biffin, R. D. Johnson, I. Kimchi, R. Morris, A. Bombardi, J. G. Analytis, A. Vishwanath, and R. Coldea, "Noncoplanar and counterrotating incommensurate magnetic order stabilized by kitaev interactions in $\gamma-$li$_2$iro$_3$," *Phys. Rev. Lett.*, vol. 113, p. 197201, Nov 2014.

[124] E. K.-H. Lee and Y. B. Kim, "Theory of magnetic phase diagrams in hyperhoneycomb and harmonic-honeycomb iridates," *Phys. Rev. B*, vol. 91, p. 064407, Feb 2015.

[125] E. K.-H. Lee, J. G. Rau, and Y. B. Kim, "Two iridates, two models, and two approaches: A comparative study on magnetism in three-dimensional honeycomb materials," *Phys. Rev. B*, vol. 93, p. 184420, May 2016.

[126] C. Price and N. B. Perkins, "Finite-temperature phase diagram of the classical kitaev-heisenberg model," *Phys. Rev. B*, vol. 88, p. 024410, Jul 2013.

[127] J. Reuther, R. Thomale, and S. Rachel, "Spiral order in the honeycomb iridate li$_2$iro$_3$," *Phys. Rev. B*, vol. 90, p. 100405, Sep 2014.

[128] Y. Tokura and S. Seki, "Multiferroics with spiral spin orders," *Advanced Materials*, vol. 22, no. 14, pp. 1554–1565.

[129] X. Yao, "Stable and locally stable conditions for a conical spin state in the spinel structure," *EPL (Europhysics Letters)*, vol. 102, no. 6, p. 67013, 2013.

[130] T. Kimura and Y. Tokura, "Magnetoelectric phase control in a magnetic system showing cycloidal/conical spin order," *Journal of Physics: Condensed Matter*, vol. 20, no. 43, p. 434204, 2008.

[131] S. M. Winter, A. A. Tsirlin, M. Daghofer, J. van den Brink, Y. Singh, P. Gegenwart, and R. Valentí, "Models and materials for generalized kitaev magnetism," *Journal of Physics: Condensed Matter*, vol. 29, no. 49, p. 493002, 2017.

[132] A. Ruiz, A. Frano, N. P. Breznay, I. Kimchi, T. Helm, I. Oswald, J. Y. Chan, R. J. Birgeneau, Z. Islam, and J. G. Analytis, "Correlated states in b-li2iro3 driven by applied magnetic fields," *Nature Communications*, vol. 8, no. 1, p. 961, 2017.

[133] F. L. Buessen, M. Hering, J. Reuther, and S. Trebst, "Quantum spin liquids in frustrated spin-1 diamond antiferromagnets," *Phys. Rev. Lett.*, vol. 120, p. 057201, Jan 2018.

[134] Y. Iqbal, T. Müller, P. Ghosh, M. J. P. Gingras, H. O. Jeschke, S. Rachel, J. Reuther, and R. Thomale *arXiv:1802.09546 [cond-mat.str-el]*, Feb 2018.

[135] Y. Iqbal, T. Müller, H. O. Jeschke, R. Thomale, and J. Reuther, "Stability of the spiral spin liquid in mnsc2s4," *ArXiv e-prints*, Feb 2018.

[136] D. Buessen, Finn Lasse Roscher, S. Diehl, and S. Trebst *arXiv:1711.02182 [cond-mat.str-el]*, Dec 2017.

[137] D. Roscher, F. L. Buessen, M. M. Scherer, S. Trebst, and S. Diehl *arXiv:1711.02183 [cond-mat.str-el]*, Dec 2017.

[138] A. Keleş and E. Zhao, "Absence of long-range order in a triangular spin system with dipolar interactions," *Phys. Rev. Lett.*, vol. 120, p. 187202, May 2018.

[139] A. Keleş and E. Zhao *arXiv:1803.02904 [cond-mat.quant-gas]*, March 2018.

Dedication and acknowledgements

Tea is where we explain to each other what we do not understand.

Robert Oppenheimer.

First and foremost, I want to thank my advisor, Johannes, I've become the scientist I am right now because of him, and I will be forever thankful for that.

The DCCQS has been my home for the past three years, and I am lucky to have had the chance to learn from those who make it work. Felix and Piet, I cannot begin to express how thankful I am that you two let me follow you around and ask you whatever question was in my mind. You two have been an inspiration and the best role models I could hope for. Thank you.

All of the DCCQS, lunches and coffee breaks have provided many amazing laughs, and exciting conversations, about physics or something else. You are the ones that make the institute great. The quote at the beginning of this chapter has been chosen because of how much it reminds me of our coffee breaks.

My family in Germany, Vega and Esther. Ustedes dos son las mejores hermanas, compañeras, y amigas que he encontrado en Berlin. Las cenas en su casa se sienten tan naturales como so hubiéramos estado cenando juntas desde que nací, me han acompañado y animado como si siempre hubiera sido miembro de su familia, y la diferencia que eso ha hecho en estos años es algo que siempre les voy a agradecer. Sin ustedes dos, mi estadía en Berlin hubiera sido mucho mas oscura. Las quiero.

To Jörg and Christian F. Your office was a sanctuary in the DCCQS, and you never failed to encourage me. Finishing this thesis was a lot of work, and in part I finished it thanks to you two. Because you always pushed me for more, and you never hesitated at helping me understand some FRG or numeric problem I was trying to wrap my head around. I've learned a lot from you two, and this whole science experience would not have been half as fun without you.

Christian K, I cannot remember a time in which I was as happy of having someone come into my office and start talking about solving integrals as when you did it. Whether it was numerics, analytics, physics, or politics, you always provided some of the most stimulating conversations I've had in Berlin. With that no being enough, climbing and just plainly hanging out with you has always been extremely fun, you never failed to

make me laugh out loud. Thank you for always being there to rant about whatever it was we needed to rant about, and for being a hell of a climbing partner.

To the obst office, Markus “Spin liquids, the liquids that when you drink them, make your head spin”, Andi “Bananas and pillows, I only do bananas and pillows”, and Alex “5, the Nietner number”. You guys are some of the nicest, most caring (though sometimes noisy) people I’ve had the pleasure of meeting in Berlin. Your office is the wild wide west, fruit will be thrown at you, jokes will be made, tickles will be given, and if you are not careful, a physics question will be thrown at you that will keep you thinking for days. You guys are awesome, and made the institute orders of magnitude better since you arrived, just because you are who you are.

My favorite neutron scatterers Christan B, and Alex S. I am a theorist that likes experiments, and one that if you let her, will ask you questions about your experiments for hours. Christian, you always welcomed my questions, and were happy to explain whatever I wanted to know. After that, we would always grab a beer and talk about the rest of life. Even now that you are in ORNL and me here, we still are able to keep a very beautiful friendship and collaboration. Alex, you have been the best companion and confidante, I cannot imagine something I wouldn’t tell you, and I cannot imagine a day at HZB when we wouldn’t just scape the office to gossip about whatever. HZB has been my favorite lab thanks to you.

Rico and Milan, you two are a breath of fresh air in a world full of physics. You are the ones that pull me back to the ground, and make me remember that there are other things out there besides work. You make the good moments better, and the bad moments less bad for being there. You have been the best brothers I could have asked for, and I am glad to have met such awesome people.

Finally, but not less important, to my family. A mamá y papá, mis hermanos, cuñadas, y sobrinos. Hace casi cuatro años que me fui de casa, y en ningún momento sentí que estaba de hecho lejos de casa. Me han acompañado a la distancia de una manera que nunca llegue a sentirme sola. Ustedes siempre me apoyaron a hacer todo lo que quería, aunque me llevara tan geográficamente lejos. Tener su apoyo fue una de las cosas que mas me han ayudado en estos años. Gracias!

Publication List

This thesis is based on the following papers

"Numerical treatment of spin systems with variable spin length S: A functional renormalization group study"
M. L. Baez, J. Reuther.
Phys. Rev. B 96, 045144 (2017)

"Physics of α-Li_2IrO_3: Minimal model, ground state properties, and magnetization processes."
M. L. Baez, J. Reuther.
In preparation

The following papers are not part of this thesis

"The 3D Kasteleyn transition in dipolar spin ice: a numerical study with the Conserved Monopoles Algorithm."
M. L. Baez, R. A. Borzi.
Journal of Physics: Condensed Matter 29, 055806 (2017)

"Quantum Paramagnetism and nematicity in the frustrated Heisenberg model on the BCC lattice."
M. L. Baez, Y. Iqbal, P. Ghosh, T. Müller, F. P. Toldin, J. Reuther, and R. Thomale.
In preparation

Curriculum Vitae

For reasons of data protection, the curriculum vitae is not published in the electronic version

AUTHOR'S DECLARATION

Selbstständigkeitserklärung Hiermit versichere ich, dass ich in meiner Dissertation alle Hilfsmittel und Hilfen angegeben habe, und auf dieser Grundlage die Arbeit selbstständig verfasst habe. Diese Arbeit habe ich nicht schon einmal in einem früheren Promotionsverfahren eingereicht. Berlin, Juli 2018.

SIGNED: ..... DATE: .....